

Topological Spin Textures in Synthetic Antiferromagnets: Stabilization, Nucleation and Dynamics

of (Bi)merons, Skyrmions and Skyrmion–Bimeron Pairs (Skymerons)



Dissertation

zur Erlangung des Grades

„Doktor

der Naturwissenschaften“

am Fachbereich Physik, Mathematik und Informatik

der Johannes Gutenberg-Universität

in Mainz

Mona Minakshee Manjaree Bhukta

geboren am 19th April 1997

in Deogarh, Indien

Examination date : 29th January 2026

This work is licensed under a Creative Commons Attribution 4.0 International License (CC BY 4.0).

<https://creativecommons.org/licenses/by/4.0/>

Berichtstatter: **** (Removed in the electronic version for data protection)

**** (Removed in the electronic version for data protection)

Anhänge gemäß Prüfungsordnung

I hereby declare that I wrote the dissertation submitted without any unauthorized external assistance and used only sources acknowledged in the work. All textual passages that are appropriated verbatim or paraphrased from published and unpublished texts, as well as all information obtained from oral sources, are duly indicated and listed in accordance with bibliographical rules. In carrying out this research, I complied with the rules of standard scientific practice as formulated in the statutes of Johannes Gutenberg-University Mainz to ensure standard scientific practice.

Mona Bhukta
Institut für Physik – FB 08
Staudingerweg 7
Johannes Gutenberg University
D-55128 Mainz

Dedicated to

My Parents, Nayani, Pradyumna
and my Brother Pratyush.

Abstract

In the emerging landscape of post-CMOS technologies, spintronics-based devices have garnered growing interest for their potential to enable non-volatile, energy-efficient, and densely integrated logic and memory technologies. Among the various strategies explored, the utilization of topologically non-trivial magnetic spin textures, such as skyrmions and bimerons, has emerged as a strong candidate for several spintronic devices owing to their nanoscale dimensions, topologically enhanced stability, and susceptibility to manipulation by electrical currents. While skyrmions in ferromagnets have enabled seminal advances in racetrack memories, logic gates, and unconventional computing concepts, their practical use is hampered by stray fields, limited thermal stability, and the intrinsic skyrmion Hall effect during dynamics. These challenges motivate the exploration of alternative topological spin textures beyond skyrmions and their realization in compensated magnetic systems, where antiparallel sublattice magnetizations cancel the net moment, suppress the skyrmion Hall effect, and enable the stabilization of spin textures over a broad range of magnetic fields suitable for device applications.

This thesis addresses these challenges by establishing an experimental framework to investigate the stabilization, nucleation, and dynamics of various topological spin textures stabilized by the interfacial Dzyaloshinskii–Moriya interaction (iDMI) in synthetic antiferromagnets (SyAFMs). SyAFMs, consisting of ferromagnetic layers antiferromagnetically coupled through metallic spacers, exhibit compensated spin textures with negligible net dipolar fields. Their magnetic properties can be finely tuned via the thickness of the constituent sublattices, enabling independent control over key material parameters such as the effective perpendicular magnetic anisotropy, iDMI, and saturation magnetization. This work demonstrates the stabilization of chiral in-plane antiferromagnetic topological spin textures, namely merons, antimerons, and bimerons, by primarily tuning the net effective anisotropy of the system to achieve a nearly vanishing condition [1, 2]. Perpendicular synthetic antiferromagnetic multilayers are engineered to host skyrmions with radii of 50–100 nm that exhibit distinct static

and dynamic characteristics. Element-specific pump–probe X-ray microscopy enables the sublattice-resolved nanosecond dynamic imaging of skyrmion–skyrmion interactions such as scattering, recoil, and collective flow dynamics [3]. Beyond two-dimensional spin textures, by tuning the saturation magnetization of each ferromagnetic sublattice, this thesis demonstrates a three-dimensional extension of skyrmions, referred to as hybrid skyrmion tubes [4]. Finally, this thesis introduces and experimentally realizes a new topological spin texture, termed the skymeron, which emerges from the near-orthogonal alignment of skyrmions and bimerons. Overall, these findings establish a quantitative framework for the stabilization and nucleation of various topological spin textures in synthetic antiferromagnets and demonstrate their fully reproducible collective dynamics over billions of cycles, even in the incoherent flow regime, thereby paving the way for their utilization in future spintronic devices.

Kurzzusammenfassung *

Im aufstrebenden Forschungsfeld der post-CMOS-Technologien haben spintronikbasierte Bauelemente zunehmendes Interesse erlangt, da sie das Potenzial bieten, nicht-flüchtige, energieeffiziente und hochintegrierte Logik- und Speichertechnologien zu realisieren. Unter den verschiedenen untersuchten Ansätzen hat sich die Nutzung topologisch nicht-trivialer magnetischer Spintexturen, wie Skyrmionen und Bimeronen, als vielversprechender Kandidat für spintronische Anwendungen herausgestellt. Diese Strukturen zeichnen sich durch ihre Größenordnung im Nanometerbereich, ihre topologisch bedingte Stabilität sowie leichte Beweglichkeit durch elektronische Ströme aus. Während Skyrmionen in Ferromagneten zu grundlegenden Fortschritten in Racetrack-Speichern, Logikschaltungen und unkonventionellen Rechenkonzepten geführt haben, wird ihre praktische Anwendbarkeit durch Streufelder, begrenzte thermische Stabilität und den intrinsischen Skyrmion-Hall-Effekt eingeschränkt. Diese Herausforderungen motivieren die Erforschung alternativer topologischer Spintexturen jenseits der Skyrmionen sowie deren Realisierung in kompensierten magnetischen Systemen, in denen antiparallele Untergitter-Magnetisierungen das Gesamtmoment aufheben, den Skyrmion-Hall-Effekt unterdrücken und die Stabilisierung von Spintexturen über einen großen Bereich magnetischer Felder ermöglichen, der für Applikationen geeignet ist.

Diese Arbeit begegnet diesen Herausforderungen durch die Etablierung eines experimentellen Rahmens zur Untersuchung der Stabilisierung, Nukleation und Dynamik verschiedener topologischer Spintexturen, die durch die grenzflächen Dzyaloshinskii–Moriya-Wechselwirkung ([iDMI](#)) in synthetischen Antiferromagneten ([SyAFMs](#)) stabilisiert werden. SyAFMs, bestehend aus ferromagnetischen Schichten, die über metallische Zwischenlagen antiferromagnetisch gekoppelt sind, weisen kompensierte Spintexturen mit vernachlässigbaren makroskopischen Dipolfeldern auf. Ihre magnetischen Eigenschaften lassen sich präzise über die Schichtdicke der einzelnen Untergitter-Komponenten

*ChatGPT 5 and DeepL Translate were utilized in translating the English version of the Abstract into German. I am grateful to Kilian Leutner and Robert Frömter for proofreading and revising the translation.

einstellen, wodurch eine unabhängige Kontrolle wesentlicher Materialparameter wie der effektiven senkrechten magnetischen Anisotropie, der iDMI und der Sättigungsmagnetisierung ermöglicht wird. Zunächst wird in dieser Arbeit die Stabilisierung chiraler antiferromagnetischer topologischer Spintexturen mit einem Magnetisierungshintergrund in der Filmebene – namentlich Meronen, Antimeronen und Bimeronen – demonstriert, indem vor allem die effektive Anisotropie des Gesamtsystems so eingestellt wird, dass sie nahezu verschwindet [1, 2]. Senkrecht synthetische antiferromagnetische Multilagenn werden so gestaltet, dass sie antiferromagnetische Skyrmionen mit Radien von 50–100 nm beherbergen, die ausgeprägte statische und dynamische Eigenschaften zeigen. Elementspezifische Pump-Probe-Röntgenmikroskopie ermöglicht eine subgitteraufgelöste dynamische Abbildung der Skyrmion-Skyrmion-Wechselwirkungen im Nanosekundenbereich, wie Streuung, Rückstoß und kollektive Flussdynamik [3]. Über zweidimensionale Spintexturen hinaus wird in dieser Arbeit durch gezielte Einstellung der Sättigungsmagnetisierung der einzelnen ferromagnetischen Untergitter eine dreidimensionale Erweiterung der Skyrmionen, sogenannte hybride Skyrmionröhren, in synthetischen Antiferromagneten demonstriert [4]. Abschließend wird in dieser Arbeit eine neuartige topologische Spinstruktur, das sogenannte Skymeron, eingeführt und experimentell realisiert. Diese Struktur entsteht aus der nahezu orthogonalen Ausrichtung von Skyrmionen und Bimeronen in synthetischen Antiferromagneten. Insgesamt liefern diese Ergebnisse ein quantitatives Rahmenwerk für die Stabilisierung und Nukleation verschiedener topologischer Spintexturen in synthetischen Antiferromagneten und zeigen deren vollständig reproduzierbare kollektive Dynamik über Milliarden von Zyklen, selbst im inkohärenten Flussregime, wodurch der Weg für ihre Nutzung in zukünftigen spintronischen Bauelementen geebnet wird.

Contents

1	Introduction	1
I	Theory and Methods	8
2	Theoretical Background	9
2.1	Introduction	9
2.2	Magnetism in Thin Films	10
2.2.1	Micromagnetic Framework	11
2.2.2	Heisenberg Exchange Interaction	11
2.2.3	Magnetic Anisotropy	15
2.2.4	Dzyaloshinskii-Moriya Interaction	16
2.2.5	Magnetic Dipolar Interaction	19
2.2.6	Interlayer Exchange Interaction	20
2.2.7	Zeeman Energy	21
2.3	Magnetic Spin Textures	22
2.3.1	Domain and Domain Walls	22
2.3.2	Bubbles	24
2.4	Topological Spin Textures in Magnetism	26
2.4.1	Magnetic Skyrmions	26
2.4.2	Magnetic Bimerons	31
2.5	Magnetization Dynamics	33
2.5.1	Landau-Lifshitz-Gilbert (LLG) Equation	33
2.5.2	Spin Torques Induced by Current	35
2.5.3	Spin-Orbit Torque	37
2.5.4	Skyrmion Dynamics with SOTs	41
2.5.5	Antiferromagnetic skyrmion dynamics in synthetic antiferromagnets	45

2.6	Conclusion	47
3	Experimental Techniques	48
3.1	Introduction	48
3.2	Sample Fabrication	49
3.2.1	Thin Film Deposition by Magnetron Sputtering	49
3.2.2	Measurement of Magnetic Properties	52
3.2.3	Nanofabrication by Electron Beam Lithography	54
3.3	Lab-based Magnetic Microscopy Techniques	55
3.3.1	Scanning Electron Microscopy with Polarization Analysis	56
3.3.2	Magnetic Force Microscopy	60
3.4	Synchrotron-Based Magnetic Microscopy	61
3.4.1	Synchrotron Radiation	63
3.4.2	X-ray Magnetic Circular Dichroism	63
3.4.3	Photoemission Electron Microscopy	66
3.4.4	Scanning Transmission X-ray Microscopy	67
3.4.5	Time-Resolved imaging using Pump–Probe STXM	69
II	Results and Discussion	71
4	Merons, Antimerons and Bimerons in Synthetic Antiferromagnets	72
4.1	Introduction	72
4.2	Spin Configuration of AFM (Anti)merons in a SyAFM Platform	73
4.3	Essential Considerations for the Stabilization of (Bi)merons	75
4.3.1	Material Stack Optimization	77
4.3.2	Magnetic Properties of the SyAFM Stacks	81
4.4	Multimodal 3D-Vector Imaging of (Bi)merons	83
4.4.1	Quantitative Analysis of (Anti)merons Cores	86
4.5	Manipulating the (Anti)merons	88
4.5.1	Tailoring the Helicity of (Anti)merons	88
4.5.2	Temperature-Driven Evolution of (Bi)merons	91

4.6	Direct Imaging of the Antiferromagnetic Nature of (Bi)merons	94
4.7	Micromagnetic Study of Bimeron in SyAFM	95
4.8	Conclusion	98
5	Stabilization, Nucleation, and Dynamics of Antiferromagnetic Skyrmions	100
5.1	Introduction	100
5.2	Engineering of the SyAFM Stacks to Stabilize AFM Skyrmions	102
5.3	Nucleation of AFM Skyrmions	105
5.3.1	Magnetic-Field-Induced AFM Skyrmion Nucleation	106
5.3.2	Current-Induced Nucleation of AFM Skyrmions	109
5.3.3	Infra-red Laser-Induced Nucleation of AFM Skyrmions	112
5.4	Dynamics of Antiferromagnetic Skyrmions	119
5.4.1	Dynamic Hopping of a Single AFM Skyrmion	120
5.4.2	Dynamic Imaging of AFM Skyrmion Scattering	123
5.4.3	Real-Time Investigation of the cancellation of the Skyrmion Hall Effect	135
5.5	Conclusion	138
6	Non-reciprocal Current-Induced Dynamics of Hybrid Skyrmion Tubes	140
6.1	Introduction	140
6.2	Strategy to Stabilize Hybrid Skyrmions	141
6.2.1	Observation of Hybrid Skyrmions and Néel Skyrmion Tubes	144
6.2.2	Role of Magnetic Compensation	147
6.3	Current-Induced Dynamics of SyAFM Skyrmion Tubes	148
6.3.1	Non-reciprocity in the SkHE	151
6.4	Micromagnetic Simulations of Hybrid Skyrmions	152
6.4.1	Dynamics of Hybrid Skyrmion Tubes	153
6.5	Conclusion	158
7	Skymeron: An Orthogonally Coupled Skyrmion–Bimeron Pair	159
7.1	Introduction	159
7.2	Energy Landscape to Stabilize Skyrmion–Bimeron Pair (Skymeron)	160
7.3	Experimental Conditions for the Stabilization of Skymerons	165
7.3.1	Nucleation and Observation of the Skymerons	167

7.4	Micromagnetic Study of Skymerons	173
7.5	Conclusion	176
8	Summary And Outlook	178
III	Appendices	182
A	Appendix Author Contributions for each Experimental Chapter	183
B	Appendix Additional Information for Chapter 04	185
B.1	XAS Spectra	185
B.2	XMCD-PEEM Images of Stack #M12	186
B.3	Deleting and Recreating the (Anti)merons	187
B.4	SEMPA-Based Identification of Merons and Antimerons	188
B.5	Parameters for Micromagnetic Simulation	188
B.6	Open Questions	189
C	Appendix Additional Information for Chapter 05	195
C.1	Structural and Compositional Details of the SyAFM Stacks	195
D	Appendix Additional Information for Chapter 06	198
D.1	Types of Hybrid AFM Skyrmion in SyAFM	198
D.2	Derivation of SkHE for Hybrid Skyrmion	200
D.3	Sample Optimization and Extraction of the Material Parameters	202
E	Appendix Additional Information for Chapter 07	206
E.1	MuMax ³ Code for Skymeron Stabilization	206
F	Appendix Use of AI Tools	212
	Bibliography	235
	List of Abbreviations	236
	List of Figures	257
	List of Tables	258
	Mona Minakshee Manjaree Bhukta	261
	Acknowledgements	266

Introduction

Lock up your libraries if you like; but there is no gate, no lock, no bolt that you can set upon the freedom of my mind.

Virginia Woolf, A Room of One's Own

In recent years, emerging technologies such as artificial intelligence, robotics, augmented and virtual reality, and the Internet of Things have revolutionized modern life while simultaneously placing unprecedented demands on large-scale data processing, computational power, and energy efficiency. This demand imposes stringent constraints on existing microelectronic infrastructures, with increasing requirements for speed, storage capacity, and energy efficiency that conventional complementary metal-oxide-semiconductor (CMOS) architectures struggle to meet. For several decades, the development of CMOS technology followed the trend predicted by Moore's law [5], namely that the number of transistors on an integrated circuit doubles approximately every two years, accompanied by continuous miniaturization and reduction in cost per function. At present, Moore's law approaches its physical and economic limits. At low feature sizes, quantum tunneling induces leakage currents and excessive heat dissipation, setting fundamental limits for CMOS scaling [6]. These effects restrict further miniaturization and present a fundamental challenge for conventional CMOS scaling.

This has driven interest in beyond-CMOS technologies that aim to replace or extend charge-based transistor logic. Over the years, several approaches have been proposed, including spin-based electronics (spintronics) and, more recently, orbital-based electronics (orbitronics). Spintronics exploits the intrinsic angular momentum of the electron, its spin, as an additional degree of freedom

to encode and process information. These spin-based devices form the field of "spintronics" [7, 8]. This field has witnessed significant practical applications driven by the discovery of the giant magnetoresistance (GMR) effect in 1988 [9–11], a breakthrough that enabled a rapid tenfold increase in the areal density of magnetic data storage [12] and was recognized with the Nobel Prize in Physics in 2007. The subsequent discovery of tunnel magnetoresistance (TMR) in magnetic tunnel junctions (MTJs) [13–15] further advanced the field, leading to the replacement of GMR sensors by TMR-based MTJs in read heads and storage technologies. Building on these developments, magnetoresistive random access memory (MRAM) was proposed, in which data storage relies on the relative magnetization orientation of MTJs. Conventional MRAM operated using Oersted fields generated by current-carrying lines to switch magnetization, which introduced limitations in power consumption and scalability. To overcome these challenges, spin-transfer torque MRAM (STT-MRAM) was developed [16]. Motivated by this advancement, magnetic nanostructures have been intensively developed for a wide range of technological applications, including high-density data storage [17, 18], magnetic sensing [19], and biomedical devices [20, 21]. In the 2000s, the concept of magnetic racetrack memory was introduced, where information is encoded in magnetic domains and read out using fixed sensor elements [8, 22]. Such dynamic memories enable read and write operations significantly faster than conventional hard disk drives. After 2010, the introduction of chirality due to the Dzyaloshinskii-Moriya interaction (DMI) and the concepts of spin-orbit torques (SOTs) to drive chiral spin textures [23, 24] have further enhanced their efficiency and strengthened their prospects for practical implementation.

The Nobel Prize in Physics in 2016 was awarded to Thouless, Haldane, and Kosterlitz for their pioneering work on topological concepts in condensed matter systems. Topology, once regarded as a purely mathematical framework, has become central to the description of robust and measurable physical phenomena. It provides a means to classify condensed matter states in terms of global invariants, enabling effective descriptions without requiring complete microscopic detail. This thesis focuses on a rapidly developing branch of condensed matter physics where spintronics intersects with topology, namely "skyrmionics". Magnetic skyrmions are topologically non-trivial quasiparticles in which the local magnetization forms a characteristic winding associated with an integer-valued topological invariant, the skyrmion number. Since their first real-space observation [25, 26], skyrmions have attracted significant attention [27, 28]. Their unique combination of dimensions down to the nm scale, topologically enhanced stability [29, 30], and susceptibility to manipulation by electrical currents [31–33] makes them ideal for applications in several spintronics devices such as racetrack memories [34–36], logic gates [37], reshuffler devices [38], neuromorphic computing [39, 40], Brownian reservoir computing [41, 42] and many others.

Recently, the growing demand for high-speed, low-power technologies has therefore boosted the search for more complex topological spin textures beyond the skyrmion paradigm [43] and has led to exploration of other topological spin textures such as biskyrmions [44–46], skyrmionium [47, 48] and skyrmion bags [49], etc. One such spin texture, the bimeron [50, 51], has recently attracted attention due to its richer current-induced dynamics compared to skyrmions [52, 53]. Bimerons are robust topological textures that are homeomorphic to skyrmions and can be visualized as the combination of two half-skyrmions (merons). When the meron and antimeron cores are arranged in different in-plane configurations, bimerons offer additional degrees of freedom compared to conventional skyrmions, making them an important focus in fundamental quasi-particle research as well as topology-based computing approaches.

While these topological spin textures are typically confined to thin films and interfaces, recent advances in unconventional fabrication techniques have enabled their realization in three-dimensional (3D) magnetic architectures [54, 55]. In 3D, the extension of spin textures along the thickness gives rise to topologically rich magnetic objects with distinct properties. A canonical example is the skyrmion tube [56, 57], which can be viewed as an extension of a two-dimensional Néel-type skyrmion along the film thickness. These skyrmion tubes can undergo complex topological transformations, including merging, termination at Bloch points [58], or the formation of closed-loop configurations. The latter case gives rise to hopfions [59, 60], which are toroidal spin textures characterized by a nonzero Hopf index [61]. When a skyrmion tube terminates partway into the magnetic medium, it forms a localized structure known as a chiral bobber [62, 63]. These three-dimensional textures exhibit robust topological protection and can interact in ways fundamentally distinct from their two-dimensional counterparts. Such 3D spin configurations could enhance the density and stability of information storage while simultaneously enabling functionalities that mimic biological processes. For instance, the intricate connectivity and dynamic behavior of 3D magnetic networks could resemble the synaptic interactions found in neural networks. By emulating neuronal architectures, 3D magnetic topological spin textures offer a promising avenue for developing energy-efficient, brain-inspired computing systems [64].

When stabilized by interfacial DMI [65–67] in ferromagnets (FM), these topological spin textures are homochiral and efficiently driven by SOTs. However, their scalability and device integration face several limitations: insufficient thermal stability [30], long-range dipolar interactions that hinder stackability [68], and the intrinsic skyrmion Hall effect (SkHE) [32, 33, 69]. The latter, originating from their non-zero topological charge, induces a transverse deflection during current-driven motion and often causes annihilation at device edges. Moreover, spin textures in FMs are highly sensitive to external magnetic fields, restricting their stability to narrow operational windows and further limiting

their applicability.

Topological spin textures in an antiferromagnet (AFM), characterized by their net-zero topological charge, offer a compelling alternative in overcoming the intrinsic limitations of their FM counterparts [70–72]. In particular, the compensated spin angular momentum in AFMs eliminates the skyrmion Hall effect, enabling current-driven motion without transverse deflection [70, 71, 73]. The absence of net magnetization suppresses dipolar fields, enabling denser skyrmion packing and higher storage density. While single-crystalline AFMs are appealing in this context, their practical implementation is hindered by the difficulty of stabilizing homochiral spin textures. This challenge arises from the absence of Lifshitz invariants in centrosymmetric lattices, which prevents a well-defined chiral preference and results in spin structures with random chirality [50, 53, 74–76]. An alternative and more experimentally accessible route involves the use of ferrimagnetic materials [48, 77]. These systems comprise two antiferromagnetically coupled magnetic sublattices with unequal moments, yielding a finite but reduced net magnetization. Ferrimagnetic multilayers have recently enabled the robust stabilization of topological spin textures, including skyrmions, under ambient conditions [78, 79]. These materials consist of antiferromagnetically coupled transition-metal and rare-earth elements, whose FM sublattices exhibit different gyromagnetic ratios. As a result, the magnetic moment compensation point (MCP) and the angular momentum compensation point (ACP) occur at different temperatures [80]. At the MCP, the net magnetic moment vanishes, leading to minimal stray fields. This condition supports the formation of smaller skyrmions and enables denser skyrmion packing. However, since the angular momentum is not compensated at the same point, the system remains subject to a finite gyrotropic force when driven by electrical currents [77].

Considering this, in this thesis, a different approach is adopted to stabilize antiferromagnetic topological spin textures. That is, using antiferromagnetically coupled FM layers, referred to as a synthetic antiferromagnet (SyAFM) system. By engineering ferromagnetic layers separated by non-magnetic spacers with precisely controlled thicknesses, the interlayer exchange coupling can be tuned from ferromagnetic to antiferromagnetic, enabling control over magnetic order and dynamics at nanometre scales [9, 81]. SyAFMs offer a unique combination of tunability (offering an additional degree of freedom by enabling independent engineering of the two FM sublattices*), functionality, and compatibility with established spintronic technologies, making them a versatile platform for both fundamental research and applications [82]. Compared with intrinsic antiferromagnets, SyAFMs provide easier electrical detection, more accessible manipulation of the antiferromagnetic state, and compatibility with conventional magneto-optical and transport probes. This has led to advances in high-performance devices such as magnetic random access memory [17, 18], magnetic sensors [19],





*Material parameters such as uniaxial magnetic anisotropy, saturation magnetization, and iDMI can be tailored individually in each sublattice, in contrast to intrinsic AFMs, where the sublattices are equivalent.

and spin-torque oscillators [83–85]. Based on these motivations, the main goals for this thesis are the following:

Goals of the Thesis

1. To establish an experimental methodology enabling the stabilization, nucleation, and unambiguous detection of antiferromagnetic topological spin textures in SyAFMs.
2. To investigate their current-driven dynamics and elucidate the interactions between AFM spin textures in real-time for the spintronics applications.
3. To extend the study to three-dimensional spin textures in SyAFMs by tuning parameters such as magnetic compensation and effective anisotropy, and to identify the unique dynamical signatures arising from their three-dimensional character.

This thesis investigates the stability, nucleation, and current-driven dynamics of topological spin textures, namely skyrmions, merons, antimerons, bimerons, and skymerons (skyrmion–bimeron pairs). The structure of the thesis is outlined below:

- Part I: Theory and Methods
 - Chapter 2: Theoretical Background
 - Chapter 3: Experimental Techniques
- Part II: Results and Discussion
 - Chapter 4: Merons, Antimerons and Bimerons in Synthetic Antiferromagnets
( labbook experiment ID 18946)
 - Chapter 5: Stabilization, Nucleation, and Dynamics of Antiferromagnetic Skyrmions
( labbook experiment ID 19296)
 - Chapter 6: Non-reciprocal Current-Induced Dynamics of Hybrid Skyrmion Tubes
( labbook experiment ID 18907)
 - Chapter 7: Skymeron: An Orthogonally Coupled Skyrmion–Bimeron Pair
( labbook experiment ID 18985)
 - Chapter 8: Summary And Outlook
- Part III: Appendices

Part I establishes the theoretical and experimental framework for studying topological spin textures and their dynamics. **Chapter 2** introduces the fundamental magnetic interactions that determine the stability and evolution of magnetization patterns, together with their coupling to electrical currents. **Chapter 3** presents the experimental techniques that provide the foundation for the investigations discussed in the subsequent chapters.

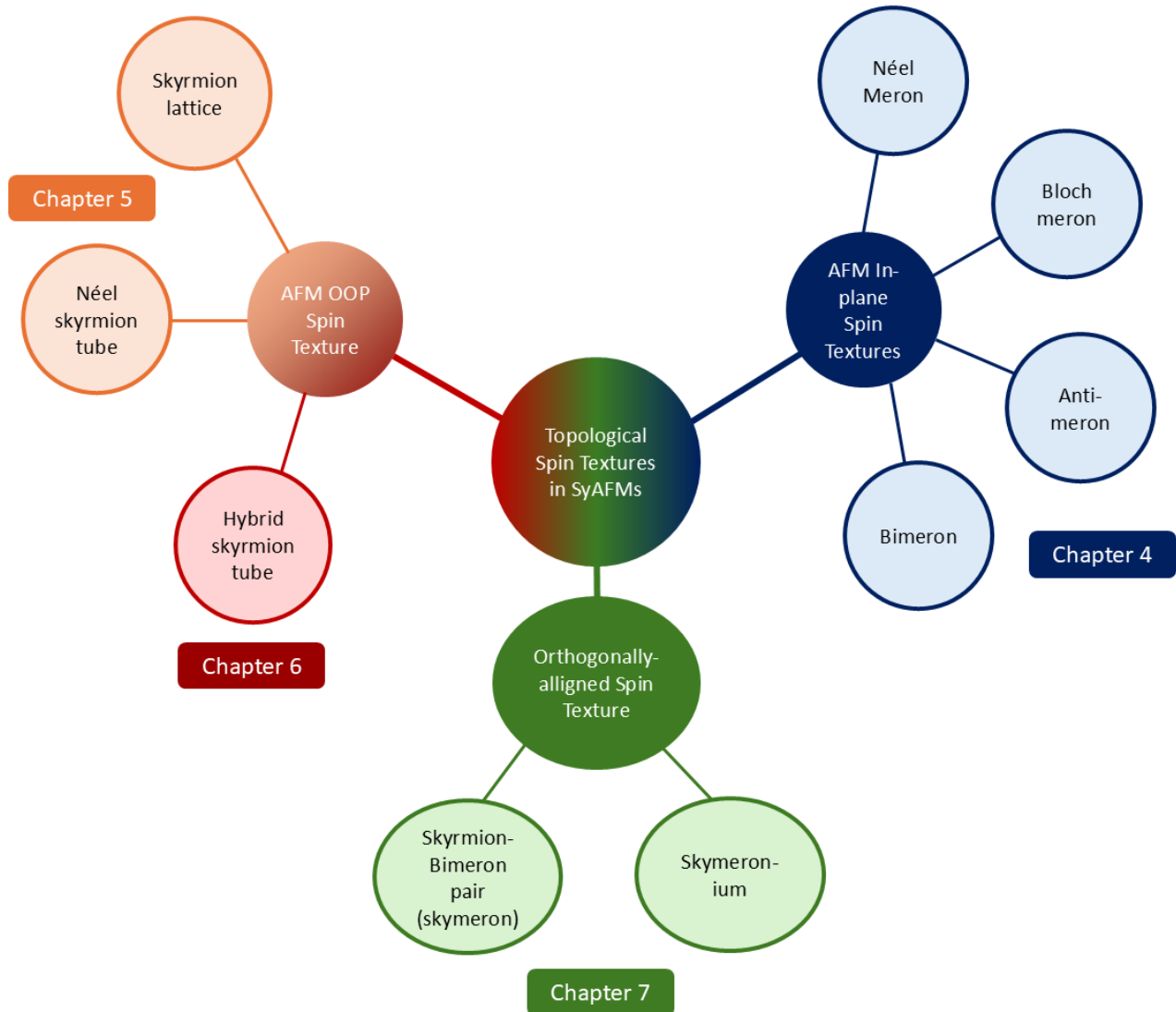


Figure 1.1: **Overview of topological quasiparticles in synthetic antiferromagnets discussed and experimentally observed in this thesis.**

Part II begins with **Chapter 4**, which discusses the in-plane topological textures, including merons, antimerons, and bimerons. **Chapter 5** addresses the stabilization and nucleation of **AFM** skyrmions and their time-resolved dynamics under **SOT**s, demonstrating **AFM** skyrmion scattering

and the real-time cancellation of the skyrmion Hall effect. Moreover, the sublattice-specific tunability of SyAFMs allows independent engineering of the ferromagnetic layers, enabling the stabilization of three-dimensional hybrid skyrmions and the demonstration of the non-reciprocal skyrmion Hall effect (NSkHE) in **Chapter 6**. Finally, by leveraging independent anisotropy control of the ferromagnetic sublattices in SyAFMs, **Chapter 7** introduces and experimentally realizes a new topological spin texture, the skymeron, which arises in SyAFMs from the near-orthogonal alignment of skyrmions and bimerons. An overview of the textures discussed in this work is shown in Fig. 1.1. Finally, this part concludes with a comprehensive summary of the key results and an outlook on future research directions presented in **Chapter 8**.

Lastly, **Part III** contains the appendices, which provide supplementary data, extended discussions, and details supporting the main results. They serve as a reference for additional analyses that complement the core chapters of the thesis.

Throughout the thesis, the term “antiferromagnetic skyrmion (bimeron)” refers to a skyrmion (bimeron) structure with total magnetization that compensates across the thickness of the multilayer stack, regardless of whether it exists in a proper AFM layer or a SyAFM system. The chosen approach to explore topological spin textures in SyAFMs relies on the fact that most of the dipolar field cancels out within a SyAFM structure due to the average magnetization compensation along the vertical dimension. However, the field outside the film does not vanish completely, allowing for the detection of magnetization configurations. By adjusting the degree of compensation, these structures can achieve an arbitrarily small magnetic moment and thereby combine the principal advantages of ferromagnetic and antiferromagnetic systems. These include minimal stray fields, stabilization of homochiral spin textures, and access to ultrafast spin dynamics, all within a device-compatible polycrystalline multilayer setting.

Part I

Theory and Methods

Theoretical Background

One cannot escape the feeling that these mathematical formulas have an independent existence and an intelligence of their own.

Heinrich Hertz

2.1 Introduction

This chapter presents the theoretical foundations and notational conventions necessary for interpreting the results discussed in the following chapters. A central theme of this work is the investigation of chiral magnetic textures, particularly (bi)merons and skyrmions, in magnetic multilayer systems. The chapter begins by introducing the key magnetic interactions responsible for stabilizing these topologically nontrivial spin configurations. Building on this, their dynamic behavior under the influence of electric currents is examined. The Landau–Lifshitz–Gilbert (LLG) equation is introduced to describe magnetization dynamics, incorporating the transfer of angular momentum from applied currents. The discussion then turns to the role of spin-orbit torques (SOTs) in driving the motion of chiral textures, with a particular focus on skyrmions. Finally, the chapter concludes by extending the concept of topological spin textures to antiferromagnetic systems, particularly synthetic antiferromagnets, which constitute the primary experimental platform explored in this thesis.

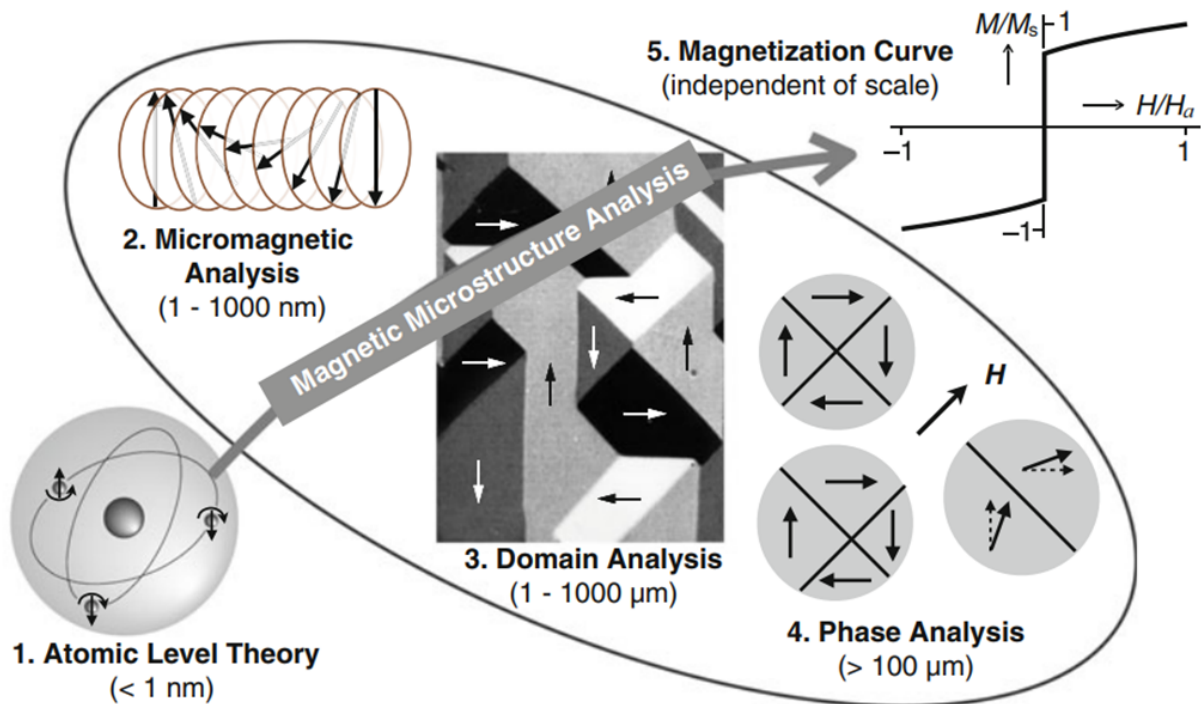


Figure 2.1: **Five levels of magnetic modeling across spatial scales:** (1) atomistic theory (<1 nm); (2) micromagnetic analysis (1–1000 nm), modeling magnetization as a continuous vector field; (3) domain analysis (1–1000 μm), capturing domain structures and boundaries; (4) phase analysis (>100 μm), describing domain orientation distributions; and (5) macroscopic-scale magnetization curves, representing the average magnetic response to external fields. Adapted from Ref. [86].

2.2 Magnetism in Thin Films

Magnetism spans multiple length scales, from atomic interactions to macroscopic behavior. To capture this inherently multiscale nature, distinct theoretical frameworks are employed at each level, as illustrated in Fig. 2.1 [87]. At the atomic scale, magnetic properties originate from the intrinsic magnetic moments of electrons and their interactions. As the scale increases, direct quantum mechanical descriptions become computationally prohibitive. To overcome this, micromagnetic theory models the magnetization as a continuous vector field. This approach is particularly suited for analyzing complex magnetic structures such as domain walls, vortex states, and skyrmions. At the micrometer scale, magnetic domains, defined as regions of uniform magnetization, become prominent, and their spatial distribution and boundaries are captured through domain and phase analysis [86, 88]. At the macroscopic scale, magnetic behavior is characterized by integrating measurable quantities such as hysteresis loops and magnetization curves, which describe the average response of a material to external magnetic fields. Accurate modeling of magnetic phenomena requires careful consideration of

the relevant length and time scales. For example, the theoretical description of magnetic skyrmions often draws on both atomistic and micromagnetic models, depending on the required resolution and scale of interest.

2.2.1 Micromagnetic Framework

Within the scope of this thesis, magnetic interactions are described using the micromagnetic framework, which assumes that the magnetization varies continuously in space on length scales much larger than interatomic distances. In ferromagnets, the magnetization can be described as a continuum vector field $\mathbf{M}(\mathbf{r}, t)$, where the vector's magnitude remains constant and equals the saturation magnetization M_s at temperatures well below the Curie point. Consequently, a normalized magnetization field $\mathbf{m}(\mathbf{r}, t) = \frac{\mathbf{M}(\mathbf{r}, t)}{M_s}$ is introduced to represent the local magnetization direction. The continuum approximation is justified because the exchange interaction typically causes magnetization changes over length scales much larger than inter-atomic distances. For the thin magnetic layers considered in this thesis, with thicknesses typically below 2 nm, magnetization variations are assumed to occur primarily within the sample's xy -plane.

To study magnetism in thin films, which host a dense ensemble of interacting spins, it is essential to understand how spins interact with each other. In the following section, we discuss the various interactions between magnetic moments and their roles in stabilizing topological spin textures in thin films. An isolated spin interacting with an external magnetic field experiences a torque that tends to align the spin with the field's direction. This type of interaction is known as the Zeeman interaction. In systems with an ensemble of spins, the spins interact with each other through various mechanisms, such as dipole-dipole interactions and exchange interactions. These interactions give rise to long-range magnetic order, such as ferromagnetism, antiferromagnetism, and ferrimagnetism. When spins interact with the crystal lattice, the interaction is known as spin-orbit coupling. This coupling is the primary source of magnetic anisotropy, which determines the preferred directions of magnetization within the material. The strength and nature of these interactions can be tuned by adjusting parameters such as composition, film thickness, and structural properties. Although these interactions arise from different mechanisms, their magnitudes are often comparable, making each essential to the overall magnetic configuration. Therefore, variations in any single interaction can profoundly influence the stability and characteristics of magnetic spin textures.

2.2.2 Heisenberg Exchange Interaction

Exchange interactions are fundamental to understanding magnetic ordering and arise from the interplay between electrostatic Coulomb interactions with the symmetrization postulates of quantum

mechanics [89, 90]. The nature of the exchange interaction determines whether it favors parallel or antiparallel spin alignment. To illustrate this, consider a model with two electrons. The total wavefunction is the product of a spatial part and a spin part. According to the symmetrization postulates, the total wavefunction of electrons (fermions) must be antisymmetric under particle exchange [91]. This requirement implies that if one part of the wavefunction is symmetric, the other must be antisymmetric. When the spin part is symmetric and the spatial part is antisymmetric, the state is called a triplet state with energy E_T . Conversely, when the spin part is antisymmetric, the state is known as a singlet state with energy E_S . The difference between the singlet and triplet states can be parameterized using the spin dot product $\mathbf{S}_1 \cdot \mathbf{S}_2$, where \mathbf{S}_1 and \mathbf{S}_2 represent the spins of the two electrons. For a singlet state, the spin correlation is $\langle \mathbf{S}_1 \cdot \mathbf{S}_2 \rangle = -\frac{3}{4}$, while for a triplet state, the spin correlation is $\langle \mathbf{S}_1 \cdot \mathbf{S}_2 \rangle = \frac{1}{4}$. Therefore, the Hamiltonian can be expressed as an effective Hamiltonian [89]:

$$\hat{\mathcal{H}}^{\text{exchange}} = \frac{1}{4} (E_S + 3E_T) - (E_S - E_T) \mathbf{S}_1 \cdot \mathbf{S}_2 \quad (2.1)$$

This expression consists of a constant term and a spin-dependent term. The constant term can be absorbed into other constant energy contributions, while the spin-dependent term is more significant. The exchange constant (or exchange integral) J_{ex} is defined as $J_{\text{ex}} = \frac{E_S - E_T}{2}$. Thus, the spin-dependent part of the effective Hamiltonian, known as the Heisenberg exchange Hamiltonian, can be written as [89]:

$$\hat{\mathcal{H}}_{\text{spin}}^{\text{exchange}} = -2J_{\text{ex}} \mathbf{S}_1 \cdot \mathbf{S}_2 \quad (2.2)$$

The sign of J_{ex} determines which state is favored:

- When $J_{\text{ex}} > 0$, then $E_S > E_T$ and the triplet state ($S = 1$) is lower in energy, leading to ferromagnetic alignment of the spins.
- When $J_{\text{ex}} < 0$, then $E_S < E_T$ and the singlet state ($S = 0$) is lower in energy, resulting in antiferromagnetic alignment of the spins.

For a system of n spins with a homogeneous nearest-neighbor interaction constant J_{ex} , the exchange energy can be expressed as [88]:

$$E_{\text{ex}} = -J_{\text{ex}} \sum_{\langle i,j \rangle} \mathbf{S}_i \cdot \mathbf{S}_j \quad (2.3)$$

where the summation $\sum_{\langle i,j \rangle}$ runs over all pairs of nearest-neighbor spins \mathbf{S}_i and \mathbf{S}_j . If electrons on

neighboring magnetic atoms interact through an exchange interaction, this is referred to as direct exchange.

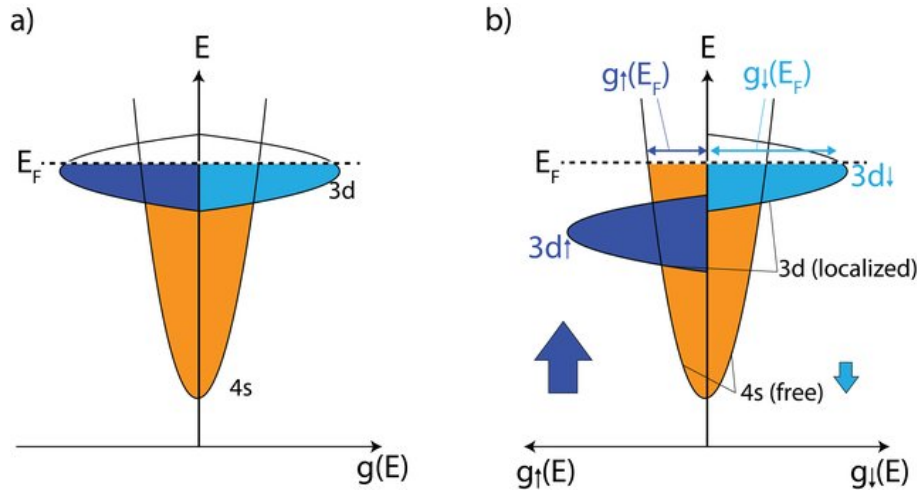


Figure 2.2: **Band diagrams representing the density of states (DOS), $g(E)$.** (a) Band structure of a non-magnetic metal with partially filled 4s and 3d bands. The spin-up and spin-down sub-bands are equally populated. (b) Band structure of a ferromagnetic metal. Exchange splitting shifts the spin sub-bands, resulting in a net magnetic moment. The figure is schematic and not to scale; the 3d bands host a larger electron population than the 4s bands. Taken from Ref [92].

In many cases, direct exchange is not the dominant mechanism controlling magnetic properties due to insufficient overlap between neighboring magnetic orbitals. For example, in rare earth elements, the 4f electrons are highly localized, and their probability density does not extend beyond a tenth of the interatomic spacing, making direct exchange ineffective in these materials. Even in transition metals such as Fe, Co, and Ni, where the 3d orbitals extend further from the nucleus, it is difficult to attribute the observed magnetic properties solely to direct exchange [89]. The role of conduction electrons cannot be ignored. Therefore, a complete description of their magnetic properties must consider both the localized nature of the 3d electrons and the band character of the conduction electrons. This behavior is described by the Stoner model of itinerant ferromagnetism [93]. In this model, the redistribution of electrons between spin-up and spin-down sub-bands at the Fermi level lowers the exchange energy while increasing the kinetic energy. Ferromagnetism is favored when the exchange gain exceeds the kinetic cost, which is expressed by the Stoner criterion [87] $Ig(E_F) > 1$, where I is the Stoner exchange parameter and $g(E_F)$ is the density of states at the Fermi level. The corresponding exchange splitting δE produces a net spin polarization, as illustrated in Fig. 2.2: panel (a) shows the non-magnetic case with equally populated sub-bands, while panel (b) shows the ferromagnetic case with shifted sub-bands. In 3d ferromagnets, the narrow and partially filled 3d bands satisfy this condition, giving rise to spontaneous ferromagnetism.

In the micromagnetic formalism for a ferromagnetic system, using the continuum approximation, the exchange energy is expressed as:

$$E_{\text{ex}} = \frac{A_{\text{ex}}}{M_s^2} \int \left[\left(\frac{\partial \mathbf{M}}{\partial x} \right)^2 + \left(\frac{\partial \mathbf{M}}{\partial y} \right)^2 + \left(\frac{\partial \mathbf{M}}{\partial z} \right)^2 \right] dV \quad (2.4)$$

where the exchange stiffness constant is defined as $A_{\text{ex}} = \frac{J_{\text{ex}} S^2 C}{a}$, with S the spin quantum number, C a geometrical factor depending on the crystal structure, and a the lattice constant. For FM materials such as Co, Ni, and Fe, the exchange stiffness typically ranges between 10 pJ/m and 30 pJ/m. In the magnetic multilayer system studied in this thesis, Co and Fe are selected as the ferromagnetic materials. Since the exchange interaction is predominant, adjusting its strength is not a focus of this thesis [94]. The exchange interaction allows magnetization variation over a characteristic length scale given by [95, 96]:

$$l_{\text{ex}} = \sqrt{\frac{2A_{\text{ex}}}{\mu_0 M_s^2}} \quad (2.5)$$

where μ_0 is the vacuum permeability. For 3d elements, this characteristic length l_{ex} typically reaches about 10 nm. In this thesis, the individual FM thin film layers are in the sub-nanometer range. Since the film thickness is smaller than l_{ex} , the magnetization can be considered uniform along the vertical direction. In micromagnetic simulations, the computational cell size should be smaller than l_{ex} .

Spontaneous Magnetization

A FM exhibits a finite magnetization M below the Curie temperature T_c without the application of an external magnetic field. At $T = 0$, the maximum spontaneous magnetization $M_s(0)$ is present, corresponding to the fully ordered spin state. With increasing temperature, $M_s(T)$ decreases due to thermal excitation of spin waves (magnons). At low temperatures, this behavior is described by Bloch's $T^{3/2}$ law:

$$M_s(T) = M_s(0) \left(1 - \left(\frac{T}{T_c} \right)^{3/2} \right) \quad (2.6)$$

Close to the Curie temperature, the temperature dependence of M_s deviates from Bloch's law and is expressed as

$$M_s(T) \propto (T_c - T)^\beta \quad (2.7)$$

Here β is the critical exponent specific to the material. At $T = T_c$, a second-order phase transition occurs from the ferromagnetic to the paramagnetic state.

2.2.3 Magnetic Anisotropy

Magnetic anisotropy refers to the tendency of magnetic moments to align along specific crystallographic directions [97, 98]. In magnetic thin films, anisotropy can result from mechanisms such as the presence of sharp interfaces, strain in materials [99], chemical bonding, or hybridization of neighboring atomic orbitals influenced by spin-orbit coupling (SOC). In the sputtered amorphous multilayer systems considered here, magnetoelastic anisotropy, caused by structural strain like lattice mismatch, is negligible and therefore not discussed further*.

Due to the interaction between the atomic lattice and the electron's orbital moment via SOC, the lattice structure affects the spin wave functions and their overlap along specific directions. This alters the electron density distribution and can break the symmetry, resulting in easy axes and hard axes. The combined effects of these interactions typically produce perpendicular magnetic anisotropy (PMA), where the easy axis is out-of-plane, or easy-plane anisotropy, where spins prefer to align within the plane. These anisotropy types are relatively straightforward to model in thin films. The anisotropy energy E_{ani} can be expressed as:

$$E_{\text{ani}} = -\frac{K_u}{M_s^2} \int M_z^2 dV, \quad \text{with} \quad K_u = \frac{K_s}{t} + K_v \quad (2.8)$$

where K_v is the volume contribution and K_s is the surface (interfacial) contribution of anisotropy for a ferromagnetic layer of thickness t . The origin of surface anisotropy stems from the interplay between SOC and broken symmetry or structural changes at interfaces. In thin films, interfacial anisotropy is significant, arising at the interfaces and scaling inversely with the film thickness [100, 101]. In the multilayers considered here, where $t < 1$ nm, the bulk anisotropy K_v is negligible, as there is minimal strain contribution from the interface.

Shape anisotropy arises from the dipolar field generated by the magnetization. The associated demagnetizing energy is minimized when the magnetization aligns along the longest axis of the magnetic structure, thereby reducing surface magnetic charges. In thin films, the demagnetizing field favors in-plane magnetization to reduce stray-field energy. The corresponding contribution is expressed as

$$K_{\text{shape}} = -\frac{\mu_0 M_s^2}{2} \quad (2.9)$$

The effective anisotropy of the system is obtained by combining the interfacial and shape contributions:

*While the microscopic origins of magnetic anisotropy are often complex, the overall contribution typically results in either an easy-axis PMA or an easy-plane anisotropy in the amorphous sputtered magnetic layers.

$$K_{\text{eff}} = \frac{K_s}{t} - \frac{1}{2}\mu_0 M_s^2 \quad (2.10)$$

By tuning the thickness of the ferromagnetic layer, the effective anisotropy can transition from positive to negative. The thickness at which the effective anisotropy becomes zero is known as the spin reorientation transition (SRT) thickness. In 3d metallic multilayers, this transition typically occurs at thicknesses of a few nanometers. For $K_{\text{eff}} > 0$, the system favors an out-of-plane (OOP) magnetization, while for $K_{\text{eff}} < 0$, it favors an in-plane (IP) magnetization orientation.

2.2.4 Dzyaloshinskii-Moriya Interaction

In 1958, Igor Dzyaloshinskii proposed a model to describe weak ferromagnetism in AFM materials [65]. Later, Moriya identified the origin of this ferromagnetism as arising from spin-orbit interaction [66]. They introduced a new type of magnetic interaction known as the Dzyaloshinskii-Moriya Interaction (DMI). It is an antisymmetric exchange interaction that emerges in systems with strong SOC. For two spins \mathbf{S}_1 and \mathbf{S}_2 , the Hamiltonian for DMI is expressed as:

$$\hat{\mathcal{H}}_{\text{DMI}} = \mathbf{D}_{12} \cdot (\mathbf{S}_1 \times \mathbf{S}_2) \quad (2.11)$$

The orientation of the DMI vector \mathbf{D}_{12} is determined by the symmetry of the lattice. For spins having finite angle θ in a plane perpendicular to \mathbf{D}_{12} , the Hamiltonian simplifies to

$$H_{\text{DMI}} = D_{12} S_1 S_2 \sin \theta \quad (2.12)$$

After accounting for the symmetric exchange interaction, the total Hamiltonian becomes

$$\hat{\mathcal{H}}_{\text{tot}} = D_{12} S_1 S_2 \sin \theta - 2J_{\text{ex}} S_1 S_2 \cos \theta \quad (2.13)$$

where J_{ex} denotes the symmetric exchange constant. The equilibrium spin configuration can be determined by minimizing $\hat{\mathcal{H}}_{\text{tot}}$ with respect to θ :

$$\frac{\partial \hat{\mathcal{H}}_{\text{tot}}}{\partial \theta} = D_{12} S_1 S_2 \cos \theta + 2J_{\text{ex}} S_1 S_2 \sin \theta = 0, \quad (2.14)$$

$$\Rightarrow \theta = \tan^{-1} \left(\frac{-D_{12}}{2J_{\text{ex}}} \right) \quad (2.15)$$

The canting angle θ is determined by the ratio of antisymmetric to symmetric exchange interactions. Importantly, the sign of $\hat{\mathcal{H}}_{\text{DMI}}$ changes upon exchanging $\mathbf{S}_1 \leftrightarrow \mathbf{S}_2$, demonstrating its antisymmetric

nature. This antisymmetry ($\mathbf{D}_{12} = -\mathbf{D}_{21}$) results in the breaking of inversion symmetry and gives rise to chiral spin textures. As such, the **DMI** is often referred to as a chiral exchange interaction. It vanishes in systems that preserve inversion symmetry (i.e., parity-conserving systems). The form of the **DMI** Hamiltonian clearly indicates that **DMI** energetically favors a non-collinear, chiral arrangement of neighboring spins, in contrast to the collinear alignment preferred by the symmetric Heisenberg exchange interaction. For different crystallographic classes such as C_n , C_{nv} , D_n , S_4 , and D_{2d} , the **DMI** energy E'_{DMI} takes the following form [102].

$$C_{nv} : E'_{\text{DMI}} = \int D_{nv} w_1 dV, \quad (2.16)$$

$$D_n : E'_{\text{DMI}} = \int D_n w_2 dV, \quad (2.17)$$

$$D_{2d} : E'_{\text{DMI}} = \int D_{2d} w'_2 dV, \quad (2.18)$$

$$C_n : E'_{\text{DMI}} = \int (D_{n1} w_1 + D_{n2} w_2) dV, \quad (2.19)$$

$$S_4 : E'_{\text{DMI}} = \int (D_{s41} w'_1 + D_{s42} w'_2) dV. \quad (2.20)$$

Here, D denotes the **DMI** constant corresponding to the specific crystallographic class, and the associated Lifshitz invariants are given by:

$$w_1 = M_z \frac{\partial M_x}{\partial x} - M_x \frac{\partial M_z}{\partial x} + M_z \frac{\partial M_y}{\partial y} - M_y \frac{\partial M_z}{\partial y}, \quad (2.21)$$

$$w_2 = M_z \frac{\partial M_x}{\partial y} - M_x \frac{\partial M_z}{\partial y} + M_y \frac{\partial M_z}{\partial x} - M_z \frac{\partial M_y}{\partial x}, \quad (2.22)$$

$$w'_1 = M_z \frac{\partial M_x}{\partial x} - M_x \frac{\partial M_z}{\partial x} - M_z \frac{\partial M_y}{\partial y} + M_y \frac{\partial M_z}{\partial y}, \quad (2.23)$$

$$w'_2 = M_z \frac{\partial M_x}{\partial y} - M_x \frac{\partial M_z}{\partial y} + M_z \frac{\partial M_y}{\partial x} - M_y \frac{\partial M_z}{\partial x} \quad (2.24)$$

In bulk materials, **DMI** is induced by the breaking of crystal inversion symmetry and the presence of atoms with strong **SOC** in the ferromagnetic alloy [34]. In such systems, the **DMI** vector is oriented perpendicular to the bond between neighboring spins, as shown in Fig. 2.3(a). Later, in 1981, Fert and Levy predicted the existence of interfacial **DMI** (**iDMI**) at the interfaces of layered structures [103] (see Fig. 2.3(b)). In thin-film systems (corresponding to the C_{nv} symmetry class), ferromagnetic spins couple to a heavy-metal layer with strong **SOC**, such as Pt or Ir [34], where the **DMI** vector lies parallel to the interface. This type of **DMI** favors spin configurations in which the magnetization rotates within the plane perpendicular to the interface normal, thereby stabilizing

chiral domain walls and Néel-type skyrmions. Within the scope of this thesis, only *iDMI* is considered. The origin of interfacial *DMI* is influenced by multiple mechanisms. Initially, it was proposed that proximity-induced magnetic moments (*PIMs*) in the heavy-metal (*HM*) layer were responsible for *DMI* [104]. However, first-principles calculations revealed that the properties of the ferromagnetic layer, rather than *PIMs* in the *HM*, primarily determine the strength of *DMI* [105]. Later, the concept of heavy-metal–ferromagnet (*HM–FM*) hybridization emerged as a more accurate explanation for interfacial *DMI* [106] (see Fig. 2.3(c)). Recent observations show that the magnitude of *DMI* is governed by a combination of *HM–FM* hybridization and spin mixing effects [107, 108]. The sign of *DMI* is dictated by the orbital contributions from the *HM* layer [99], which are influenced by *SOC* and the symmetry of the interface.

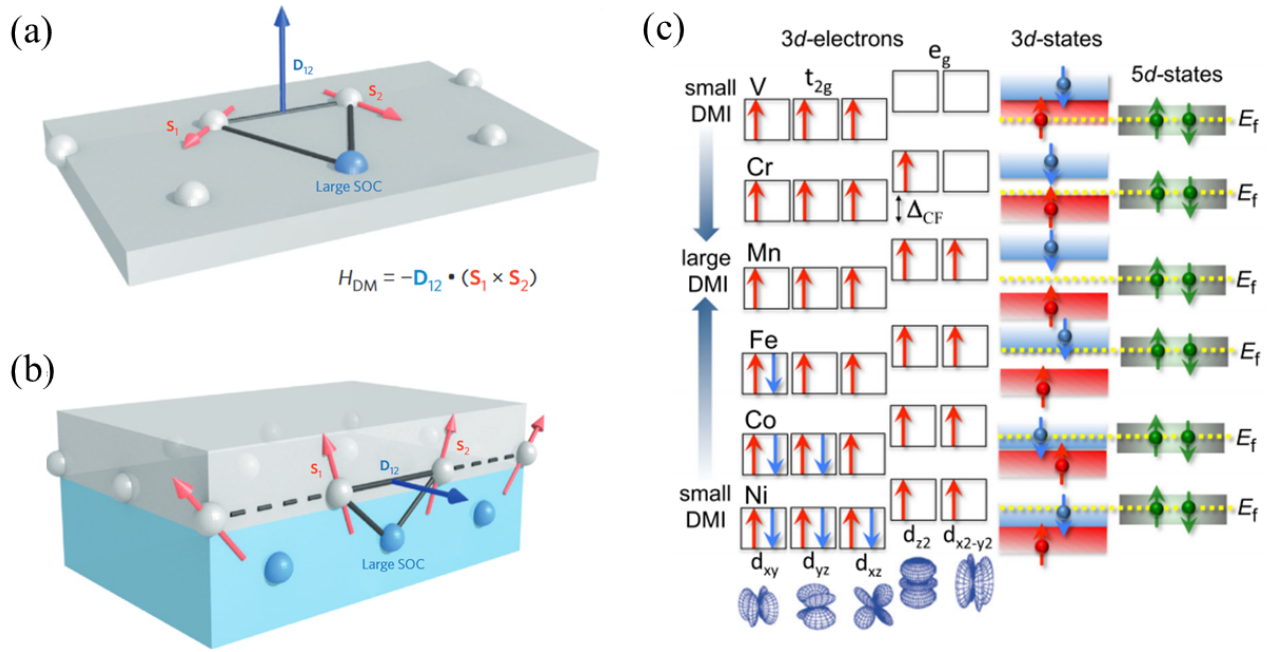


Figure 2.3: **Origin of DMI due to SOC.** (a) Schematic representation of the DMI vector \mathbf{D}_{12} (blue arrow) in a bulk material. Adapted from [34]. (b) Illustration of the DMI vector \mathbf{D}_{12} at the interface between a ferromagnetic layer and a HM layer with strong SOC. In this case, \mathbf{D}_{12} lies perpendicular to the plane formed by the two ferromagnetic atoms (blue) and the atom with strong SOC (red), pointing along the interface. Adapted from [34]. (c) DMI and the filling of the 5*d*-band, which illustrates the relationship for various transition metals including V, Cr, Mn, Fe, Co, and Ni. Adapted from [106].

The *iDMI* energy, expressed within a micromagnetic framework, is given by [109]:

$$E_{iDMI} = \frac{D_{iDMI}}{M_s^2} \int (M_z \nabla \cdot \mathbf{M} - (\mathbf{M} \cdot \nabla) M_z) dV \quad (2.25)$$

where D_{iDMI} is the interfacial DMI constant. In multilayer systems, the design of interfaces plays a crucial role in determining both the magnitude and the sign of the iDMI. Adding a top layer that contributes positively to the DMI, such as in Pt/FM/Gd [110], Pt/FM/Ir [111, 112], Pt/FM/ AlO_x [113], or Pt/FM/MgO [31, 33], enhances the overall iDMI of the system. On the other hand, in a symmetric Pt/FM/Pt structure, inversion symmetry is restored: the DMI contributions from the bottom Pt/FM and top FM/Pt interfaces are equal in magnitude and opposite in direction, leading to cancellation and an expected net iDMI of zero. Nevertheless, a small residual iDMI can still be observed due to variations in the growth conditions of the bottom and top FM interfaces [114, 115]. For this thesis, the Pt/FM/Ir interface is used, with two types of FM layers, namely CoB and CoFeB.

2.2.5 Magnetic Dipolar Interaction

In a magnetic material, each atomic site carries a magnetic moment that behaves like an individual magnetic dipole. The interaction between these dipoles, known as the dipolar interaction, arises from the coupling between magnetic moments. Consequently, the system acquires a self-energy contribution arising from the collective dipolar interactions. Unlike the previously described interactions, which are local and confined to neighboring moments, dipolar interactions are long-range in nature. They can influence magnetic order over distances from a few hundred nanometers to several hundred micrometers. For a single pair of spins, this interaction energy is given by:

$$E_{\text{dipole}} = \frac{\mu_0}{4\pi r^3} \left[\boldsymbol{\mu}_1 \cdot \boldsymbol{\mu}_2 - 3 \frac{(\boldsymbol{\mu}_1 \cdot \mathbf{r})(\boldsymbol{\mu}_2 \cdot \mathbf{r})}{r^2} \right] \quad (2.26)$$

where r is the distance between the two spins, and $\boldsymbol{\mu}_i = -g\mu_B \mathbf{S}_i$ represents the magnetic moment associated with the spin angular momentum $\hbar \mathbf{S}_i$. Here, g is the Landé factor, and μ_B is the Bohr magneton. Within the micromagnetic framework, these dipolar interactions are described by the demagnetizing field $\mathbf{H}_{\text{demag}}$, which is derived from the overall magnetization distribution rather than from individual magnetic moments. This field arises from the magnetization distribution within the system and acts back on the magnetization itself. As the magnetization configuration changes, $\mathbf{H}_{\text{demag}}$ continuously adapts to minimize the total energy and is expressed as $\mathbf{H}_{\text{demag}} = -\nabla\psi$, where ψ is the magnetostatic potential. The potential ψ satisfies Poisson's equation with appropriate boundary conditions, incorporating contributions from both volume and surface magnetic charges [116]. The corresponding demagnetizing energy is given by:

$$E_{\text{demag}} = -\frac{\mu_0}{2} \int \mathbf{M} \cdot \mathbf{H}_{\text{demag}} dV \quad (2.27)$$

Since dipolar interactions depend on the spatial distance between magnetic sites, they are typ-

ically evaluated through computational methods. In a uniformly magnetized layer, these interactions can be viewed as a rescaling of the PMA, resulting in an effective magnetic anisotropy. However, in FM layers exhibiting non-uniform magnetization, dipolar interactions promote the formation and stabilization of alternating magnetic domains separated by domain walls. In such cases, they cannot be approximated as a simple rescaling of the PMA in non-uniform magnetic configurations.

While the dipolar field generated by a given magnetization configuration cannot be directly controlled experimentally, the influence of dipolar interactions on the magnetization can be tuned by selecting different FM elements or alloys to modify M_s . This tuning is particularly relevant for the thin film stack optimization in Chapters 5 and 6. The demagnetizing energy E_{demag} scales with M_s^2 , meaning that even slight variations in M_s can lead to substantial changes in magnetic compensation and dipolar interactions within coupled FM systems. In synthetic antiferromagnetic multilayers, the strength of the dipolar field can be significantly altered by adjusting the vertical structure, such as varying the FM layer thickness t_{FM} , modifying the magnetic compensation, or changing the number of repeated FM blocks.

2.2.6 Interlayer Exchange Interaction

In metals, the exchange interaction between magnetic ions is mediated through conduction electrons. A localized magnetic moment induces spin polarization in the surrounding conduction electrons, which subsequently interact with neighboring localized moments. This mechanism gives rise to the Ruderman–Kittel–Kasuya–Yosida (RKKY) interaction. The RKKY interaction is long-range in nature and characterized by an oscillatory dependence on the inter-ionic distance. The exchange constant for the RKKY interaction can be expressed as [89]:

$$J_{\text{RKKY}}(r) \propto \frac{\cos(2k_F r)}{r^3} \quad (2.28)$$

where k_F is the Fermi wave vector and r is the distance between the magnetic ions. The exchange constant changes sign with distance, thereby mediating either ferromagnetic or antiferromagnetic coupling.

In 1986, interlayer antiferromagnetic exchange was first observed in Fe films separated by a non-magnetic Cr spacer layer [9, 118]. Later, Parkin *et al.* [81] realized that the interlayer exchange coupling in Fe/Cr/Fe and Co/Ru/Co multilayers oscillates with variations in the spacer layer thickness and is RKKY-type by nature. This coupling between FM layers, mediated by a non-magnetic spacer, is termed interlayer exchange coupling (IEC) [117, 119]. By varying the thickness of the FM layer, the exchange coupling oscillates, transitioning between AFM and FM states, as illustrated in Figure

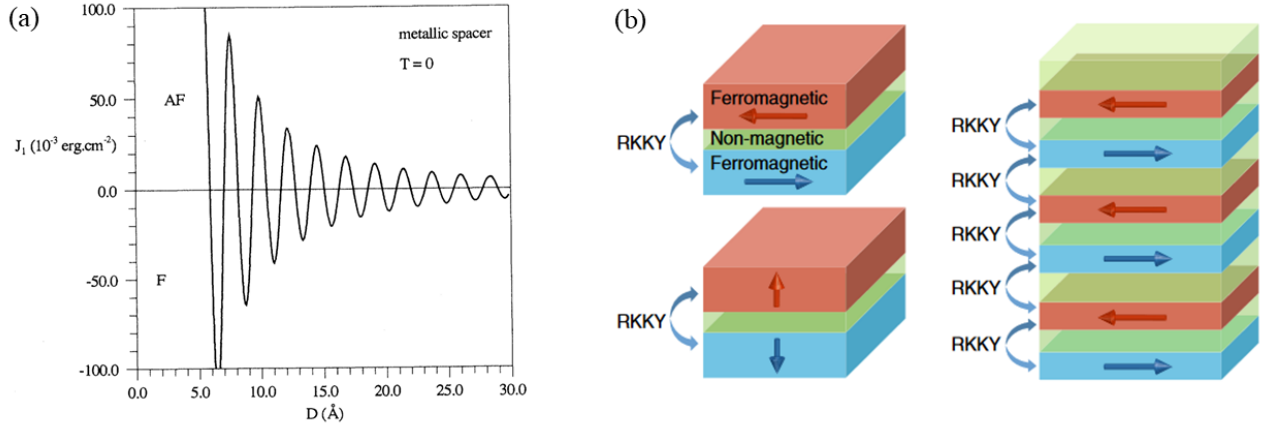


Figure 2.4: **RKKY interaction and SyAFMs.** (a) Oscillatory dependence of the interlayer exchange interaction on the spacer layer thickness. Taken from [117]. (b) Schematic representation of SyAFMs: (i) bilayers with in-plane magnetization, (ii) bilayers with out-of-plane magnetization, and (iii) multilayer structures. The arrows indicate the magnetization direction in each ferromagnetic layer. Taken from [82].

2.4(a). The IEC energy is

$$E_{\text{IEC}} = -\frac{J_{\text{IEC}}}{M_{\xi}^2} \int (\mathbf{M}_1 \cdot \mathbf{M}_2) d^2r \quad (2.29)$$

where \mathbf{M}_1 and \mathbf{M}_2 are the magnetization vectors of two ferromagnetic layers. The parameter J_{IEC} (in J/m^2) represents the surface energy density of the interlayer exchange coupling, which is independent of the ferromagnetic layer thickness. By convention, the coupling is AFM when $J_{\text{IEC}} < 0$ and FM when $J_{\text{IEC}} > 0$.

Since its discovery, IEC has attracted significant research interest and is widely utilized in the design of SyAFMs. Fig. 2.4(b) illustrates the schematic of a SyAFM, where FM layers are coupled through a non-magnetic spacer layer. SyAFMs play a crucial role in various magnetic technologies, serving as key components in MTJs, spin valves, magnetic sensors, and other spintronic devices [10, 120].

2.2.7 Zeeman Energy

The Zeeman interaction arises from the presence of an external magnetic field. Both its magnitude and orientation can be tuned to alter the effective field acting on the magnetization. Consequently, it provides a means to control the magnetization distribution. The associated energy term is expressed as:

$$E_Z = -\mu_0 \int \mathbf{M} \cdot \mathbf{H}_{\text{ext}} dV \quad (2.30)$$

where \mathbf{H}_{ext} is the external magnetic field. The energy is minimized when the magnetization aligns with the external field.

Depending on the relative strengths of the interactions discussed above, different magnetic spin textures can form, which are discussed in the next section. The following summarizes the magnetization configurations that minimize the total energy for each interaction.

Summary of Energy Terms and Corresponding Spin Configurations

1. **Exchange interaction:** For $A_{\text{ex}} > 0$, spins prefer to align parallel to each other, regardless of their orientation relative to the sample.
2. **Anisotropy:** In thin films with **PMA**, spins align along the anisotropy easy axis, pointing **OOP**, either upward or downward.
3. **Zeeman interaction:** Spins align with the direction of the external magnetic field.
4. **Dipolar interaction:** To minimize magnetic surface and volume charges, spins tend to lie **IP** along the longest sample axis in thin films, often forming flux-closure patterns.
5. **iDMI:** Spins favor canted or spiral configurations, promoting 90° tilt between neighboring spins.
6. **IEC:** Spins in adjacent layers align either parallel or antiparallel, depending on the sign of the **IEC**.

2.3 Magnetic Spin Textures

The formation of various magnetic textures arises from the interplay of different energy contributions. However, the strengths of these interactions are not equal, and in real materials, the minimization of their combined energies leads to the stabilization of more complex spin structures, such as domain walls and vortices. In this section, we focus on exploring chiral magnetic textures that are stabilized in magnetic thin films.

2.3.1 Domain and Domain Walls

In ferromagnetic thin films with **PMA**, a uniform **OOP** magnetization creates magnetic charges at the opposite surfaces of the film, increasing the system's demagnetizing energy. To minimize this

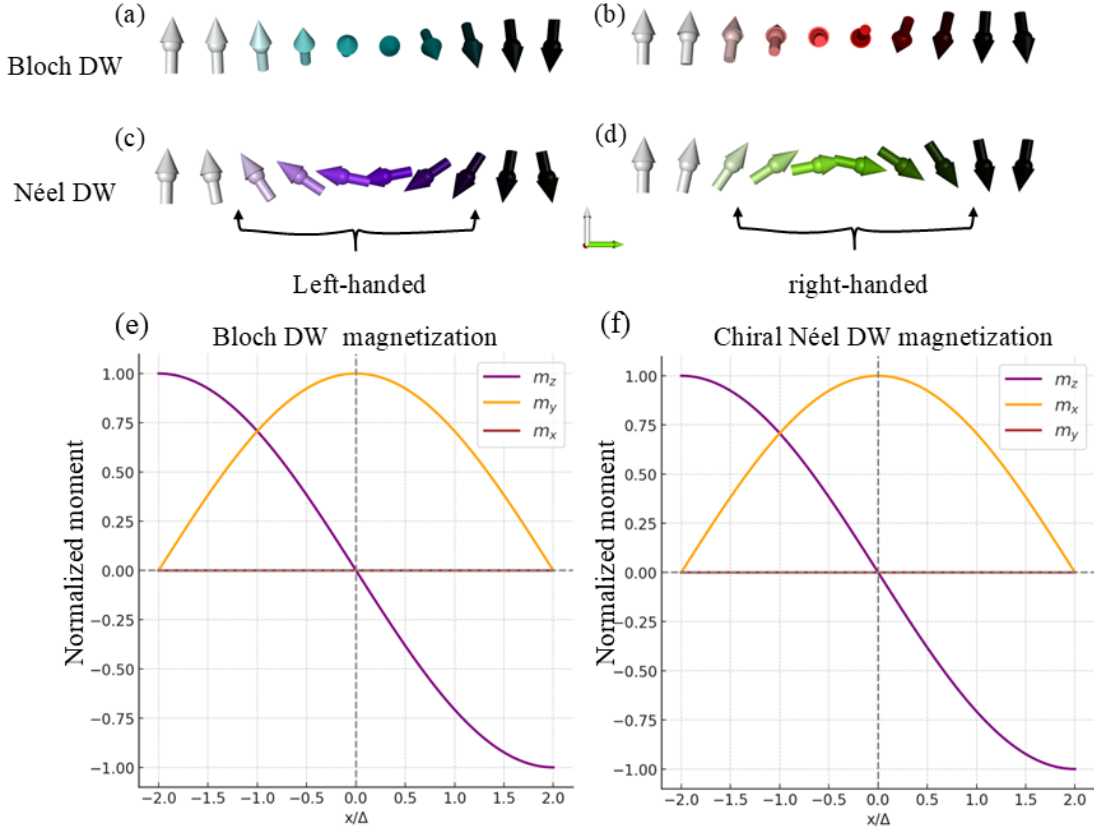


Figure 2.5: **Different wall types and their profile.** (a) Left-handed Bloch wall and (b) right-handed Bloch DW. (c) Left-handed chiral Néel DW and (d) right-handed chiral Néel DW. (e) Bloch and (f) Néel domain walls with their corresponding magnetization profiles.

energy, the film forms domains with opposite magnetization directions. The boundary between two such domains is called a domain wall (DW), having DW energy ϵ_{DW} . Within the DW, which typically spans 10 to 100 nm, the magnetization gradually rotates between the directions of the adjacent domains. In such thin films, two types of DW configurations can occur: Bloch DW and Néel DW. In a Bloch DW, the magnetization smoothly transitions from pointing down ($-\hat{z}$) to up ($+\hat{z}$) within the plane of the wall (the yz plane, as shown in Fig. 2.5(a,b)). The energy ϵ_{Bloch} and the width Δ_{Bloch} of the Bloch DW are given by:

$$\epsilon_{\text{Bloch}} = 4\sqrt{A_{\text{ex}}K_{\text{eff}}} \quad (2.31)$$

$$\Delta_{\text{Bloch}} = \pi\sqrt{\frac{A_{\text{ex}}}{K_{\text{eff}}}} \quad (2.32)$$

The Bloch wall at a position x within the domain wall profile takes the form:

$$\Theta_{\text{Bloch}}(x) = 2 \arctan\left(\exp\left(\frac{x}{\Delta_{\text{Bloch}}}\right)\right) \quad (2.33)$$

In contrast, in a Néel DW, the magnetization rotates within the plane perpendicular to the wall (the xz plane in Fig. 2.5(c,d)). For both types, the magnetization component perpendicular to the wall plane remains zero: along the x -axis for the Bloch wall and along the y -axis for the Néel wall. A schematic illustration of Bloch and Néel walls, along with their corresponding magnetization profiles, is shown in Fig. 2.5(e,f). The Bloch DW is generally more energetically stable than the Néel DW due to differences in magnetic volume charge distribution. In a Néel wall, the magnetization perpendicular to the wall plane (\hat{x}) generates magnetic volume charges on both sides of the domain wall, creating a demagnetizing field in the $-\hat{x}$ direction. In the context of this thesis, a finite DMI supports the formation of a Néel DW, as the rotational sense aligns with the direction imposed by the symmetry of the DMI [121, 122]. The energy density $\epsilon_{\text{Néel}}$, width $\Delta_{\text{Néel}}$, and the profile of the Néel DW are given by:

$$\epsilon_{\text{Néel}} = 4\sqrt{A_{\text{ex}}K_{\text{eff}}} - \pi D_{\text{iDMI}} \cos \phi \quad (2.34)$$

$$\Delta_{\text{Néel}} = \pi \sqrt{\frac{A_{\text{ex}}}{K_{\text{eff}}}} \quad (2.35)$$

$$\Theta_{\text{Néel}}(x) = 2 \arctan\left(\exp\left(-\frac{x}{\Delta_{\text{Néel}}}\right)\right) - \frac{\pi}{2} \quad (2.36)$$

Here, D_{iDMI} represents the strength of the iDMI, and ϕ is the angle between the domain wall propagation direction and the projection of the magnetization in the sample plane. The DMI constant D_{iDMI} selects a specific chirality depending on its sign, leading to left-handed or right-handed Néel walls [67, 123] (see Fig. 2.5(c,d)). The domain wall energy ϵ_{DW} is a key energy scale in magnetic systems. When $\epsilon_{\text{DW}} < 0$, magnetic textures form spontaneously in thin films, giving rise to a multidomain ground state (e.g., stripe domains, spin spirals). In the multilayer systems studied in this thesis, ϵ_{DW} is consistently negative, resulting in spontaneous domain formation at ambient conditions.

2.3.2 Bubbles

Magnetic bubbles are non-chiral cylindrical magnetic domains stabilized in thin films with perpendicular magnetic anisotropy. They were first observed in single-crystal rare-earth iron garnet films [88].

When a perpendicular magnetic field is applied to a demagnetized film, stripe domains collapse into isolated circular domains, known as magnetic bubbles, that persist as stable or metastable configurations. These bubbles behave like quasi-particles: they can be individually nucleated, manipulated, and annihilated, making them useful for studying magnetic microstructures and dynamics. The formation and stability of magnetic bubbles are governed by the competition between anisotropy and the demagnetizing stray field. A key parameter in this context is the *quality factor*, defined as

$$Q_{\text{factor}} = \frac{2K_u}{\mu_0 M_s^2}, \quad (2.37)$$

where a condition of $Q_{\text{factor}} > 1$ implies that the anisotropy energy exceeds the demagnetizing energy, thereby favoring an out-of-plane magnetization orientation, which is an essential requirement for bubble domain stabilization.

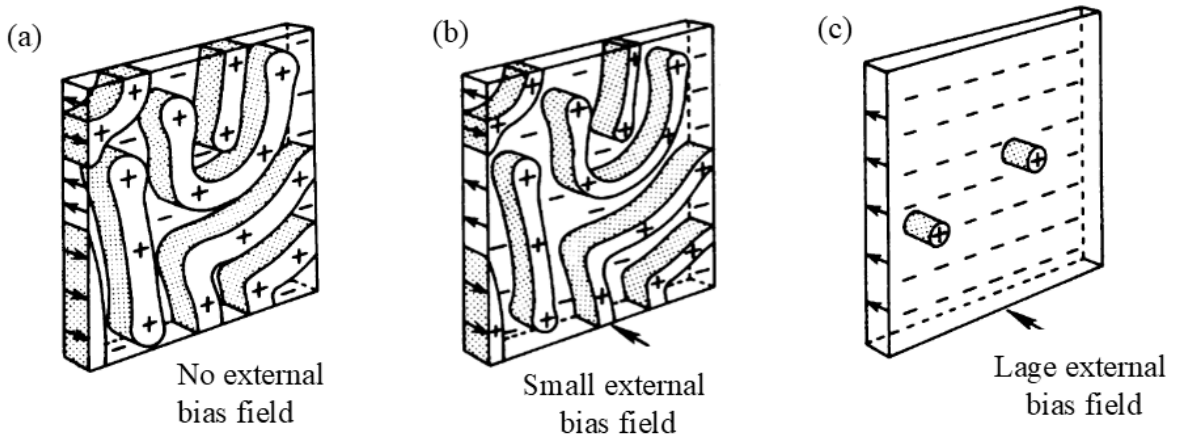


Figure 2.6: **Field-driven evolution of magnetic bubble domains in a uniaxial thin film under an increasing out-of-plane bias field.** Beginning from the zero field state, the external field is increased from (a) to (c), resulting in the nucleation of bubble domains. Adapted from [124].

The characteristic length between domain wall and dipolar energies is described by the dipolar characteristic length ℓ_w , given by

$$\ell_w = \frac{\epsilon_{\text{DW}}}{\mu_0 M_s^2}, \quad (2.38)$$

where ϵ_{DW} is the domain wall energy per unit area. For stable magnetic bubble formation, the film thickness must exceed ℓ_w , allowing the system to energetically sustain the magnetostatic cost of isolated domains. The size and shape of magnetic bubbles are strongly field-dependent. Under out-of-plane bias magnetic fields, bubbles expand or shrink continuously until they collapse or merge into stripe domains. In contrast, in plane magnetic fields distort bubbles to elliptical shapes due to the

anisotropy of the domain wall energy. A schematic of field-stabilized magnetic bubbles is shown in Fig. 2.6. In the demagnetized state, the system exhibits a multi-domain stripe configuration with approximately equal up and down domains. Upon applying an out-of-plane magnetic field, domains antiparallel to the field contract, and isolated cylindrical domains, known as magnetic bubbles, can emerge within a specific field range before the film reaches magnetic saturation (Fig. 2.6(c)). However, magnetic bubbles lack a defined chirality, since clockwise and counterclockwise Bloch domain walls are degenerate. The absence of homochirality in these spin textures limits their potential for controlled manipulation and, consequently, restricts their applicability in spintronic devices. In contrast, chiral quasiparticles such as skyrmions [27, 102, 125], bimerons [50, 51], hopfions [60], or chiral bobbers have garnered increasing attention due to their well-defined topology and robust dynamical behavior. The following section provides a detailed discussion of these topological spin textures.

2.4 Topological Spin Textures in Magnetism

Topology classifies geometric objects according to properties that remain invariant under continuous deformations, such as bending or stretching, and change only under discontinuous operations, such as tearing or gluing. Two objects are considered homeomorphic if one can be continuously transformed into the other. This equivalence defines topological classes that are characterized by topological invariants distinguishing distinct topological phases. For example, a torus and a coffee cup, each with a single genus, are homeomorphic, whereas a sphere and a torus belong to different classes. Despite its abstract mathematical origin, topology plays a central role in classifying physical states that retain robustness against smooth deformations. In condensed matter physics, topological concepts enable the identification of phases and excitations protected by global invariants rather than local symmetries. Magnetic skyrmions [102, 125] represent a prime example of such topologically nontrivial spin textures, characterized by a quantized topological charge and intrinsic stability against external perturbations.

2.4.1 Magnetic Skyrmions

The concept of skyrmions was originally introduced by Tony Skyrme in the context of nuclear physics, where they emerged as topological soliton solutions modeling baryons. In magnetism, skyrmions were first proposed by Bogdanov [102] as stable, topologically stabilized spin configurations. A significant development followed in 2006, when Binz and Vishwanath [126] formulated a theoretical framework for skyrmions in the chiral magnet MnSi, leading to their experimental observation soon after [25]. Since then, magnetic skyrmions have been realized in various platforms, including chiral lattice ferromagnets [127, 128], centrosymmetric systems [129], and geometrically confined nanostruc-

tures [130]. In 2015, room-temperature skyrmions were first observed in ultrathin Ta/CoFeB/TaO_x films [131]. Shortly thereafter, skyrmions were reported in Pt/Co/Ta and Pt/CoFeB/MgO multilayers by our group members in Mainz [31], followed by subsequent demonstrations in Pt/Co/MgO [132] and Ir/Co/Pt multilayers [133]. Since then, hundreds of studies have established the stabilization of skyrmions in sputtered thin-film heterostructures.

Magnetic skyrmions are two-dimensional, circular spin textures in which the magnetization exhibits a continuous and chiral rotation along any radial path. This characteristic swirling of spins imparts a non-trivial topological structure, distinguishing skyrmions from trivial configurations such as the ferromagnetic ground state or magnetic bubbles. Owing to their topological nature, skyrmions are inherently robust against small perturbations. This enhanced stability, often referred to as "*topological protection*", is quantified by an integer-valued topological charge Q_{sk} , which remains invariant under continuous deformations of the spin configuration. Topological protection for skyrmions is not absolute due to the discrete and non-continuous nature of the atomic lattice. Transition from a skyrmion to a trivial state requires crossing a finite energy barrier (such as a Bloch point). This barrier yields metastability and suppresses decay under small perturbations and weak external fields; however does not imply absolute stability [34].

Q_{sk} is defined in the continuum limit by Eq. 2.39. The normalized spin field $\mathbf{m}(\mathbf{r})$ takes values on the two-dimensional surface of a sphere S^2 . The skyrmion number Q_{sk} counts how many times $\mathbf{m}(\mathbf{r})$ wraps around S^2 as the coordinates (x, y) span the entire plane, and is given by [34].

$$Q_{sk} = \frac{1}{4\pi} \iint q d^2\mathbf{r}, \quad q = \mathbf{m} \cdot \left(\frac{\partial \mathbf{m}}{\partial x} \times \frac{\partial \mathbf{m}}{\partial y} \right) \quad (2.39)$$

Here, q denotes the topological charge density. The local magnetization at position (\mathbf{r}, φ) is described by two spherical angles: the polar angle $\Theta(r)$, which specifies the inclination of the spins with respect to the film normal, and the azimuthal angle $\Phi(\varphi)$, which specifies the in-plane rotation of the spins. With this parametrization, the spin field at position \mathbf{r} is written as

$$\mathbf{m}(\mathbf{r}) = (\cos \Phi(\varphi) \sin \Theta(r), \sin \Phi(\varphi) \sin \Theta(r), \cos \Theta(r)) \quad (2.40)$$

Substituting Eq. 2.40 into Eq. 2.39, where we introduce the polar coordinates $\mathbf{r} = (r \cos \varphi, r \sin \varphi)$, gives [29]

$$Q_{sk} = \frac{1}{4\pi} \int_0^\infty dr \int_0^{2\pi} d\varphi \frac{d\Theta(r)}{dr} \frac{d\Phi(\varphi)}{d\varphi} \sin \Theta(r) = [\cos \Theta(r)]_{r=0}^{r \rightarrow \infty} [\Phi(\varphi)]_{\varphi=0}^{\varphi=2\pi} \quad (2.41)$$

Eq. 2.41 can be expressed as a product of two terms, $Q_{sk} = p \cdot w$. Here, p denotes the core polarity of the skyrmion and w the winding number (also referred to as vorticity) [29]. These

quantities are defined as

$$p = \frac{-\cos\Theta(r)|_{r=0}^{r\rightarrow\infty}}{2} = \frac{m_z(0) - m_z(\infty)}{2}, \quad w = \frac{\Phi(\varphi)|_{\varphi=0}^{\varphi=2\pi}}{2\pi} \quad (2.42)$$

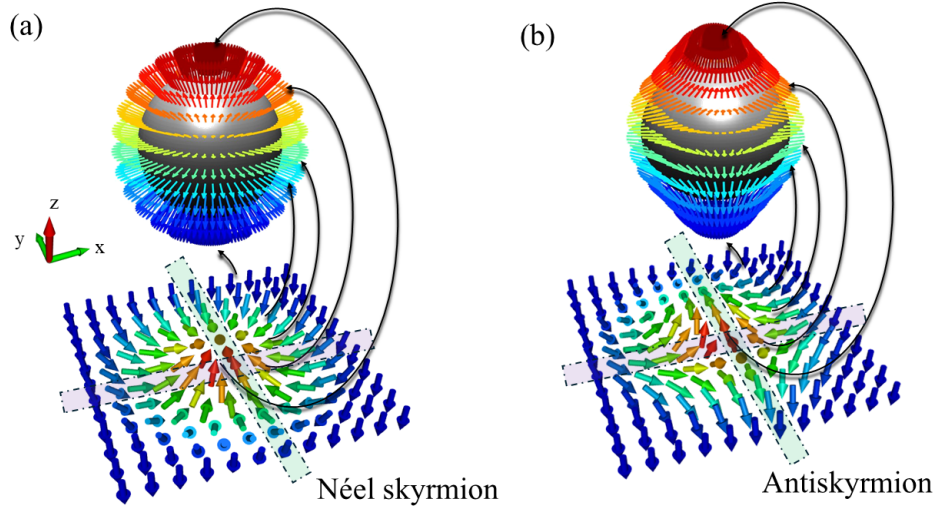


Figure 2.7: **Spin texture and topology of a Néel skyrmion and an antiskyrmion.** (a) Schematic of a Néel skyrmion and (b) an antiskyrmion, each shown both as a two-dimensional spin texture and as the corresponding mapping onto the unit sphere. The color scale indicates the out-of-plane magnetization component: red corresponds to spins aligned along $+\hat{z}$, blue to spins aligned along $-\hat{z}$, and green to in-plane magnetization.

The core polarity p assumes discrete values $p = \pm 1$, depending on the orientation of the magnetization at the skyrmion center. Specifically, $p = +1$ corresponds to the core magnetization pointing along $+\hat{z}$, while $p = -1$ indicates alignment along $-\hat{z}$. The winding number w accounts for the azimuthal winding of the in-plane magnetization component, and the polarity p reflects the difference in the out-of-plane component of magnetization between the core and the periphery. Therefore, the skyrmion number is determined by the winding number once the boundary condition at $r \rightarrow \infty$ is fixed. For skyrmions, the winding number takes the value $w = +1$, while for antiskyrmions it is $w = -1$. Ferromagnetic monodomain states and other topologically trivial configurations are characterized by $w = 0$. Consequently, a continuous transition from a skyrmion ($w = \pm 1$) to the ferromagnetic ground state ($w = 0$) is topologically forbidden and would require overcoming a significant energy barrier. Fig. 2.7 illustrates typical (a) skyrmion and (b) antiskyrmion spin structures, both of which map the planar spin configuration onto a unit sphere exactly once, corresponding to a topological charge $Q_{\text{sk}} = \pm 1$. In the case of the skyrmion, the in-plane magnetization exhibits

a uniform azimuthal rotation. In contrast, the antiskyrmion shows an anisotropic in-plane rotation, with the sense of rotation varying along orthogonal directions. Furthermore, the helicity γ is defined as the phase appearing in

$$\Phi(\varphi) = w\varphi + \gamma \quad (2.43)$$

γ determines the helicity, which distinguishes different types of skyrmions. The helicity is defined modulo 2π , i.e., $\gamma \equiv \gamma + 2\pi$. Specific values of γ correspond to characteristic skyrmion types: for instance, $\gamma = 0, \pi$ for Néel skyrmions and $\gamma = \pm\pi/2$ for Bloch skyrmions (Fig. 2.8(a–d)). A similar classification applies to antiskyrmions, as shown in Fig. 2.8(e–h), where spin textures are illustrated for $w = -1$ with helicity values $\gamma = 0, \pi, \pm\pi/2$.

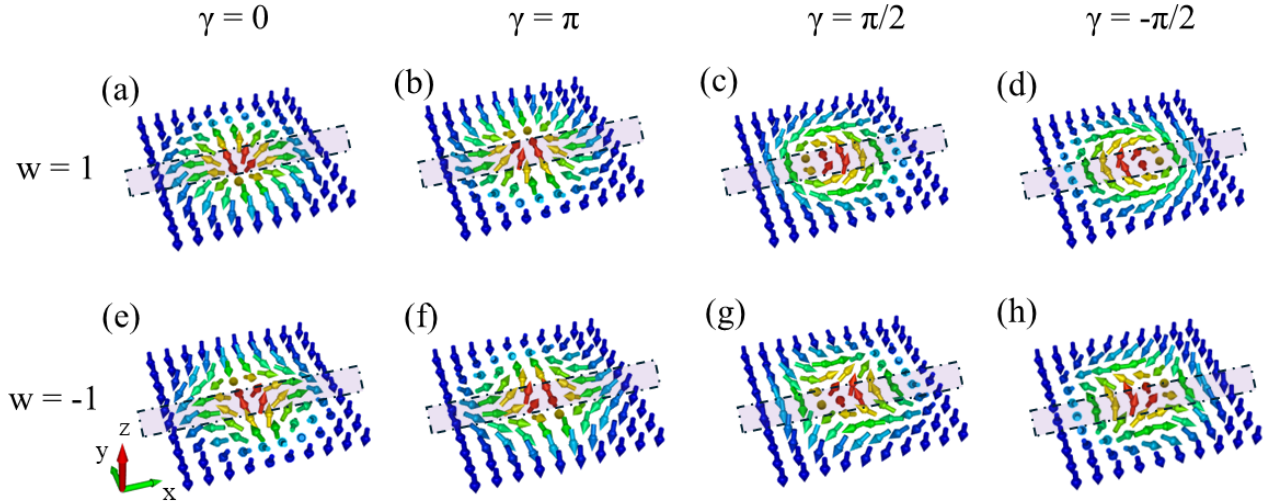


Figure 2.8: **Magnetization textures of skyrmions and antiskyrmions for different helicities.** The top row **(a)–(d)** corresponds to skyrmions with $w = +1$, while the bottom row **(e)–(h)** represents antiskyrmions with $w = -1$. Columns (a)–(d) correspond to helicities $\gamma = 0, \pi/2, \pi$, and $3\pi/2$, respectively. These configurations represent: (a) clockwise (CW) Néel, (b) counterclockwise (CCW) Néel, (c) CCW Bloch, and (d) CW Bloch textures.

Skyrmions in magnetic systems can emerge from various stabilization mechanisms, often acting in combination. Their characteristics, such as helicity, size, and topological charge, are governed by the dominant interaction responsible for their formation.

(1) Dipolar stabilized skyrmions: In magnetic thin films with perpendicular anisotropy, long-range dipolar interactions favor in-plane magnetization, while the anisotropy promotes alignment along the out-of-plane (z -axis) direction. The competition between these interactions results in the formation of periodic stripe domains, where the magnetization gradually rotates within the plane

normal to the film. Under an external magnetic field applied perpendicular to the film, the stripe phase transitions into a lattice of magnetic bubbles or skyrmions. Dipolar stabilized skyrmions typically have diameters between 100 nm and 10 μm , comparable to the stripe period set by the dipolar to exchange interaction ratio. To reduce magnetostatic energy associated with volume magnetic charges, the system stabilizes Bloch skyrmions with vorticity $w = +1$ and helicity $\gamma = \pm\pi$, as shown in Fig. 2.8(c,d). Both helicity states are energetically equivalent, allowing their coexistence within the same material.

(2) Frustrated exchange or four-spin interactions: Frustrated magnetic interactions, arising from next-nearest-neighbor or higher-order couplings such as four-spin exchange, can stabilize skyrmions in centrosymmetric magnets. These skyrmions are typically of atomic scale dimensions, with diameters comparable to the lattice constant, making discrete lattice models more appropriate than continuum descriptions. In this case, skyrmions and antiskyrmions with winding numbers $w = \pm 1$ are energetically degenerate. Moreover, the helicity γ remains arbitrary, allowing for a continuous range of skyrmion-like solutions.

(3) DMI stabilized skyrmions: In non-centrosymmetric magnetic materials, skyrmions can be stabilized by the **DMI**, which arises from **SOC** in the absence of inversion symmetry. The characteristic size of such skyrmions is set by the **DMI** strength and typically ranges from 5 to 100 nm. **DMI** stabilized skyrmions commonly exhibit vorticity $w = +1$ and helicities $\gamma = 0, \pi, \pm\pi/2$. The specific helicity is determined by the type and sign of the **DMI** vector \mathbf{D} , which in turn is governed by the material's crystal chirality and the form of the Lifshitz invariants, as discussed in Section 2.2.4. Beyond bulk crystals, significant **DMI** can also be engineered in artificial multilayer systems, composed of thin layers (typically 0.5–2 nm thick). In such heterostructures, inversion symmetry is broken at the interfaces, giving rise to interfacial **DMI**. This interfacial **DMI** favors cycloidal spin textures and stabilizes Néel skyrmions, characterized by helicity $\gamma = 0$ or π , as shown in Fig. 2.8(a,b). In the scope of this Ph.D. work, the focus is placed on Néel skyrmions stabilized by **iDMI**.

In most cases, skyrmions are stabilized through the interplay of multiple mechanisms. For instance, in thin films, the combined effect of dipolar interactions and **iDMI** leads to the formation of μm -sized skyrmion bubbles [38, 41, 134]. The skyrmions studied in this thesis are stabilized in ultra-thin ferromagnetic layers with sub-nanometer thickness, lying in the xy plane, having thickness t . The total energy of the system is expressed as

$$E = E_{\text{ex}} + E_{\text{iDMI}} + E_{\text{ani}} + E_{\text{Z}} + E_{\text{demag}} \quad (2.44)$$

where the individual energy contributions have been introduced in Section 2.2 of this chapter. Assuming the simplest case of zero helicity, the micromagnetic energy functional in terms of the radial

profile $^\dagger\Theta(r)$ can be written as [135]

$$E_{\text{sk}} = 2\pi t \int_0^\infty \left\{ A_{\text{ex}} \left[\left(\frac{d\Theta}{dr} \right)^2 + \frac{\sin^2 \Theta}{r^2} \right] + D_{\text{iDMI}} \left[\frac{d\Theta}{dr} + \frac{\cos \Theta \sin \Theta}{r} \right] + K_u \sin^2 \Theta + \mu_0 M_s H_{\text{ext}} (1 - \cos \Theta) \right\} r dr + E_{\text{demag}} \quad (2.45)$$

Note that, compared to the one-dimensional domain wall texture, two additional curvature terms appear, $\sin^2 \Theta / r^2$ in the exchange and $\cos \Theta \sin \Theta / r$ in the **DMI**, which represent the cost of curving the spin texture in a circular geometry. The consequence of this curvature is that, as $R \rightarrow 0$, the skyrmion energy is dominated by the exchange interaction and approaches the lower bound for a continuous spin texture with integer topological charge [30]: $E_{\text{sk}} \approx 8\pi A_{\text{ex}} t |Q_{\text{sk}}|$ [136]. Importantly, continuum models permit a continuous, energetically accessible path to annihilation, allowing skyrmions to be destroyed without encountering a divergent energy barrier [137]. Thus, while skyrmions are topologically nontrivial objects, topology alone does not provide absolute protection against annihilation; their stability in real materials is determined by the detailed micromagnetic energy landscape.

The stable skyrmion profile minimizes Eq. 2.45 and is characterized by the skyrmion radius R and the domain wall width Δ .[‡] Skyrmion stability can be classified into two regimes based on the sign of the domain wall energy (Eq. 2.34). For positive domain wall energy, the uniform ferromagnetic state is the lowest energy configuration and skyrmions are metastable with radius $R = \Delta / \sqrt{2(1 - D_{\text{iDMI}}/D_c)}$ [121], where $D_c = (4/\pi)\sqrt{A_{\text{ex}}K_{\text{eff}}}$ is the critical **DMI**.[§]

When the domain wall energy is negative ($D_{\text{iDMI}} > D_c$), the uniform ferromagnetic state is unstable and modulated states are stabilized; skyrmions exist as metastable textures under external control, such as an external field or confinement. The expressions above neglect dipolar coupling, which is justified for very thin films or for materials with small magnetization, such as ferrimagnets and synthetic antiferromagnets.

2.4.2 Magnetic Bimerons

Magnetic bimerons can be described as the in-plane magnetized counterparts of magnetic skyrmions. Bimerons were first theoretically predicted in 2017 as a bimeron crystal [138], and were subsequently observed in chiral magnets [139]. Later, bimerons were proposed as isolated quasiparticles in monoclinic systems [52, 140]. Their existence in thin films stabilized by iDMI was later predicted by Moon

[†]Impose cylindrical symmetry with $\Theta = \Theta(r)$ and $\Phi(\varphi) = \varphi$. In polar coordinates, $(\nabla \mathbf{m})^2 = (d\Theta/dr)^2 + \sin^2 \Theta / r^2$ and the iDMI density reduces to $-D_{\text{iDMI}} [d\Theta/dr + \cos \Theta \sin \Theta / r]$.

[‡]In thin films with thickness $t < l_w = \epsilon_{\text{DW}} / (\mu_0 M_s^2)$ the demagnetizing energy is often approximated as $\mu_0 M_s^2 \cos^2 \Theta / 2$ and absorbed into an effective anisotropy K_{eff} .

[§]For $R \gg \Delta$, a skyrmion can be treated as a circular domain with wall width Δ and total energy (neglecting the dipolar interaction) $E_{\text{sk}}(R) \simeq 2\pi R t \epsilon_{\text{DW}} + \frac{4\pi A_{\text{ex}} t \Delta}{R}$. Minimization yields $dE_{\text{sk}}/dR = 0 \Rightarrow R = \sqrt{\frac{2A_{\text{ex}} \Delta}{\epsilon_{\text{DW}}}} = \frac{\Delta}{\sqrt{2(1 - D_{\text{iDMI}}/D_c)}}$.

et al. [51].

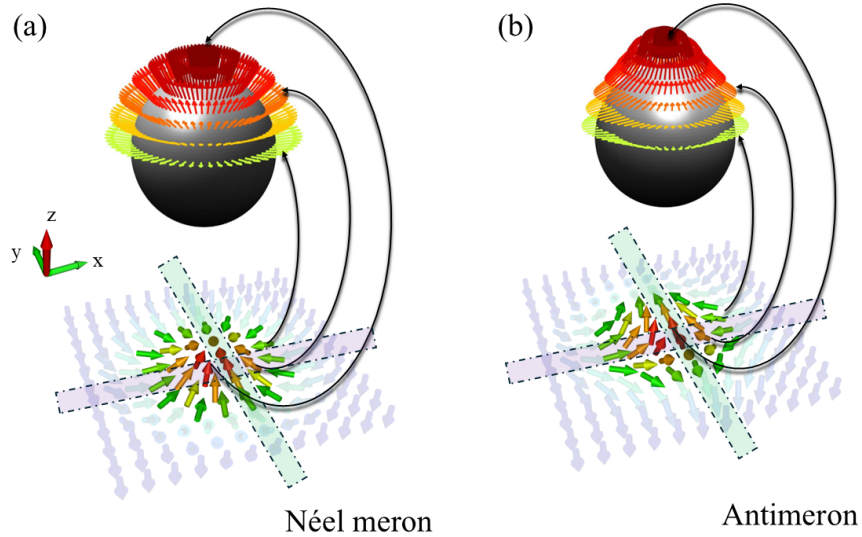


Figure 2.9: **Spin texture and topology of a Néel meron and an antimeron.** (a) Schematic of a Néel-type meron and (b) an antimeron, each represented both in the two-dimensional spin texture and in a corresponding mapping onto the unit sphere. The color scale indicates the out-of-plane magnetization component: red denotes spins aligned along $+\hat{z}$, blue along $-\hat{z}$, and green corresponds to in-plane magnetization.

Bimerons are topological spin textures that arise in magnetic systems with in-plane anisotropy. Structurally, a bimeron consists of two components: a meron [141, 142] and an antimeron [143], together forming the in-plane counterpart of a skyrmion. Fig. 2.9 shows the spin configurations of a Néel-type meron (a) and antimeron (b), visualized both in two-dimensional real space and through their mappings onto the unit sphere. The color scale indicates the out-of-plane magnetization component: red for $+\hat{z}$, blue for $-\hat{z}$, and green for in-plane orientation. The meron and antimeron possess topological charges of $+1$ and -1 , respectively. The stability and formation of bimerons in thin films are governed by the balance between *iDMI*, *PMA*, and the demagnetizing field. In an easy-plane magnetic system, a finite out-of-plane magnetization component is required to stabilize the chiral bimeron core, which otherwise collapses in a purely in-plane configuration. The *iDMI* acts as an effective internal field that enforces a fixed sense of rotation of the spins across the in-plane domain wall separating regions magnetized along $+y$ and $-y$.

When a meron and an antimeron with the same core polarity are combined, their topological charges cancel, resulting in a trivial meron–antimeron pair with a net topological charge $Q_{\text{sk}} = 0$, as illustrated in Fig. 2.10(a). In contrast, a bimeron consists of a meron and an antimeron with opposite out-of-plane magnetizations, i.e., opposite core polarities. This configuration gives both

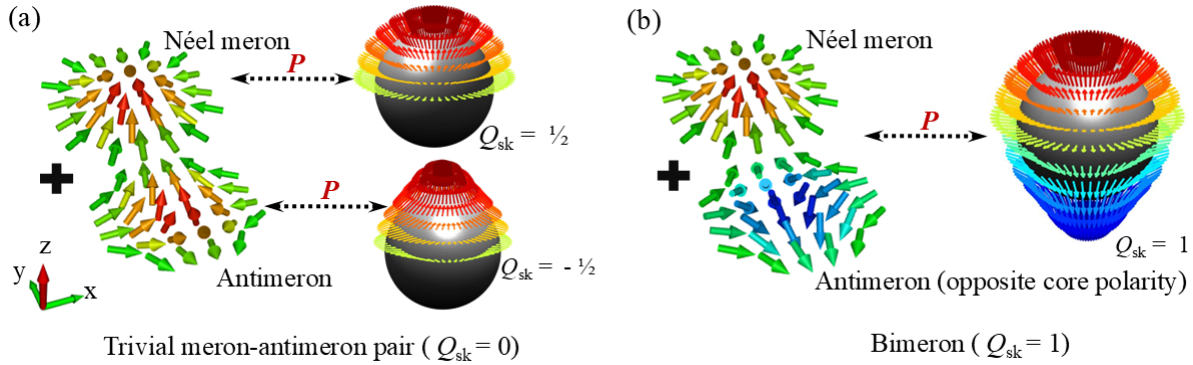


Figure 2.10: **Topological charge composition of a meron–antimeron pair and a bimeron.** (a) A trivial meron–antimeron pair formed by combining a Néel meron and an antimeron with the same core polarity. Each substructure carries the opposite topological charge, resulting in a total topological charge $Q_{sk} = 0$. (b) A bimeron formed by pairing a meron and an antimeron with opposite core polarities. In this case, both constituents carry the same topological charge $Q_{sk} = 1/2$, yielding a net topological charge $Q_{sk} = \pm 1$.

substructures the same topological charge of either $+1/2$ or $-1/2$, yielding a net topological charge of $Q_{sk} = \pm 1$ for the bimeron, as shown in Fig. 2.10(b). In this context, a bimeron can be viewed as a skyrmion-like excitation in a magnet with in-plane anisotropy. In bimerons, the background magnetization can be freely oriented within the plane, introducing an additional continuous degree of freedom. Experimentally, individual bimerons have been realized through local vortex imprinting in a permalloy film using an overlying Co disk [144].

2.5 Magnetization Dynamics

The previous sections covered magnetic interactions and fundamental spin textures like chiral domain walls, skyrmions, and bimerons. This section explores how these textures can be manipulated using external influences such as magnetic fields and electric currents. Understanding magnetization dynamics under magnetic fields and angular momentum transfer driven by electric currents is essential for the dynamics of the spin textures.

2.5.1 Landau-Lifshitz-Gilbert (LLG) Equation

In 1935, Landau and Lifshitz proposed a phenomenological equation describing the dynamics of magnetization [145]. This equation, known as the Landau–Lifshitz (LL) equation, captures the precessional motion of magnetization in solids. It primarily describes the gyromagnetic motion of

magnetization and is expressed as

$$\frac{d\mathbf{M}}{dt} = -\gamma_0 \mathbf{M} \times \mathbf{H}_{\text{eff}} \quad (2.46)$$

Here, \mathbf{M} denotes the magnetization vector, and $\gamma_0 = \mu_0 \gamma$ with $\gamma = \frac{g|e|}{2m_e}$ being the gyromagnetic ratio, where g is the Landé factor, $|e|$ the absolute value of the electron charge, and m_e the electron mass. The effective magnetic field \mathbf{H}_{eff} is obtained from the functional derivative of the total energy E_{eff} with respect to the magnetization,

$$\mathbf{H}_{\text{eff}} = -\frac{1}{\mu_0} \frac{\delta E_{\text{eff}}}{\delta \mathbf{M}} \quad (2.47)$$

The first term on the right-hand side of Eq. 2.46 is referred to as the precessional term (see Fig. 2.11), as it describes the precession of the magnetic moment \mathbf{M} around \mathbf{H}_{eff} . When the magnetization is not aligned with \mathbf{H}_{eff} , it experiences a torque that induces precession with frequency $f = \frac{\gamma_0 |\mathbf{H}_{\text{eff}}|}{2\pi}$. This precessional motion conserves the magnetic free energy, meaning the system cannot reach equilibrium through precession alone. In real materials, energy dissipation is always present and must be considered for an accurate description of magnetization dynamics. To account for dissipation, a phenomenological term was introduced, yielding the modified LL equation [145]

$$\frac{d\mathbf{M}}{dt} = -\gamma_0 \mathbf{M} \times \mathbf{H}_{\text{eff}} - \frac{\lambda_{\text{LL}}}{M_s} \mathbf{M} \times (\mathbf{M} \times \mathbf{H}_{\text{eff}}) \quad (2.48)$$

Here, λ_{LL} denotes the LL damping constant. Gilbert later proposed an alternative formulation of the damping interaction, leading to the widely adopted LLG equation [146]:

$$\frac{d\mathbf{M}}{dt} = -\gamma_0 \mathbf{M} \times \mathbf{H}_{\text{eff}} + \frac{\alpha}{M_s} \mathbf{M} \times \frac{d\mathbf{M}}{dt} \quad (2.49)$$

Here α is the dimensionless Gilbert damping constant.[¶]

A schematic representation of this motion is shown in Fig. 2.11. The second term in Eq. 2.49 corresponds to the phenomenological Gilbert damping, which accounts for energy dissipation and drives the magnetization toward alignment with the effective field. The associated damping torque, $\mathbf{M} \times \frac{d\mathbf{M}}{dt}$, is orthogonal to both the magnetization \mathbf{M} and the precessional torque, acting in a direction that drives \mathbf{M} toward alignment with the effective field \mathbf{H}_{eff} . Both torques are illustrated in Fig. 2.11. Typical values of the Gilbert damping constant α in thin-film magnetic systems range

[¶]The Gilbert form can be algebraically transformed into the LL form. Solving Eq. 2.49 for $d\mathbf{M}/dt$ gives

$$\frac{d\mathbf{M}}{dt} = -\frac{\gamma_0}{1 + \alpha^2} \mathbf{M} \times \mathbf{H}_{\text{eff}} - \frac{\alpha \gamma_0}{M_s(1 + \alpha^2)} \mathbf{M} \times (\mathbf{M} \times \mathbf{H}_{\text{eff}}),$$

which has the structure of Eq. 2.48 with renormalized constants $\gamma^* = \gamma_0/(1 + \alpha^2)$ and $\lambda_{\text{LL}} = \alpha \gamma_0 M_s/(1 + \alpha^2)$.

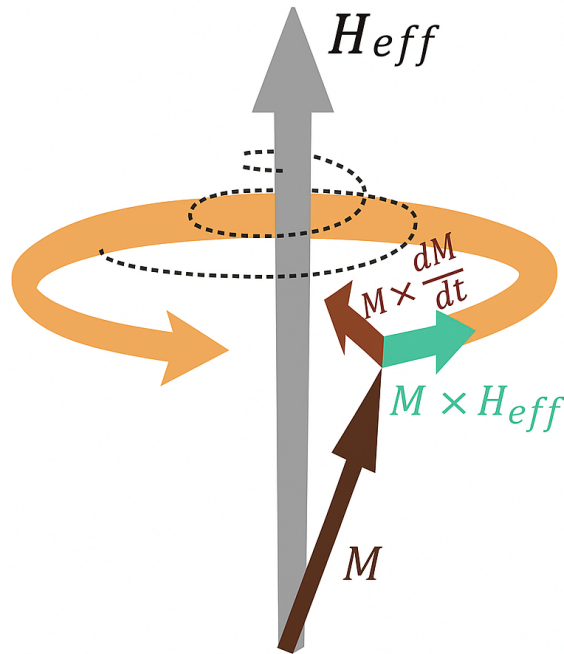


Figure 2.11: **Magnetization dynamics: showing the effect of precession and damping term.** Whereas precession induces an angular motion around the effective field, damping progressively orients the spin toward the field axis, producing a spiral path.

from 10^{-3} to 0.5 [31]. Solving the [LLG](#) equation provides a theoretical framework for analyzing magnetization reversal, domain wall motion, and spin dynamics, and plays a central role in advancing the understanding of magnetic textures and their applications in spintronics.

2.5.2 Spin Torques Induced by Current

The dynamics of magnetic textures can be controlled through spin torques generated by spin-polarized charge currents or pure spin currents. These torques act on the local magnetization, modifying its configuration and enabling precise control of magnetic dynamics [147]. This modulation by current provides the basis for the skyrmion dynamics studied in this thesis and is discussed in the following section.

Spin-Transfer Torque

Spin-transfer torque ([STT](#)) originates from the exchange of angular momentum between conduction electrons and localized magnetic moments in a ferromagnetic layer. It represents one of the most

effective mechanisms to manipulate magnetization by means of spin-polarized electrical currents and has thus become a central concept in spintronics. The earliest theoretical models were introduced by Berger [148–150] and by Slonczewski [151], who demonstrated that a spin-polarized current can reverse the magnetization of a thin film when driven perpendicular to the layers.

In the current-perpendicular-to-plane (CPP) geometry (see Fig. 2.12(a)), a multilayer stack consists of a fixed ferromagnetic layer, a nonmagnetic spacer, and a free ferromagnetic layer. When an electrical current flows perpendicular to the film plane, the fixed layer acts as a spin polarizer, having spin polarization \mathbf{p} . Upon entering the free layer, the transverse component of the spin current is absorbed, transferring angular momentum to the local magnetization \mathbf{M} . This exerts the STT, which can be expressed as the sum of two contributions,

$$\boldsymbol{\tau}_{\text{STT}} = \tau_{\text{DL}} \mathbf{M} \times (\mathbf{M} \times \mathbf{p}) + \tau_{\text{FL}} \mathbf{M} \times \mathbf{p} \quad (2.50)$$

Here τ_{DL} and τ_{FL} denote the amplitudes of the damping-like (DL) and field-like (FL) components, respectively. The DL torque has the same vector form as the Gilbert damping term in the classical LLG equation and is commonly referred to as the Slonczewski torque, or (anti-)damping torque. The interplay between these two torque components and intrinsic damping enables current-induced switching between parallel and antiparallel magnetization states, which constitutes the operational principle of STT-MRAM.

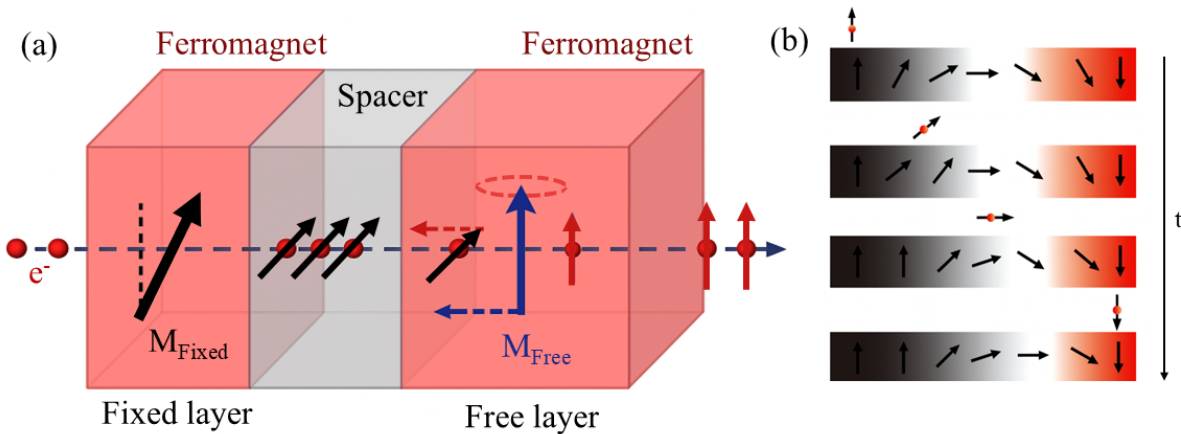


Figure 2.12: **Spin-transfer torques in CPP and CIP geometry.** (a) A spin-polarized current generated in a fixed magnetic layer is transmitted into the free layer, where itinerant spins reorient with the local magnetization, exerting a torque through angular momentum conservation. (b) In a magnetic stripe, itinerant spins progressively reorient in response to a magnetization gradient, which is displaced along the electron flow direction.

A different scenario arises when the current flows in-plane through a magnetic material, com-

monly referred to as the current-in-plane (CIP) geometry (see Fig. 2.12(b)). Conduction electrons drift along the ferromagnet and interact with a spatially varying magnetization profile, such as a domain wall or a skyrmion. As they traverse the texture, their spins tend to align with the local magnetization direction via the s - d exchange interaction, thereby transferring angular momentum to the magnetic system [152]. In the ideal adiabatic limit, where the conduction electron spins remain perfectly aligned with the local magnetization, the torque is expressed as

$$\boldsymbol{\tau}_{\text{ad}} = -\frac{1}{M_s^2} \mathbf{M} \times (\mathbf{M} \times (\mathbf{u} \cdot \nabla) \mathbf{M}) = -(\mathbf{u} \cdot \nabla) \mathbf{M} \quad (2.51)$$

with $\mathbf{u} = \frac{Pg\mu_B}{2eM_s} \mathbf{J}$ the spin drift velocity, where P is the spin polarization of the current, g the Landé g -factor, μ_B the Bohr magneton, e the electron charge, and \mathbf{J} the current density. This torque acts as a convective term that transports the magnetic texture along the electron flow direction and defines the maximum velocity a domain wall can reach in the adiabatic limit.

However, experimental observations of current-driven domain wall and skyrmion dynamics revealed deviations from the purely adiabatic picture, necessitating the introduction of a phenomenological nonadiabatic term [153, 154]. This additional contribution accounts for spin relaxation and scattering processes that prevent conduction electron spins from remaining perfectly aligned with the local magnetization. The non-adiabatic torque is written as

$$\boldsymbol{\tau}_{\text{non-adiab}} = \frac{\beta}{M_s} \mathbf{M} \times [(\mathbf{u} \cdot \nabla) \mathbf{M}] \quad (2.52)$$

Here β is a dimensionless parameter quantifying the degree of non-adiabaticity. Under the action of spin-transfer torque CIP geometry, magnetic textures translate along the electron flow direction and, by convention, opposite to the current direction.

2.5.3 Spin-Orbit Torque

Contrary to the effect of STT, experimental studies in 2011–2012 on ferromagnet/heavy-metal bilayers such as Pt/Co/AIO_x and Ta/CoFeB/MgO [23, 24] revealed that magnetic textures can move opposite to the electron flow. To account for this behavior, a new torque mechanism, termed spin-orbit torque (SOT), was introduced. SOT arises from the interplay between charge currents and SOC in magnetic heterostructures, providing an efficient mechanism to manipulate magnetization electrically. Unlike STT, which requires a spin-polarized current generated by a fixed magnetic layer, SOT exploits intrinsic or interfacial spin-orbit effects to generate spin currents directly from charge transport in heavy metals. This effect typically occurs in structures where an ultrathin ferromagnetic layer is interfaced with a material possessing strong SOC. The two main microscopic origins of SOT

are the spin Hall effect and the inverse spin galvanic effect, both of which generate spin currents or spin accumulation that exert torques on the magnetization of the ferromagnet. The spin Hall effect generates a transverse spin current that is predominantly absorbed as a DL-SOT on the ferromagnet. The inverse spin galvanic effect creates a nonequilibrium interfacial spin density that usually yields a FL-SOT, although both mechanisms can contribute to both symmetries depending on interface transparency, spin mixing conductance, and relaxation. Hence, the corresponding torques due to the SOT can be expressed as

$$\boldsymbol{\tau}_{\text{SOT}} = \frac{\tau_{\text{DL}}^{\text{SOT}}}{M_s^2} \mathbf{M} \times (\mathbf{M} \times \boldsymbol{p}) + \frac{\tau_{\text{FL}}^{\text{SOT}}}{M_s} \mathbf{M} \times \boldsymbol{p} \quad (2.53)$$

Here \boldsymbol{p} is the spin polarization direction of the spin accumulation generated by SOC, and $\tau_{\text{DL}}^{\text{SOT}}$ and $\tau_{\text{FL}}^{\text{SOT}}$ denote the DL and FL contributions, respectively. Since the first demonstrations, considerable efforts have been devoted to quantifying the efficiency of charge-to-spin conversion, distinguishing between FL and DL torque components, and optimizing material platforms for device applications.

Spin Hall Effect

The spin Hall effect (SHE) [155, 156] refers to the generation of a transverse spin current in response to a longitudinal charge current mediated by SOC [157]. It originates from both intrinsic and extrinsic mechanisms [158]. The intrinsic contribution arises from the Berry curvature of the electronic bands in the relativistic band structure [159, 160]. Under an applied electric field \mathbf{E} , the Bloch wave function acquires a geometric phase associated with the Berry curvature, which acts as an effective magnetic field in momentum space. This induces an anomalous transverse velocity of opposite sign for electrons with opposite spins, $\mathbf{v}_{\text{anomalous}} = \mathbf{E} \times \boldsymbol{\Omega}^n(\mathbf{k})$, giving rise to a transverse spin current even in a perfectly clean crystal without impurity scattering [158]. Here $\boldsymbol{\Omega}^n(\mathbf{k})$ denotes the Berry curvature of band n in momentum space.

The extrinsic SHE originates from the scattering of electrons by impurities, lattice defects, or phonons in the presence of SOC [155, 157]. Even in systems composed of relatively light atoms, extrinsic contributions can be significant [156]. Two main mechanisms are distinguished: Mott skew scattering and side-jump scattering. In Mott skew scattering [161] (see Fig. 2.13(a)), electrons are asymmetrically deflected by impurities depending on their spin orientation, producing a transverse spin current that scales with the longitudinal charge conductivity. In contrast, the side-jump mechanism [162] (see Fig. 2.13(b)) causes a lateral displacement of the electron wave packet during each scattering event, giving rise to a transverse spin current that is independent of charge conductivity. The overall extrinsic spin Hall conductivity is the combined result of these two processes, both of

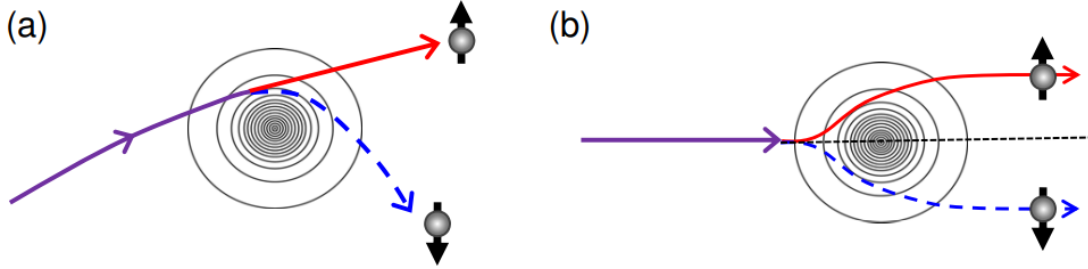


Figure 2.13: **Mechanisms of spin Hall effect.** Schematic illustration of **(a)** skew scattering and **(b)** side-jump contributions to the SHE. Adapted from [158].

which generate a transverse spin current in response to a longitudinal charge current.

Consider a uniform charge current density \mathbf{J}_c flowing in a nonmagnetic metal with spin-orbit coupling. The SHE converts \mathbf{J}_c into a transverse pure spin current,

$$\mathbf{J}_{s,\hat{\sigma}} = \frac{\hbar}{2e} \theta_{\text{SH}} (\hat{\sigma} \times \mathbf{J}_c) \quad (2.54)$$

Here $\mathbf{J}_{s,\hat{\sigma}}$ is the spin current density whose spin polarization is along $\hat{\sigma}$ and whose flow direction is $\hat{\sigma} \times \mathbf{J}_c$, and θ_{SH} is the spin Hall angle. This spin current is orthogonal to both $\hat{\sigma}$ and \mathbf{J}_c . The factor $\hbar/2e$ converts charge current units (A m^{-2}) into angular momentum current density, and the overall sign is set by the sign of θ_{SH} . The interface normal $\hat{\mathbf{n}}$ point from the spin Hall metal to the ferromagnet. The spin accumulation at the interface has polarization $\hat{\mathbf{p}} \parallel \text{sgn}(\theta_{\text{SH}}) (\mathbf{J}_c \times \hat{\mathbf{n}})$, so reversing the stacking reverses $\hat{\mathbf{p}}$. The spin accumulation exerts two torques on the magnetic layer: a DL part and an FL part. In metallic stacks the damping like term is usually dominant, and it is convenient to write it by means of an effective field \mathbf{H}_{DL} directed along $\mathbf{M} \times \hat{\mathbf{p}}, \boldsymbol{\tau}_{\text{DL}} = -\gamma_0 \mathbf{M} \times \mathbf{H}_{\text{DL}}$. The quantity H_{DL} is what is measured in SOT experiments and can be compared directly with an external field. A spin torque efficiency for the DL torques is defined as

$$\xi_{\text{DL}} = \frac{J_s}{J_c} T_{\text{int}} = \mu_0 H_{\text{DL}} \frac{2eM_s t}{\hbar J_c} \quad (2.55)$$

Here J_s is the spin current density absorbed by the ferromagnet (flowing along $\hat{\mathbf{n}}$), T_{int} is an interface transparency factor that accounts for spin backflow and spin mixing conductance. Note that ξ_{DL} is distinct from the spin Hall angle θ_{SH} : θ_{SH} is a material-dependent spin-charge conversion parameter, where ξ_{DL} accounts for spin diffusion, spin memory loss [163, 164], spin mixing conductance [165] and interface transparency [166].

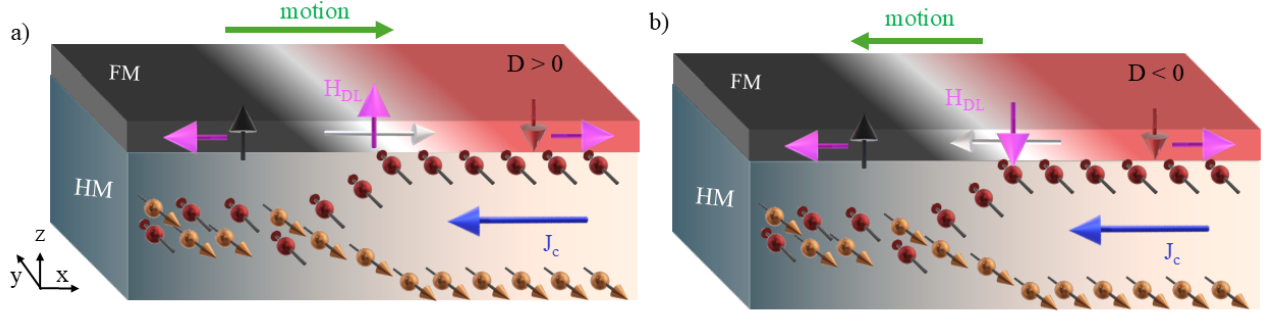


Figure 2.14: **Current-induced motion of chiral Néel domain walls driven by damping-like spin-orbit torque.** (a) For a right-handed Néel wall ($D_{\text{iDMI}} > 0$), the wall core magnetization points along $+x$, yielding an effective damping-like field \mathbf{H}_{DL} oriented upward $+z$ at the wall center. (b) For a left-handed Néel wall ($D_{\text{iDMI}} < 0$), the wall core magnetization points along $-x$, resulting in a reversed \mathbf{H}_{DL} along $-z$ and domain wall motion in the direction $-x$ under the same current polarity.

Fig. 2.14 illustrates how the DL-SOT drives chiral Néel domain walls depending on the sign of the iDMI. When a charge current density \mathbf{J}_c flows along the heavy metal layer along $-x$, the SHE generates a spin accumulation polarized transverse to the current along $-y$. For a right-handed Néel wall ($D_{\text{iDMI}} > 0$, Fig. 2.14 (a)), the wall core magnetization points along $+x$. The resulting DL effective field \mathbf{H}_{DL} is oriented upward $+z$ at the domain wall center. This field couples to the out-of-plane domains and produces a force that shifts the wall position in the $+x$ direction. In contrast, for a left-handed Néel wall ($D_{\text{iDMI}} < 0$, Fig. 2.14 (b)), the wall core magnetization points along $-x$. In this case, the sign of the effective field is along $-z$, and the wall is driven in the direction of $-x$ under the same current polarity. Bloch walls, by comparison, have a core magnetization parallel to the spin polarization, which yields $\mathbf{M} \times \hat{\mathbf{p}} = 0$; hence, they do not experience a finite damping-like driving field and remain immobile under DL-SOT. Thus, for unambiguous dynamics of spin textures in device applications, homochiral Néel spin textures become a requisite.

Inverse Spin-Galvanic Effect

The inverse spin-galvanic effect (iSGE), also known as the Edelstein effect [167], arises in systems with strong spin-orbit coupling and broken inversion symmetry, such as heavy-metal/ferromagnet interfaces. Its microscopic origin is described by the Rashba Hamiltonian, which expresses the coupling between electron momentum and spin:

$$H_R = \alpha_R (\hat{\mathbf{z}} \times \mathbf{k}) \cdot \boldsymbol{\sigma} = \alpha_R (-k_y \sigma_x + k_x \sigma_y), \quad (2.56)$$

Here, α_R is the Rashba coefficient, \mathbf{k} is the electron crystal momentum in the two-dimensional plane, $\hat{\mathbf{z}}$ denotes the interface normal (axis of structural inversion asymmetry), and $\boldsymbol{\sigma}$ is the Pauli matrix acting on the electron spin [‡]. In the presence of Rashba SOC, an in-plane charge current induces a nonequilibrium spin accumulation at the interface, which couples to the magnetization of the adjacent FM layer [168–170]. This interfacial spin accumulation can be described as an effective magnetic field acting on the ferromagnet, denoted \mathbf{H}_{FL} . Alongside the interfacial effective field, the Rashba-induced spin accumulation may generate an additional torque, termed the indirect Rashba effect, which originates from spin diffusion within the FM in a manner analogous to the SHE. The efficiency of the FL torque can be calculated as $\zeta_{\text{FL}} = \mu_0 \mathbf{H}_{\text{FL}} \frac{2eM_s t}{\hbar J_c}^{**}$.

Role of iDMI and Spin-Orbit Torques in Determining Chirality and Motion.

- The sign of the interfacial DMI, D_{iDMI} , governs the chirality of the spin textures.
- For DL-SOT-driven dynamics, homochiral Néel spin textures are essential, since the chirality dictates the direction of motion.
- Bloch and Néel DWs experience SOTs oriented perpendicular to each other; the Néel configuration driven efficiently by the DL-SOT.

2.5.4 Skyrmion Dynamics with SOTs

The manipulation of magnetic textures relies on transferring angular momentum to the local magnetization. While uniform magnetic fields can deform skyrmions, they are generally ineffective for inducing directed motion. Skyrmion displacement under field gradients has been demonstrated [171, 172], while this approach requires large spatial variations in the field, making it impractical for device integration. A more efficient method involves the use of spin-polarized electric currents. In systems with iDMI, SOTs have gained significant attention due to their enhanced efficiency compared to conventional spin-transfer torques STTs. SOTs arise from the conversion of charge current into spin current via spin Hall or Rashba effects in adjacent heavy-metal layers such as Pt [168, 173], enabling fast and energy-efficient control of skyrmion motion in multilayer systems.

[‡]To simplify Eq. 2.56, note that for a two-dimensional electron gas $\mathbf{k} = (k_x, k_y, 0)$ and the inversion-asymmetry axis $\hat{\mathbf{z}} = (0, 0, 1)$. The cross product is then $\hat{\mathbf{z}} \times \mathbf{k} = (-k_y, k_x, 0)$. Taking the dot product with $\boldsymbol{\sigma} = (\sigma_x, \sigma_y, \sigma_z)$ yields

$$H_R = \alpha_R [(-k_y)\sigma_x + (k_x)\sigma_y] = \alpha_R(-k_y\sigma_x + k_x\sigma_y).$$

**Disentangling SOT contributions from bulk SHE and interfacial iSGE is difficult in bilayers with nanometer-scale spin diffusion lengths and magnetic layer thicknesses. A key distinction is that iSGE is purely interfacial and independent of the nonmagnetic layer thickness, whereas SHE is a bulk effect and strongly influenced by the thickness of the heavy-metal layer.

The Thiele equation provides a reduced model for the dynamics of magnetic textures, derived from the LLG equation under the assumption of translational invariance [174]. It is particularly useful for describing solitonic structures such as skyrmions [175, 176]. The magnetization texture is represented as

$$\mathbf{m}(\mathbf{r}, t) = \mathbf{m}_0(\mathbf{r} - \mathbf{R}(t)) + \delta\mathbf{m}(\mathbf{r}, t) \quad (2.57)$$

where $\mathbf{R}(t)$ is the time-dependent skyrmion position, and $\delta\mathbf{m}$ accounts for deviations from the rigid profile \mathbf{m}_0 . The Thiele formalism neglects $\delta\mathbf{m}$, assuming rigid translation. Within this approximation, the skyrmion is treated as a quasi-particle whose dynamics are governed by the Thiele equation [174, 177]

$$\mathbf{G} \times \mathbf{v} - \alpha D\mathbf{v} + \mathbf{F}_{\text{SOT}} = 0 \quad (2.58)$$

where $\mathbf{v} = \dot{\mathbf{R}}(t)$ is the skyrmion velocity and α is the Gilbert damping constant. The first term in Eq. 2.58 describes the gyrotropic force, with $\mathbf{G} = 4\pi L_s t Q_{\text{sk}} \hat{\mathbf{z}}$, where $L_s = \frac{M_s}{\gamma}$ is the angular momentum density, M_s the saturation magnetization, γ the gyromagnetic ratio, t the film thickness, and Q_{sk} the topological charge (defined in Eq. 2.41). The second term represents the dissipative force, with the tensor elements

$$D_{\mu\nu} = L_s t d_{\mu\nu}, \quad d_{\mu\nu} = \iint (\partial_\mu \mathbf{m}_0 \cdot \partial_\nu \mathbf{m}_0) d^2\mathbf{r}, \quad \mu, \nu \in \{x, y\}, \quad (2.59)$$

For circular symmetric quasiparticles such as skyrmions and $n\pi$ skyrmions, the dissipative tensor becomes diagonal owing to rotational symmetry, where the tensor elements $D_{xx} = D_{yy} = L_s t \iint (\partial_x \mathbf{m}_0 \cdot \partial_x \mathbf{m}_0) d^2\mathbf{r}$. The last term in Eq. 2.58, \mathbf{F}_{SOT} , represents forces due to external stimuli. For an in-plane charge current J_c in the adjacent heavy metal, the spin Hall effect generates a transverse spin current polarized along the y -axis, exerting a DL-SOT torque on the magnetization [23, 24]. This results in an effective driving force.

$$\mathbf{F}_{\text{SOT}} = -\frac{\hbar}{2e} \theta_{\text{SH}} J_c \mathbf{l} \quad (2.60)$$

Here θ_{SH} is the spin Hall angle. The tensor \mathbf{l} , often referred to as the SOT-efficiency tensor, quantifies the chirality of the magnetization profile and is defined as

$$l_{\mu\nu} = \iint [(\partial_\mu \mathbf{m}_0) \times \mathbf{m}_0]_\nu d^2\mathbf{r}, \quad \mu, \nu \in \{x, y\} \quad (2.61)$$

For an isotropic Néel skyrmion^{††}, the tensor becomes diagonal, whereas for a Bloch skyrmion it becomes an off-diagonal (antisymmetric) form. Consequently, Néel and Bloch skyrmions experience SOT-induced forces that are oriented perpendicular to each other when driven by the same current. Assuming the current flows along the x-axis, the solution of Eq. 2.58 yields

$$v_x = \frac{F_{\text{SOT}} \alpha D}{G^2 + (\alpha D)^2}, \quad (2.63)$$

$$v_y = \frac{F_{\text{SOT}} G}{G^2 + (\alpha D)^2} \quad (2.64)$$

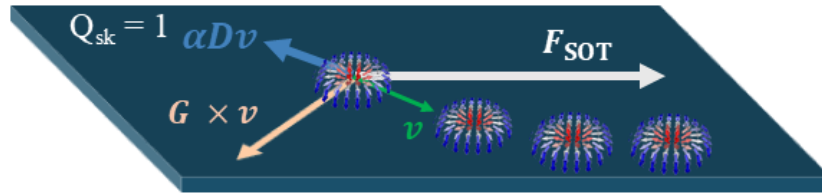


Figure 2.15: **Skyrmion Hall effect.** Schematic illustration of skyrmion motion under a spin-orbit torque SOT driving force F_{SOT} . The skyrmion with topological charge $Q_{\text{sk}} = 1$ experiences a transverse gyrotropic force and a dissipative drag in addition to the driving force. The resulting velocity \mathbf{v} acquires both longitudinal and transverse components, giving rise to the SkHE.

This transverse motion, resulting from the gyrotropic deflection of the skyrmion under an applied force, is referred to as the skyrmion Hall effect (SkHE) as shown in Fig. 2.15. The associated skyrmion Hall angle θ_{SkHE} quantifies the deviation of the skyrmion trajectory from the direction of the driving force and is defined as

$$\theta_{\text{SkHE}} = \tan^{-1} \left(\frac{v_y}{v_x} \right) = \tan^{-1} \left(\frac{G}{\alpha D} \right) \quad (2.65)$$

^{††}For a Néel-type skyrmion, the tensor \mathbf{I} becomes diagonal, and its nonzero components are given by

$$I_{xx} = I_{yy} = \iint \left(m_x \frac{\partial m_z}{\partial x} - m_z \frac{\partial m_x}{\partial x} \right) d^2 \mathbf{r} \quad (2.62)$$

Experimental Observation of Skyrmion Dynamics and Deviation from the Thiele Formalism

Due to the **SkHE**, the skyrmion trajectory acquires a transverse component, eventually leading the skyrmion to interact with the boundary of the magnetic medium. Upon reaching the edge, a repulsive force arises, directed normal to the boundary. This force counteracts the transverse motion and, together with the longitudinal **SOT**-induced driving force, results in a rectified motion predominantly along the **x**-axis [178, 179]. The first direct observation of current-driven skyrmion motion in **FM/HM** multilayer structures was reported by Woo et al. [31]. Subsequent time-resolved and real-space imaging studies enabled the direct observation of the **SkHE** [32, 33]. These experimental results [33, 131, 180], however, deviate from the rigid-particle dynamics expected from the Thiele model. In particular, skyrmion motion requires a finite depinning current density, below which skyrmions remain immobilized. Once this threshold is exceeded, the velocity increases with current density. Furthermore, the skyrmion Hall angle has been observed to vary as a function of skyrmion velocity [33], in contrast to the constant value predicted by the Thiele model. These observations demonstrate that skyrmion dynamics are strongly influenced by material disorder and cannot be described by an idealized rigid-body picture. When pinning and defects are present, the dynamics of skyrmion motion can be divided into three regimes: (i) a creep regime, characterized by extremely slow, thermally activated motion; (ii) a depinning regime, where skyrmion velocity starts to increase with current above the depinning threshold; and (iii) a flow regime, accessible at larger currents, where skyrmion motion is relatively insensitive to pinning and follows the linear dependence predicted by the Thiele equation. It has been shown that the maximum skyrmion velocity in ferromagnetic systems is limited by surface tension and deformation, where the skyrmion elongates and transforms into a stripe domain [181]. It should be noted that the Thiele formalism treats skyrmions as rigid objects, whereas in practice, pinning-induced deformations and rotational symmetry breaking under strong **SOTs** give rise to deviations from this simplified description. These aspects form the basis of the skyrmion dynamics investigated in Chapters 4 and 5. Furthermore, experimental studies have shown that, at finite temperature, the skyrmion velocity exhibits strong temperature dependence, whereas the **SkHA** remains nearly constant and deviates from the Thiele equations of motion [181].

Strategy to Suppress the **SkHE**

The **SkHE** is a major challenge for the implementation of skyrmions in racetrack memories and logic devices. When a current is applied, the topological nature of skyrmions gives rise to a transverse deflection due to the gyroforce, which results in motion at a finite Hall angle with respect to the current direction as discussed above. Consequently, skyrmions drift toward the sample edges, where they can be annihilated, leading to reduced device stability and data loss. For robust and scalable

skyrmion-based memory technologies, minimizing or eliminating the **SkHE** is therefore essential.

As discussed in Eq. 2.65, the skyrmion Hall angle (**SkHA**) is given by the inverse tangent of the ratio between the gyrovector and the dissipative force. The most direct approach to suppressing the **SkHE** is to achieve a net topological charge Q_{sk} of zero, which effectively nullifies the gyroforce. One natural platform for this is an antiferromagnet or an antiferromagnetically coupled system. In an **AFM** skyrmion [70, 72, 182], the material consists of two sublattices with opposite local magnetizations and opposite skyrmion core polarities. This configuration corresponds to two skyrmions with charges $(+1, -1)$, yielding a net $Q_{\text{sk}} = 0$. **AFM** systems also offer a potential route to circumvent key limitations associated with **FM** skyrmions. In particular, the compensated spin angular momentum in **AFMs** eliminates the skyrmion Hall effect, enabling current-driven motion without transverse deflection [70, 71, 73]. The absence of net magnetization suppresses dipolar fields, enabling denser skyrmion packing and higher storage density. In **SyAFMs**, skyrmions in adjacent layers have opposite core polarities and move together as a rigid composite object, resulting in cancellation of the transverse velocity components and suppression of the **SkHE**. Skyrmion dynamics in antiferromagnetically coupled sublattices are discussed in the following subsection.

Topological objects of higher degree can suppress the **SkHE**. One example is the skyrmionium (or 2π skyrmion), which is a bound state of two concentric skyrmions with opposite helicities, yielding a composite quasi-particle with $Q_{\text{sk}} = 0$ [183, 184]. Its internal structure consists of a core skyrmion nested inside another with opposite topological charge, such that the net gyroforce cancels. Although skyrmionium offers the advantage of zero **SkHE**, its stabilization and efficient deterministic nucleation at low energy cost remain open challenges. Another approach is the formation of chimera or Q_{sk} skyrmions, where one half of the structure has skyrmion topology and the other half antiskyrmion topology. These objects are predicted to emerge in frustrated magnets and can, in principle, exhibit zero Hall angle motion under current drive [185, 186]. Notably, frustrated magnets can also host a rich variety of topological objects with arbitrary Q_{sk} and helicity, which can result in ambiguous motion under **SOT**.

2.5.5 Antiferromagnetic skyrmion dynamics in synthetic antiferromagnets

In this section, the dynamics of skyrmions in magnetic bilayer systems composed of two antiferromagnetically coupled sublattices, denoted as A and B, are discussed. This forms the fundamental basis of **SyAFM** studies presented in this thesis. The magnetization dynamics in each sublattice, represented by the unit vectors \mathbf{m}_A and \mathbf{m}_B , follows the **LLG** equation with the respective parameters: saturation magnetizations M_A , M_B , and angular momentum densities L_A , L_B . In the limit of strong inter-sublattice exchange, the system maintains an antiparallel configuration ($\mathbf{m}_A = -\mathbf{m}_B$).

Under this approximation, the bilayer can be mapped onto an effective ferromagnetic system described by a single magnetization vector $\mathbf{m} = \mathbf{m}_A = -\mathbf{m}_B$, as shown in Refs. [187, 188]. The effective material parameters are obtained by summing the two LLG equations, each integrated over the thickness of its respective layer. This formulation eliminates the inter-sublattice exchange term due to the assumed antialignment^{‡‡}. The effective LLG equation is then determined by comparing the resulting expression term by term with the standard LLG form for a single layer. The effective parameters are [188]: the saturation magnetization $M_{s,\text{eff}} = \frac{M_A t_A - M_B t_B}{t}$, the angular momentum density $L_{s,\text{eff}} = \frac{L_A t_A - L_B t_B}{t}$, the dissipative angular momentum $L_{\alpha,\text{eff}} = \frac{L_A t_A + L_B t_B}{t}$, the effective damping $\alpha_{\text{eff}} = \frac{L_{\alpha,\text{eff}}}{L_{s,\text{eff}}}$, and the effective gyromagnetic ratio $\gamma_{\text{eff}} = \frac{M_{s,\text{eff}}}{L_{s,\text{eff}}}$. Here $t = t_A + t_B$ is the total film thickness for stacked layer geometries such as SyAFMs and multilayer ferrimagnets. For spatially merged sublattices, such as in ferrimagnetic alloys or intrinsic antiferromagnets, one typically assumes $t = t_A = t_B$.

Two characteristic points arise in this framework: the magnetization compensation point (MCP), defined by $M_A t_A = M_B t_B$, and the angular momentum compensation point (ACP), defined by $L_A t_A = L_B t_B$. These coincide when the sublattices are magnetically identical ($\gamma_A = \gamma_B$), as in ideal SyAFMs or intrinsic AFMs, however differ if $\gamma_A \neq \gamma_B$ (in the case of ferrimagnets). Consider that each sublattice is assumed to host a Néel-type skyrmion. In the presence of strong inter-sublattice coupling, these form a bound skyrmion pair whose dynamics is governed by coupled Thiele equations:

$$\mathbf{G}_A \times \mathbf{v}_A - \alpha_A D_A \mathbf{v}_A + \mathbf{F}_A + \mathbf{F}_{B/A} = 0, \quad (2.67)$$

$$\mathbf{G}_B \times \mathbf{v}_B - \alpha_B D_B \mathbf{v}_B + \mathbf{F}_B + \mathbf{F}_{A/B} = 0 \quad (2.68)$$

Here $\mathbf{F}_{B/A}$ and $\mathbf{F}_{A/B}$ represent the inter-skyrmion interaction forces between sublattices A and B. By Newton's third law, $\mathbf{F}_{B/A} = -\mathbf{F}_{A/B}$. Assuming steady-state motion with equal skyrmion velocities $\mathbf{v}_A = \mathbf{v}_B = \mathbf{v}$, the coupled Thiele equations can be summed, resulting in an effective Thiele equation

^{‡‡}The effective LLG equation takes the form

$$(L_A t_A - L_B t_B) \frac{\partial \mathbf{m}}{\partial t} = -(M_A t_A - M_B t_B) \mathbf{m} \times \mathbf{H}^{\text{eff}} + (L_{\alpha,A} t_A + L_{\alpha,B} t_B) \mathbf{m} \times \frac{\partial \mathbf{m}}{\partial t} \quad (2.66)$$

expressed in terms of renormalized parameters:

$$\mathbf{G}_{\text{eff}} = 4\pi L_{s,\text{eff}} t Q_{\text{sk}} \hat{z}, \quad (2.69)$$

$$(\alpha D)_{\text{eff}} = (\alpha_A L_A t_A + \alpha_B L_B t_B) d = L_{\alpha,\text{eff}} t d, \quad (2.70)$$

$$\mathbf{F}_{\text{tot}} = -\frac{\hbar}{2e} \mathbf{J} (\theta_{\text{SH},A} + \theta_{\text{SH},B}) I = -\frac{\hbar}{2e} \mathbf{J} \theta_{\text{SH}} I \quad (2.71)$$

where $\theta_{\text{SH}1}$, $\theta_{\text{SH}2}$ are the spin Hall angles corresponding to sublattices A and B. The total spin Hall angle is defined as $\theta_{\text{SH}} = \theta_{\text{SH}1} + \theta_{\text{SH}2}$. The solutions to the steady-state dynamics with the [SkHA](#) as

$$\theta_{\text{SkHA}} = \tan^{-1} \left(\frac{v_y}{v_x} \right) = \tan^{-1} \left(\frac{4\pi L_{s,\text{eff}} Q_{\text{sk}}}{L_{\alpha,\text{eff}} d} \right) \quad (2.72)$$

In Eq. 2.72, the [SkHE](#) vanishes when the effective angular momentum density $L_{s,\text{eff}}$ approaches zero. In ferrimagnets, this condition is generally more complex due to unequal gyromagnetic ratios γ across sublattices, particularly in systems comprising rare-earth and transition-metal elements. As a result, even when the net magnetization M_s is compensated, the [SkHE](#) may persist because $L_{s,\text{eff}}$ remains finite. This demonstrates a key distinction in ferrimagnets: the [MCP](#) and the [ACP](#) do not coincide, and the [SkHE](#) vanishes only at the [ACP](#). By contrast, in [SyAFMs](#), the focus of this thesis, CoFeB and CoB are employed as the ferromagnetic layers. These materials exhibit nearly identical gyromagnetic ratios, resulting in the [MCP](#) and [ACP](#) coinciding. Consequently, the [SkHE](#) vanishes in [SyAFMs](#) when the net magnetization M_s is compensated.

2.6 Conclusion

In summary, this chapter introduced the theoretical formalisms required to describe the magnetic properties of ultrathin ferromagnetic films, particularly when interfaced with heavy-metal layers providing strong [SOC](#). The micromagnetic framework and fundamental energy contributions were outlined as the basis for stabilizing diverse spin textures, including skyrmions and bimerons. Furthermore, magnetization dynamics were formulated within the [LLG](#) framework together with spin-orbit torques, providing a theoretical description of the motion of these textures under applied current. This theoretical foundation provides the basis for understanding the stability and dynamics of topological spin structures in synthetic antiferromagnets studied in the following chapters.

Experimental Techniques

Most of us who become experimental physicists do so for two reasons; we love the tools of physics because to us they have intrinsic beauty, and we dream of finding new secrets of nature as important and as exciting as those uncovered by our scientific heroes.

Luis Walter Alvarez

3.1 Introduction

This chapter presents the experimental methodologies employed to obtain the results discussed in the subsequent chapters. The work presented in this thesis is based on thin film multilayers fabricated on silicon nitride substrates and free-standing silicon nitride membranes. The experimental methodological framework is divided into three main sections: fabrication, in-house imaging, and synchrotron-based imaging. The fabrication stage involves thin-film deposition, magnetic characterization, and nanofabrication techniques. These processes enable precise control over layer thickness, composition, and lateral geometry, ensuring faithful realization of the designed multilayer structures. Imaging was performed using both in-house and synchrotron-based techniques. In-house methods include scanning electron microscopy with polarization analysis (SEMPA) and magnetic force microscopy (MFM), which provide surface-sensitive magnetic and topographical contrast, respectively. Synchrotron-based imaging techniques were conducted using X-ray magnetic circular dichroism (XMCD) combined with

photoemission electron microscopy (PEEM) [189, 190] and scanning transmission X-ray microscopy (STXM) [191]. The XMCD-PEEM measurements were performed at the CIRCE beamline of the ALBA Synchrotron, while the XMCD-STXM experiments were carried out at the MAXYMUS beamline of BESSY II and the PoLux beamline, Swiss Light Source (SLS, PSI, Switzerland).

3.2 Sample Fabrication

The fabrication of synthetic antiferromagnetic multilayers was carried out by magnetron sputtering, followed by magnetic characterization using SQUID magnetometry and nanofabrication using electron-beam lithography. Detailed procedures are described in this section.

3.2.1 Thin Film Deposition by Magnetron Sputtering

Precise control of the multilayer architecture is essential to tailor the magnetic properties, such as the *iDMI* and the effective anisotropy K_{eff} . All samples discussed in this thesis were fabricated at Johannes Gutenberg University Mainz using a commercial Singulus Rotaris magnetron sputtering system operating under ultra-high vacuum (UHV) conditions, with a base pressure below 10^{-9} mbar. The depositions were carried out by *Maria-Andromachi Syskaki* and *Dr. Takaaki Dohi*.

Magnetron sputtering is a physical vapor deposition technique in which atoms from a solid target are ejected by energetic ion bombardment and subsequently condense on a substrate to form a thin film. The substrates employed in this work include Si/SiO₂ wafers, silicon nitride (SiN_x) wafers, and SiN_x membranes, while the target materials comprise metals (e.g. Ta, Pt, Ir) and alloys (e.g. Co₂₀Fe₆₀B₂₀, Co₆₀Fe₂₀B₂₀, and Co₂₀B₈₀). During deposition, an inert argon gas is introduced into the sputtering chamber. Applying a constant voltage to the target generates a plasma in which argon atoms are ionized. The positively charged argon ions are accelerated towards the negatively biased target, causing the ejection of target atoms that travel toward the substrate, where they condense and form the film. To enhance the ionization efficiency, a magnetic field is applied parallel to the target surface. This field leads to a circular trajectory of secondary electrons near the target, increasing the probability of further ionizing collisions and thereby sustaining a dense plasma, a process known as magnetron sputtering (illustrated in Fig. 3.1).

The morphology and homogeneity of the deposited layers depend sensitively on the argon pressure and the sputtering power, which determine the growth rate and surface mobility of adatoms. Optimized deposition parameters enable the formation of atomically smooth and continuous films, which are crucial for the reproducible magnetic properties required in multilayer stacks. Compared to other deposition techniques (such as thermal evaporation), sputtering offers superior uniformity, higher deposition rates, and compatibility with refractory materials such as Pt, Ta, and Ir. It is

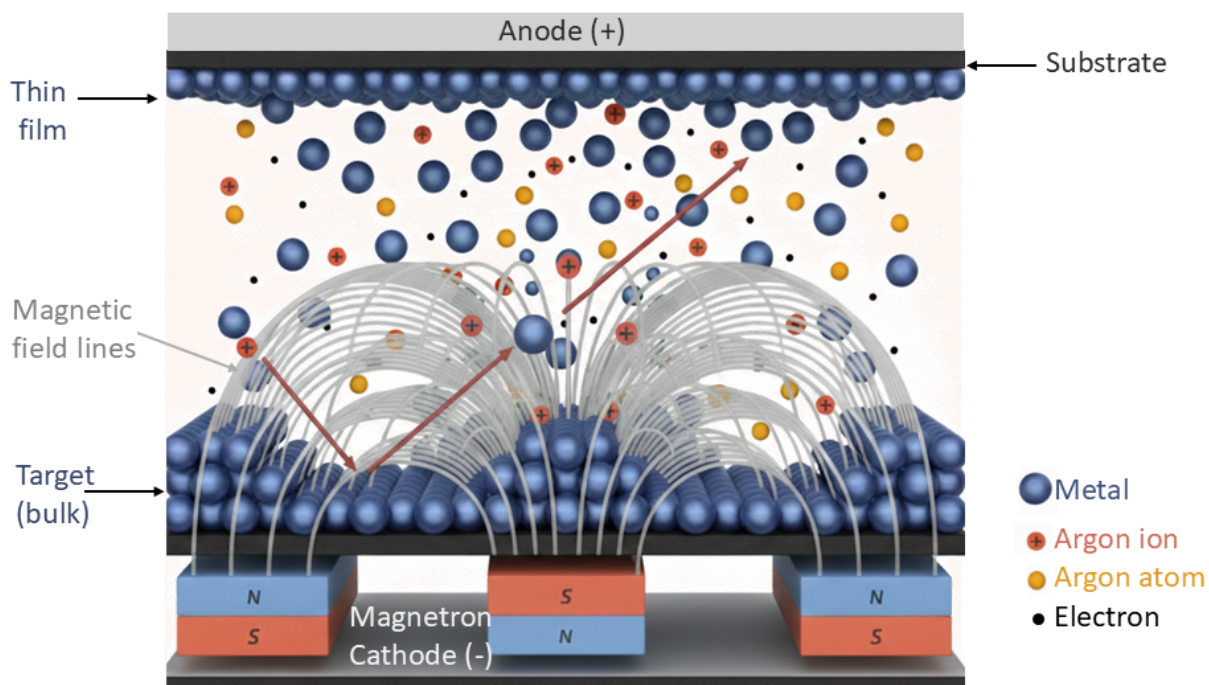


Figure 3.1: **Schematic illustration of the magnetron sputtering process.** Argon gas is ionized near the target, and the resulting Ar^+ ions are accelerated toward the negatively biased target, ejecting metal atoms that deposit on the substrate to form a thin film. Redrawn based on [192].

therefore one of the preferred techniques for both research and industrial thin-film fabrication. The operating principle of the magnetron sputtering process is schematically shown in Fig. 3.1. In this thesis, instead of a single SyAFM block, multiple repetitions comprising 14 to 25 SyAFM layers were deposited. The deposition parameters and conditions for the multilayer stacks investigated in this thesis are documented in the eLabFTW logbooks. The corresponding experiment identifiers for each dataset are referenced in Chapter 1 and in the introductory sections of the respective results chapters. The resulting smoothness of the individual layers was verified using X-ray reflectivity measurements.

In this work, we investigate the direct real-space imaging of antiferromagnetic skyrmions, bimerons, and complex spin textures, where the magnetizations of the two ferromagnetic sublattices are orthogonally aligned. For unambiguous detection, different magnetic materials (Fe and Co) are employed in the two sublattices to enable element-specific contrast by tuning the X-ray energy in synchrotron-based imaging, as discussed in the later Section 3.4. Cross-sectional transmission electron microscopy (TEM) was performed on a representative SyAFM multilayer stack comprising 25 repetitions (stack #S3c) to assess the chemical separation of the Fe- and Co-rich sublattices and the uniformity of the Ir and Pt spacer layers, as shown in Fig. 3.2(a). A high-resolution zoom-in reveals a slight waviness propagating through the entire film thickness, suggesting that its origin

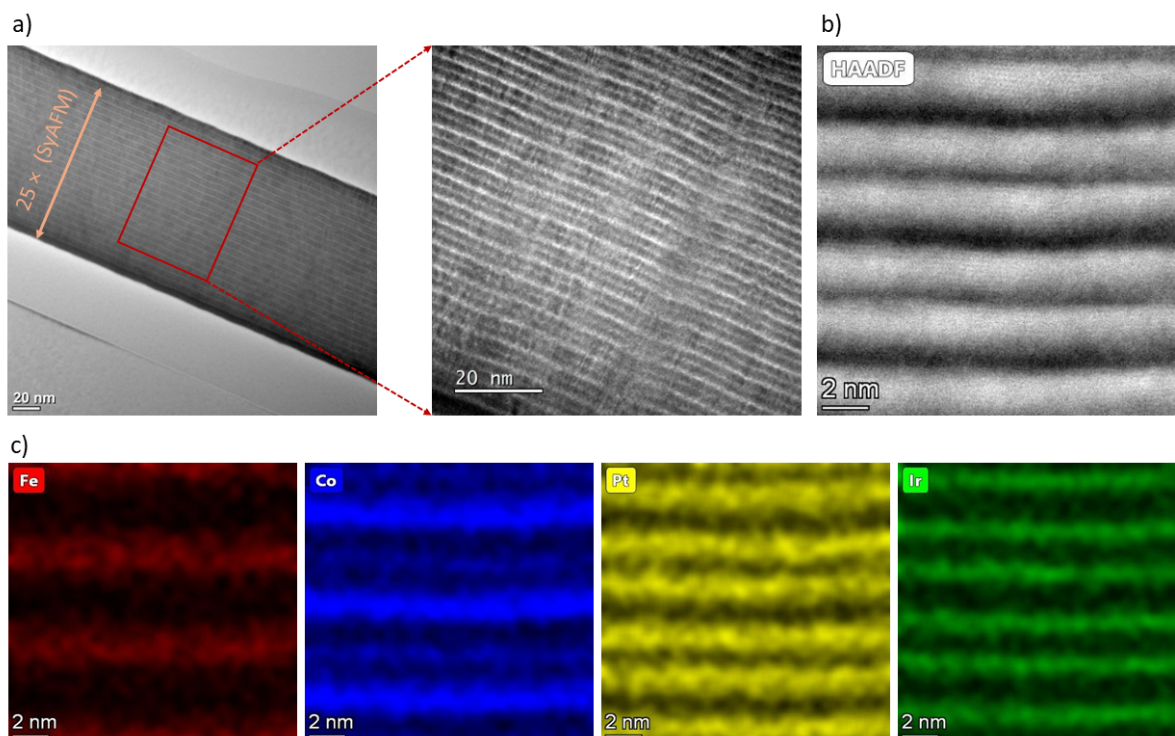


Figure 3.2: **Structural and compositional analysis of stack #S3d.** (a) Cross-sectional TEM image of the multilayer showing 25 repetitions of the SyAFM unit. The magnified view highlights the well-defined multilayer periodicity and uniform layer thickness. (b) High-angle annular dark-field (HAADF) image revealing sharp interfaces and clear contrast between the heavy-metal and ferromagnetic layers. (c) EDX elemental maps for Fe (red), Co (blue), Pt (yellow), and Ir (green). The maps confirm distinct chemical layering of Fe- and Co-rich sublattices and precise control of spacer layers.

stems from the substrate roughness (RMS roughness in the range of 0.2-0.3 nm). No shorts are observed between the SyAFM blocks, and 25 well-defined repetitions of the SyAFM unit cell are clearly resolved, demonstrating robust interlayer spacing and consistent interlayer exchange coupling. This structural precision is critical, as deviations at the sub-nanometer level could directly influence the interlayer exchange coupling strength and the effective anisotropy, both of which govern the stability of topological spin textures present. Fig. 3.2(b,c) presents high-angle annular dark-field (HAADF) scanning TEM imaging with energy-dispersive X-ray spectroscopy (EDX) elemental mapping at the same cross-sectional position. The elemental maps of Fe, Co, Ir, and Pt confirm the presence and spatial separation of the chemically engineered sublayers. The Fe- and Co-rich ferromagnetic layers, corresponding to sublattices A and B, are clearly resolved, providing the basis for element-specific probing of their magnetization states via XMCD contrast. The TEM measurements were performed by Dr. Thibaud Denneulin at Forschungszentrum Jülich.

3.2.2 Measurement of Magnetic Properties

During this study, a superconducting quantum interference device (**SQUID**) magnetometer was employed to quantify the interlayer exchange coupling strength, effective anisotropy, saturation magnetization, magnetic compensation, and low-temperature magnetic properties of the synthetic antiferromagnetic multilayers.

A **SQUID** is an ultra-sensitive magnetometer that measures extremely small magnetic fields by exploiting quantum interference effects in a superconducting loop [193]. It can operate in either AC or DC mode and consists of a superconducting loop incorporating one (AC) or two (DC) Josephson junctions. Each Josephson junction comprises a normal metal or an insulating barrier sufficiently thin to permit the quantum tunneling of Cooper pairs. In a DC **SQUID**, two such junctions are connected in parallel to form a closed superconducting loop, as illustrated in Fig 3.3(a). The non-superconducting barriers permit the loop to carry a supercurrent through the phase-coherent tunneling of Cooper pairs, a phenomenon known as the Josephson effect [194]. The operating principle of **SQUID** relies on the quantization of magnetic flux in a superconducting loop. The flux quantum is defined as

$$\Phi_0 = \frac{h}{2e} = 2.07 \times 10^{-15} \text{ Wb}, \quad (3.1)$$

where h denotes the Planck constant and e the electron charge. A change in the external magnetic flux induces a circulating supercurrent I_S in the superconducting loop to maintain flux quantization. This screening current adjusts its magnitude and direction such that the total magnetic flux through the loop remains an integer multiple of Φ_0 . For an applied flux $\Phi < \Phi_0/2$, I_S flows in a direction opposing the external field, thereby compensating the induced flux. When the applied flux exceeds $\Phi_0/2$, increasing I_S further becomes energetically unfavorable; instead, the current reverses its direction to assist the applied flux, producing a net flux of one quantum Φ_0 in accordance with flux quantization. Consequently, the reversible circulation of I_S varies periodically with the applied flux, exhibiting a period of Φ_0 (see Fig.3.3(b)). The presence of I_S also reduces the maximum bias current that can be applied to the junctions without generating a voltage, known as the critical current, thereby modulating the I - V characteristics of the **SQUID**.

In magnetometric operation, a constant bias current slightly exceeding the **SQUID**'s critical current is applied to ensure that a measurable voltage is maintained across the device. When a bias current flows through the **SQUID** loop, it is parallel to the screening current I_S in one branch and anti-parallel in the other. If the combined bias and screening currents in one junction exceed its critical value, that junction becomes resistive, forcing the entire bias current through the opposite arm, which then also transitions to the resistive state. Consequently, the maximum bias current

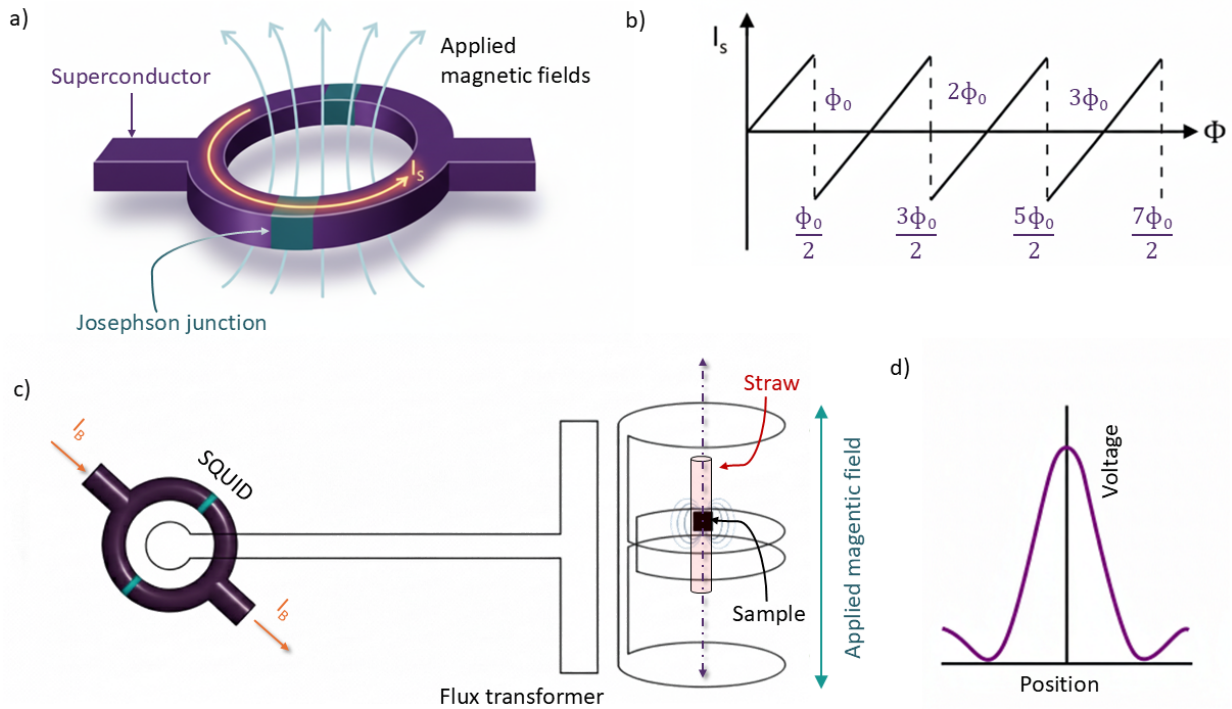


Figure 3.3: **Illustration of the working principle of SQUID magnetometry.** (a) Schematic of a DC SQUID consisting of a superconducting loop with two Josephson junctions. The magnetic flux threading the loop is quantized in integer multiples of the flux quantum Φ_0 . (b) Variation of I_S with the applied magnetic flux Φ , showing its periodic behavior arising from flux quantization. (c) Schematic of the SQUID magnetometer setup. The sample is moved through superconducting pick-up coils, inducing a current that is transferred to the SQUID input coil via a flux transformer. A perpendicular magnetic field can be applied to the sample using a superconducting magnet. The resulting flux in the input coil is detected by the SQUID, which converts it into a voltage signal proportional to the sample's magnetic moment. (d) Example of the measured SQUID voltage signal as a function of the sample position within the pick-up coils.

that can be applied without developing a voltage decreases by $2I_S$ from its zero-flux value I_C . The critical current thus reaches a minimum I_C^0 when the screening current is maximal, corresponding to half-integer multiples of the flux quantum Φ_0 . The dependence of the I - V characteristics on I_S causes the measured voltage across the SQUID to vary periodically with the applied magnetic flux. The output voltage oscillates between well-defined limits V_{\min} and V_{\max} with a period of Φ_0 , analogous to the periodic variation of I_S . Hence, variations in the applied flux Φ can be directly inferred from the corresponding voltage modulation, which forms the basis of SQUID magnetometry. Since the SQUID converts magnetic flux into a measurable voltage, it functions as a flux-to-voltage transducer.

In a practical magnetometer, the sample typically does not couple directly to the SQUID loop.

Instead, it is positioned within superconducting pick-up coils that detect the magnetic response and inductively transfer the associated flux to the SQUID via a superconducting flux transformer, as schematically shown in Fig. 3.3(c). The resulting voltage signal exhibits a characteristic dependence on the sample position within the pick-up coils, as illustrated in Fig. 3.3(d). The pick-up coils are usually located inside a superconducting magnet capable of applying a controlled magnetic field to the sample (e.g., for measuring hysteresis). The SQUID itself is placed in a magnetically shielded region, spatially separated from the field source, to prevent interference from the applied magnetic field [193].

Magnetic characterization in this thesis was carried out using a Quantum Design MPMS XL SQUID magnetometer, offering a magnetic moment sensitivity on the order of 10^{-11} A m². Given the low magnetic signal from the ultrathin layers (0.4-1.1 nm used in this work) and, in particular, from synthetic antiferromagnetic samples, special care was taken during these measurements. Since a small amount of material is inevitably deposited along the sample edges during sputtering, this can lead to an overestimation of the saturation magnetization (M_s) and consequently to an incorrect estimation of the effective anisotropy. To minimize this effect, all samples were carefully cut along all four edges before measurements.

3.2.3 Nanofabrication by Electron Beam Lithography

After the deposition of the synthetic multilayer structures on Si/SiN substrates, the samples exhibiting promising magnetic properties, as identified from SQUID magnetometry, were selected for further studies. Samples intended for investigating the nucleation and dynamics of topological magnetic textures were further deposited on 100 nm thick SiN membranes supported by Si frames containing 300 μ m windows. Here, micrometre-scale wire patterns were pre-patterned as negative structures [195] in a resist mask using electron-beam lithography (EBL) [196, 197]. This process yielded patterned magnetic tracks of defined dimensions after lift-off, followed by a second EBL step for the deposition of contact pads. A range of wire widths, 0.5, 1, 2, 5, and 10 μ m, was patterned. For each width, the wire length was adjusted to yield a room-temperature resistance of ≈ 50 Ω . This subsection outlines the nanofabrication process employed for this purpose. The main steps of this process are illustrated in Fig. 3.4(a), and a brief description of the procedure is provided in Appendix C. After fabrication, an optical microscope image of the patterned device on the membrane is shown in Fig. 3.4(b). Another approach involves depositing the multilayer thin film directly onto the SiN substrate, followed by EBL using a negative resist and controlled etching monitored by an end-point detector. However, during this process, the membrane often develops wrinkles as shown in Fig. 3.4(c).

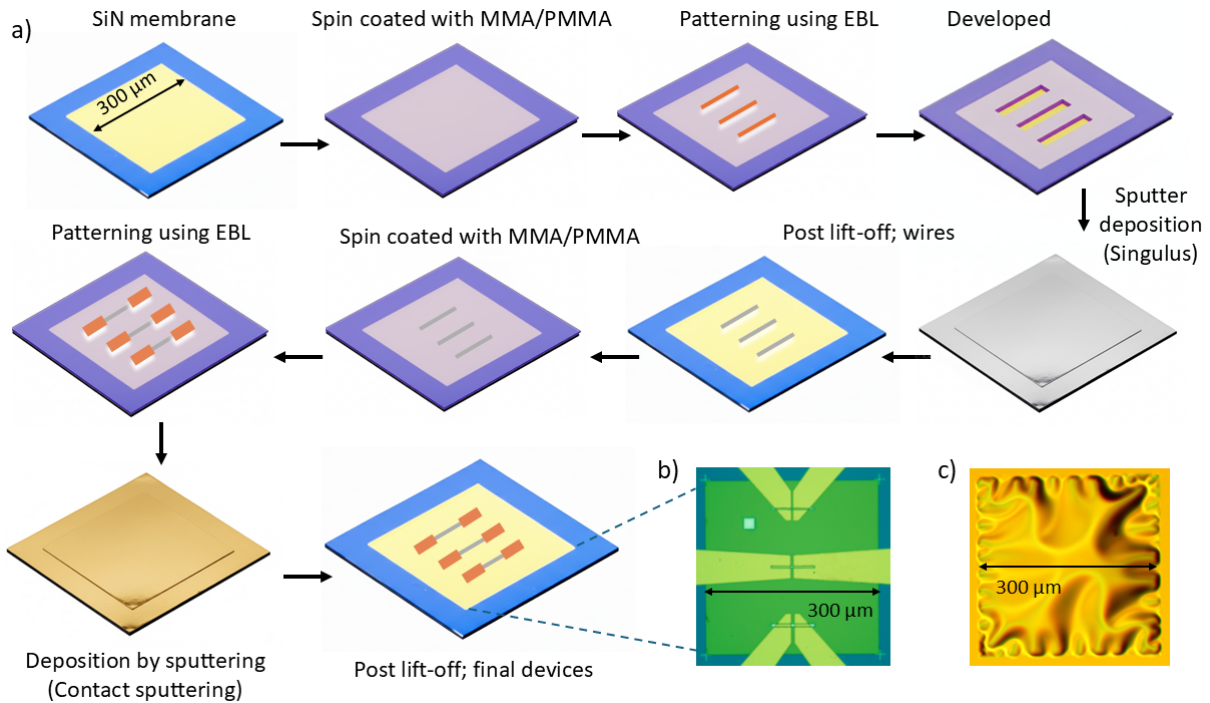


Figure 3.4: **Nanofabrication procedure on silicon nitride membranes.** (a) Schematic illustration of the fabrication process. The SiN membrane (300 μm window) is first coated with an MMA/P-MMA bilayer resist, patterned using EBL, and developed. The magnetic multilayer is then deposited by sputtering (using a Singulus system), followed by lift-off to define the magnetic wires. A second EBL step is used to pattern the contact pads, which are deposited by sputtering and finalized after lift-off. (b) Optical micrograph of a completed device showing the patterned magnetic tracks and contact pads. (c) Example of membrane wrinkling observed when the film is deposited directly on a bare SiN membrane.

3.3 Lab-based Magnetic Microscopy Techniques

Magnetic imaging techniques constitute a cornerstone of experimental research in micro- and nano-magnetism. They enable direct visualization of magnetic domains and spin textures, thereby providing a microscopic understanding of phenomena that are otherwise inferred indirectly from bulk measurements. Such imaging has been crucial for interpreting magneto-transport experiments, where resistance changes arise from magneto-resistive effects sensitive to the magnetic configuration [198, 199]. It is also crucial for elucidating magnetization reversal and domain-wall dynamics, complementing macroscopic techniques such as Kerr-effect hysteresis measurements [200], SQUID magnetometry [201], and vibrating sample magnetometry [202].

The first direct visualization of magnetic domains was achieved in 1932 by Francis Bitter [203]. Since then, a wide variety of imaging techniques have been developed, exploiting different physical

contrast mechanisms and operating across diverse spatial and temporal scales. A comprehensive overview of these methods can be found in recent review articles [204]. Among the most established real-space techniques is magneto-optical Kerr microscopy [205, 206]. It provides rapid and direct access to domain patterns with minimal sample preparation and enables the observation of micrometer skyrmions [38, 41, 42, 134]. However, the spatial resolution of optical microscopy is fundamentally limited by the wavelength of visible light to a few hundred nanometres. As magnetic nanostructures and spintronic devices continue to shrink, this diffraction-limited resolution increasingly constrains the ability to resolve nanoscale spin textures. To overcome this limitation, high-resolution magnetic microscopy techniques capable of probing magnetic structures below the visible light diffraction limit have become indispensable. At the nanoscale, resolving the full three-dimensional spin configuration is essential for correctly identifying and classifying topological spin textures. In particular, for textures such as bimerons, the distinction between a topologically trivial meron–antimeron pair and a non-trivial bimeron state critically depends on the relative core polarities of the constituent (anti)merons and their in-plane magnetization orientation. Therefore, comprehensive magnetic characterization requires experimental access to both the **IP** and **OOP** components of the magnetization vector.

In this thesis, two complementary in-house magnetic microscopy techniques are employed to achieve real-space visualization of domain configurations and spin textures in **SyAFM**: scanning electron microscopy with polarization analysis (**SEMPA**) and magnetic force microscopy (**MFM**). **SEMPA** provides quantitative, vector-resolved imaging of 360° in-plane magnetization, thereby mapping the local spin orientation at 20–25 nm resolution. In contrast, **MFM**, when operated with a magnetically coated tip sensitive to the **OOP** field gradient, provides complementary information on the out-of-plane magnetization component with a spatial resolution of approximately 20–25 nm. By combining these two techniques, a multimodal approach is realized that enables reconstruction of the full three-dimensional magnetization texture in **SyAFM** systems. This sections describe the physical principles, contrast mechanisms, and experimental implementations of **SEMPA** and **MFM** as used in this thesis.

3.3.1 Scanning Electron Microscopy with Polarization Analysis

Scanning electron microscopy with polarization analysis (**SEMPA**), also referred to as spinSEM, was first proposed by T. H. DiStefano in 1978 [207] and subsequently developed by J. Unguris *et al.* in 1982 [208]. The first experimental realization was reported by Koike *et al.* in 1984 [209]. Comprehensive reviews of the technique were later provided by Koike [210], Scheinfein [211], and Allenspach [212]. **SEMPA** is a scanning electron microscopy (**SEM**)–based magnetic imaging technique that detects the spin polarization of secondary electrons emitted from the sample surface.

The method provides quantitative, vector-resolved information about the in-plane magnetization direction within the topmost few nanometres of a material. Typical spatial resolution is better than 30 nm, and in optimized systems, values down to 3 nm have been reported [210]. In contrast to transmission-mode techniques such as Lorentz microscopy, [SEMPA](#) is inherently surface-sensitive. This makes it particularly suitable for the study of thin films and multilayer heterostructures, where interfacial magnetism plays a dominant role. However, the strong surface sensitivity also necessitates ultraclean sample conditions, as even slight surface contamination can suppress the spin polarization of emitted electrons.

While imaging [SyAFM](#), [SEMPA](#) offers a unique advantage. Because the detected secondary electrons originate only from the uppermost atomic layers, the technique selectively probes the magnetization of the top ferromagnetic sublattice. This enables direct imaging of spin textures even under conditions of complete magnetic compensation, where the net stray field is vanishingly small. Such sensitivity makes [SEMPA](#) particularly powerful for resolving domain structures and spin configurations that are inaccessible to other in-house or electron-based techniques such as [MFM](#), Kerr microscopy, or Lorentz transmission electron microscopy. A practical limitation of [SEMPA](#) arises from the inherently low efficiency of spin-polarized electron detection, which results in relatively long acquisition times. Extended beam exposure (4–6 hours for the [SyAFM](#) studied here) is therefore often required to achieve adequate signal-to-noise ratios, making the technique comparatively slower than conventional [SEM](#) imaging.

Spin-Polarized Secondary Electron Emission and its Detection

Spin-polarized secondary electron emission was first demonstrated by Chrobok and Hofmann in 1976 [213]. When high-energy primary electrons impinge on a metallic surface, they transfer energy to valence electrons, which are subsequently excited into unoccupied states above the Fermi level. The energy distribution of emitted electrons comprises several contributions: elastically backscattered primary electrons at the high-energy end, inelastically scattered electrons, Auger electrons, and a broad low-energy peak below approximately 50 eV corresponding to secondary electrons generated through multiple inelastic scattering events. The high intensity of this low-energy peak arises from the cascade multiplication of secondary electrons.

In ferromagnetic materials such as Fe, Co, and Ni, these emitted secondary electrons exhibit a distinct spin polarization that is strongly energy dependent [214]. The polarization is maximal at low kinetic energies and gradually approaches the *d*-band polarization at higher energies [215]. The highest polarization values are typically observed for Fe (because it has the largest exchange splitting and a more unfilled 3d band), followed by Co and Ni [216, 217]. This combination of high intensity

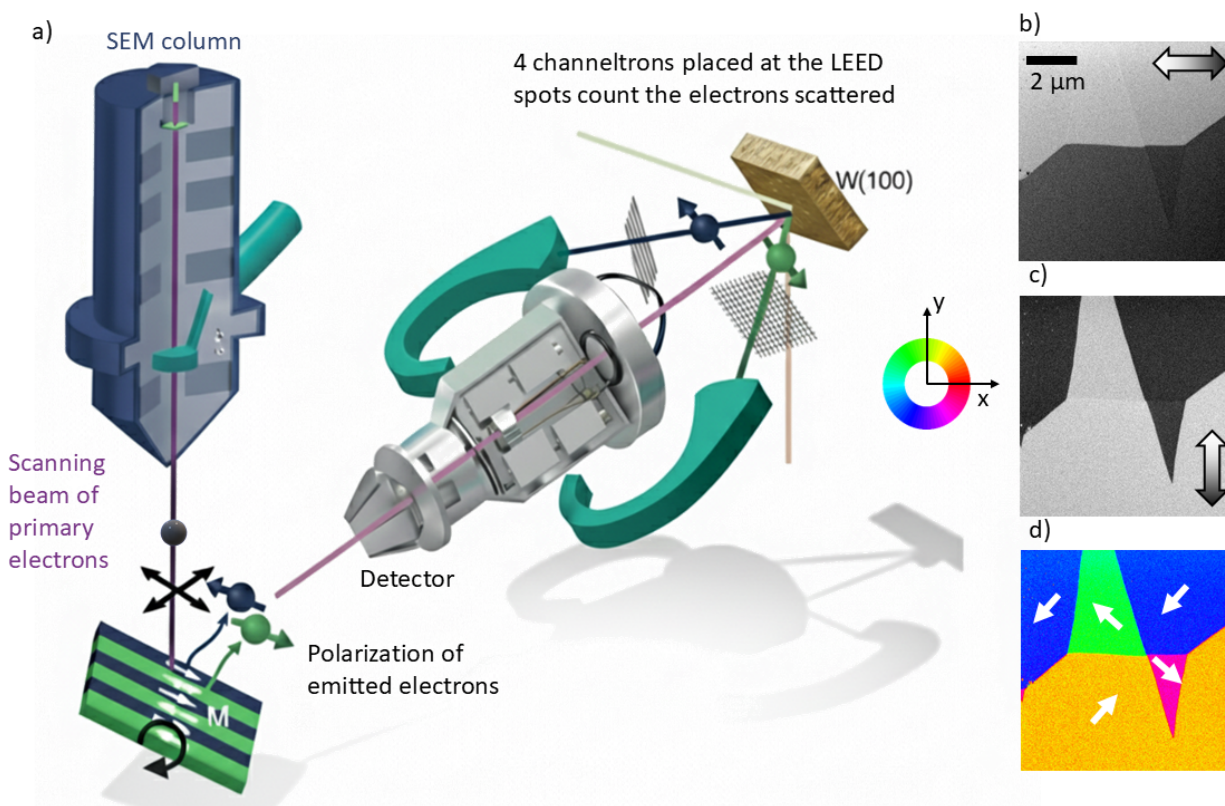


Figure 3.5: **Working principle and vector magnetization mapping in SEMPA.** (a) Schematic illustration of the SEMPA setup showing the detection of spin-polarized secondary electrons scattered from a W(100) SPLEED crystal and counted by four Channeltron detectors positioned at the LEED diffraction spots. (b, c) Spatially resolved spin contrast along two orthogonal in-plane magnetization components obtained from an $\text{MgAl}_2\text{O}_4/\text{Fe}(001)/\text{Pt}(1\text{ nm})$ sample. (d) Reconstructed color-coded vector magnetization map, where the hue represents the in-plane magnetization direction.

and large spin polarization at low energies forms the physical basis of magnetic contrast in SEMPA. The microscopic origin of the spin polarization of secondary electrons lies in the spin-dependent electronic structure of ferromagnets. Due to the exchange splitting of the d -bands, the density of states near the Fermi level E_F differs for majority and minority spins. A minority electron with energy $E_S > E_F$ can scatter with a majority d -electron, leading to the creation of an electron–hole pair (a Stoner excitation) accompanied by a spin-flip transition. Because such scattering events that result in the emission of majority-spin electrons are statistically more probable than those emitting minority-spin electrons, the emitted secondary electrons acquire a net spin polarization. The characteristic energy scale of this asymmetry is determined by the exchange splitting Δ_{ex} of the d -bands [215]. Later, Schönhense and Siegmann [218] proposed that the enhanced spin polarization of low-energy

secondary electrons arises from the spin-dependent inelastic mean free path within the ferromagnetic surface region, which correlates inversely with the number of holes in the d -bands.

The population of secondary electrons emitted from a magnetized region is spin polarized and undergoes spin-dependent scattering within the detector at the W(001) spin-polarized low-energy electron diffraction (SPLLED) single crystal [219, 220] (Fig. 3.5(a)). The optimum performance of the SPLLED detector in SEMPA was achieved at a scattering energy of 104.5 eV (crystal potential of 102.5 eV). Channeltrons, serving as electron multipliers and positioned at the LEED diffraction spots, record the number of scattered electrons to determine the spin polarization, and thus the magnetization direction, of the scanned region. Our detector is equipped with channeltrons from Photonis, providing typical count rates of $(0.5\text{--}2) \times 10^6$ counts s^{-1} per channel. The spin polarization P is defined as

$$P \propto \frac{N_{\uparrow} - N_{\downarrow}}{N_{\uparrow} + N_{\downarrow}}, \quad (3.2)$$

where N_{\uparrow} and N_{\downarrow} denote the electron count with spin-up and spin-down orientations, respectively. This measurement enables SEMPA to resolve the magnetic domain structure of ferro- and ferrimagnetic samples. By employing two mutually orthogonal pairs of channeltrons, any in-plane magnetization can be determined by decomposing it into horizontal and vertical components. All measurements are performed under ultrahigh vacuum conditions (typically $\sim 5 \times 10^{-11}$ mbar). The W single crystal is periodically heated to around 2300 K for 30s, a procedure known as flash cleaning, to remove surface oxides and adsorbed impurities that would otherwise degrade its spin sensitivity. The SEMPA measurements presented in this thesis were conducted in a commercial ultrahigh-vacuum system from Omicron (now Scienta Omicron GmbH).

SEMPA Imaging Example

Here we present an example of SEMPA imaging and describe the post-processing procedure used to generate the color-coded magnetization vector maps. Fig. 3.5(a) illustrates the working principle of the SEMPA setup employed in this study. Figs. 3.5(b) and 3.5(c) display the spatially resolved spin contrast along two orthogonal in-plane magnetization components obtained from the $\text{MgAl}_2\text{O}_4/\text{Fe}/\text{Pt}(1\text{ nm})$ sample, where the Fe layer exhibits a in-plane magnetic anisotropy along the [010] and [100] crystallographic directions*. Fig. 3.5(d) shows the reconstructed color-coded vector magnetization map. The hue indicates the in-plane magnetization direction, as indicated by the color wheel shown. This post-processing enables quantitative visualization of complex magnetic domain

*The samples were provided by Dr. Anna Ravensburg from the Department of Physics and Astronomy, Uppsala University. The Fe layer has a thickness of 10 nm. SEMPA measurements were performed using a primary electron beam energy of 7.5 kV, and a dwell time of 0.05 s per pixel. The measured spin asymmetry is approximately 4 %.

configurations with precise determination of the in-plane magnetization angle.

3.3.2 Magnetic Force Microscopy

Magnetic force microscopy (MFM) is an imaging technique derived from atomic force microscopy that exploits the magnetic force gradient to map the magnetic structure of a sample [221, 222]. The basic working principle of MFM is illustrated in Fig. 3.6. The setup consists of a cantilever with a spring constant C_0 that oscillates at or near its resonance frequency f_0 . The cantilevers used in this work were commercial *MESP-LM-V2* probes from Bruker, with typical resonance frequencies in the range of 50–90 kHz. A sharp magnetic tip, coated with a thin ferromagnetic layer (CoCr), is mounted at the free end of the cantilever. In the measurements presented here, the tips were magnetized along the tip axis, perpendicular to the sample surface, ensuring sensitivity to the out-of-plane component of the sample's stray magnetic field.

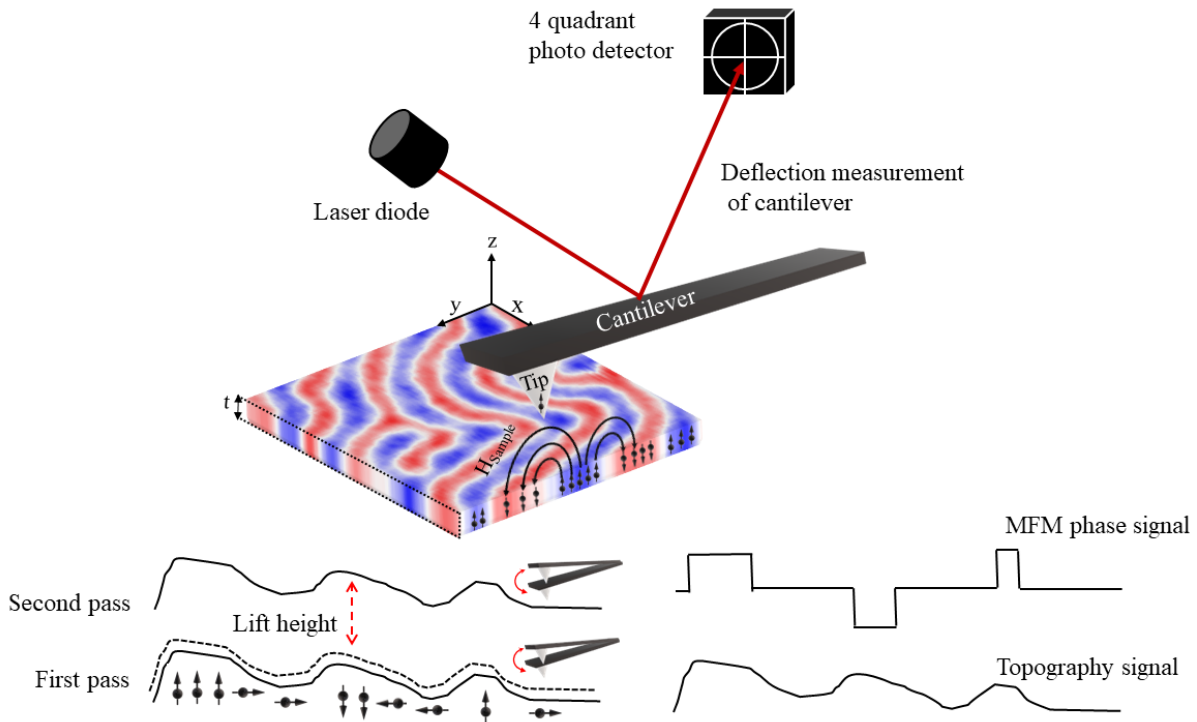


Figure 3.6: **Basic principle of MFM.** MFM in double pass mode showing the first pass topo-scan for surface topography and the second pass lift for the magnetic image.

When a magnetic thin film is brought close to the tip of volume V_{tip} , the spatial gradient of the sample's magnetic stray field H_{sample} exerts a magnetic force F_{mag} on the tip, which can be expressed as [221, 222]

$$F_{\text{mag}} = \mu_0 \int \nabla (\mathbf{M}_{\text{tip}} \cdot \mathbf{H}_{\text{sample}}) dV_{\text{tip}}. \quad (3.3)$$

The vertical gradient of the magnetic force between the tip and the sample effectively modifies the cantilever stiffness, such that the effective spring constant becomes $C_{\text{eff}} = C_0 - \frac{\partial F_z}{\partial z}$. In the case of a large cantilever oscillation amplitude, the force derivative will not be constant, resulting in non-harmonic oscillation. For low amplitudes, however, a constant $\frac{\partial F}{\partial z}$ can be assumed. An attractive interaction with $\frac{\partial F}{\partial z} > 0$ will effectively soften the cantilever spring, decreasing its resonance frequency by δf (usually by 5-10 Hz). The modified resonance frequency is given by

$$f = f_0 \sqrt{1 - \frac{1}{C_0} \frac{\partial F_z}{\partial z}}. \quad (3.4)$$

A shift in resonance frequency will lead to a change in the oscillation amplitude of the cantilever and its phase. All of these are measurable quantities that can be used to map the lateral variation of $\frac{\partial F}{\partial z}$, and can be detected using a split photo detector (as shown in 3.6). Among different detection schemes, phase detection and frequency modulation methods yield the highest signal-to-noise ratio [221, 222]. The measurements were performed in phase-detection mode. The force derivative can originate from a wide range of sources, including electrostatic probe-sample interactions, van der Waals forces, damping, or capillary forces [221]. The MFM images presented in this thesis were acquired using the double-pass lift-mode technique. In this method, the tip scans the same sample area twice. During the first pass, the tip approaches the surface under feedback control to maintain a constant tip-sample separation. At this short distance, the interaction is dominated by van der Waals forces, and the sample topography is recorded. In the second pass, the cantilever oscillates at a fixed lift height, typically 20–50 nm above the surface, following the previously recorded topography. At this distance, the van der Waals contribution remains constant, and the magnetic coating of the tip renders the cantilever primarily sensitive to magnetic interactions with the sample. Owing to its magnetic nature, the tip can, in certain cases, perturb the local magnetic configuration of the sample. To ensure that the magnetic structures, particularly bimerons, remain unperturbed during MFM imaging, the samples were first characterized by SEMPA, then imaged by MFM, and subsequently re-examined using SEMPA to confirm that the magnetic configuration was not altered by the tip-sample interaction.

3.4 Synchrotron-Based Magnetic Microscopy

To visualize antiferromagnetic skyrmions, bimerons, or more complex spin configurations such as skymerons in real space, it is essential to employ imaging techniques capable of resolving the magne-

tization of each ferromagnetic layer independently. Conventional laboratory-based methods, such as [SEMPA](#), [MFM](#), [LTEM](#), and magneto-optical Kerr microscopy, provide surface sensitive information in this regard. [SEMPA](#) is inherently surface-sensitive and thus cannot access buried magnetic layers; [MFM](#) primarily probes long-range stray fields and therefore lacks quantitative sensitivity to the sublattice-resolved magnetization profile; Kerr microscopy suffers from insufficient spatial resolution to resolve nanoscale spin textures; and [LTEM](#) averages across all layers. Consequently, none of these techniques achieves the layer-resolved sensitivity necessary to disentangle the magnetization contributions of the individual ferromagnetic sublattices in synthetic antiferromagnets. An alternative approach to achieve sublattice-resolved imaging would be the use of advanced three-dimensional techniques such as X-ray laminography or electron holography, which can reconstruct volumetric magnetization textures. However, these methods require highly specialized instrumentation and are generally constrained by limited temporal resolution, rendering them unsuitable for time-resolved investigations of dynamic spin textures, which are central to this thesis[†]. A more practical and effective strategy is to exploit the intrinsic element specificity of [XMCD](#) in combination with X-ray-based microscopy. To this end, the two ferromagnetic sublattices were intentionally engineered with chemically distinct compositions, Fe-rich and Co-rich alloys, corresponding to sublattices A and B, respectively. By tuning the incident X-ray photon energy to the Fe L_3 edge or the Co L_3 edge, the magnetization dynamics of each sublattice can be selectively probed with nanometer-scale spatial and nanosecond temporal resolution.

This section describes the X-ray microscopy techniques utilized in this thesis. To image the antiferromagnetic coupling of (anti)merons and bimerons, [XMCD-PEEM](#) was employed. These measurements were performed at the ALBA synchrotron (beamline BL-24, CIRCE) with the assistance of beamline scientists *Dr. Michael Foerster* and *Dr. Miguel Ángel Niño*. For the investigation of skyrmions and skyrmion-related textures, scanning transmission-based X-ray microscopy, [STXM](#), was used. The [STXM](#) experiments were carried out at multiple synchrotron facilities. Measurements at BESSY II (Berliner Elektronenspeicherring-Gesellschaft für Synchrotronstrahlung) in Berlin were performed with the support of beamline scientists *Dr. Sebastian Wintz* and *Dr. Markus Weigand*, while the experiments at the Swiss Light Source (SLS) in Villigen, Switzerland, were conducted with the assistance of *Dr. Simone Finizio* and *Dr. Jörg Raabe*. Detailed contributions for each measurement are provided in Appendix A.

[†]The spatial resolution of these techniques is typically limited to 2–20 nm along the thickness direction and is therefore not suitable for the investigated [SyAFM](#), which contains sub-nanometre-thick ferromagnetic sublattices.

3.4.1 Synchrotron Radiation

Synchrotron radiation refers to the photon radiation generated by radially accelerated electrons. Natural synchrotron radiation, originating from charged particles spiraling along cosmic magnetic fields, for instance, in the Crab Nebula, has existed for 1000 years. Short-wavelength synchrotron radiation produced by relativistic electrons in circular accelerators is a comparatively recent development. The first observation of synchrotron radiation was made on April 24, 1947, at the General Electric Research Laboratory in Schenectady, New York, where visible light was detected as a by-product of electron acceleration in a synchrotron. In the early 1970s, the advantages of synchrotron radiation obtained from parasitic accelerator use were recognized, giving rise to the first-generation synchrotron light sources. The success of these initial studies motivated the construction of dedicated electron storage rings in the early 1980s, where electrons with energies of a few GeV travel at velocities close to the speed of light and emit radiation when passing through bending magnets, marking the emergence of second-generation synchrotron light sources. The storage ring is essentially a polygon composed of multiple straight sections interconnected by bending magnets that deflect the electron beam through the magnetic field. The resulting radial acceleration causes the charged electrons to emit electromagnetic radiation, referred to as *synchrotron radiation* in the context of storage rings. Bending magnets [191] represent the earliest method for generating synchrotron radiation, producing a broad spectrum that ranges from infrared and visible light to hard X-rays. A more efficient generation of synchrotron radiation is realized through insertion devices such as undulators and wigglers [223]. In the 1990s, storage rings were specifically designed with straight sections to accommodate these devices, marking the emergence of third-generation synchrotron light sources. Insertion devices consist of periodic arrays of permanent magnets that induce oscillations of the electron beam along its propagation direction, resulting in the emission of X-rays. The operating principle of an undulator is based on guiding relativistic electrons through a periodic array of permanent magnetic elements. The device consists of two parallel arrays of permanent magnets separated by an adjustable gap. The relative lateral shift between the magnet arrays determines the polarization of the emitted X-rays: a zero shift produces linearly polarized radiation, while a 90° phase shift guides the electron beam onto a helical path, resulting in circularly polarized light.

3.4.2 X-ray Magnetic Circular Dichroism

The X-ray magnetic circular dichroism (XMCD) effect is a magneto-optical phenomenon that arises from the difference in absorption of right- (CR) and left-circularly (CL) polarized X-rays, which depends on the magnetization direction of the absorbing material. The XMCD effect was initially

predicted by Erskine et al. in 1975 [224] at the $M_{2,3}$ edges of Ni and experimentally verified by Gisela Schütz et al. in 1987 [225] at the K edge of an Fe foil. Since then, the XMCD effect has served as the foundation for several synchrotron-based imaging techniques, including PEEM, STXM, and magnetic transmission X-ray microscopy, which enable direct visualization of magnetic domain structures. Within the one-electron model, the origin of the XMCD effect observed at the L_3/L_2 absorption edges of magnetic 3d transition metals (such as Fe, Co, and Ni) can be described as a two-step process [226] (see Fig. 3.7(a)).

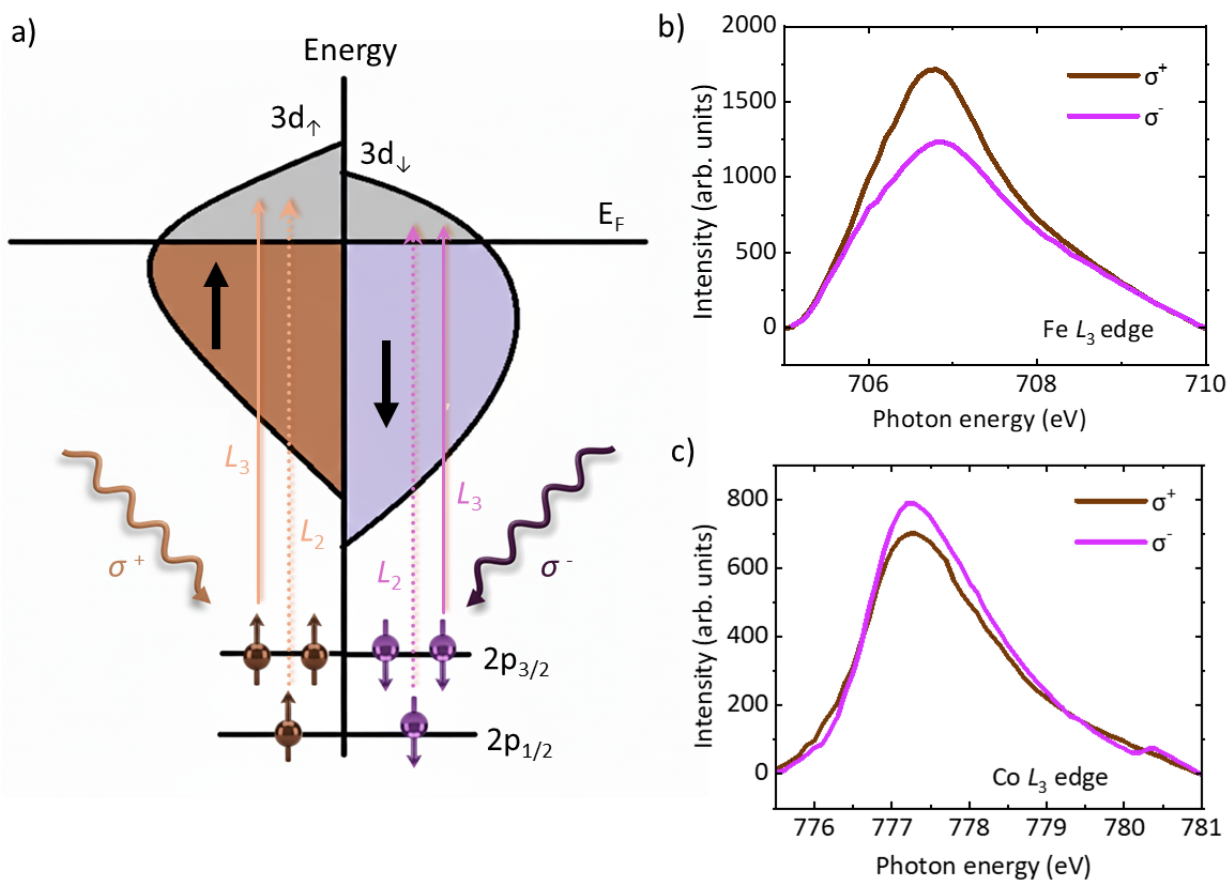


Figure 3.7: **Illustration of the XMCD two-step model.** (a) Schematic illustration of the XMCD process. Circularly polarized X-rays (σ^+ and σ^-) excite electrons from the spin-orbit split $2p_{3/2}$ and $2p_{1/2}$ core levels into unoccupied $3d$ states, giving rise to the L_3 and L_2 absorption edges, respectively. (b) and (c) XAS recorded at the Co and Fe L_3 edges for stack #M12 at a monodomain state (discussed in Chapter 4).

In the first step, circularly polarized X-rays excite electrons from the $2p$ shell into unoccupied $3d$ states according to the electric dipole selection rules ($\Delta l = \pm 1$, $\Delta m = 0, \pm 1$, and $\Delta s = 0$). The spin-orbit coupling splits the $2p$ shell into $2p_{3/2}$ and $2p_{1/2}$ states, corresponding to the L_3 and L_2

absorption edges, which exhibit opposite spin-orbit coupling. For a given photon helicity, this results in XMCD signals of opposite sign at the two edges. Depending on the photon helicity, the X-rays preferentially excite either spin-up or spin-down electrons into the unoccupied 3d state. The spin-up and spin-down states are defined relative to the X-ray propagation direction. Without inducing a spin flip, the photon helicity determines which spin channel is preferentially excited, giving rise to the dichroic response characteristic of XMCD.

In the second step, the spin asymmetry of the 3d band is considered. The exchange-split 3d states favour the occupation of one spin channel over the other, effectively acting as a partial spin filter. Since X-ray absorption of a 2p electron depends on the availability of unoccupied 3d states, right- (σ^+) and left-circularly (σ^-) polarized photons produce different absorption probabilities for a uniformly magnetized region of the sample, such as a ferromagnetic domain. An X-ray absorption spectrum (XAS) is shown in Fig. 3.7b,c for stack #M12 at a monodomain state (discussed in Chapter 4) and demonstrates the differential absorption at the Fe and Co L_3 edges in the SyAFM stack[‡]. At a given photon energy, the dichroism is then defined as:

$$\text{XMCD} = \frac{I_{\sigma^-} - I_{\sigma^+}}{I_{\sigma^-} + I_{\sigma^+}}, \quad (3.5)$$

where I_{σ^+} and I_{σ^-} denote the X-ray absorption intensities measured with CR and CL, respectively. Opposite magnetic domains can therefore be distinguished by the sign of their XMCD contrast. The magnitude of the XMCD signal follows a cosine dependence on the angle θ between the X-ray incidence direction (parallel to the photon angular momentum) and the magnetization vector. It reaches a maximum for parallel and antiparallel orientations ($\theta = 0^\circ$ and 180°) and vanishes when $\theta = 90^\circ$, where both σ^+ and σ^- photons are absorbed equally. Thus, under normal incidence, it primarily probes the out-of-plane component (m_z), while tilting the sample allows access to in-plane components.

The XMCD effect is inherently element specific, as it probes the absorption edges corresponding to core-level transitions of individual elements. The observed dichroism depends on the spin and orbital magnetic moments of the unoccupied electronic states, providing a detailed fingerprint of the local magnetic environment. By analyzing the L_2 and L_3 absorption edges and applying the established sum rules, XMCD can also be used to quantitatively determine the spin and orbital magnetic moments [227]. In the SyAFM investigated here, the use of two distinct ferromagnetic materials in the sublattices enables sublattice-resolved magnetic imaging. Within this thesis, XMCD serves as the fundamental contrast mechanism for X-ray microscopy techniques, namely PEEM and

[‡]Note that the measured absorption peaks for Fe and Co may deviate slightly from their absolute L_3 edge energies due to calibration offsets in the beamline monochromator.

STXM, which are employed to visualize magnetic textures.

3.4.3 Photoemission Electron Microscopy

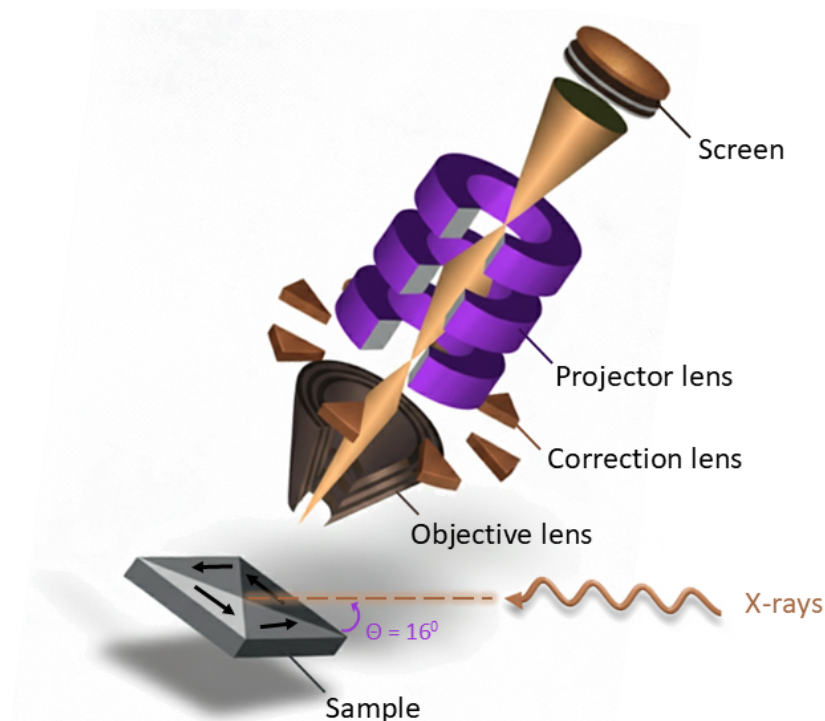


Figure 3.8: **Schematic of the operating principle of PEEM.** Photoelectrons excited by incident X-rays are spin polarized and emitted from the sample surface. A high accelerating voltage accelerates the electrons through an electromagnetic lens system that focuses and magnifies the image onto a detector screen. Magnetic contrast can be achieved either by using circularly polarized photons or by incorporating a spin detector into the electron path (not shown here). In the schematic, gray on the sample indicates regions with magnetization perpendicular to the X-ray beam, while white and black regions correspond to magnetization parallel and antiparallel to the X-ray beam, respectively. To obtain a full in-plane 360° magnetization map, the sample is rotated by 90° , and the two orthogonal images are combined to reconstruct the complete in-plane color-coded magnetization vector field.

To verify the antiferromagnetic coupling between the (anti)merons in the ferromagnetic sublattices, it is essential to image both magnetic layers at the same spatial position using synchrotron-based X-ray microscopy. Photoemission electron microscopy (PEEM) visualizes a surface by detecting variations in the intensity of emitted secondary electrons. In contrast to SEMPA, which employs a focused electron beam, PEEM utilizes unfocused-monochromatic X-rays from a synchrotron light source to induce photoemission, enabling element-specific and magnetic contrast. Although X-rays could penetrate several hundred nanometers into the material and excite photoelectrons throughout this depth,

only those generated within the top few nanometers can escape into the vacuum. Consequently, this makes PEEM an inherently surface-sensitive technique. This strong surface sensitivity requires flat and homogeneous samples, and applying external magnetic fields can reduce the maximum achievable spatial resolution. An advantage of this technique compared to transmission-based measurements is that it does not require membrane-based samples, as no X-ray transmission is involved. A schematic of the basic PEEM setup is shown in Fig. 3.8.

In PEEM, the sample is typically biased at a high voltage of about 20 kV and illuminated with circularly polarized X-rays. The applied voltage accelerates the electrons away from the surface. Afterward, they are focused by an electrostatic lens system onto a two-dimensional detector, typically a phosphorous screen coupled to a charge-coupled device (CCD) camera (or a CMOS camera). The resulting image shows contrast based on the magnetization direction with respect to the X-ray beam: regions with magnetization parallel to the beam are bright, antiparallel regions are dark, and regions perpendicular to the beam are gray (see sample at Fig. 3.8). XMCD-PEEM images presented in this thesis were acquired at the ALBA synchrotron (BL-24 Circe) facility, where the X-ray beam impinges at an angle of 16° with respect to the sample surface. Hence, the magnetic contrast in the images is mainly sensitive to the in-plane component of the magnetization. To obtain the full in-plane 360° magnetization map, the sample is rotated by 90° , and the two orthogonal images are combined to reconstruct the complete in-plane vector field [228].

3.4.4 Scanning Transmission X-ray Microscopy

Scanning transmission X-ray microscopy (STXM) is a transmission-based imaging technique that utilizes a focused soft X-ray beam to probe the internal magnetic and structural properties of thin samples. In contrast to PEEM, which operates in electron emission geometry, STXM detects the transmitted X-ray intensity as the beam is raster-scanned across the sample [191]. The operating principle of a scanning transmission X-ray microscope is illustrated in Fig. 3.9.

X-rays generated by an undulator are directed through a monochromator and a series of slits and pinholes before being focused by a high-resolution Fresnel zone plate (FZP). The monochromator filters higher harmonics and nonlinear contributions from the undulator, thereby increasing the signal-to-noise ratio. The zone plate focuses the monochromatic beam onto the sample, where photons are transmitted according to the XMCD absorption contrast and subsequently detected by a single-photon detector, typically an avalanche photo-diode that ensures high detection efficiency even at low count rates. Two-dimensional imaging is achieved by raster-scanning the sample perpendicular to the X-ray beam, recording the intensity point by point for each beam position. High spatial resolution, down to about 15 nm, requires a highly brilliant and coherent X-ray source, ideally provided

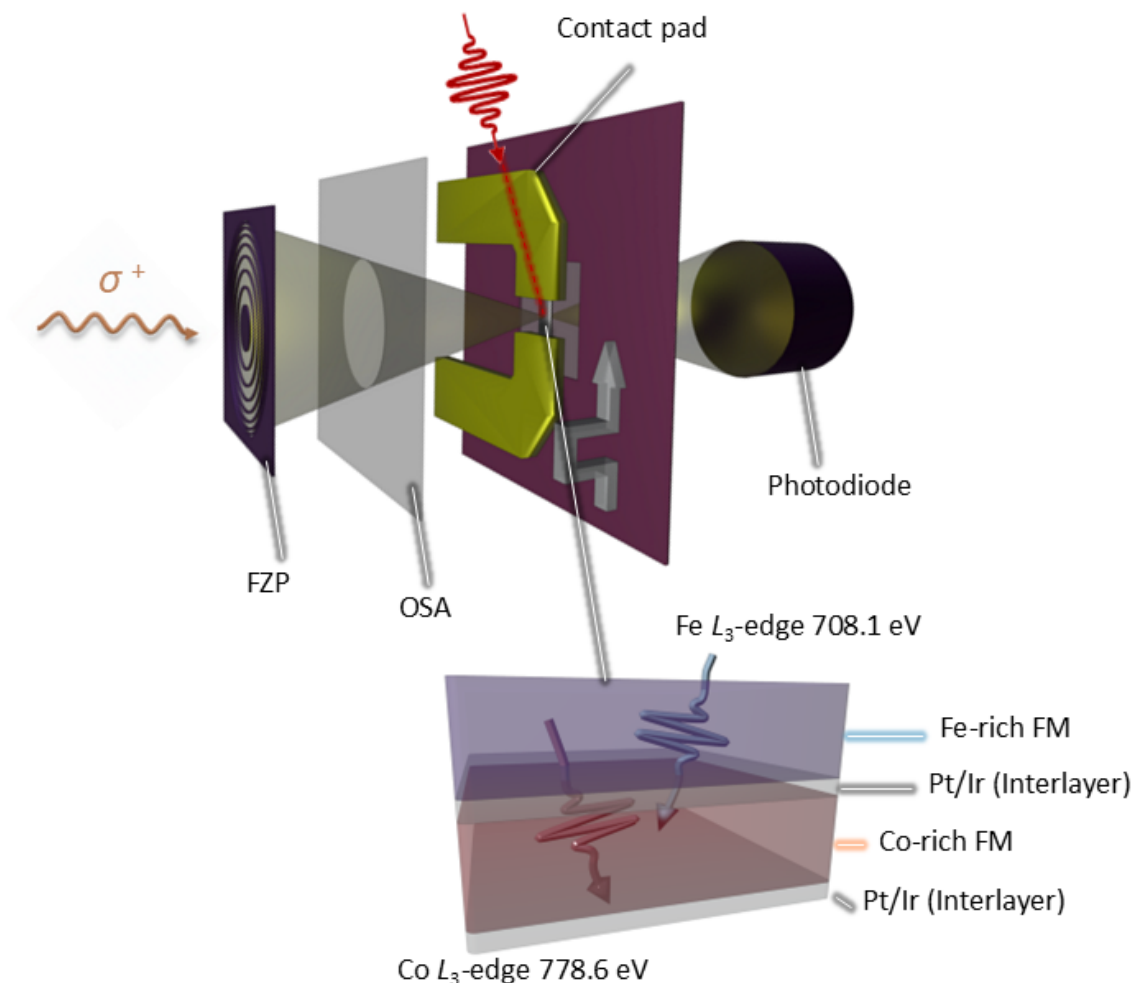


Figure 3.9: **Schematic illustration of the STXM.** Circularly polarized X-rays are focused onto the sample by an FZP and pass through an OSA to isolate the first diffraction order. The transmitted photons are collected by a photodiode. The sample consists of two ferromagnetic sublattices (Fe-rich and Co-rich) separated by nonmagnetic spacers, allowing element-specific imaging at the respective Fe and Co L_3 absorption edges. A picosecond IR laser provides localized heating that transiently modifies the magnetic energy landscape, leading to skyrmion nucleation. Contact pads enable in-situ electrical excitation during measurements.

by an undulator. To suppress unwanted diffraction orders from the zone plate, an order-separating aperture (OSA) is placed in the beam path, transmitting only the desired first diffraction order, which is used for imaging. In addition to the main optical components described above, the microscope is equipped with a magnet setup capable of generating out-of-plane magnetic fields (up to ± 250 mT at MAXYMUS and PolLux), which are essential for stabilizing spin configurations of different sizes and geometries. At the MAXYMUS STXM microscope, a Max Born Institute (MBI)-developed

custom-built picosecond fiber laser system by *Dr. Bastian Pfau* (wavelength: 1039 nm, spot size: 6.5 μm FWHM, pulse duration: 1 ps) enables *in situ* optical excitation of the sample, which was employed in this work for laser-induced skyrmion nucleation experiments.

3.4.5 Time-Resolved imaging using Pump–Probe STXM

Magnetic imaging provides essential insights into the behavior of magnetic materials. To access dynamical processes, time-resolved imaging is required. Since typical ferromagnetic dynamics occur in the gigahertz range, a temporal resolution of nanoseconds or below is necessary. In this thesis, STXM is employed to achieve high spatial and temporal resolution using a pump–probe scheme [229–231] at the MAXYMUS beamline at BESSY II Synchrotron [191]. The basic operating principle is outlined in the following subsection.

The pump–probe method is based on repeated excitation (pump) and measurement (probe) with controlled delay times to capture the temporal evolution of the system. The pump–probe technique is applicable only to fully reproducible processes. In this work, the "pump" is an excitation induced by an electrical current pulse passing through the sample. The current, operating at a repetition rate of 500 MHz, drives the magnetic textures due to the SOTs. In the multi-bunch mode of BESSY II, electrons circulate in evenly spaced bunches with a temporal separation of 2 ns, corresponding to a repetition rate of 500 MHz. Each bunch passage through the undulator generates a soft X-ray pulse shorter than 100 ps, which serves as the "probe" in the experiment, and its duration defines the intrinsic temporal resolution of the technique. By tuning the photon energy to the L_3 absorption edge of the element of interest (Co and Fe in this case), the magnetization of the sample is recorded through the XMCD effect. Thus, varying the delay between the pump and the probe pulses, the temporal evolution of the magnetization can be reconstructed [229]. A controlled variation of the delay requires a defined timing relation between the excitation and the synchrotron clock. This can be achieved either when the excitation frequency is an exact multiple of the synchrotron repetition rate (synchronous excitation) or when a slight frequency offset creates a beat between the excitation and probe pulses (asynchronous excitation).

The operation mode used in this thesis is the asynchronous excitation scheme. Here, the excitation period P can be chosen arbitrarily (2 μs for this work) but must satisfy the condition [191]

$$P = T \cdot 2 \text{ ns} + \Delta t, \quad (3.6)$$

where T is an integer and Δt is the small temporal shift of each excitation pulse relative to the preceding one. The value of 2 ns corresponds to the bunch spacing of the synchrotron. The shift

must be expressible as a rational fraction of the bunch spacing and can be written as [191]

$$\Delta t = \frac{R \cdot 2 \text{ ns}}{M}, \quad (3.7)$$

where R and M are integers. This relation ensures that after M excitation periods, the excitation and the synchrotron ring are again synchronized. Each 2 ns interval between consecutive synchrotron bunches is sampled M times at evenly spaced delay positions, resulting in a temporal resolution of [191]

$$\tau = \frac{2 \text{ ns}}{M}. \quad (3.8)$$

The parameter M is often referred to as the *magic number*. For the time-resolved measurements presented in this work, $M = 2$. For image acquisition, the duration of one complete excitation cycle is divided into N time channels, each representing a time interval of τ [230]. The total number of channels is given by [191]

$$N = \frac{P}{\tau} = T \cdot M + R, \quad (3.9)$$

The measurement is carried out in a pixel-by-pixel scanning mode, where each pixel is recorded for a defined dwell time and subsequently combined into a two-dimensional image. The acquired data are automatically sorted into time channels and stored as individual frames of a time-resolved image sequence. Each frame thus represents the photon counts detected within the N -th fraction of the dwell time. To maintain an adequate signal-to-noise ratio in each pixel, relatively long dwell times are required. In this work, 2001 time channels were used, corresponding to an effective temporal resolution of 1 ns. The full excitation period of 2 μs was uniformly sampled across all channels, covering one complete excitation cycle. A bipolar current pulse sequence with a 1 μs delay between successive positive and negative pulses was applied to ensure reproducible skyrmion trajectories while minimizing cumulative heating. All measurements were performed at room temperature, with a residual helium gas pressure of 10 mbar maintained in the chamber to allow for additional thermal dissipation.

Part II

Results and Discussion

Merons, Antimerons and Bimerons in Synthetic Antiferromagnets ^{*}

What we observe is not nature itself, but nature exposed to our method of questioning.

Werner Heisenberg

4.1 Introduction

The current chapter investigates the stability and observation of in-plane topological spin textures, including merons [232], antimerons [143], and bimerons [138, 139, 141, 142]. Bimerons are topologically robust spin textures, homeomorphic to skyrmions, and can be viewed as bound states of two merons (or half-skyrmions) [51, 52]. The directional arrangement of merons in the plane introduces an additional internal degree of freedom beyond those available in conventional skyrmions, positioning them as promising candidates for both fundamental studies of magnetic quasiparticles and for applications in topology-driven information processing. In antiferromagnetic systems, the experimental realization of merons remains limited, with existing reports primarily focused on their helicity, despite recent progress in their controlled generation using advanced protocols [50, 53, 74, 75]. The helicity plays a critical role in their response to SOTs, with Bloch and Néel-type configurations exhibiting motion perpendicular and parallel to the current direction, respectively [28]. However, the lack of ho-

^{*}Most of the chapter is adapted from: Bhukta, M., et al. Homochiral antiferromagnetic merons, antimerons, and bimerons realized in synthetic antiferromagnets. Nat. Commun. 15, 1641 (2024) <https://www.nature.com/articles/s41467-024-45375-z>

mochirality [53, 75, 76] in native single-crystalline antiferromagnets continues to hinder deterministic control over these textures, limiting their applicability. Here, we employ multimodal vector imaging of the 3D staggered magnetization to demonstrate the successful stabilization of all members of the class of in-plane AFM topological spin textures emerging in a specifically designed layered SyAFM, namely merons, antimerons, and bimerons at zero magnetic fields. Our experiments combine MFM, SEMPA, and XMCD-PEEM, which enable us to identify spin textures possessing enhanced stability, classified by integer, nonzero topological invariants, as well as topologically trivial ones. We find that in the vicinity of the spin-reorientation transition, where the effective anisotropy vanishes, the SyAFM platform can host homochiral AFM merons, as determined from their helicity and core polarity. A detailed list of contributions, outlining everyone's involvement in this and the following chapters, can be found in Appendix A. This chapter presents the final form of the analytical model developed by V.K. Bharadwaj to demonstrate the existence of bimerons in SyAFM. Furthermore, the stabilization of bimeron is explained through micromagnetic simulations conducted by the author of this thesis. The experimental details, including sample structure and characterization for this chapter, can be found in eLab logbook (📖 labbook experiment ID 18946).

4.2 Spin Configuration of AFM (Anti)merons in a SyAFM Platform

From a phenomenological point of view, a SyAFM can be conceptually described as a bipartite magnetic sublattice system, where each sublattice corresponds to one of the constituent ferromagnetic layers. These sublattices are denoted as FM_A and FM_B , with their respective saturation magnetizations given by $M_{s,A}$ and $M_{s,B}$. In the general case, particularly when the system is far from the magnetic moment compensation point—defined by the condition $\Theta \equiv M_{s,A}^2 - M_{s,B}^2 = 0$ —the magnetic behavior of the SyAFM resembles that of a ferrimagnet. The effective long-wavelength theory describing the low-energy excitations of the system can be formulated in terms of the Néel order parameter \mathbf{L} and the total magnetization \mathbf{M} , where

$$\mathbf{L} \equiv \mathbf{M}_A - \mathbf{M}_B, \quad \mathbf{M} \equiv \mathbf{M}_A + \mathbf{M}_B. \quad (4.1)$$

The antiferromagnetic spin textures in a SyAFM can be characterized by their winding number w , which quantifies the topological wrapping of the Néel order parameter \mathbf{L} around the unit sphere. This invariant serves as a classification tool for the topology of the spin configuration. For bimerons and skyrmions, the winding number takes the values $w = \pm 1$, whereas for merons and antimerons, it assumes fractional values $w = \pm \frac{1}{2}$. The corresponding topological charge Q can be defined as the

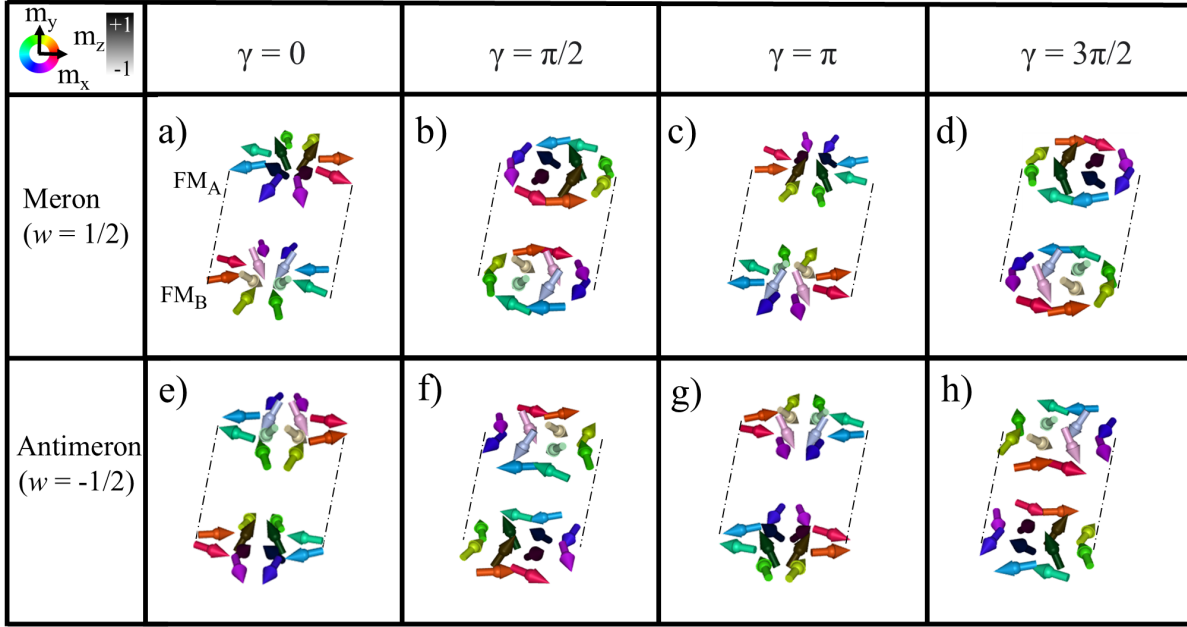


Figure 4.1: **Spin configuration of AFM merons and antimerons in a SyAFM platform having $Q = \frac{1}{2}$.** (a)–(d) $Q = \frac{1}{2}$ AFM meron with helicities $\gamma = 0, \frac{\pi}{2}, \pi,$ and $\frac{3\pi}{2}$, respectively. (e)–(h) $Q = \frac{1}{2}$ AFM antimeron with helicities $\gamma = 0, \frac{\pi}{2}, \pi,$ and $\frac{3\pi}{2}$, respectively. Adapted from [1]

product of the winding number and the core polarity. Specifically,

$$Q = w \cdot \text{sgn}(\mathbf{L}_z|_{\text{core}}), \quad (4.2)$$

where $\mathbf{L}_z|_{\text{core}}$ denotes the z-component of the Néel order at the core of the spin texture, determining its polarity. In addition to the topological charge, the helicity γ provides an important descriptor of the internal structure of the spin texture. Analogous to skyrmions, the helicity describes the in-plane orientation of the spins along the azimuthal direction and plays a critical role in their current-driven dynamics[29].

Three-dimensional illustrations of antiferromagnetically coupled meron–meron composites with helicities $\gamma = 0, \frac{\pi}{2}, \pi,$ and $\frac{3\pi}{2}$ are shown in Fig. 4.1(a–d). Néel-type merons correspond to helicities $\gamma = 0$ or π , depending on the sign of the **DMI**, while Bloch-type merons are characterized by $\gamma = \frac{\pi}{2}$ or $\frac{3\pi}{2}$, as illustrated in panels (b) and (d), respectively. The black and white shading represents upward and downward core polarities, respectively, whereas the IP spin orientation is encoded by the color map shown in the top-left inset of Fig. 4.1. Panels (e–h) of Fig. 4.1 depict antiferromagnetically coupled antimerons with a topological charge $Q = \frac{1}{2}$ and helicities $\gamma = 0, \frac{\pi}{2}, \pi,$ and $\frac{3\pi}{2}$, respectively. Notably, antimerons exhibit an inverted angular sequence of the in-plane spin color contrast in **SEMPA**

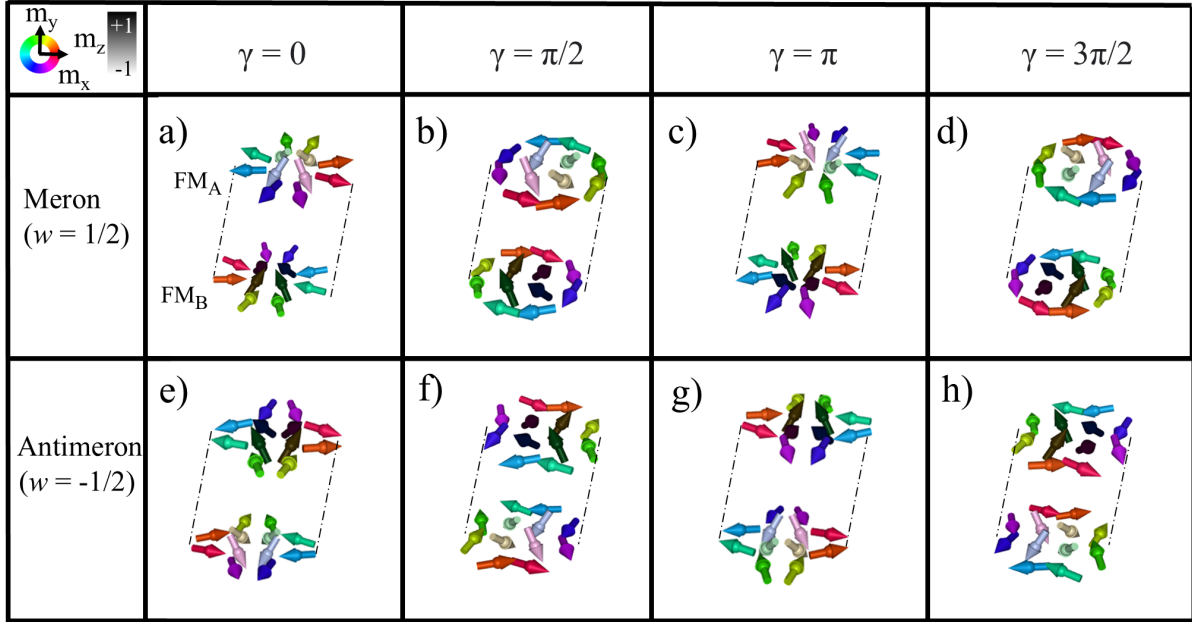


Figure 4.2: **Spin configuration of AFM merons and antimerons in a SyAFM platform having $\mathbf{Q} = -\frac{1}{2}$.** (a)–(d) $Q = -\frac{1}{2}$ AFM meron with helicities $\gamma = 0, \frac{\pi}{2}, \pi,$ and $\frac{3\pi}{2}$, respectively. (e)–(h) $Q = -\frac{1}{2}$ AFM antimeron with helicities $\gamma = 0, \frac{\pi}{2}, \pi,$ and $\frac{3\pi}{2}$, respectively.

imaging of the in-plane components, compared to their meron counterparts. Additionally, it should be noted that the solitons in adjacent FM layers exhibit identical winding numbers but opposite core polarities, and their helicities differ by a factor of π .

In homochiral spin textures, the helicity and core polarity are intrinsically coupled, resulting in (anti)merons with well-defined and unambiguous topological charges Q . Antiferromagnetic merons and antimerons with $Q = -\frac{1}{2}$ and helicities $\gamma = 0, \frac{\pi}{2}, \pi,$ and $\frac{3\pi}{2}$ are illustrated in Fig. 4.2. A bimeron can be understood as a composite object formed by pairing a meron and an antimeron with opposite topological charges. This pairing restores an integer topological charge ($Q = \pm 1$) and yields a topologically protected soliton analogous to a skyrmion but with in-plane magnetization boundary conditions.

4.3 Essential Considerations for the Stabilization of (Bi)merons

In this section, we present an analytical framework for describing a bilayer SyAFM, modeled as a system comprising two FM layers separated by a non-magnetic metallic spacer, as illustrated in Fig. 4.3. Each FM layer includes the key energetic contributions required for stabilizing topological solitons: direct exchange interaction, *iDMI*, and uniaxial anisotropy. In addition to the intra-layer interactions, the metallic spacer hosts itinerant carriers that mediate an indirect interlayer exchange

coupling between the two FM layers. Notably, magnetic dipolar interactions between the layers become particularly relevant near the SRT point, where competition between interfacial anisotropy and dipolar energies can significantly affect the stability of in-plane textures such as (anti)merons. Taking these factors into account, the total energy functional describing the bilayer SyAFM system in the low-energy, long-wavelength limit is expressed as (derived by V. K. Bharadwaj) as follows [1]:

$$\begin{aligned}
 \mathcal{E}[\mathbf{M}_A, \mathbf{M}_B] = \int_{\mathcal{S}} d^2\vec{r} \left\{ \frac{J_{\text{ex,A}}}{2} (\nabla \mathbf{M}_A)^2 + \frac{J_{\text{ex,B}}}{2} (\nabla \mathbf{M}_B)^2 \right. \\
 + D_{\text{iDMI,A}} \mathcal{L}_N[\mathbf{M}_A] + D_{\text{iDMI,B}} \mathcal{L}_N[\mathbf{M}_B] \\
 - K_{\text{eff,A}} M_{A,z}^2 - K_{\text{eff,B}} M_{B,z}^2 \\
 \left. - \mathbf{H}_d \cdot (\mathbf{M}_A + \mathbf{M}_B) + J_{\text{AFM}} (\mathbf{M}_A \cdot \mathbf{M}_B) \right\}. \quad (4.3)
 \end{aligned}$$

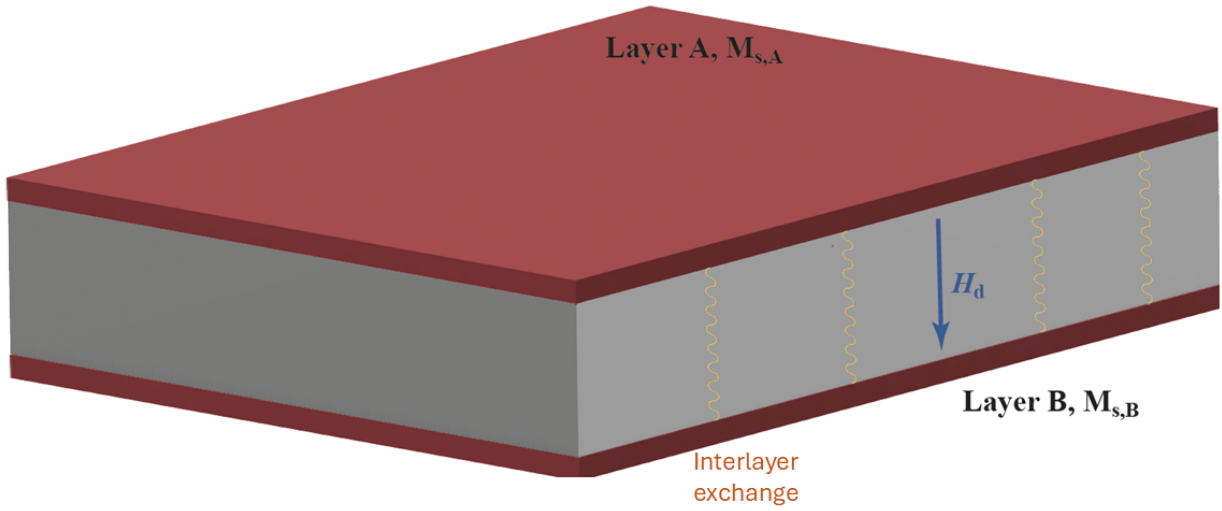


Figure 4.3: **Sketch of the bilayer SyAFM.** The metallic spacer (grey) is sandwiched between two ferromagnetic layers (red), which present different saturation magnetizations, $M_{s,A}$ (sub-lattice A) and $M_{s,B}$ (sub-lattice B). The itinerant charges flowing through the spacer mediate the interlayer (antiferromagnetic) exchange interaction. Furthermore, the two ferromagnetic layers also interact via a demagnetizing field \mathbf{H}_d along the normal to the heterostructure. An effective low-energy long-wavelength description of the SyAFM can be obtained in terms of the Néel order $\mathbf{L} = \mathbf{M}_A - \mathbf{M}_B$ and macroscopic spin density $\mathbf{M} = \mathbf{M}_A + \mathbf{M}_B$, which corresponds to that of a ferrimagnet (far from the compensation point $\Theta = M_{s,A}^2 - M_{s,B}^2 = 0$). Adapted from [1]

where $\mathbf{M}_i(\vec{r})$ denotes the magnetization of the i -th ferromagnetic layer ($i = A, B$), $M_{s,i} \equiv |\mathbf{M}_i|$, are the corresponding saturation magnetizations, and the basal plane \mathcal{S} extends in the x and y directions. Here, $J_{\text{ex,A/B}}$ and $D_{\text{iDMI,A/B}}$ are the spin stiffness constants and the DMI of the FM

layers, respectively, and J_{AFM} represents the interlayer exchange constant, which depends strongly on the interlayer distance. We note that this distance is chosen so that the indirect exchange interaction is antiferromagnetic. The interlayer demagnetizing field $\mathbf{H}_d = H_d \hat{e}_z$ is, by symmetry arguments, directed along the normal to the heterostructure. Its strength scales as $H_d \propto \frac{1}{d_{\text{spacer}}}$ with the distance d_{spacer} between the FM layers. In addition, the effective anisotropy constants $K_{\text{eff},i} = K_i - \frac{\mu_0}{2} M_{s,i}^2$ ($i = \text{A, B}$), are composed of into the magnetocrystalline terms $K_{\text{A,B}}$ and the effective magnetostatic contributions $K_{d,i} \equiv -\frac{\mu_0}{2} M_{s,i}^2$, the latter resulting from the structure $\hat{N} = \text{diag}(0, 0, 1)$ for the demagnetizing tensor in the thin-film approximation. The fabrication process of the heterostructure is such that each ferromagnetic layer is in the vicinity of the SRT point, namely $K_{\text{eff}} \simeq 0$. It is noted that the interplay between the interlayer exchange and magnetic dipolar interactions determines the orientation (IP vs. OOP) of the magnetization fields $\mathbf{M}_{\text{A,B}}$ in this SRT regime since the energy scale ascribed to the demagnetizing field \mathbf{H}_d becomes dominant here. In the compensated case, the minimal model for the SyAFM contains exchange, DMI, and anisotropy contributions, and thus its total free energy reads

$$\mathcal{E}_{\text{cp}}[\mathbf{L}] = \int_S d^2\mathbf{r} \left[\frac{J_{\text{ex,A}}}{2} (\nabla \mathbf{L})^2 + D_{\text{iDMI}} \mathbf{L} \cdot (\tilde{\nabla} \times \mathbf{L}) - \left(K_{\text{eff}} - \frac{H_d^2}{2J_{\text{AFM}} L^2} \right) L_z^2 \right]. \quad (4.4)$$

A strong interlayer AFM coupling between successive FM layers, almost zero effective PMA, and a finite iDMI are the key enablers to stabilize meronic spin textures. Taking these requirements into account, we have optimized Ir-based multilayer SyAFM systems, as discussed in the following subsection.

4.3.1 Material Stack Optimization

To stabilize bimerons in SyAFMs, the multilayer system must be designed to fulfill the following requirements: (i) strong iDMI, (ii) robust interlayer antiferromagnetic exchange coupling, (iii) near-zero effective anisotropy, (iv) magnetic moment compensation, and (v) low pinning. Based on these criteria, a Pt/CoFeB/Ir-based multilayer SyAFM has been optimized to stabilize (anti)merons and bimerons at room temperature. The schematic of the stack is shown in Fig. 4.4 (a). The stacks were deposited on thermally oxidized Si/SiO₂ substrates using the Singulus Rotaris magnetron sputtering tool, which ensures reproducibility and sub-angstrom thickness accuracy. DC magnetron sputtering was performed at a base pressure of 4×10^{-8} mbar for the growth of metallic layers including Ta, Pt, Ir, Co_{0.6}Fe_{0.2}B_{0.2} (CFB), Fe_{0.6}Co_{0.2}B_{0.2} (FCB), and Co_{0.8}B_{0.2} at room temperature. The respective deposition rates, determined via X-ray reflectivity, were 0.54, 0.91, 0.56, 0.51, 0.66, and

0.37 Å/s, under a pure Ar atmosphere used as the sputtering gas. The FM films consist of the bilayer FCB/CFB and are sandwiched between the nonmagnetic spacers Pt and Ir. This structural asymmetry breaks the mirror symmetry of the heterostructure, resulting in a finite iDMI, denoted by D . The topmost Pt layer serves as a protective capping to prevent oxidation during deposition and post-fabrication processes such as patterning. The thickness $d_{\text{Ir}} = 0.4$ nm of the Ir layer is chosen so as to maximize the AFM interlayer exchange between the FM layers. Precise control over the effective magnetic anisotropy is critical for stabilizing bimerons. In our multilayer design, the CFB layer induces PMA (K_u) at the interface with the heavy metal, whereas the thickness ratio to the FCB layer is used to control the magnetic dipolar anisotropy $K_d = -\frac{1}{2}\mu_0 M_s^2$. We have kept the FM layers as thin as possible ($d_{\text{FM}} = 0.9$ nm) to maximize the interlayer exchange coupling as well as optimized the ratio between the FCB (x nm) and CFB ($0.9 - x$ nm) thicknesses to be in the vicinity of the SRT (namely, to obtain a vanishing effective anisotropy $K_{\text{eff}} = K_u + K_d$).

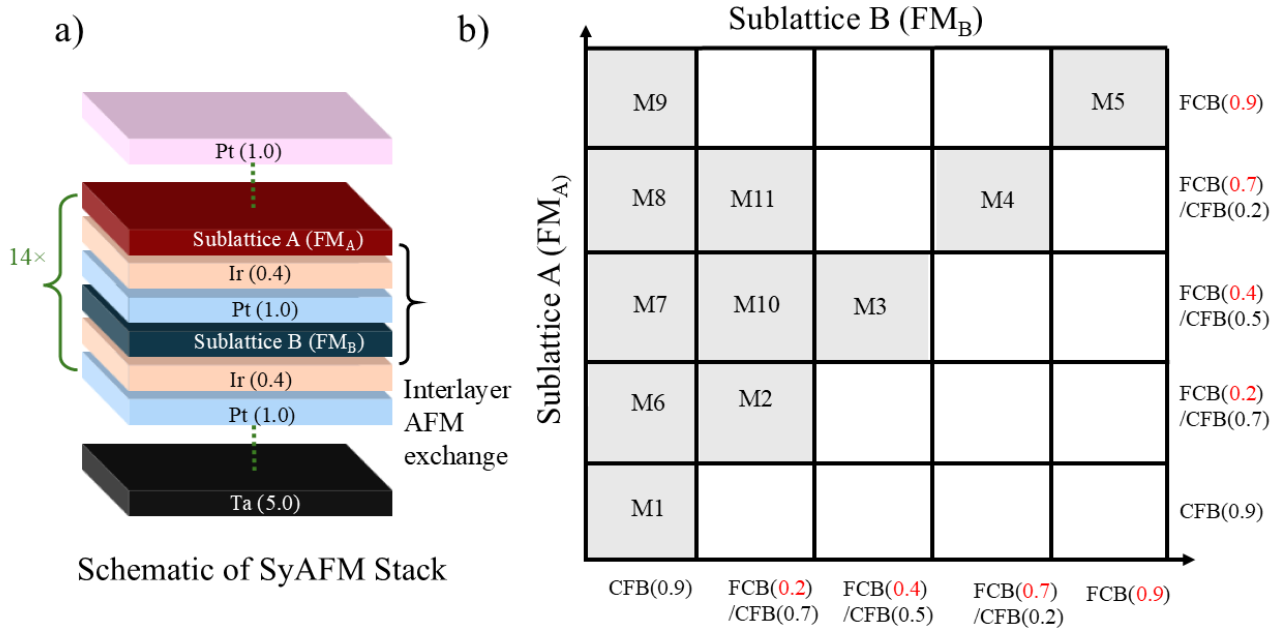


Figure 4.4: **Material stack and composition of the SyAFM.** (a) Schematic representation of the multilayer SyAFM stack, consisting of alternating ferromagnetic sublattices A (FM_A) and B (FM_B) that are antiferromagnetically coupled via interlayer exchange. The layers are separated by Pt and Ir, with thicknesses (in nm) indicated in parentheses. (b) Composition map of the SyAFM sublattices for the sample stacks #M1-#M11. Each grid cell represents a sample with sublattice compositions defined by the x and y axes, indicating the respective richnesses of Co_{0.6}Fe_{0.2}B_{0.2} (CFB) and Fe_{0.6}Co_{0.2}B_{0.2} (FCB) in sublattices A and B.

Fig. 4.4(b) presents the composition map of the SyAFM stack series #M1-#M11. Each cell

in the matrix represents a bilayer configuration consisting of FCB and CFB with varying thickness ratios. The horizontal and vertical axes correspond to the composition of sublattice B (FM_B) and sublattice A (FM_A), respectively. Both sublattices are formed by ferromagnetic layers with a fixed total thickness of 0.9 nm, while the ratio between CFB and FCB is systematically varied. Grey-shaded cells indicate the specific stack compositions that were fabricated and studied experimentally (stack #M1 to stack #M11). Stacks #M1 to #M5 are positioned along the diagonal of the composition map (Fig. 4.4(b)), where sublattices A and B are identical in composition. As a result, these stacks are fully magnetically compensated. Here, we can finely tune the effective anisotropy without altering the total thickness of the ferromagnetic sublattices, offering precise control of K_{eff} . However, due to the absence of net magnetization, these stacks are suitable for imaging using SEMPA but not for techniques such as MFM or STXM. To overcome this limitation, we prepare a vertical series of stacks #M6 to #M11, in which sublattice B is fixed and only sublattice A is varied. This allows imaging using both SEMPA and MFM, while still enabling systematic tuning of the anisotropy.

Topological spin textures in bilayer SyAFM have been shown to exhibit significantly enhanced thermally activated diffusive motion due to their cancellation of the topological charge [233]. This intrinsic diffusivity poses a major limitation for deterministic control, rendering conventional bilayer systems suboptimal for device applications. To perform 3D vector imaging of the magnetization, we have employed a combination of the MFM and SEMPA techniques. However, the time to transition from one setup to another is of the order of days due to the stringent ultra-high vacuum requirements. Moreover, SEMPA is an inherently slow imaging technique, with each single in-plane two-dimensional magnetization vector image taking 3–4 hours to acquire. To ensure precise determination of the chirality and helicity of the domains and spin textures, these spin textures must remain unaffected by thermal diffusion over time scales of days. To address this challenge, we employ multilayer repetitions of the SyAFM stack for two key reasons. First, increasing the number of repetitions reduces thermal diffusion of the topological spin textures, even when using materials with intrinsically low pinning strength. The second reason is to maximize the effective saturation field [234].

In a multilayer configuration, the FM layers at the surfaces are coupled to only one adjacent FM layer, whereas the FM layers in the middle are coupled to two layers, one above and one below. As a result, saturating the entire stack requires a magnetic field approximately twice as large as that needed to saturate a single bilayer SyAFM. In line with this, our characterization experiment on stack #M1 has indicated that increasing the number of repetitions in the SyAFM stack results in an augmentation of the effective AFM exchange field (H_{sat}), as depicted in Fig. 4.6. In this case, we have determined an effective anisotropy of 0.2 MJ m^{-3} , indicating a positive anisotropy and thereby indicating the presence of an OOP multidomain state in the sample. Due to the stack's complete

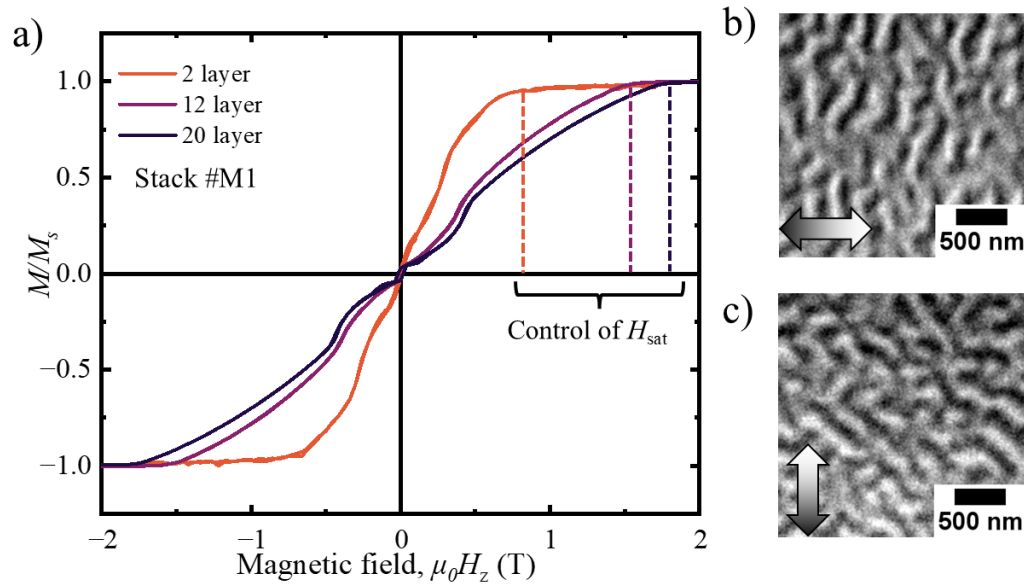


Figure 4.5: **Magnetic properties and OOP domains in stack # M1.** (a) Magnetic hysteresis loop as a function of the number of repetitions (2, 12, and 20 layers) of the stack # M1 measured using SQUID magnetometry. (b,c) SEMPA images of the same stack. (b) Horizontal and (c) vertical in-plane components of the surface magnetization. The direction of magnetization is indicated by the grayscale contrast, as displayed on the double arrows.

compensation, MFM imaging was not feasible. To overcome this challenge, we employed SEMPA, which enabled successful imaging of the IP domain walls of stack #M1 as shown in Fig. 4.5(b,c). Let us consider a simplified case where two FM spins are aligned antiferromagnetically, either in an IP or OOP configuration. In the IP arrangement, the antiparallel spins form a flux-closure pattern at the interface, which minimizes the magnetostatic energy and stabilizes the in-plane alignment. On the other hand, when the spins are aligned antiferromagnetically in the OOP direction, flux closure is not achieved. This leads to the accumulation of magnetic surface charges at the interface between the FM layers and results in an increase in the demagnetizing energy. This interlayer demagnetizing H_d contribution acts against the OOP alignment and effectively favors in-plane magnetization. It can be interpreted as an additional anisotropy term, as expressed in Eq. 4.4. When the interlayer exchange coupling is strong, the effect of this demagnetizing field becomes more significant, pushing the system toward an in-plane configuration even near the SRT. Under such conditions, the critical DMI strength required to stabilize out-of-plane bimeron cores is reduced.

4.3.2 Magnetic Properties of the SyAFM Stacks

Understanding the magnetic properties of the SyAFM stacks is crucial for identifying the parameter regimes that support the stabilization of topological spin textures such as (anti)merons and bimerons. In particular, near the SRT, the nature of the stabilized textures, whether skyrmions or bimerons, depends sensitively on the sign and magnitude of the effective magnetic anisotropy. To identify these regimes, we systematically characterize the hysteresis behavior of all stacks, enabling a direct link between magnetic configuration and the conditions required for realizing robust, tunable topological states.

Fig. 4.6(a)–(i) show the $M(H)$ hysteresis loops for stacks #M2 to #M11, measured using SQUID magnetometry. Red and blue curves correspond to IP and OOP magnetic field orientations, respectively. The corresponding MFM images, acquired at zero magnetic field (as grown) and room temperature for stacks #M2, #M6–#M9, and #M11, are shown as insets in each panel. Hysteresis loops corresponding to stacks with positive K_{eff} are shown on a white background, while those with nearly zero effective anisotropy are displayed on a light red background. As can be seen in Fig. 4.6(a), (b), (d), and (e), corresponding to stacks #M2, #M3, #M6, and #M7, a clear separation between the IP and OOP loops is observed, indicating a positive effective perpendicular anisotropy ($K_{\text{eff}} > 0$). This anisotropy favors the formation of out-of-plane multidomain states at remanence and room temperature. Stacks #M1 to #M4 are fully magnetically compensated, and thus their near-zero net moment renders them unsuitable for phase-sensitive imaging techniques such as MFM. Stacks #M6–#M11 were intentionally engineered to exhibit a small, normalized uncompensated magnetization, defined as $m_{\text{uncomp}} = \frac{|M_{s,A} - M_{s,B}|}{M_{s,A} + M_{s,B}} \approx 5\%$. This slight imbalance preserves the essential characteristics of the compensated SyAFM platform while enabling the detection of OOP spin components via MFM imaging. Stack #M6 displays large labyrinth OOP domain patterns at zero field, consistent with its relatively strong positive K_{eff} . Stack #M7 exhibits worm-like domains, reflecting a reduced anisotropy compared to Stack #M6, yet still maintaining an OOP-preferred multidomain configuration.

For stacks #M4, #M8, #M9, #M10, and #M11 (Figs. 4.6(c), (f)–(i)), the IP and OOP hysteresis loops are nearly identical, indicating a vanishing effective anisotropy ($K_{\text{eff}} \simeq 0$). The absence of remanent magnetization in these stacks makes them promising candidates for stabilizing (anti)merons and bimerons, which are theoretically expected to form in systems with near-zero net moment and a degenerate multidomain ground state. Although stacks #M8 and #M9 exhibit K_{eff} values close to zero, the corresponding MFM images acquired under ambient conditions reveal multi-domain stripes with multiple phase contrasts, as shown in the insets. These features suggest a transitional regime between conventional domain patterns and emergent topological textures. Notably, stack #M11 shows clear evidence of merons and antimerons in the MFM images, marked by

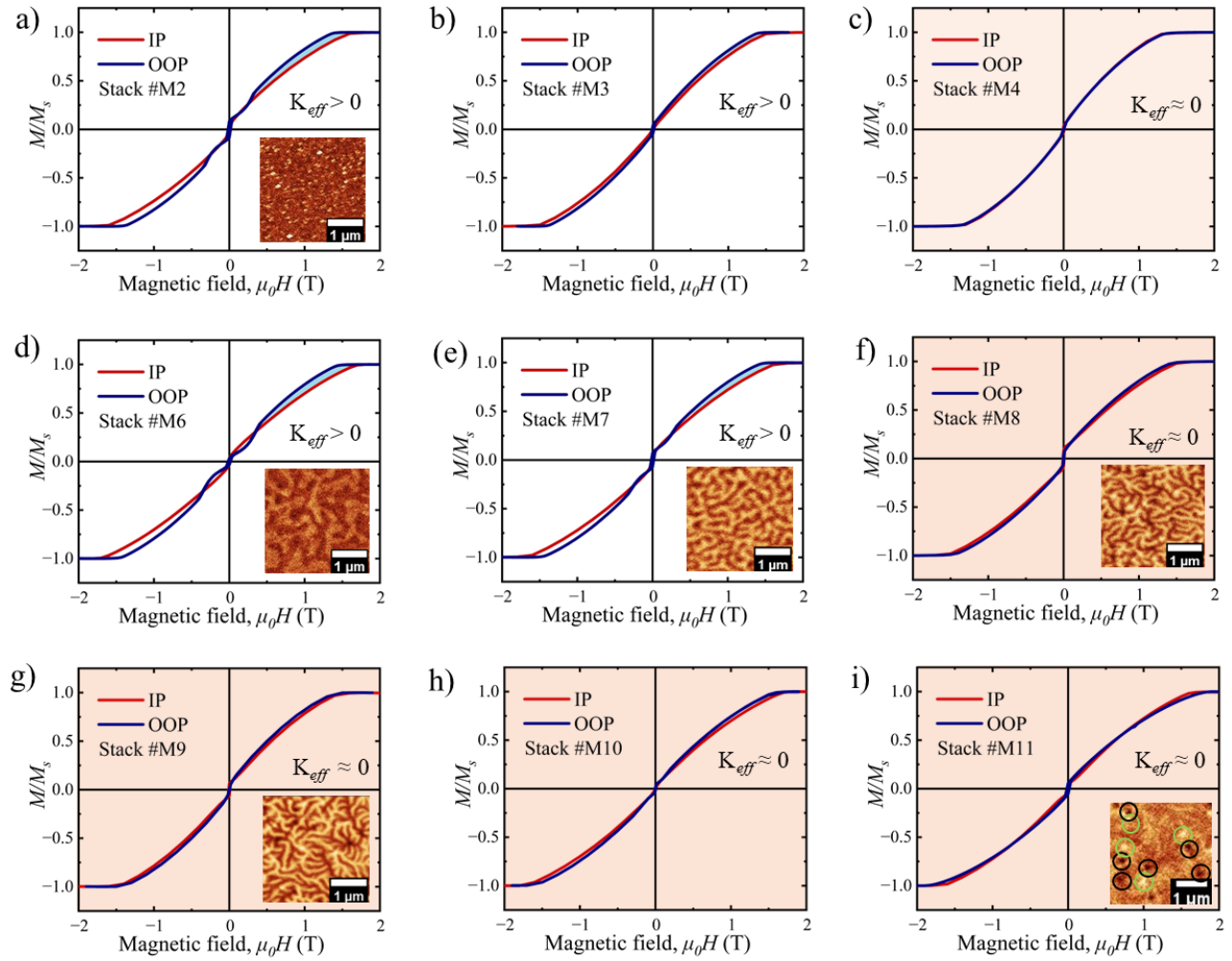


Figure 4.6: **Magnetic properties of SyAFM stacks #M2 to #M11.** (a)–(i) OOP (blue) curves and IP (red) hysteresis loops measured using SQUID magnetometry. Insets show the corresponding MFM images taken at room temperature and zero magnetic field. Stacks #M2, #M3, #M6, and #M7 ((a), (b), (d), and (e)) exhibit a separation between the IP and OOP loops, indicating a positive K_{eff} . In contrast, stacks #M4, #M8–#M11 ((c), (f)–(i)) show nearly identical IP and OOP loops, indicating vanishing effective anisotropy ($K_{\text{eff}} \approx 0$), a key requirement for stabilizing (anti)merons and bimerons. MFM images of stack #M11 show the presence of merons and antimerons as marked in black and green circles, respectively. Hysteresis loops having positive K_{eff} are shown on a white background, while those with near-zero anisotropy are highlighted with a light red background.

distinct circular features with opposite contrast, highlighted by black and green circles, respectively. A more detailed [SEMPA](#) imaging at various conditions of these stacks is presented in Appendix B section B.6.

4.4 Multimodal 3D-Vector Imaging of (Bi)merons

In this section, we directly visualize the three-dimensional topological spin textures present in the SyAFM system. To fully reconstruct the Néel order parameter $\mathbf{L} = \mathbf{M}_A - \mathbf{M}_B$, it is necessary to simultaneously access both the IP and OOP components of the spin configuration. This is achieved through a multimodal imaging approach that combines SEMPA for mapping the IP components and MFM for detecting the OOP component. Stack #M11, which was intentionally engineered to exhibit a slight magnetic imbalance. As a result, the topmost FM layer generates weak but detectable stray fields, which are sufficient to provide magnetic contrast in MFM measurements while preserving the essential characteristics of a compensated SyAFM. By combining two imaging methods, SEMPA and MFM, on the same region of the stack #M11, we reconstruct the full vectorial Néel order characterizing the topological spin textures. Note that SEMPA is surface sensitive and probes only the topmost ferromagnetic layer, whereas MFM measures the net stray-field contrast and therefore reflects the difference between the two antiferromagnetically coupled sublattices. Fig. 4.7(a) and 4.7(b) show the in-plane and out-of-plane spin components, imaged via SEMPA and MFM, respectively, at room temperature and zero applied magnetic field. The textures were nucleated by applying a damped oscillating out-of-plane magnetic field with a frequency of 1 Hz and an amplitude of 10 mT prior to the first imaging.

Due to the high surface sensitivity of the SEMPA technique [235], the image in Fig. 4.7(a) captures solely the IP magnetization of the topmost ferromagnetic layer (FM_A). This measurement thus reflects the in-plane projection of the Néel order parameter in the SyAFM stack. By examining the spatial variation of the IP magnetization direction encoded in the color map, we extract the winding number w associated with each observed spin texture. The winding number quantifies the topological wrapping of the Néel vector around the unit sphere and allows us to classify the textures: $w = \pm 1$ corresponds to skyrmions or bimerons, while $w = \pm \frac{1}{2}$ is characteristic of merons and antimerons. Moreover, the analysis of the in-plane rotation direction of these structures from Fig. 4.7(a) provides the precise helicity γ of these meron spin structures. γ is given, akin to skyrmions [29], by the angle between the IP projection of the Néel order and the radial direction. A color-coded schematic for distinguishing different meron types is provided in Appendix B section B.4. The observation reveals the presence of three distinct spin textures: 1) Néel merons having $\gamma = \pi$, indicated by black dotted circles, 2) Néel merons having $\gamma = 0$, indicated by white double circles, and 3) the spin texture of antimerons, indicated by double black dotted circles.

In this SyAFM stack, the saturation magnetization of layer A, ($M_{s,A}$), surpasses that of layer B, ($M_{s,B}$). As a result, the MFM measurement primarily detects the stray field from the A layers, similar to SEMPA, thus indicating the OOP component of the Néel order parametrizing the SyAFM.

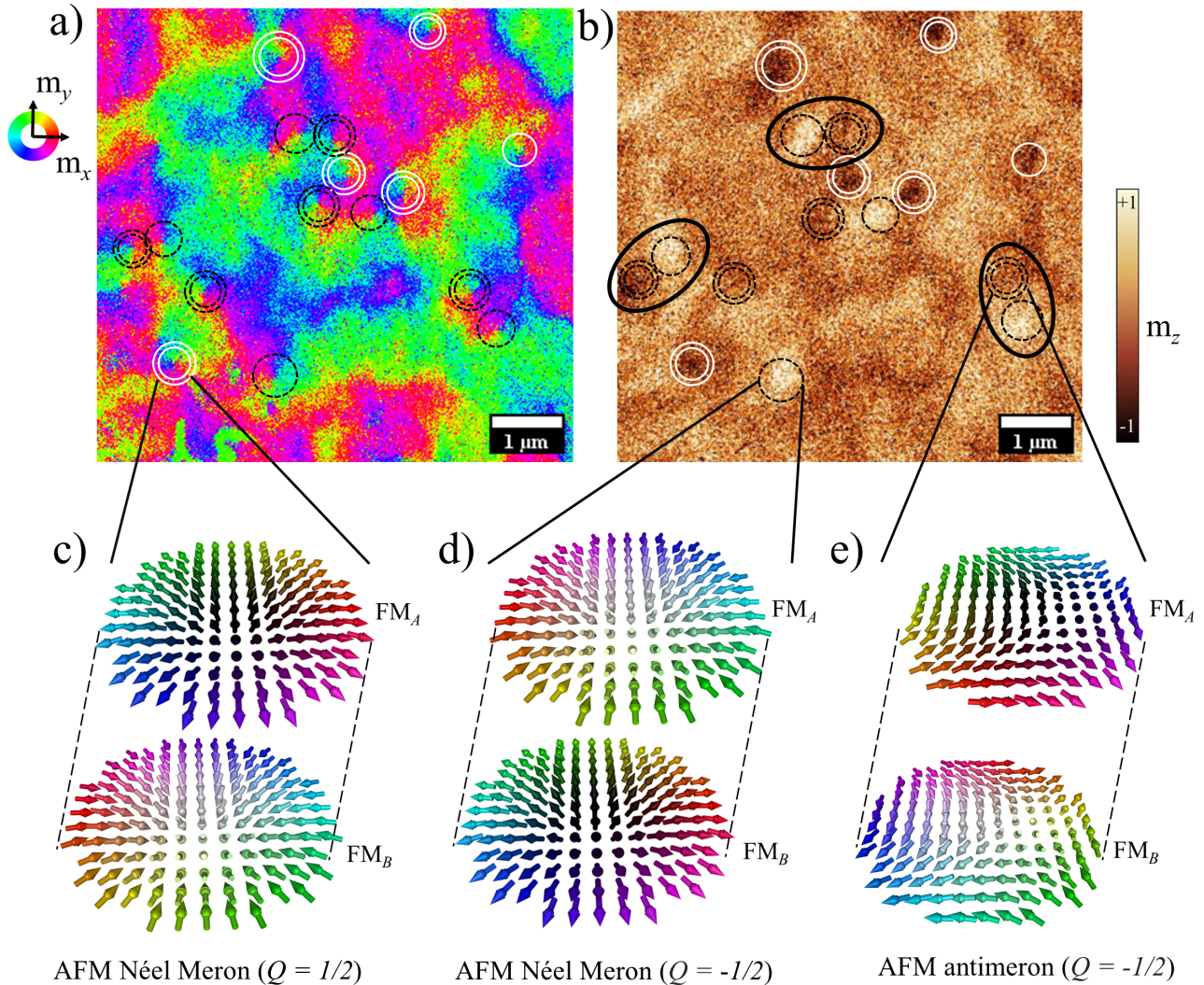


Figure 4.7: **Imaging the Néel order parameter of (anti)merons and bimerons in synthetic antiferromagnets.** **(a)** SEMPA image showing the IP spin components of the topmost FM_A layer, or, equivalently, the IP component of the Néel order of the meron texture in the stack #M11. **(b)** MFM image showing the OOP spin component of the FM_A layers, that is, the OOP component of the Néel order of the meron structure from the same area. Dark brown and white MFM contrasts indicate the upward and downward direction, respectively. The color map for the SEMPA image is shown on the right side. Black dotted circles represent merons of helicity $\gamma = \pi$, whereas double black dotted circles indicate antimerons, both with $Q = -\frac{1}{2}$. White circles represent merons having an arbitrary helicity with $Q = \frac{1}{2}$ and white double circles denote merons of helicity $\gamma = 0$ and $Q = \frac{1}{2}$. Two adjacent black circles (single and double) are identified as bimerons with net topological charge $Q = -1$ and are additionally highlighted by ellipses. **(c)** an AFM Néel meron having $\gamma = 0$ and $Q = \frac{1}{2}$, **(d)** an AFM Néel meron having $\gamma = \pi$ and $Q = -\frac{1}{2}$ and **(e)** an AFM antimeron having $Q = \frac{1}{2}$. Adapted from [1]

Consequently, through the visualization of the OOP core polarities of the spin textures identified in Fig. 4.7(a), we reveal the full 3D Néel vector of the SyAFM. This allows us to determine their topological charge Q , which can be cast as the product of the winding number and the core polarity, namely $Q = w \cdot L_z|_{\text{core}}$, the core polarity being defined as the z component of the Néel order at the texture core. The white and dark brown contrasts in Fig. 4.7(b) show the downward and upward core polarity, respectively. Furthermore, black and white circles in both images correspond to $Q = -\frac{1}{2}$ and $Q = \frac{1}{2}$, respectively. The analysis of both images reveals the topological nature of the meron spin textures: black dotted circles represent Néel-type merons having $Q = -\frac{1}{2}$ with core polarity pointing downward ($L_z = -1$) as indicated in Fig. 4.7(d). White double circles correspond to merons of $Q = \frac{1}{2}$ having upward core polarity, as described in Fig. 4.7(c). We note that for merons the helicities $\gamma = 0, \pi$ always correspond to the core polarities $L_z = 1$ and -1 , respectively, which indicates the presence of homochiral merons in the system. Double black dotted circles mark antimerons with topological charge $Q = -\frac{1}{2}$, see Fig. 4.7(e). Changes in γ do not affect the topological charge of the antimeron as they only lead to a geometrical rotation of its IP spin components. Hence, we consider all of them as topologically equivalent. The combination of a single black circle adjacent to a double one can be identified as a bimeron with $Q = -1$ and is marked by an ellipse.

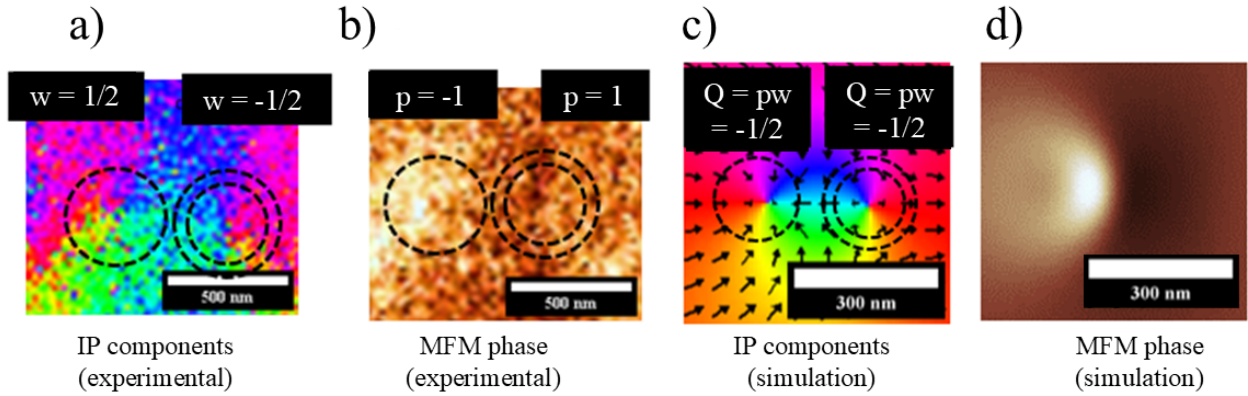


Figure 4.8: **Structure of a single bimeron.** Zoomed-in view of IP (a) and OOP (b) component of single bimeron. (c) Micromagnetic simulation results giving the spin structures of a bimeron. (d) Simulated MFM phase contrast of the bimeron.

A bimeron, as defined in this study, consists of a bound pair comprising a meron and an antimeron with opposite core polarities. It is important to note that if the meron—antimeron pair shares the same core polarity, their individual topological charges cancel, resulting in a net topologically trivial configuration with $Q_{\text{net}} = 0$. A detailed structural analysis of a single bimeron is presented in Fig. 4.8. Panels (a) and (b) show a magnified view of the region highlighted around one of the identified bimeron from Fig. 4.7. From the in-plane magnetization map in Fig. 4.8(a), the winding

numbers of the individual textures can be determined: the meron (with $w = +\frac{1}{2}$) is indicated by a black single circle, while the antimeron (with $w = -\frac{1}{2}$) is marked by a black double circle. To confirm that these textures do not annihilate each other's topological charge upon pairing, the same region was examined in the MFM phase image (Fig. 4.8(b)). The contrast reveals opposite phase polarities for the meron and antimeron, indicating that both possess a topological charge of $Q = \rho w = -\frac{1}{2}$, resulting in a combined charge of $Q = -1$ for the bimeron. In contrast, if the core polarities had been identical, the MFM contrast would have exhibited the same sign for both textures, and their combination would yield a trivial configuration. To further support the experimental findings, micro-magnetic simulations were performed using *MuMax*³ to compute both the in-plane magnetization structure and the corresponding MFM phase contrast of a bimeron. The simulated results, shown in Fig. 4.8(c) and 4.8(d), closely reproduce the experimental features observed in the SEMPA and MFM images, confirming the presence of a bimeron with distinct meron and antimeron components.

4.4.1 Quantitative Analysis of (Anti)merons Cores

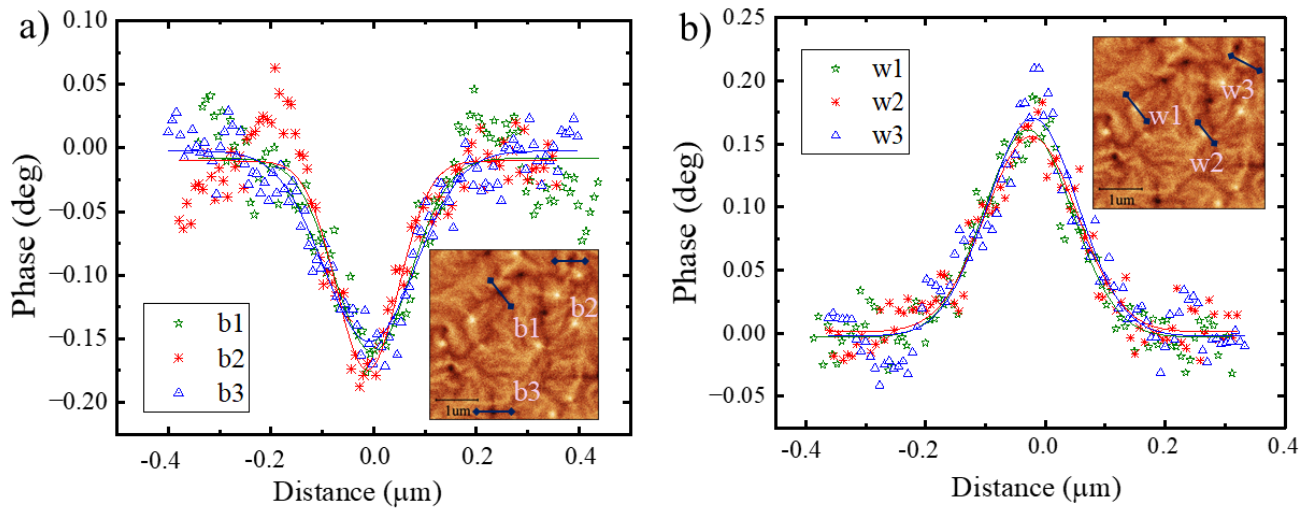


Figure 4.9: **Quantitative analysis of the MFM contrast.** (a) Line profiles b1, b2, and b3 show the MFM signal of the up core polarity. (b) The line profiles w1, w2, and w3 represent the MFM signal of the down core polarity. The solid curves correspond to fits of the measured points using Gaussian peak functions. The horizontal axis gives the distance along each corresponding line profile from the meron cores, as depicted in the insets.

In this part, we quantify the spin structures and their statistics. Fig. 4.9(a,b) presents typical line profiles of the MFM phase image representing the up and down core polarities. These line profiles were acquired for stack #M11 under zero magnetic field and correspond to the positions specified in

the insets. The Gaussian peak functions fitted to the measured points along the line profiles reveal that the profiles from different cores coincide within the resolution limit of the instrument. The full width at half maximum (FWHM) of the Gaussian fit provides a measure of the diameter of the cores [236]. The diameter distribution of the (anti)meron cores, as extracted from the larger MFM image, is shown in Fig. 4.10(a). We find average diameters of (230 ± 50) nm and (220 ± 60) nm for up and down cores, respectively, which are identical within the given uncertainty.

When examining the spatial arrangement of the (anti)merons in Fig. 4.9(a,b), it is apparent that in most cases merons and antimerons are positioned in close proximity to each other. Meron–antimeron composites can exhibit either a non-zero topological charge, arising when the core polarities are different, or be trivial spin textures with $Q = 0$, occurring when the core polarities are the same. To gain a more comprehensive understanding of the length scale of their interaction, we conducted a statistical analysis of the distance between these meron textures over a larger sample area.

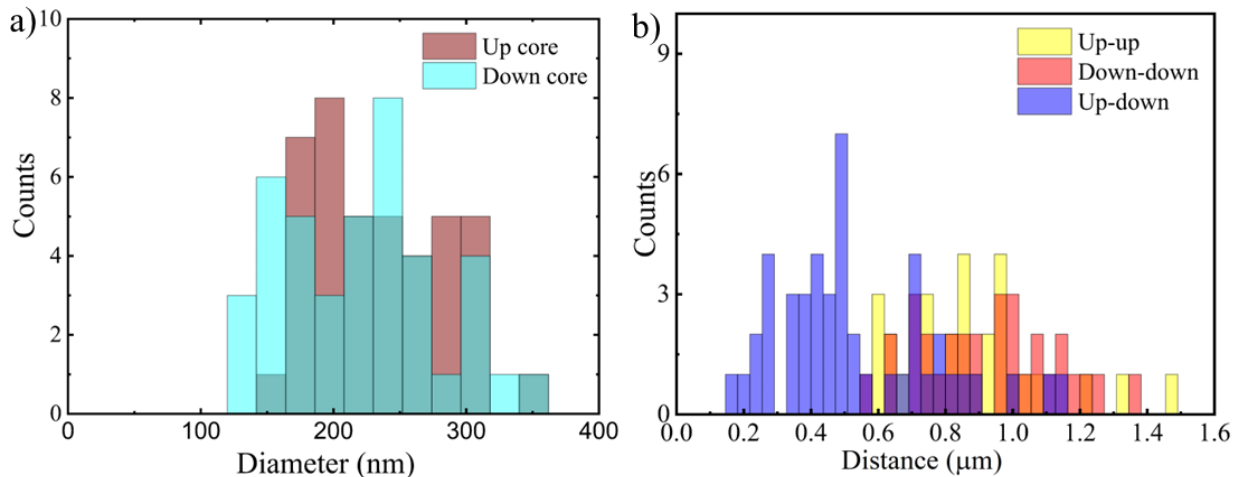


Figure 4.10: **Quantitative analysis of (anti)merons cores.** (a) Distribution of different core diameters obtained from various MFM images. (b) Histogram of the next-neighbour separation between the centers of structures with up-up, down-down, and up-down core polarities from the MFM phase contrast. Adapted from [1]

In Fig. 4.10(b), three histograms of the next-neighbour distances between different core polarities, as observed in the MFM images, are presented. Up-down pairs exhibit an average separation of (530 ± 240) nm, which is significantly closer than the separation between two up or two down pairs. This closer proximity strongly suggests the presence of non-zero topological charge in the meron–antimeron pairs and indicates the prevalence of bimerons in the sample. Additionally, this observation implies a different interaction potential with an energy minimum at the shorter distance between two different core polarities due to the presence of iDMI. The statistical analysis presented

in this work considers only the next-nearest neighbour distances between meron spin textures. This choice is based on the fact that the stabilization of merons is attributed to the **iDMI**, as supported by the existence of homochiral Néel merons in the system [51].

4.5 Manipulating the (Anti)merons

The chirality and helicity of skyrmions are intricately related to their stabilization mechanisms. Néel Skyrmions, primarily stabilized by **iDMI**, exhibit energy minima for helicities $\gamma = 0$ or $\gamma = \pi$, while Bloch skyrmions, stabilized through dipolar interactions, tend to favor $\gamma = \pi/2$ or $\gamma = 3\pi/2$ [29]. Consequently, identifying and manipulating the helicity plays a pivotal role in unravelling the underlying stabilization mechanisms and engineering the **SOT**-induced dynamics. In their in-plane counterparts, a compelling question arises regarding the effective manipulation of (anti)meron helicity. As depicted in Fig. 4.9(a,b), there are instances where (anti)merons occur clustered. It has been reported that, as a result of manipulating temperature and magnetic fields, the intermittent emergence of densely packed spin-texture clusters can be observed [50]. In this section, we discuss how the helicity, density, and type of spin textures of the (bi)merons can be effectively manipulated using dipolar interaction, magnetic field, and temperature.

4.5.1 Tailoring the Helicity of (Anti)merons

Here, we demonstrate the control of the helicity of merons in **SyAFM** by tuning the magnetic compensation ratio, which in turn controls the dipolar energy of the system. The effect of the magnetic compensation in synthetic antiferromagnets on the formation of merons has been studied in stack #M12, and the hysteresis loop is shown in Fig. 4.11(b), indicating m_{uncomp} to be 20%. In this case, ferromagnetic layers A and B are made of $\text{Co}_{0.8}\text{B}_{0.2}$ (CB) and FCB, respectively, with thicknesses of $d_{\text{FM}_A} = 1.305$ nm and $d_{\text{FM}_B} = 0.9$ nm. Another stack #M13 is purposefully designed to harness the element specificity of **XMCD-PEEM**, thus enabling the visualization of the antiferromagnetic coupling between the ferromagnetic layers (as shown in the following section). It contains one additional FM_B layer on the top of stack #M12.

Fig. 4.12(a) shows a **SEMPA** image indicating the direction of the in-plane Néel order, for the fully compensated **SyAFM** (stack #M4) in the absence of magnetic fields. We have marked all merons with white circles and all antimerons with black circles and find an almost equal proportion of both types of topological spin textures. We elucidate the relevance of the helicity by analyzing its values for the merons through a histogram, as shown in Fig.4.12(b). This histogram has been aggregated by also considering additional **SEMPA** images of the stack #M4 obtained under comparable conditions. Values of $\gamma = 0, \pi$ are significantly favoured in this **SyAFM** platform, which corresponds to the Néel-

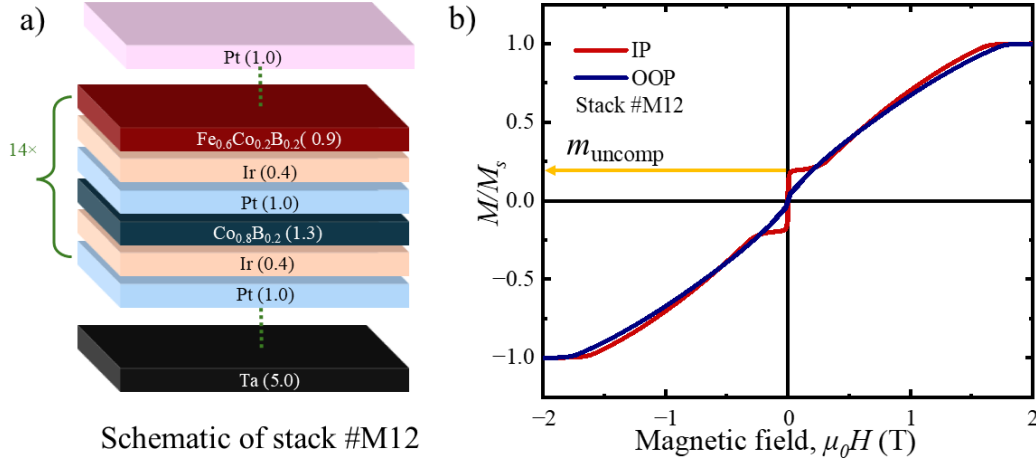


Figure 4.11: **Uncompensated SyAFM stack and its magnetic properties.** (a) Schematic illustration of the uncompensated SyAFM stack, composed of 14 repetitions of asymmetric ferromagnetic sublayers separated by spacer layers, designed to yield an uncompensated magnetic moment. (b) Normalized IP (red) and OOP (blue) $M(H)$ hysteresis loops for stack #M12, measured via SQUID magnetometry.

type rotation, and therefore confirms that the stabilization mechanism for merons in the compensated case originates from the *iDMI* [51, 52, 237]. Similarly, Néel bimerons are energetically favourable in the same range of *iDMI* [52]. For comparison, the uncompensated case has been studied in stack #M12, which presents an $m_{\text{uncomp}} = 20\%$. A *SEMPA* image of its topmost-layer magnetization is shown in Fig. 4.12(c), giving the direction of the net *IP* magnetization. We observe again a nearly equal number of merons and antimerons (same white/black color convention as before). However, for this stack, the analysis of the distribution of meron helicities, see Fig. 4.12(d), yields a prevalence of values around $\gamma = \frac{\pi}{2}, \frac{3\pi}{2}$, which indicates a Bloch-type rotation. In the picture of the analytical model developed [1], an additional Zeeman-like interaction contributes to the energetics of the *SyAFM*, which favours the *OOP* orientation of the Néel order and, therefore, the stability of Bloch-type *IP* merons at low *iDMI* [1]. We conclude that the presence of a small uncompensated magnetization in the *SyAFM* promotes the stabilization of Bloch-meron textures. Thus, by tuning the compensation ratio, we can manipulate the helicity and, consequently, one can tune the resulting *SOT*-induced dynamics.

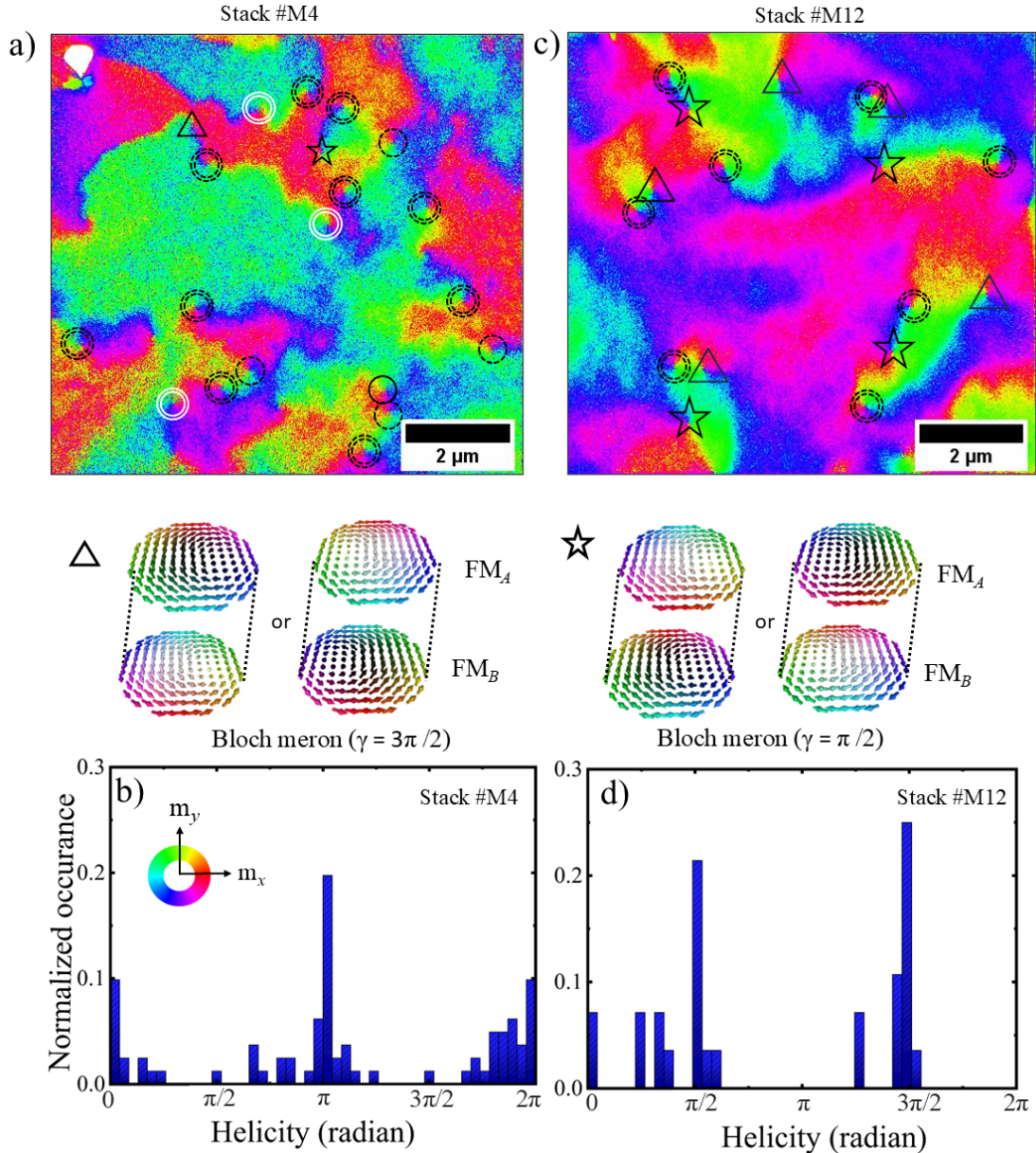


Figure 4.12: **Controlling the helicity of (anti)merons in SyAFM.** (a) SEMPA image showing the IP spin components of the meron spin texture in the stack #M4, indicating the IP orientation of the staggered magnetization. Black and white circles denote antimerons and merons, respectively. (b) Distribution of helicities of the merons present in SyAFM. The abundance of helicity values around 0 and π indicates homochiral Néel merons in the stack. (c) SEMPA image showing the IP spin components of the meron spin texture in the (uncompensated) case of stack #M12. (d) shows the prevalence of Bloch merons having helicities of $\pi/2$ and $3\pi/2$ in this stack. Adapted from [1]

4.5.2 Temperature-Driven Evolution of (Bi)merons[†]

In the previous sections, we demonstrated that tuning the thickness ratio of CFB to FCB in the SyAFM stack allows control over the sign of the effective anisotropy, K_{eff} , thereby stabilizing (bi)merons at zero magnetic fields instead of OOP multidomain configurations. In addition to the layer thickness, temperature serves as a crucial control parameter for modulating the spin reorientation transition by altering K_{eff} . As the temperature decreases, the perpendicular magnetic anisotropy in our SyAFM stack increases, predominantly originating from the interfacial contribution at the Pt/CoFeB interface. This interfacial PMA stems from the hybridization between the 3d orbitals of Co and the 5d orbitals of Pt. At low temperatures, this interfacial anisotropy becomes increasingly dominant and can overcome the demagnetizing field that otherwise favors in-plane magnetization. As a result, the effective anisotropy becomes positive, and the system transitions towards an easy axis. This thermally driven evolution leads the system toward the SRT, where spin textures gain a stronger OOP character. Consequently, we expect an increase in the core contribution from (bi)merons with decreasing temperature, as discussed here.

To investigate the temperature dependence of (bi)merons, MFM measurements are performed on stack #M11 over a temperature range from 300 K to 100 K (Fig. 4.13(a–e)). The images were acquired by Dr. Ankit Sharma at attocube systems AG, Munich, Germany. All scans are acquired over the same sample region, enabling direct tracking of individual (bi)merons as a function of temperature. MFM primarily probes the OOP component of the local stray field, making it sensitive to variations in the perpendicular magnetization within the spin textures. Upon cooling, a systematic increase in MFM phase contrast is observed. This enhancement may arise from two complementary effects. First, the saturation magnetization (M_s) increases at lower temperatures, thereby increasing the total stray field signal detected by MFM. Second, the system goes through the SRT, during which the effective magnetic anisotropy gradually shifts from an easy-plane to an easy-axis configuration. As the interfacial anisotropy increases, the spin textures exhibit an enhanced MFM phase signal and a corresponding increase in the lateral size of the (bi)meron cores. Since MFM primarily probes the vertical component of the stray field, both mechanisms, the increase in M_s and the progression toward the SRT, can contribute to the observed contrast. These contributions cannot be unambiguously separated based on MFM measurements alone. To quantify this evolution, line profiles are extracted across a single bimeron, comprising both up and down cores, indicated by the black arrows in Fig. 4.13(a–e), and plotted in Fig. 4.13(f) [2]. The MFM phase contrast for the

[†]This subsection is adapted from: M. Bhukta *et al.*, "Temperature-driven transition from Meron-type spin textures to stripe domains and revealing the nanosecond dynamics of antiferromagnetic quasiparticles through sublattice-resolved X-ray microscopy." Spintronics XVIII. Vol. 13586. SPIE, 2025. <https://www.spiedigitallibrary.org/conference-proceedings-of-spie/13586/135860K/Temperature-driven-transition-from-Meron-type-spin-textures-to-stripe/10.1117/12.3063453.short>

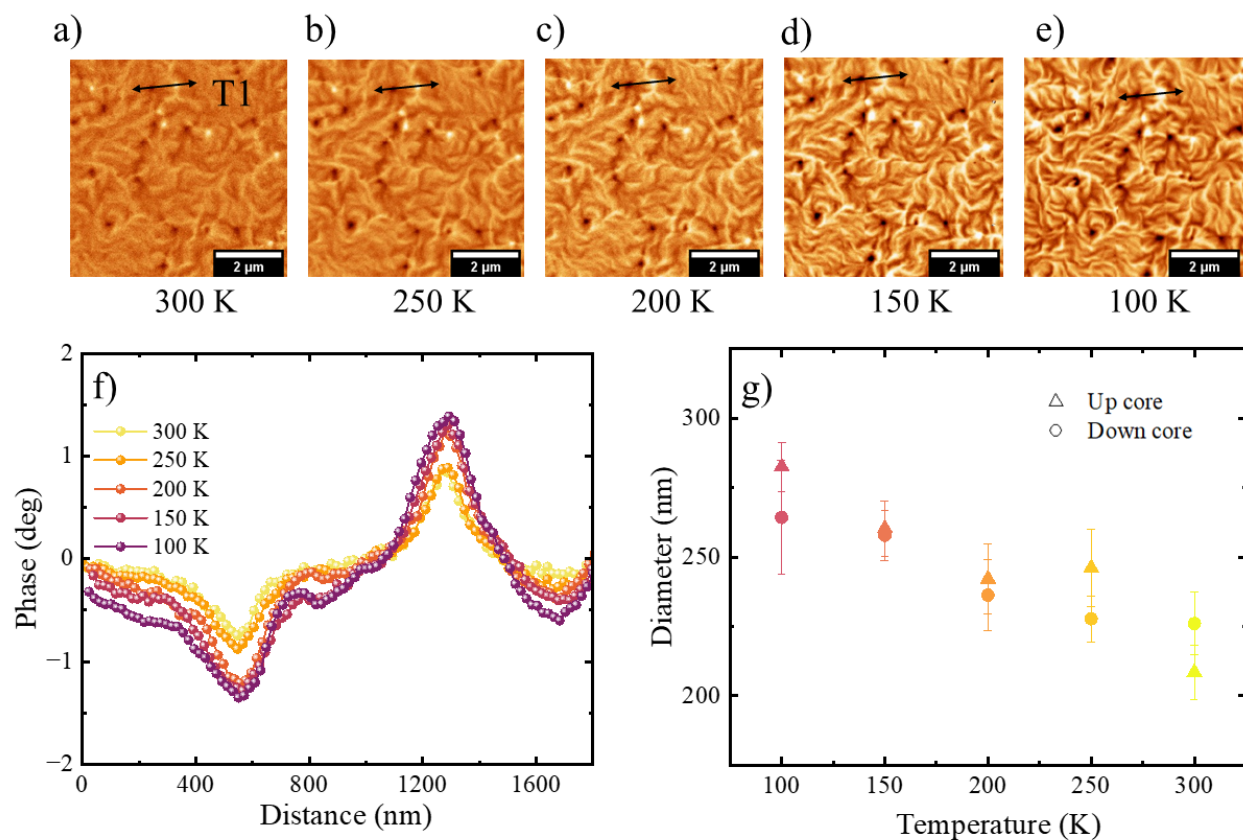


Figure 4.13: **Temperature-dependent evolution of (bi)merons in stack #M6.** (a–e) MFM phase images acquired from the same scan area at temperatures of 300 K, 250 K, 200 K, 150 K, and 100 K, respectively. A progressive enhancement in phase contrast and an apparent increase in the core size of (anti)merons are observed upon cooling. (f) Line profiles across individual (bi)merons (shown as T1) at each temperature, showing a systematic broadening of the phase signal with decreasing temperature. (g) Extracted core diameters, defined as the FWHM from Gaussian fits to the line profiles, as a function of temperature. Adapted from [2]

same (bi)meron increases systematically as the temperature is reduced. Each profile is fitted with a Gaussian function, and the core diameters are defined as the **FWHM** of the fit. The extracted diameters are summarized in Fig. 4.13(g). Both up and down cores exhibit a monotonic increase in size, from approximately $220 \text{ nm} \pm 20 \text{ nm}$ at 300 K to nearly $260 \text{ nm} \pm 22 \text{ nm}$ at 100 K [2].

SQUID magnetometry measurements of **OOP** hysteresis loops are performed at various temperatures to probe the anisotropy evolution in stack #M11, as shown in Fig. 4.14(a) [2]. At elevated temperatures (200 K to 100 K), the magnetization response remains linear with negligible coercivity and remanence, indicating a dominant easy-plane anisotropy. As the temperature decreases below 80 K, the loops begin to open, and by 50 K, a clear hysteretic behavior with finite coercivity is observed.

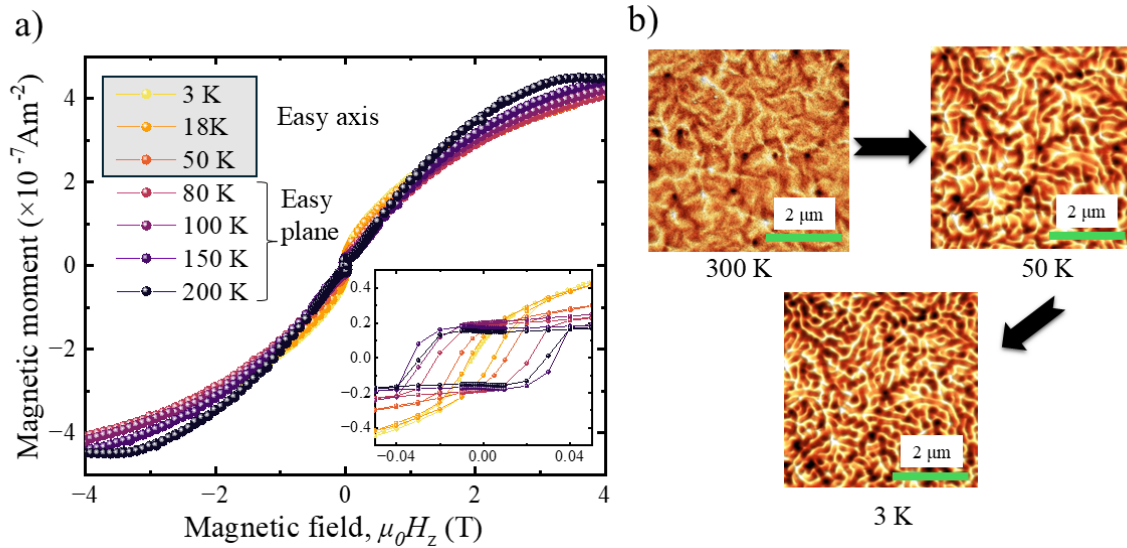


Figure 4.14: **Temperature-driven transition of (bi)merons to OOP stripe domains.** (a) OOP magnetic hysteresis loops measured at various temperatures reveal a spin reorientation transition near 50 K. The inset shows the coercive field region in greater detail, confirming the emergence of remanent magnetization with decreasing temperature. (b) Corresponding MFM images acquired at 300 K, 50 K, and 3 K, demonstrating the transition of spin textures across the SRT. At 300 K, the sample exhibits dense (anti)meron-like textures, characteristic of in-plane magnetized systems. At 3 K, the system transitions into a fully OOP multidomain state, with labyrinthine stripe domains replacing isolated meronic textures. Adapted from [2]

This transition marks the onset of an easy-axis regime. Below 50 K, the anisotropy becomes sufficiently strong to overcome the demagnetizing field, resulting in a magnetization reorientation toward the film normal. This change in the sign of effective anisotropy is accompanied by a corresponding transformation in the real-space spin texture, as captured by MFM imaging at 300K, 50 K, and 3 K (Fig. 4.14(b)). At room temperature, the magnetic contrast corresponds to a dense network of (anti)meron-like spin textures. Upon cooling to 50 K, the MFM contrast increases, indicating the emergence of significant OOP components, consistent with the proximity to the SRT [2]. At 3 K, the system fully transitions into an OOP multidomain state, characterized by labyrinthine stripe domains. These results demonstrate that temperature alone can drive a transition from stabilized (bi)merons to an OOP multidomain state, highlighting thermal control as an effective tuning parameter for spin texture.

4.6 Direct Imaging of the Antiferromagnetic Nature of (Bi)merons

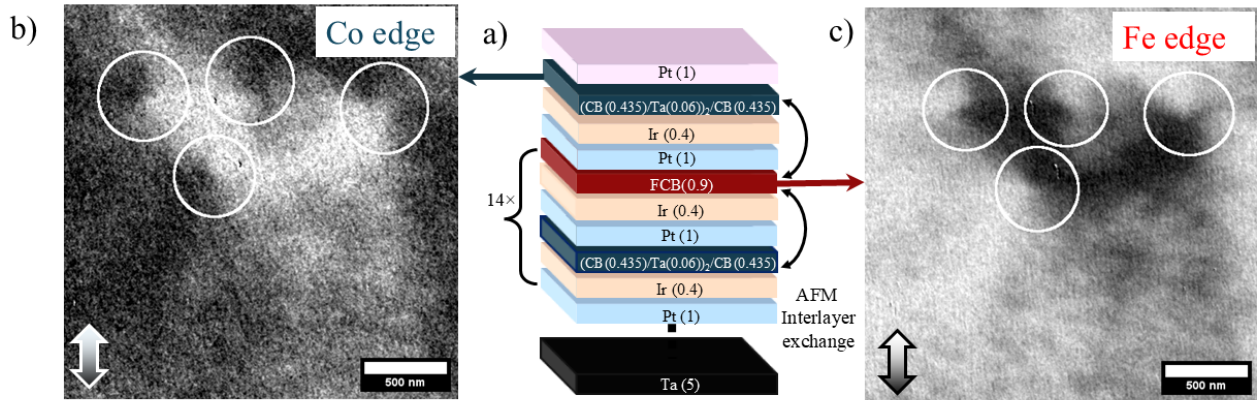


Figure 4.15: **XMCD-PEEM Imaging of stack #M13.** (a) Sample structure for stack #M13. XMCD-PEEM images of domains in the SyAFM at (b) Co edge and (c) Fe. The white circle shows meronic spin texture in the two top layers of the SyAFM. Presence of the same sign but with opposite contrast confirms the antiferromagnetic coupling between the layers.

In this section, we reveal by direct imaging of the antiferromagnetic layer coupling for the (bi)merons. We perform XMCD-PEEM experiments on stack #M12 using its element specificity to prove the AFM coupling between the ferromagnetic layers. XMCD-PEEM images are acquired at the ALBA synchrotron (BL-24 Circe) facility using PEEM, where the beam is incoming at an angle of 16° with respect to the sample surface. Magnetic contrast is obtained by calculating the asymmetry between images taken with right and left-circularly polarized radiation. X-ray absorption spectra (XAS) around the Fe and Co L_3 edges find the maxima at 707.0 eV and 777.6 eV, respectively. The XAS are presented in Appendix B (Section B.1). Owing to the surface sensitivity of this technique, element-specific contrast from individual layers can be resolved. Layer-resolved XMCD-PEEM images for stack #M12 are presented in section B.2 of Appendix B. Stack #M13 has an odd number of layers (29 layers) and is shown in Fig. 4.15(a). We note that this SyAFM is purposefully designed to have an additional FM (CB) on the top to see a clear contrast at both Co and Fe edges, representing consecutive FM layers. Figs. 4.15(b,c) show XMCD-PEEM images of the same sample area of the SyAFM stack at room temperature, but resonantly tuned to either the Co or Fe L_3 edge. Panels (b) and (c) show the magnetic contrast at the Co and Fe edges, respectively. By imaging at the Fe edge, we are able to isolate the magnetic contrast from the second magnetic layer, as there is no Fe present in the top one. The centers of the observed meron spin textures are marked with white circles. The magnetic contrast at the Co edge originates predominantly from the topmost FM layer, as the second layer has effectively less Co. We find that the (anti)merons visible in this top layer

are located exactly at the same positions as in the second layer; however, the magnetic contrast is inverted. This confirms the antiferromagnetic coupling between the domains, domain walls, and the centers of merons and antimerons in the layers of the SyAFM multilayer stack.

4.7 Micromagnetic Study of Bimeron in SyAFM

Our experimental observations confirm the presence of bimerons that are stable at room temperature in magnetically compensated synthetic antiferromagnets, even in the absence of an external magnetic field. However, these results open up several fundamental questions. In particular, the physical origin of bimeron stability in the SyAFM platform remains to be fully understood, especially given that such spin textures have so far primarily been predicted in ferromagnets with monoclinic crystal symmetry [52, 140]. In the case of skyrmions, their stabilization in SyAFMs is known to depend critically on vanishing effective anisotropy and the presence of iDMI. Since bimerons represent the in-plane counterpart of skyrmions, it becomes crucial to investigate the role of these parameters in governing their formation and stability in SyAFM systems. Hence, we have carried out micromagnetic simulations based on experimentally determined material parameters. The material parameters for the simulation can be found in Appendix B Section B.5.

In a simplified scenario, two ferromagnetic layers are antiferromagnetically coupled, with spins aligned either IP or OOP. For the IP case, antiparallel spins form a flux-closure at the interface, minimizing magnetostatic energy and favoring in-plane alignment. In the OOP configuration of two antiferromagnetically aligned spins, the absence of flux closure at the interface leads to the accumulation of magnetic surface charges. This increases the system's demagnetizing energy through an interlayer demagnetizing field, H_d , which acts to suppress the OOP alignment and promotes an effective in-plane anisotropy, as captured in Eq. 4.4. When the interlayer exchange coupling is strong, the influence of H_d becomes more pronounced, favoring IP spin textures even near the SRT. The phase diagram in Fig. 4.16(a-c) illustrates the presence of distinct ground states within the SyAFM as a function of iDMI and effective anisotropy [1]. Here, interlayer exchange strength J_{AFM} is set to $4.4 \times 10^{-4} \text{ Jm}^{-2}$, matching the interlayer exchange strength of the experiment. The bronze-colored region in the phase diagram represents the helical phase in the rz plane, wherein the ground-state phase exhibits helical magnetic ordering along an arbitrary radial direction r . As the SyAFM is tuned away from the SRT point towards an IP configuration, the critical value of iDMI to stabilize bimerons (D_c^{IP}) increases, since one needs to overcome a larger anisotropy barrier to induce the OOP tilting of the staggered magnetization. The phase boundary between the uniform IP (dark green region) and the helical phases has been calculated analytically and is described parametrically by the curve

$$D_c^{IP} = \frac{4}{\pi} \sqrt{A \left[\frac{H_d^2}{J_{AFM} L^2} - K_{\text{eff}} \right]}. \text{ Furthermore, the ground state is the uniform OOP configuration}$$

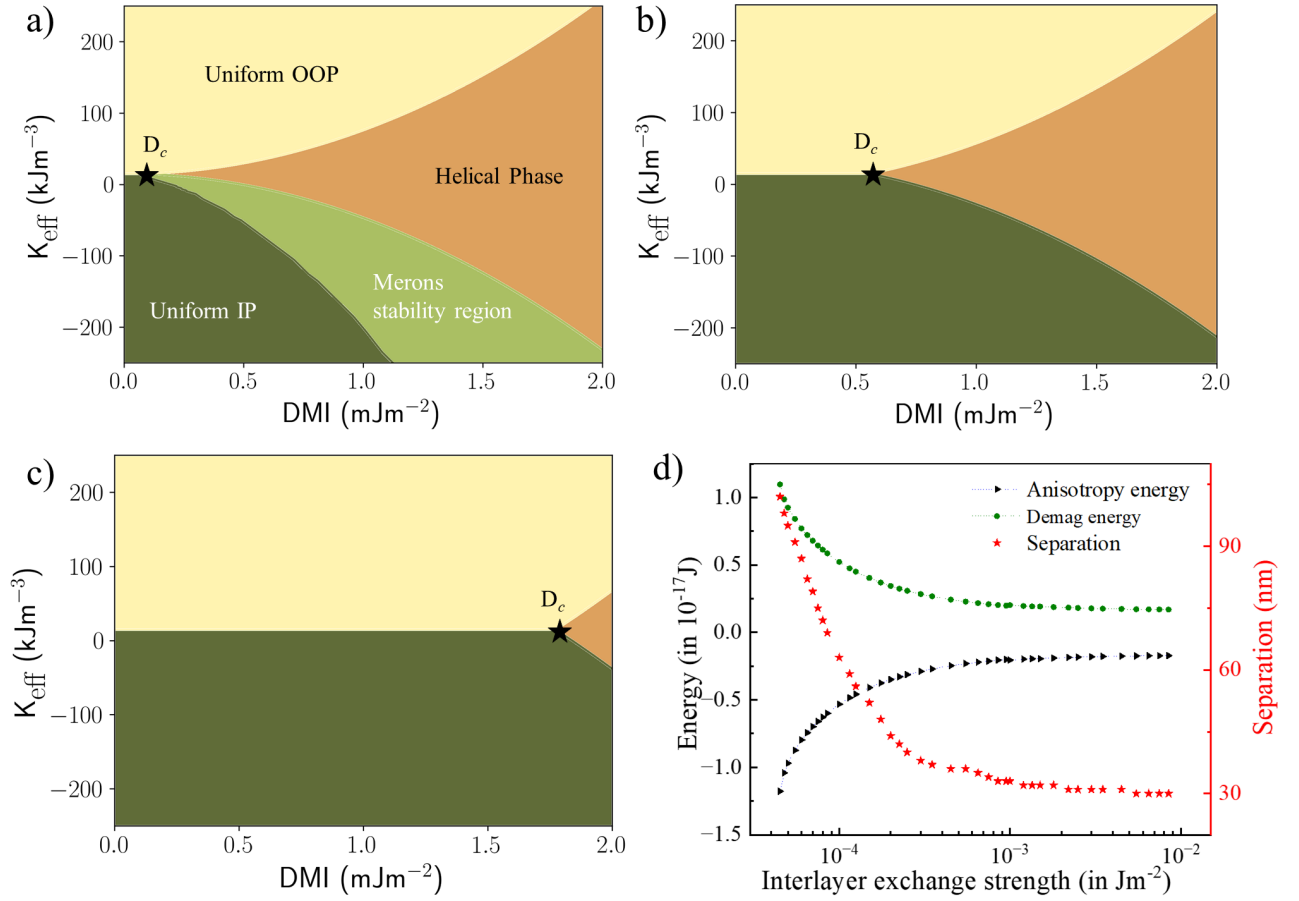


Figure 4.16: **Phase Diagram and micromagnetic simulation of bimerons in synthetic anti-ferromagnets.** (a-c) D vs K_{eff} phase diagrams corresponding to different values of J_{AFM} : (a) $J_{\text{AFM}} = 4.4 \times 10^{-4} \text{ Jm}^{-2}$, (b) $J_{\text{AFM}} = 1 \times 10^{-5} \text{ Jm}^{-2}$, and (c) $J_{\text{AFM}} = 1 \times 10^{-6} \text{ Jm}^{-2}$. The ground-state phases converge at the triple point D_c in the $D - K_{\text{eff}}$ phase diagram, indicated by a black star. Dark green, yellow, and bronze colors represent the uniform IP, uniform OOP, and helical ground-state phases in the rz plane, respectively, with r being any radial direction. The light green color depicts the region where AFM merons are stabilized in micromagnetic simulations. The phase diagrams in (b-c) illustrate a displacement of the triple point to the right. (d) Evolution of the separation between the two cores of different polarities of a bimeron and its energy terms; anisotropy energy (E_{ani}), and demagnetizing energy (E_{demag}) as a function of the interlayer exchange strength. The material parameters used in the simulations, including the volume contribution, are provided in Appendix B, Section B.5. Adapted from [1]

(yellow region) when $K > 0$ and, as the i DMI increases above D_c^{OOP} , a phase transition towards the helical state is induced, which is well-known in systems with PMA. The light green color depicts the region where AFM bimerons are stabilized as derived from micromagnetic simulations. The ground-state phases coalesce at the triple point (D_c) in the $D - K_{\text{eff}}$ phase diagram, marked with a black star,

which represents the critical **iDMI** required to stabilize homochiral **AFM** bimerons. The expression for (D_c) is derived from the condition $K_{\text{eff}} = 0$, resulting in the equation $D_c = \frac{4}{\pi} \sqrt{A \left[\frac{H_d^2}{J_{\text{AFM}} L^2} \right]}$. For a strongly **AFM**-coupled **SyAFM** (i.e, large J_{AFM}), in the vicinity of the **SRT** point, only a very small **iDMI** is needed to induce the phase transition from the uniform **IP** configuration to a helical phase (denoted by the green and bronze areas). The low D_c stems from the fact that the only contribution to the effective anisotropy at the **SRT** point comes from the interlayer magnetic dipolar field. We observe that the critical value D_c is proportional to $\frac{1}{\sqrt{J_{\text{AFM}}}}$, leading to an increase in D_c for weak **AFM** interlayer couplings, as shown in Fig. 4.16(b) with $1 \times 10^{-5} \text{ Jm}^{-2}$, and Fig. 4.16(c) with $1 \times 10^{-6} \text{ Jm}^{-2}$. Achieving a larger **iDMI** for an easy-plane system can be exceedingly challenging experimentally; consequently, systems with strong **AFM** interlayer coupling offer a more viable route for stabilizing bimerons.

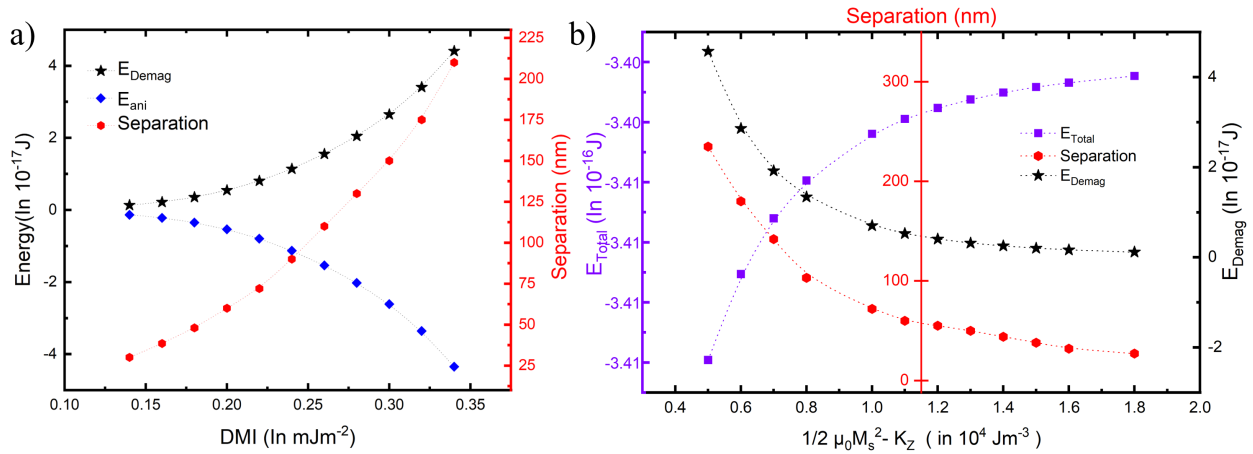


Figure 4.17: **Evolution of the separation between meron-antimeron and the energy terms, including total energy (E_{total}), demag energy (E_{demag}), and anisotropy (E_{ani}) energy as a function of (a) **iDMI**, and (b) effective anisotropy ($|K_{\text{eff}}|$).**

Further, we perform micromagnetic simulation to understand the influence of the different magnetic parameters on the antiferromagnetic bimeron properties in a **SyAFM** using MuMax³. The effect of **iDMI**, effective anisotropy, and the strength of interlayer exchange between the separation of the meron and antimeron spin textures present in a bimeron is discussed in detail. In Fig. 4.16(d), the red stars represent the separation between the cores of opposite polarities of the meron and antimeron within a bimeron. These simulations are performed for $D = 0.16 \text{ mJm}^{-2}$ and $K_{\text{eff}} = -0.08 \text{ MJm}^{-3}$ for a fully compensated **SyAFM**. As the interlayer exchange strength increases, the system's anisotropy energy (E_{ani}) decreases, as shown by the black triangular points. Consequently, this destabilizes the **OOP** magnetization within the bimeron, leading to smaller bimeron sizes and shorter separations

between the cores. Additionally, this change causes a decrease in the stray field and demagnetization energy (E_{demag}) of the bimeron. The influence of the **iDMI** on the separation between the two meron spin textures in a bimeron is examined in Fig. 4.17(a). By varying the **iDMI** from (0.14 – 0.34) mJm^{-2} at $K_{\text{eff}} = 0.1 \text{ MJm}^{-3}$ and keeping other parameters constant, our simulation results show that the separation between the meron and antimeron steadily increases with **iDMI** until the system achieves perpendicular magnetization. Increasing the **iDMI** enhances the out-of-plane spin components, which raises the demagnetization energy (E_{demag}) and reduces the anisotropy energy (E_{Aniso}). It should be noted that the **iDMI** and perpendicular magnetic anisotropy cooperate to stabilize the bimeron near the **SRT** region, unlike a skyrmion. To investigate the separation between the core polarities of the meron and antimeron in a bimeron, we varied the effective anisotropy ($|K_{\text{eff}}|$) in the range of $(0.5 - 1.8) \times 10^4 \text{ Jm}^{-3}$ for $D = 0.25 \text{ mJm}^{-2}$, as presented in Fig. 4.17(b). Increasing $|K_{\text{eff}}|$ results in a decrease in the separation between the meron and antimeron, accompanied by an increase in the total energy (E_{total}) and a decrease in the demagnetization energy (E_{demag}). This behavior can be attributed to the perpendicular magnetic anisotropy, which favors the stabilization of out-of-plane magnetization and results in a larger separation between the meron and antimeron.

4.8 Conclusion

In conclusion, in this chapter, we have demonstrated the presence of chiral merons, antimerons, and topologically stabilized bimerons in synthetic antiferromagnets at zero magnetic fields. The direction of the net magnetization and the emergent field created by topology in bimerons are mutually orthogonal [43], a key difference to their **OOP** counterparts, skyrmions. Thus, meron spin textures offer an approach to directly explore and tune the topological Hall physics. The Hall signal from bimerons will be directly sensitive to the topology, enabling the electrical readout of the topological winding number and leading to new possibilities for designing magnetic-topology-based technology, where the topology encodes the information. Our findings show that these **AFM** textures can be detected with accurate helicity and topological charge through a multimodal combination of surface-sensitive **SEMPA** imaging and **MFM** imaging. The fully compensated synthetic antiferromagnets host homochiral Néel bimerons that are stable at room temperature. Furthermore, the spin textures are found to cluster, implying potential energetic interactions among multiple neighbours. This observation raises the intriguing prospect of intricate interactions beyond next-nearest neighbours in these systems, including potential meron–antimeron lattices that can be envisaged to be nucleated by current or optical pulses. Such complexities could significantly impact the behaviour and stability of these antiferromagnetic spin textures, warranting further investigation into the underlying mechanisms. Some of the open questions related to this chapter are discussed in Section B.6 of Appendix

B. As discussed in Chapter 2, Section 2.5.3, deterministic current-driven motion in spintronic devices requires chiral spin textures. The DL-SOT efficiently propels Néel DWs and Néel skyrmions, with the propagation direction fixed by the chirality of the spin textures, whereas Bloch-type configurations are driven inefficiently or orthogonally. Here we demonstrate the presence of homochiral Néel bimerons in SyAFM. Consequently, bimerons in SyAFM gain a key advantage over previously reported AFM bimerons [50, 53] (where both Néel and Bloch merons coexist), which makes them amenable to controlled manipulation using SOTs and, in turn, opens up new possibilities for designing spintronic devices in SyAFMs.

Stabilization, Nucleation and Dynamics of Antiferromagnetic Skyrmions*

Somewhere, something incredible is waiting to be known.

Carl Sagan

5.1 Introduction

A critical challenge in realizing dense skyrmion-based devices is understanding the skyrmion-skyrmion interaction potential [178], which governs the minimum spacing and collective dynamics of skyrmions under external excitation. In most ferromagnetic systems, the interaction is short-ranged and repulsive [238], with its strength and range determined by tunable material parameters such as the **DMI** [65, 66], **PMA**, and dipolar interactions. At high densities, skyrmions form a lattice that exhibits collective behavior, such as deformation, relaxation, and emergent transport signatures, including the topological Hall effect, when driven by external stimuli. These dynamic processes are inherently transient and remain inaccessible to conventional quasi-static imaging techniques. Time-resolved microscopy has provided valuable insight into nanosecond-scale dynamical processes in ferromagnetic skyrmions, including nucleation, annihilation [239], current-driven motion [33], chaotic behavior [240], and inter-skyrmion interactions [241]. Despite these advances, a comprehensive quantitative under-

*Part of the chapter is adapted from: Bhukta, M., et al. Antiferromagnetic Skyrmion Scattering Revealed by Direct Time-Resolved Imaging of Collective Dynamics. <https://arxiv.org/abs/2508.17967>.

standing of their spatiotemporal interactions under external excitation is still lacking. In particular, the effective interaction potential governing skyrmion motion on nanometer and nanosecond scales remains experimentally unresolved.

As discussed in Chapter 2 Section 2.5.5, topological spin textures in an AFM, characterized by their net-zero topological charge, offer a compelling alternative in overcoming the intrinsic limitations of their ferromagnetic counterparts [70–72]. While thermally activated diffusive motion of skyrmions in amorphous bilayer SyAFMs [233] offers a pathway for unconventional computing architectures based on the Brownian dynamics of skyrmions [41, 42], the realization of deterministic spintronic devices [39, 40] demands robust thermal stability, coherent dynamics, and precise control over skyrmion trajectories. For such operations, isolated skyrmions in multilayer SyAFMs provide enhanced thermal stability and substantial suppression of SkHE, particularly near full compensation [4, 134]. Nevertheless, a skyrmion lattice in fully compensated systems has never been experimentally realized, despite its unique potential to simultaneously probe skyrmion–skyrmion interactions and suppression of the SkHE. Such a system would also enable the observation of emergent topological transport phenomena, including the topological spin Hall [242] and topological orbital Hall effects [243]. Yet, accessing the collective dynamics of AFM skyrmion lattices under external stimuli remains a fundamental challenge, as quasi-static imaging fails to capture transient deformation, relaxation processes, and mutual interactions. Time-resolved imaging is therefore essential to resolve these collective dynamics that govern the behavior of AFM skyrmion lattices.

This chapter explores isolated skyrmions and skyrmion lattices stabilized in synthetic antiferromagnetic multilayers. These spin textures, referred to as "AFM skyrmions," extend coherently through the multilayer stack, forming antiferromagnetically coupled skyrmion tubes. AFM skyrmion nucleation was realized through three distinct mechanisms: magnetic field application, bipolar current injection, and ultrafast laser excitation, each designed to overcome the intrinsic nucleation energy barrier [244] and drive the system into a topologically non-trivial state. Later, pump–probe X-ray microscopy with high spatiotemporal resolution (20 nm spatial and 1 ns temporal) was employed to resolve the real-space trajectories and dynamic behavior of an AFM skyrmion lattice in a SyAFM confined within a magnetic nanotrack. By leveraging the element-specific contrast of X-ray imaging, both magnetic sublattices of the AFM skyrmions were dynamically probed, enabling direct observation of skyrmion–skyrmion interactions in real space and in real time. When the applied SOT was comparable to the local pinning potential, the motion of the AFM skyrmion lattice was governed by a spatially inhomogeneous energy landscape, where variations in pinning strength produced an incoherent dynamical regime with coexisting mobile and pinned skyrmions. Upon removal of the drive, recoil of mobile skyrmions after scattering from pinned neighbours was observed, with the relaxation

governed by restoring forces arising from skyrmion–skyrmion repulsion. The skyrmions exhibited an exponential slowdown during their motion, with characteristic timescales of 3–20 ns, during which the potential landscape of surrounding skyrmions was probed, thereby providing a direct measure of the spatial range and temporal scale of the repulsive interaction. An inverse estimation method based on the Thiele equation [245, 246] was simultaneously applied to all measured relaxation trajectories, allowing the skyrmion interaction potential to be quantitatively mapped continuously from a compressed state into a relaxed state, revealing an exponential decay as well as the fundamental length scale of the interaction. The skyrmion–skyrmion interaction potential is quantitatively extracted by analyzing the experimentally observed trajectories and comparing them with micromagnetic simulations by *Kilian Leutner*. At higher current densities, where the excitation surpassed the local pinning potential, a near-flat energy landscape was dynamically approached, facilitating a transition into a viscous flow regime. In this regime, cancellation of opposing gyrotropic forces from the two sublattices was achieved owing to the compensated angular momentum of the SyAFM configuration. As a result, suppression of the skyrmion Hall effect was demonstrated by time-resolved imaging of uniform, unidirectional lattice translation without detectable internal deformations or relaxation. Details of the author contributions are provided in Appendix A. The experimental details, including sample structure and characterization for this chapter, can be found in eLab logbook (📖 labbook experiment ID 19296).

5.2 Engineering of the SyAFM Stacks to Stabilize AFM Skyrmions

In thin films having perpendicular magnetic anisotropy and iDMI, the stabilization of skyrmions is governed by the delicate interplay of competing magnetic interactions, as discussed in Chapter 2 section 2.4.1. In such systems, a positive DW energy $\epsilon_{\text{Néel}}$ supports a uniform magnetic ground state; however, under suitable conditions, skyrmions can still be stabilized as metastable excitations even in the absence of an external magnetic field [121, 176]. A negative DW energy signifies a fundamental instability in the uniform magnetic state, leading to the spontaneous formation of spin textures such as skyrmions, merons, or labyrinth domains. The key distinction in stabilizing (bi)merons versus skyrmions lies in the sign of the effective anisotropy [1, 51]. Such spin textures emerge when the reduction in domain wall energy driven by interfacial DMI outweighs the stabilizing contributions from exchange and anisotropy [1]. Beyond these short-range interactions, long-range dipolar interactions play a crucial role in the stability and formation of magnetic textures. This influence becomes especially significant in multilayer systems where the total magnetic layer thickness exceeds the characteristic length scale l_w defined by $l_w = \epsilon_{\text{Néel}}/\mu_0 M_s^2$ [132, 247]. Under such conditions, the system tends to minimize magnetostatic energy by forming flux-closure configurations, leading to a

demagnetized ground state and enabling the spontaneous emergence of non-uniform spin textures.

Near the **SRT**, where the effective anisotropy $K_{\text{eff}} \approx 0$, the **DW** energy $\epsilon_{\text{Néel}} = 4\sqrt{AK_{\text{eff}}} - \pi D$ can become negative, destabilizing the homogeneous state and promoting the emergence of chiral textures without the need for external stimuli. This regime is particularly advantageous for experimental studies, as the spontaneous appearance of topological textures provides favorable initial conditions for skyrmion stabilization. Subsequently, the application of an out-of-plane magnetic field tunes the energy landscape by penalizing antiparallel domain areas, selectively stabilizing skyrmions within a small finite field window. To stabilize **AFM** skyrmions in **SyAFM**, we adopt this approach by initially preparing the system in a multi-domain state close to **SRT**, which is realized by tuning the ferromagnetic layer thickness to balance interfacial anisotropy and demagnetization energy. This thickness control simultaneously adjusts the magnetic compensation, thereby governing the coupling to an external magnetic field. In partially compensated systems, this enables skyrmion nucleation upon applying a finite out-of-plane field along the z-direction. Note that this method is effective only for uncompensated **SyAFM** systems, whereas fully compensated **SyAFMs** remain insensitive to external magnetic fields. Following this, we fabricate a multilayer stack similar to the design used for (bi)meron stacks illustrated in Fig. 4.4(a) (Chapter 4), which ensures a finite **iDMI**. The selection of **FM** sublattices in this configuration deviates from earlier designs. In this multilayer, we use **CB** as the **B** sublattice and a bilayer combination of **CFB** and **FCB** as the **A** sublattice. This approach leverages the element-specific contrast of X-ray microscopy to detect the individual magnetic contributions from the **A** and **B** sublattices. Tuning the photon energy to the L_3 absorption edges of Fe and Co enables sublattice-specific probing of the antiferromagnetic systems, allowing independent visualization of the **A** and **B** sublattices. This facilitates sublattice-resolved imaging of skyrmions.

In **SyAFMs**, this interplay is further enriched by the ability to finely tune the magnetic compensation through controlled variation of the thickness and composition of the **FM** sublattices. We define the magnetic compensation as

$$m_c(\%) = 1 - \frac{|M_{s,A} \cdot t_A - M_{s,B} \cdot t_B|}{M_{s,A} \cdot t_A + M_{s,B} \cdot t_B} \quad (5.1)$$

where $M_{s,A}$ and $M_{s,B}$ denote the saturation magnetizations of the individual **FM** sublattices **A** and **B**, respectively, and t_A and t_B are their corresponding thicknesses. A value of $m_c = 100\%$ corresponds to a fully compensated antiferromagnetic state, whereas $m_c = 0\%$ indicates a ferromagnetic configuration. By adjusting the compensation between the magnetic layers, one can effectively tune the influence of long-range dipolar interactions and thereby stabilize skyrmions with distinct static and dynamic properties [4]. Specifically, the uncompensated moment modulates the gyroforce (pro-

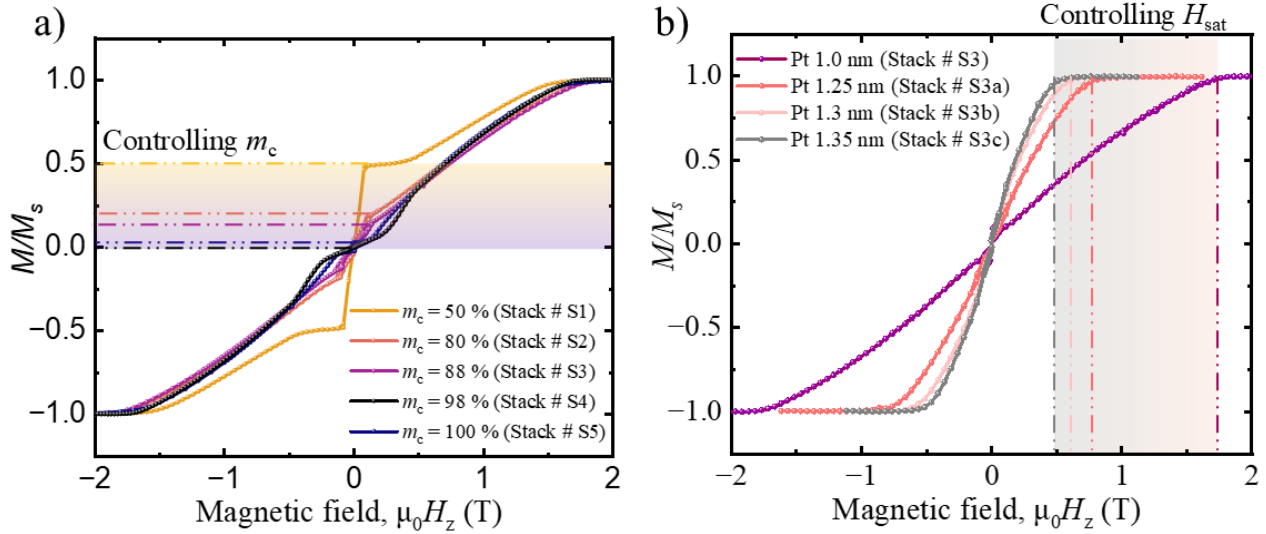


Figure 5.1: **Tuning magnetic compensation and interlayer exchange strength in SyAFM stacks.** (a) OOP hysteresis loops measured via SQUID magnetometry for Stacks #S1–#S5, demonstrating systematic control of magnetic compensation (m_c) through layer thickness engineering. (b) Hysteresis loops for Stacks #S3–#S3c, where the Pt spacer thickness is varied to modulate the interlayer exchange coupling and consequently the saturation field (H_{sat}).

portional to $4\pi(M_{s,A}t_A - M_{s,B}t_B)$ experienced by skyrmions, thereby influencing the skyrmion Hall angle under current-driven motion. To systematically investigate the influence of magnetic compensation, SyAFM stacks with varying net moments have been engineered. Fig. 5.1(a) shows the magnetic hysteresis loops measured using SQUID magnetometry for these stacks #S1–#S5. The projection of $\frac{M}{M_s}$ along the field axis reflects the stack’s net uncompensated moment. Although saturation magnetization measurements using SQUID carry an estimated uncertainty of $\sim 10\%$ due to the precision required for sample volume determination, the relative differences in uncompensated moments remain highly reliable. This is because the analysis does not depend on the absolute magnetic moment of individual layers, but rather on their difference, thereby circumventing the need for precise area measurements and leveraging the intrinsic sensitivity of SQUID magnetometry. For instance, as illustrated for stacks #S4 and #S5, a compensation difference as small as 2% can be resolved. Note that for each stack, we keep the effective anisotropy close to the SRT, as indicated by a zero remanence in the hysteresis loops. The schematic together with the structural and compositional details of these stacks are presented in Appendix C. In the current chapter, stacks #S3–#S3c are investigated to study the nucleation and stability of the antiferromagnetic skyrmions. The fully compensated SyAFM, stack #S5, is employed for time-resolved studies of nanosecond skyrmion dynamics. Control over the AFM interlayer exchange coupling provides a means to tune skyrmion

stability in SyAFM systems. To explore this, an additional series of SyAFM stacks (stacks #S3a–#S3c) is deposited by systematically varying the Pt spacer layer thickness (See 5.1(b)). These stacks host novel hybrid spin textures, termed "skymérons", which are characterized by a 90° alignment between the magnetization vectors of the two ferromagnetic sublattices, as described in detail in Chapter 7. The samples were deposited by *M-A. Syskaki*.

5.3 Nucleation of AFM Skyrmions

The implementation of skyrmions as active elements in spintronic systems requires that their creation and dynamics are both energetically controlled and structurally stable. In the context of metastable isolated skyrmions, nucleation must proceed through a deterministic pathway in phase space, yielding well-defined topological configurations over the uniformly magnetized state without stochastic fluctuations. Magnetic multilayers inherently host a variety of stable magnetic configurations at room temperature. In such thin-film structures, skyrmions generally appear as metastable spin textures. Their stabilization arises primarily from iDMI, which induces chiral canting between neighboring spins. However, the iDMI does not strongly discriminate between circular domain walls, as found in skyrmions, and extended linear walls, as in stripe domains. As a result, these systems often exhibit a near-degenerate energy landscape where skyrmions form a local minimum that can coexist with, or are superseded by, stripes or labyrinth domains. For stability, the skyrmion minimum must be separated from competing metastable states by an energy barrier $\Delta E_{\text{skyrmion}}$ exceeding the thermal energy $k_B T$ under operating conditions. At ambient conditions, skyrmions do not spontaneously nucleate under equilibrium conditions in these stacks and must be generated via external stimuli to overcome the energy barrier associated with their nucleation [244]. This energetic separation suppresses spontaneous transformations into alternative configurations, thereby ensuring that the skyrmion profile corresponds to a well-defined solution of the micromagnetic energy functional. Note that the solitonic nature of skyrmions during their motion does not arise solely from their nontrivial topology, since topological charge conservation permits continuous deformation into other textures, such as worm-like or stripe domains. Rather, it results from a substantial energetic gap between the skyrmion configuration and competing metastable states. In practical terms, this energy difference must exceed both the thermal energy and the additional energy injected by current pulses during skyrmion motion. When this condition is satisfied, skyrmions retain their equilibrium profile during translation, allowing the dynamics to be treated within the rigid-core approximation. While this metastability presents a challenge for spontaneous formation, it offers a distinct functional advantage: skyrmions can be deterministically written and deleted without uncontrolled proliferation, and with sufficient stability to persist over operational timescales. A variety of external stimuli have been employed

for skyrmion nucleation, including out-of-plane magnetic field pulses [33], spin-orbit torque-driven current pulses [31, 176, 248], and ultra-fast laser excitation [244, 249, 250]. The purpose of this section is to establish reliable methods for skyrmion nucleation, which can serve as well-defined initial states for subsequent studies of skyrmion dynamics. Here, we employ three distinct approaches: (1) application of out-of-plane magnetic field cycles, (2) current-induced skyrmion nucleation, and (3) laser-induced skyrmion nucleation.

5.3.1 Magnetic-Field-Induced AFM Skyrmion Nucleation

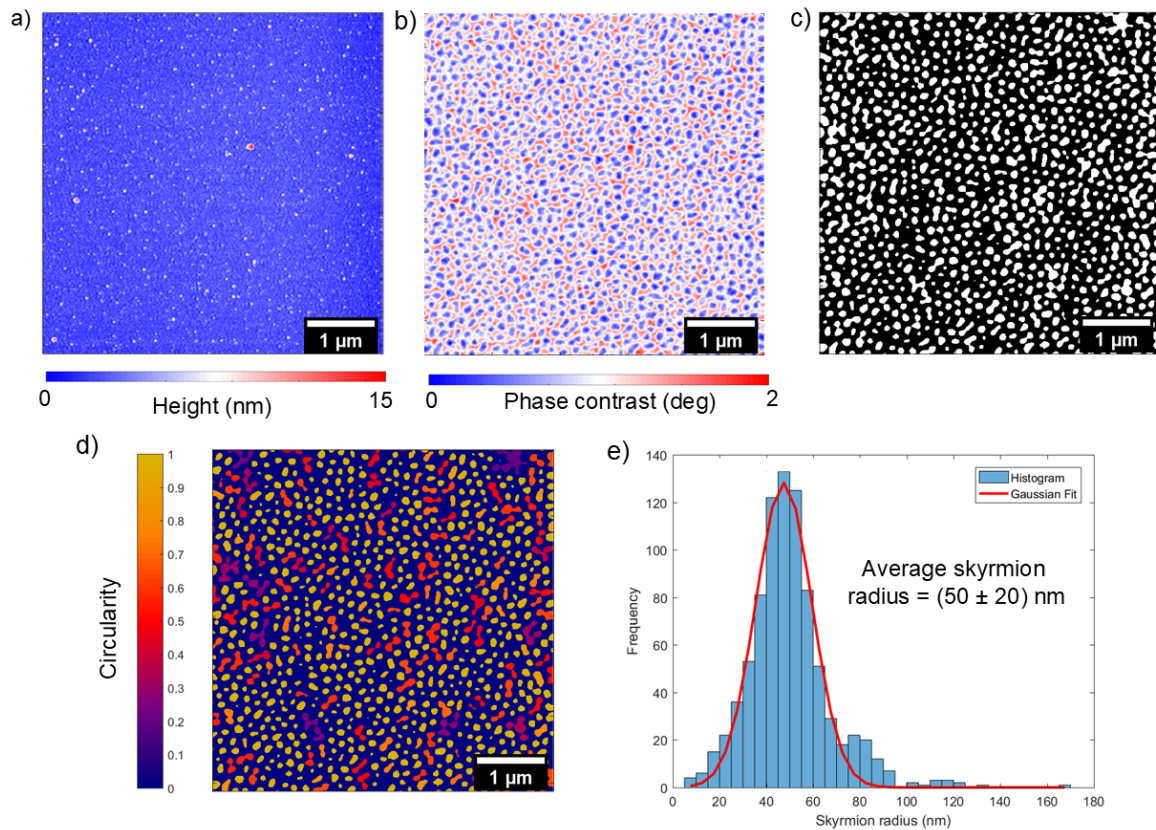


Figure 5.2: **AFM skyrmions observed using MFM.** AFM skyrmions are nucleated via annealing at 170 °C for 15 minutes in zero magnetic field in a fully compensated SyAFM stack. **(a)** AFM topography image confirming uniform surface morphology. **(b)** MFM phase image showing a dense lattice of skyrmions. **(c)** Binarized MFM image used to analyze individual skyrmions. **(d)** Skyrmion circularity map based on $C = 4\pi A/P^2$, where A and P are the area and perimeter of each skyrmion. **(e)** Histogram of skyrmion radii extracted from the MFM image shown in (b), yielding an average skyrmion radius of (50 ± 20) nm.

At remanence, SyAFM multilayer systems typically relax into domain configurations that are strongly

influenced by the magnetic preconditioning of the sample. Depending on the specific demagnetization procedure, these domains can form in random orientations or exhibit varying degrees of directional coherence. A widely adopted technique for generating such non-uniform magnetic states involves applying an alternating magnetic field with gradually decreasing amplitude, starting from above the saturation field and tapering to zero. By systematically adjusting the field amplitude, frequency, and orientation, a wide range of remanent domain configurations can be engineered. Alternatively, in-plane demagnetization tends to align domains preferentially along the applied field direction. These demagnetized states provide well-defined initial conditions for subsequent manipulation of spin textures. In this study, prior to AFM skyrmion nucleation, an OOP demagnetization protocol was applied to the sample, resulting in a labyrinth multidomain state that served as the magnetic ground state for further experiments. The most straightforward method to nucleate AFM skyrmions is via the application of an OOP magnetic field. In fully compensated SyAFM systems, the absence of net magnetization suppresses the Zeeman contribution, rendering field-induced skyrmion nucleation energetically unfavorable. Consequently, the transformation from a multidomain background into an AFM skyrmion lattice requires overcoming a finite energy barrier. A minimal perturbation capable of supplying this energy is thermal activation. Annealing the sample at 170 °C for 15 minutes in zero magnetic field initiates a spontaneous reconfiguration of the labyrinth domain state into a dense array of topologically non-trivial spin textures. This observation indicates that the skyrmion lattice constitutes a robust metastable state.

Fig. 5.2 shows the outcome of this thermal protocol in a synthetic antiferromagnetic multi-layer stack structurally analogous to stack #S5, with a Pt spacer thickness of 1.3 nm (stack #S5a). Panel (a) presents the atomic force microscopy topography image, confirming the absence of morphological inhomogeneities. The corresponding MFM phase image in panel (b) reveals a uniform lattice of skyrmions. The image is binarized using Otsu's algorithm (panel (c)), followed by contour extraction and circularity analysis based on the metric $C = 4\pi A/P^2$, where A and P denote the area and perimeter, respectively (panel (d)). The resulting map confirms the high geometric symmetry of the nucleated textures. From the binarized skyrmion area, the effective skyrmion radius is determined, and the statistical distribution is presented in panel (e). The histogram of radii is fitted with a Gaussian profile, yielding an average skyrmion radius of (50 ± 20) nm. These observations establish thermal annealing as an effective route to deterministically generate compensated Néel-type skyrmions in SyAFM systems, without requiring external magnetic or electrical stimuli.

In uncompensated SyAFM, the application of an out-of-plane magnetic field couples to the system via the Zeeman interaction, energetically favoring domains whose magnetization aligns with the field direction. This leads to a reduction of opposing (antiparallel) domains and can, under ap-

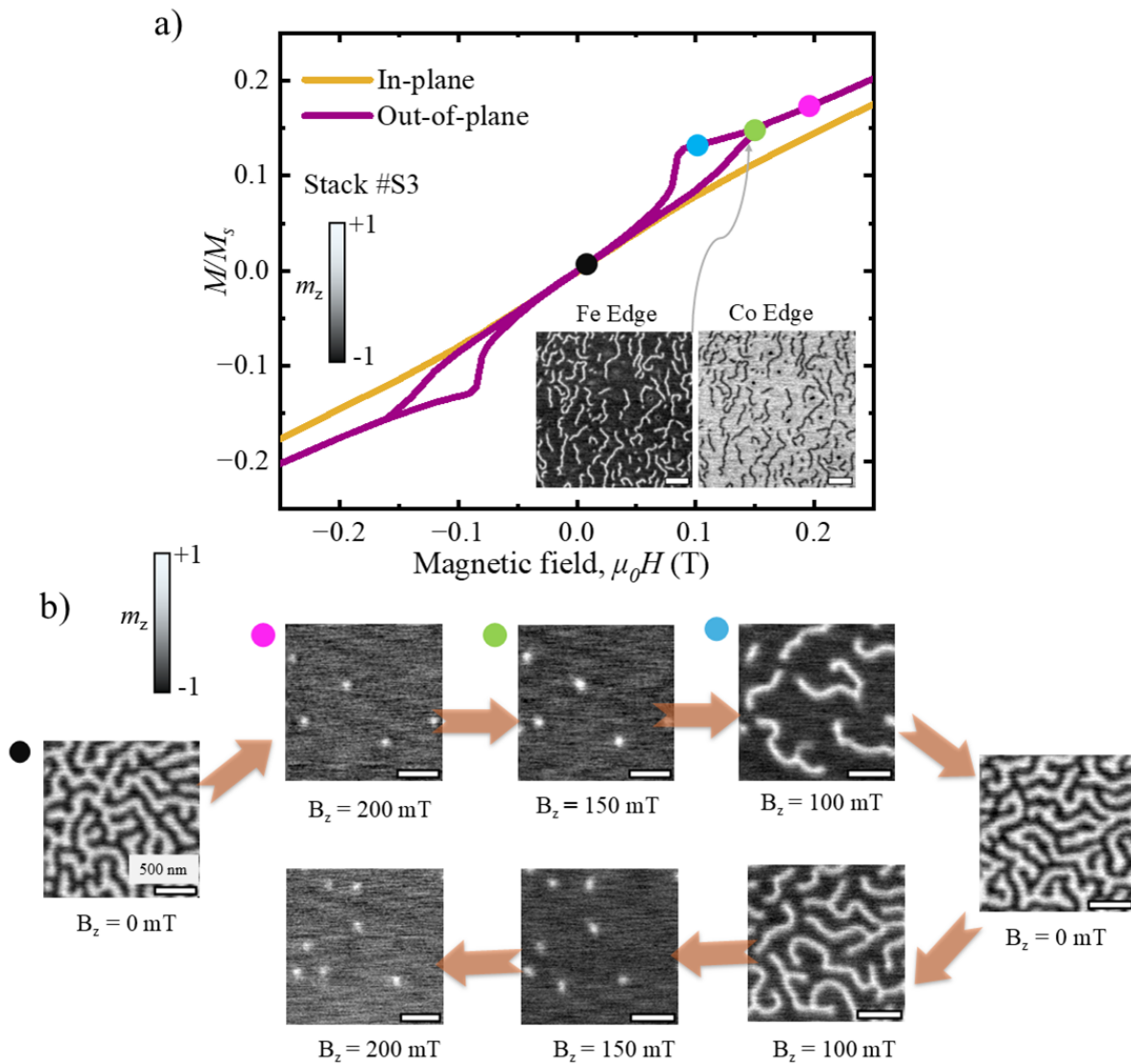


Figure 5.3: **Magnetic-field-induced AFM skyrmion nucleation.** **(a)** Zoomed-in view of hysteresis loops measured via SQUID magnetometry for stack #S3. Insets in (a) display STXM images acquired at the Fe and Co L_3 edges, revealing domain textures with opposite contrast and confirming the antiparallel alignment of sublattices A and B. **(b)** Field-driven nucleation of AFM skyrmions in stack #S3, imaged using STXM at the Fe L_3 edge. Starting from a worm-like multidomain state at $B_z = 0$ mT, skyrmions are nucleated upon application of a 200 mT out-of-plane magnetic field. As the field is decreased from 200 mT to 100 mT, skyrmions increase in size and eventually extend into stripe domains. The multidomain state is recovered at 0 mT, and skyrmions are re-nucleated upon reapplication of 150 mT.

appropriate conditions, drive the collapse of stripe or labyrinth textures into isolated skyrmions. To experimentally explore the field-induced stability window of AFM skyrmions, we focused on stack #S3, which is engineered to reside near the SRT, has 88% magnetic compensation, and exhibits strong antiferromagnetic interlayer coupling. This slight imbalance in sublattice moments introduces a finite net magnetization, allowing the external field to couple weakly but effectively with the system. Fig. 5.3(a) shows the zoomed-in in-plane and out-of-plane magnetization hysteresis loops acquired via SQUID magnetometry. The opening of the OOP hysteresis loop generally corresponds to the skyrmion pocket region, where skyrmions exist as metastable solutions. Insets in Fig. 5.3(a) display STXM images acquired at the Fe and Co L_3 edges, revealing domain textures with opposite contrast, directly confirming the antiparallel alignment of sublattices A and B.

When an out-of-plane magnetic field of 200 mT is applied, the Zeeman interaction energetically favors domains with magnetization aligned along the field direction. To investigate the reversibility and tunability of this process, we applied a sequence of out-of-plane magnetic fields and recorded the resulting magnetic states using element-resolved STXM (Fig. 5.3(b)). Starting from a zero-field multidomain configuration (black dot), increasing B_z to 200 mT produces discrete AFM skyrmions. As the field is gradually reduced to 150 mT and 100 mT, the skyrmions increase in diameter and begin to diverge into elongated, worm-like domains. Upon returning to zero field, the system reverts to its original labyrinth domain configuration, indicating that skyrmions are not the energetically favorable ground state under these conditions. Their existence is sustained only in the applied field, and once the field is removed, they expand as the system relaxes toward a lower-energy multi-domain state. However, the skyrmions formed in this process are primarily governed by the local energy landscape and are often pinned due to defect-related energy barriers. To address this limitation, two additional nucleation methods were employed in this study to achieve isolated AFM skyrmions with better spatial control, i.e., current-induced nucleation and laser-induced skyrmion nucleation.

5.3.2 Current-Induced Nucleation of AFM Skyrmions

Electrically driven nucleation offers a practical and scalable method for generating skyrmions in nanoscale devices. In heavy-metal/ferromagnet multilayers, the application of a high current density leads to skyrmion formation through a combination of SOTs [131, 239, 251] and transient Joule heating [180, 252]. The spin Hall effect in the heavy-metal layer injects a transverse spin current into the ferromagnet, producing damping-like and field-like torques that drive the local magnetization toward the film plane. When applied near pinning sites or engineered defects such as constrictions, these torques, in combination with the iDMI, initiate the formation of reversed domains. The skyrmion topology emerges as the domain wall relaxes and vertical Bloch lines are expelled, completing the

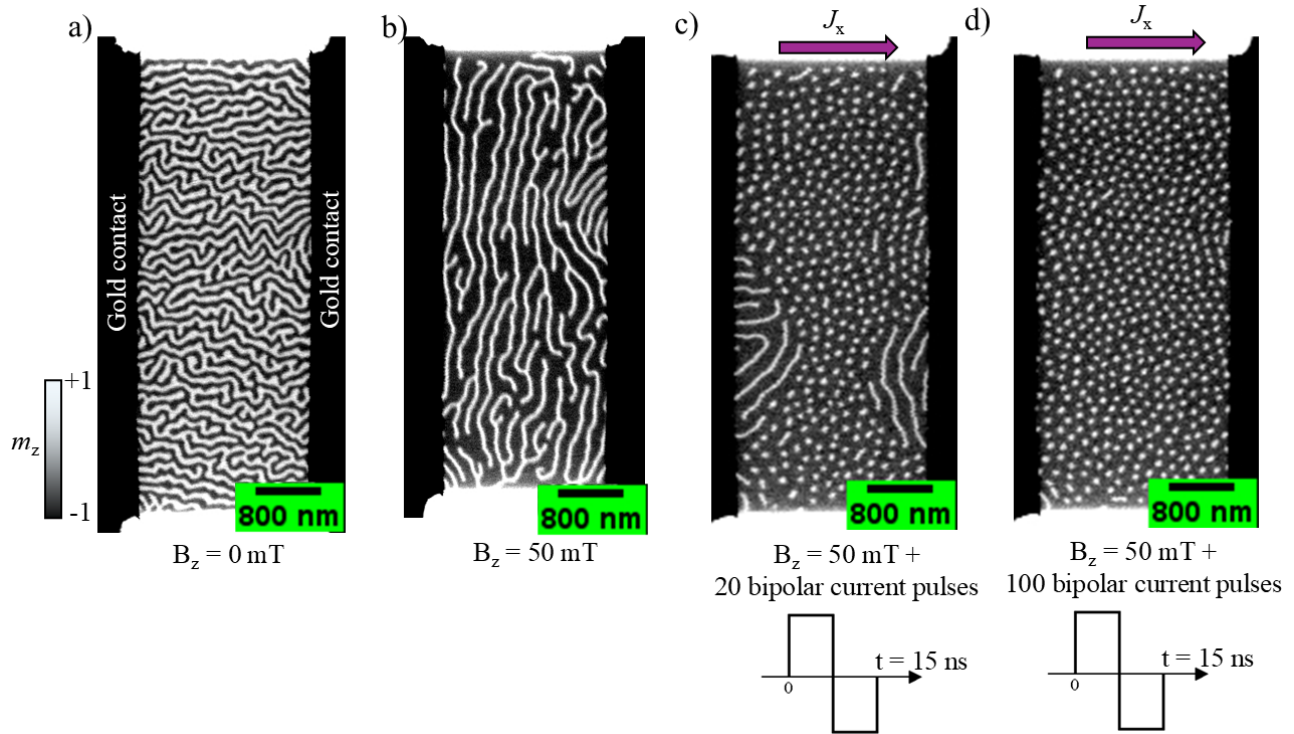


Figure 5.4: **Current-induced AFM skyrmion nucleation driven by transient Joule heating.** All STXM images were acquired at the Fe L_3 absorption edge. **(a)** At zero magnetic field, the system exhibits a disordered labyrinth domain configuration. **(b)** Application of a static out-of-plane magnetic field ($B = 50$ mT) reduces the density of domains in sublattice A. **(c)** Injection of 20 bipolar current pulses (7.5 ns duration) at $B = 50$ mT initiates AFM skyrmion nucleation. **(d)** Application of 100 bipolar pulses results in the formation of a dense and uniform skyrmion lattice across the racetrack.

transformation into a stable skyrmion [253]. In parallel, Joule heating from the current pulse elevates the local temperature, reducing the effective magnetic anisotropy and assisting the nucleation process. This thermal contribution facilitates morphological transitions from stripe domains to isolated skyrmions [248]. Notably, skyrmion nucleation driven primarily by Joule heating does not rely on defects or geometric constrictions and enables spatially uniform skyrmion generation.

To enable reproducible skyrmion generation for current-driven dynamics studies, we employed a thermally driven nucleation scheme based on current-pulse injection in patterned racetrack devices. The SyAFM film stack #S3b was fabricated into nanowire geometries with integrated gold contacts, allowing for precise delivery of high-density current pulses. In the absence of an external magnetic field, the system stabilizes in a disordered labyrinth domain configuration (see L_3 Fe edge image in Fig. 5.4(a)). Upon application of a moderate out-of-plane bias field ($B = 50$ mT),

the average domain size is reduced as expected. The apparent elongation and partial alignment of the stripe domains (Fig. 5.4(b)) is not a direct consequence of the applied out-of-plane field, but rather arises from a small residual in-plane field of approximately 3–5 mT originating from the quadrupole magnet during the measurements. Injection of 20 bipolar current pulses (7.5 ns duration, $j \approx 2 \times 10^{12}$ A/m², frequency of 33.3 MHz) initiates the fragmentation of stripe domains into shorter segments (Fig. 5.4(c)). With continued pulsing (up to 100 pulses), these segments evolve into circular domains that relax into isolated Néel-type skyrmions, resulting in a dense and spatially uniform skyrmion lattice (Fig. 5.4(d)). This method has been pioneered for ferromagnetic skyrmions in refs [31, 248]. The underlying mechanism is governed by transient Joule heating, which locally elevates the temperature during each pulse and reduces the effective perpendicular magnetic anisotropy K_{eff} , thereby lowering the energy barrier between stripe and skyrmion states. As shown by Lemesh *et al.* [248], this thermal activation plays the dominant role in current-induced skyrmion nucleation, even in the presence of spin-orbit torques. The *iDMI* ensures that the resulting skyrmions adopt a well-defined chirality, which minimizes domain wall energy and stabilizes the topology once formed. To suppress domain displacement during pulse injection, bipolar current pulses were employed, effectively canceling the net *SOT* over each cycle and preventing directional motion of pre-existing textures. This ensures that the nucleation process arises from localized thermal fluctuations rather than torque-induced translation.

This thermally assisted, deterministic method for skyrmion nucleation does not require pre-existing defects or lithographic constrictions, making it particularly effective for nucleating skyrmions even in fully compensated *SyAFMs* systems, where field cycling alone fails to induce nucleation. As shown in Fig. 5.5(a,b), a skyrmion lattice emerges in both sublattices A and B of stack #S5 after applying a series of bipolar current pulses as mentioned in the procedures before. Element-specific *STXM* imaging at the Fe and Co L_3 absorption edges reveals inverted contrast between the sublattices due to their antiferromagnetically coupled out-of-plane magnetization. Skyrmions in sublattice A carry a topological charge $Q_A = +1$, while those in sublattice B possess $Q_B = -1$, forming a compensated *AFM* skyrmion lattice as illustrated schematically in Fig. 5.5(c). This confirms strong *AFM* interlayer coupling throughout the multilayer stack. The magnetic field dependence of the skyrmion phase, depicted in Fig. 5.5(d), demonstrates its stability over a wide range of out-of-plane fields from –250 mT to +250 mT. The persistence of the lattice across the entire sweep highlights the robustness of the *AFM*-coupled skyrmion state against external perturbations. Overall, this Joule-heating-driven transition enables uniform and reproducible skyrmion nucleation across extended regions, offering a scalable and device-compatible pathway for initializing *AFM* skyrmions.

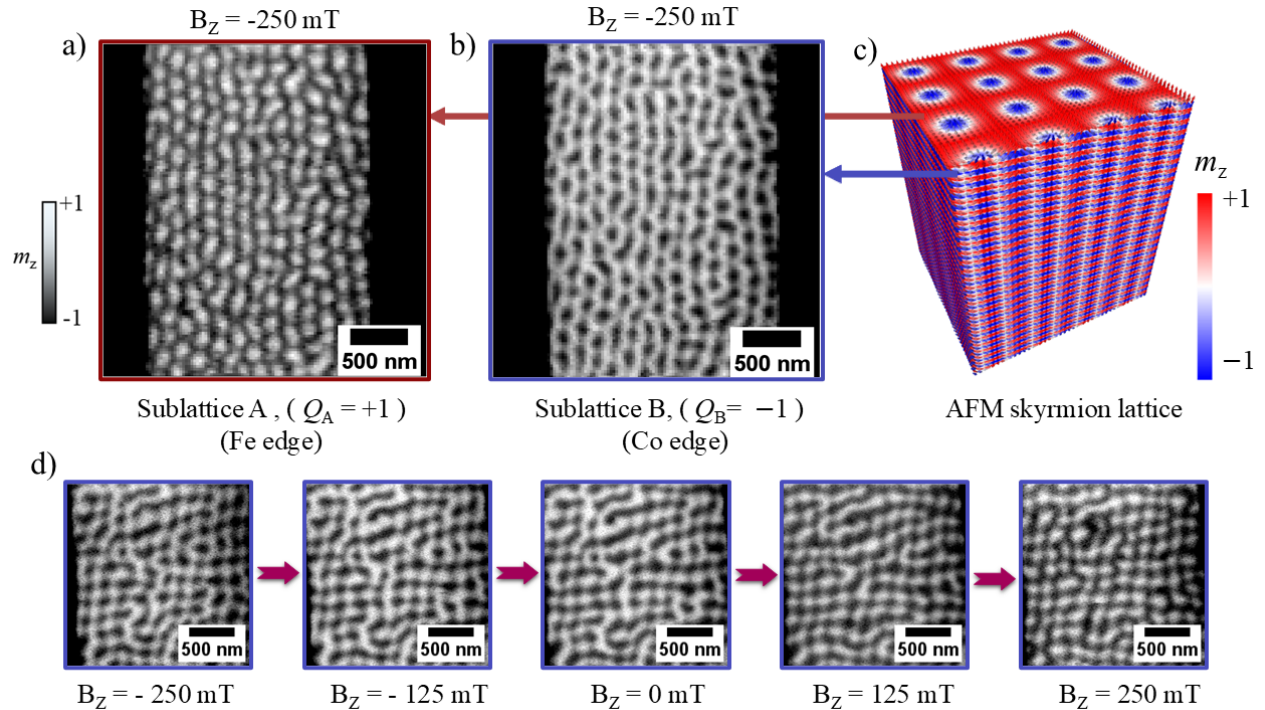


Figure 5.5: **AFM skyrmion lattice in a fully compensated SyAFM.** (a, b) Sublattice-resolved STXM images acquired at the Fe L_3 (a) and Co L_3 (b) absorption edges reveal the antiferromagnetically coupled skyrmion lattice in stack #S5. The inversion of magnetic contrast between the two sublattices confirms strong AFM interlayer coupling across the multilayer structure. (c) Schematic three-dimensional illustration of the AFM skyrmion lattice, showing alternating out-of-plane magnetization in sublattices A (red) and B (blue). (d) Magnetic field dependence of the AFM skyrmion lattice, demonstrating its stability over a wide range of out-of-plane fields from -250 mT to $+250$ mT. Adapted from [3].

5.3.3 Infra-red Laser-Induced Nucleation of AFM Skyrmions

Current-induced skyrmion nucleation, while experimentally robust, often demands relatively high current densities that exceed those required for skyrmion dynamics. This elevated energy demand increases power consumption and can introduce interference between writing and transport functions, posing challenges for scalable implementation. While current- and magnetic-field-induced mechanisms have been widely explored, ultrafast optical excitation has recently emerged as a powerful, non-contact alternative. Owing to its ability to deliver picosecond-scale thermal perturbations within diffraction-limited volumes, laser excitation provides access to transient, non-equilibrium magnetic states where topological transitions can be triggered in a highly localized and energy-efficient manner [254–256]. In ferromagnetic multilayers, femtosecond laser pulses have been successfully employed to

induce skyrmion formation via rapid heating and subsequent cooling, either from a uniform magnetization or labyrinth domain background. Je *et al.* [249] demonstrated the creation of skyrmion bubble lattices in ultrathin films with strong perpendicular magnetic anisotropy, while Büttner *et al.* [244] reported skyrmion nucleation through an intermediate topological fluctuation state on sub-nanosecond timescales. These results, supported by numerical simulations [257, 258], have established ultrafast laser excitation as a robust method for skyrmion writing in ferromagnetic systems. However, such laser-induced skyrmion nucleations have remained largely unexplored in SyAFMs [250].

To investigate the deterministic generation of AFM skyrmions via optical means, we employed ultrafast laser excitation using a single 1 ps, 1039 nm infra-red pulse with a Gaussian beam profile of radius 3.5 μm , incident at an angle of 30° with respect to the sample surface, installed at the MAXYMUS end-station (BESSY II) by Dr. Bastian Pfau [259]. † The SyAFM multilayer stack #S3 (see Fig. 5.6(a)), deposited on a SiN membrane, was initially prepared in a labyrinth multidomain state through an OOP demagnetization protocol and held under a moderate magnetic bias of $B_z = 110$ mT (Fig. 5.6(b)). This field alone does not favor spontaneous skyrmion nucleation. Upon laser irradiation, a rapid and localized temperature increase drives the system into a transient non-equilibrium regime, enabling topological reconfiguration during the subsequent cooling phase. Figs 5.6(c) and (e) present element-specific STXM images of the same laser-irradiated region, acquired at the Fe and Co L_3 edges, respectively. The emergence of circular domains within the irradiated area indicates successful skyrmion nucleation. The observed reversal of contrast between the Fe and Co edges confirms the antiferromagnetic coupling of the two sublattices, providing direct, real-space evidence for the formation of AFM skyrmions. The clear boundary between the nucleated skyrmions and surrounding stripe domains demonstrates both the spatial selectivity and localized nature of the optical excitation. A circularity map of the magnetic textures is shown in Fig. 5.6(d), confirming that near-circular features are concentrated within the laser-irradiated region, consistent with the localized formation of skyrmion tubes. The circularity parameter is defined as $C = 4\pi A/P^2$, where A and P denote the area and perimeter of the binarized contour, respectively. Its value ranges from 0 (fully elongated) to 1 (perfectly circular), supporting the identification of skyrmion textures within the irradiated region. Importantly, the nucleation process was found to be independent of laser polarization, indicating a thermally driven mechanism rather than one governed by magneto-optical selection rules.

†Due to the oblique incidence of the laser beam, the effective fluence at the sample surface is reduced by approximately a factor of three compared to the nominal fluence. Therefore, all fluence values reported correspond to the effective fluence at the sample. The calibration data points relating the applied laser current to the effective fluence are provided in Appendix C.

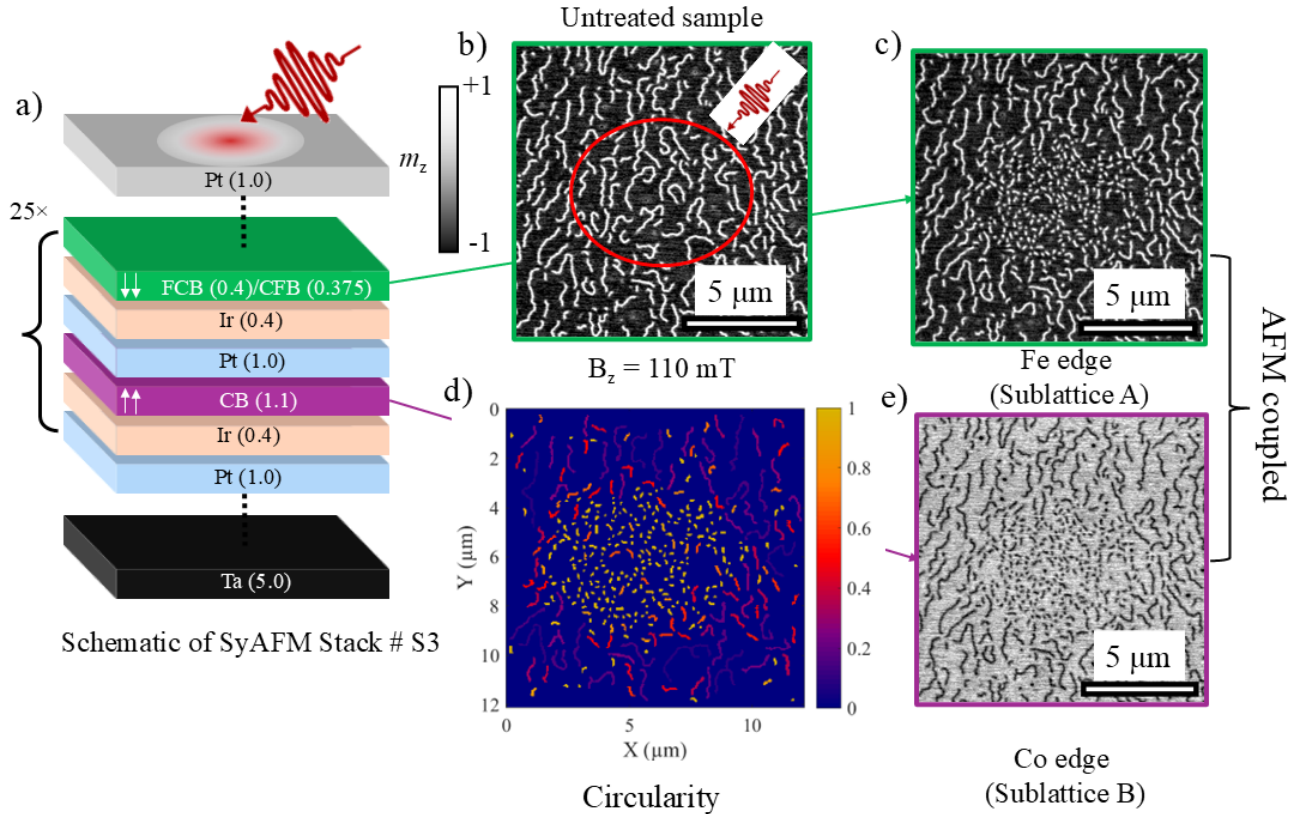


Figure 5.6: **Laser-induced nucleation of AFM skyrmions.** **(a)** Schematic of the SyAFM stack. **(b)** Magnetic domain configuration of the sample ($B_z = 110$ mT) prior to laser exposure. The red-circled region denotes the area subsequently irradiated by the laser pulse. **(c)** Image acquired at the Fe L_3 edge (sublattice A) after laser exposure. Isolated circular skyrmions appear within the laser-irradiated region, emerging from the initial labyrinth domain state. **(e)** Image at the Co L_3 edge (sublattice B), showing opposite magnetic contrast within the same region, confirming the antiparallel alignment of the skyrmions in the two sublattices. **(d)** Circularity map derived from (c), quantifying the geometric symmetry of the binarized contours using $C = 4\pi A/P^2$, where A and P denote the area and perimeter, respectively. High circularity values ($C \approx 1$, yellow) correspond to localized skyrmion textures within the irradiated region, while lower values (red) indicate elongated stripe domains outside.

Role of Magnetic Fields in Laser-Induced AFM Skyrmion Nucleation

While ultrafast laser excitation can provide the necessary thermal energy to overcome the topological energy barrier for skyrmion nucleation, the external magnetic field serves as a crucial symmetry-breaking parameter that biases the formation pathway toward specific topological outcomes. In fully compensated antiferromagnetic materials, the net magnetization ideally vanishes due to the

antiparallel alignment of magnetic sublattices, rendering them largely insensitive to external magnetic fields under static conditions. However, in uncompensated SyAFMs, such as the one studied here with 88 % sublattice compensation, a residual net moment remains. This slight imbalance introduces a finite Zeeman coupling to external magnetic fields, which, while small, can be significantly amplified during non-equilibrium processes such as laser-induced ultrafast heating. To gain deeper insight into the role of magnetic fields on laser-induced AFM skyrmion nucleation, a series of experiments are performed at constant laser fluence (16 mJ/cm^2), while varying the out-of-plane magnetic fields. In each cycle, the sample is first demagnetized into a labyrinth state, the laser pulse is applied at a selected magnetic field, and the resulting spin textures are imaged using STXM at the Fe L_3 edge. These procedures are repeated for magnetic fields ranging from $B_z = -130 \text{ mT}$ to 200 mT . The corresponding magnetic textures before and after laser exposure are shown in Fig. 5.7(a–g). AFM Skyrmion nucleation was observed only within a narrow intermediate field window, spanning approximately $100\text{--}150 \text{ mT}$. At low fields ($B_z < 75 \text{ mT}$), no skyrmions are observed post irradiation, indicating that the system remains in a stripe or disordered domain configuration where skyrmions are not energetically favorable. As the field is increased to $B_z = -75 \text{ mT}$, isolated skyrmions begin to appear. The skyrmion density peaks sharply at $B_z = 140\text{--}145 \text{ mT}$ (Fig. 5.7(e–f)), then goes down at higher fields ($B_z = 200 \text{ mT}$).

The field window for skyrmion generation corresponds closely to the open region in the hysteresis loop for stack #S3, shown in Fig. 5.3(a), suggesting that the skyrmions are nucleated in a metastable skyrmion pocket region between labyrinth and saturated magnetic states. We quantify this behavior in Fig. 5.7(h), where the total number of skyrmions nucleated is plotted as a function of applied magnetic field. The nucleation efficiency exhibits a threshold behavior near 75 mT , peaks at 145 mT , and declines rapidly beyond 150 mT . Below 50 mT , skyrmions are not observed, while above 150 mT , the Zeeman penalty associated with the formation of reversed magnetic domains becomes too high, thereby suppressing skyrmion nucleation. These results emphasize that field-tuned laser excitation provides a powerful handle for accessing metastable AFM skyrmions in SyAFMs. When operating within a well-defined magnetic field window, skyrmions can be written reliably.

Fluence-Dependence of the Laser-Induced Nucleation of AFM Skyrmions

The ability to controllably write AFM skyrmions hinges critically on the energy deposited locally during optical excitation. While the applied magnetic field defines the stability window of skyrmions within the phase diagram, the laser fluence at a fixed Gaussian beam radius of $3.5 \mu\text{m}$ determines the spatial region in which the transient temperature surpasses the nucleation threshold, thereby setting the area over which topological transitions can be thermally activated. To unravel this interplay, we

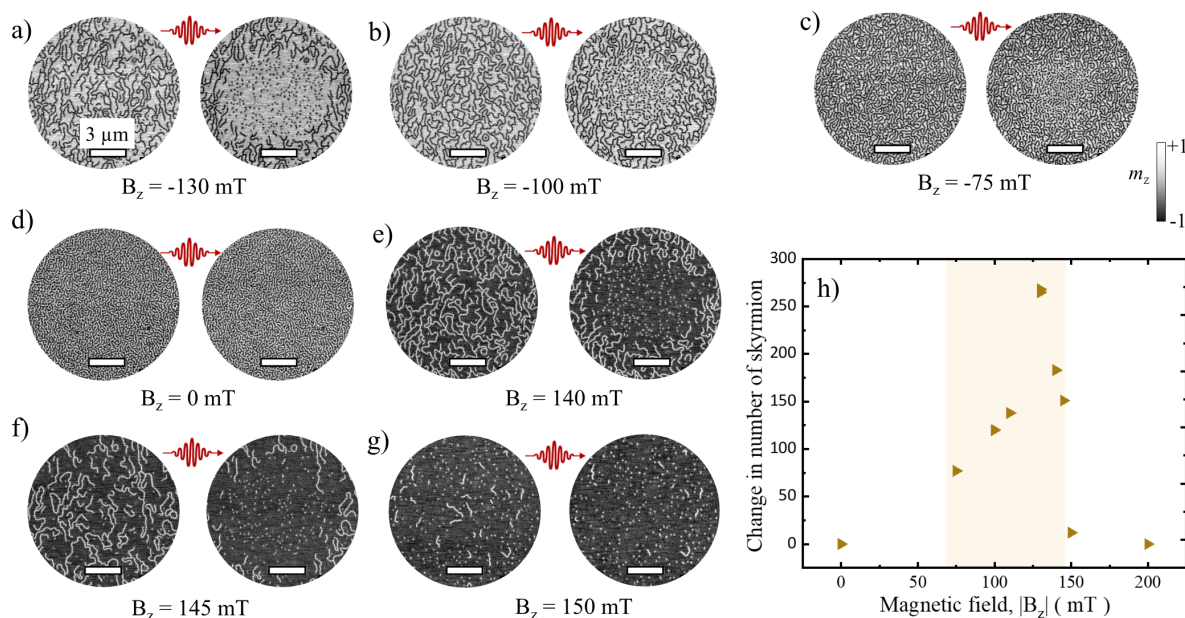


Figure 5.7: **Magnetic field dependence of laser-induced AFM skyrmion nucleation.** (a–g) STXM images acquired at the Fe L_3 edge, illustrating the effect of a single 1 ps, 1040 nm laser pulse (fluence = 16 mJ/cm²) on the domain configuration of Stack #S3 under varying out-of-plane magnetic fields, ranging from $B_z = -130$ mT to 200 mT. For each field value, the sample was first initialized into a labyrinth multidomain state via out-of-plane demagnetization, followed by (left image) laser excitation and post-irradiation imaging. (h) The change in skyrmion number as a function of magnetic fields, extracted from the right STXM images.

systematically vary the fluence of single-pulse infra-red laser excitation, keeping the external magnetic field fixed at $B_z = 140$ mT, where the skyrmion pocket is known to exist. For each fluence value \ddagger , the SyAFM multilayer is initialized into a multidomain labyrinth state via OOP demagnetization, followed by laser excitation and element-resolved STXM imaging at the Fe L_3 edge.

Fig. 5.8(a,b) shows the evolution of magnetic domain textures as the laser fluence is increased from 7 to 14 mJ/cm² at a fixed magnetic bias of 140 mT. At the fluence below 7 mJ/cm², the deposited thermal energy is insufficient to nucleate the skyrmions, and the initial stripe morphology remains unchanged. Skyrmion nucleation begins to emerge at a threshold fluence of 7.33 mJ/cm², where isolated skyrmions appear. Strikingly, rather than observing the formation or reorganization of new stripe domains, we find that the pre-existing stripes are fragmented into discrete, circular skyrmions. This mechanism, where the stripe pattern is directly severed by laser-induced thermal perturbation, is consistently observed throughout the intermediate fluence range up to 14 mJ/cm²

\ddagger Due to the oblique incidence of the laser beam, the effective fluence at the sample surface is reduced by approximately a factor of three compared to the nominal fluence. Therefore, all fluence values reported correspond to the effective fluence at the sample. The calibration data points relating the applied laser current to the effective fluence are provided in Appendix C.

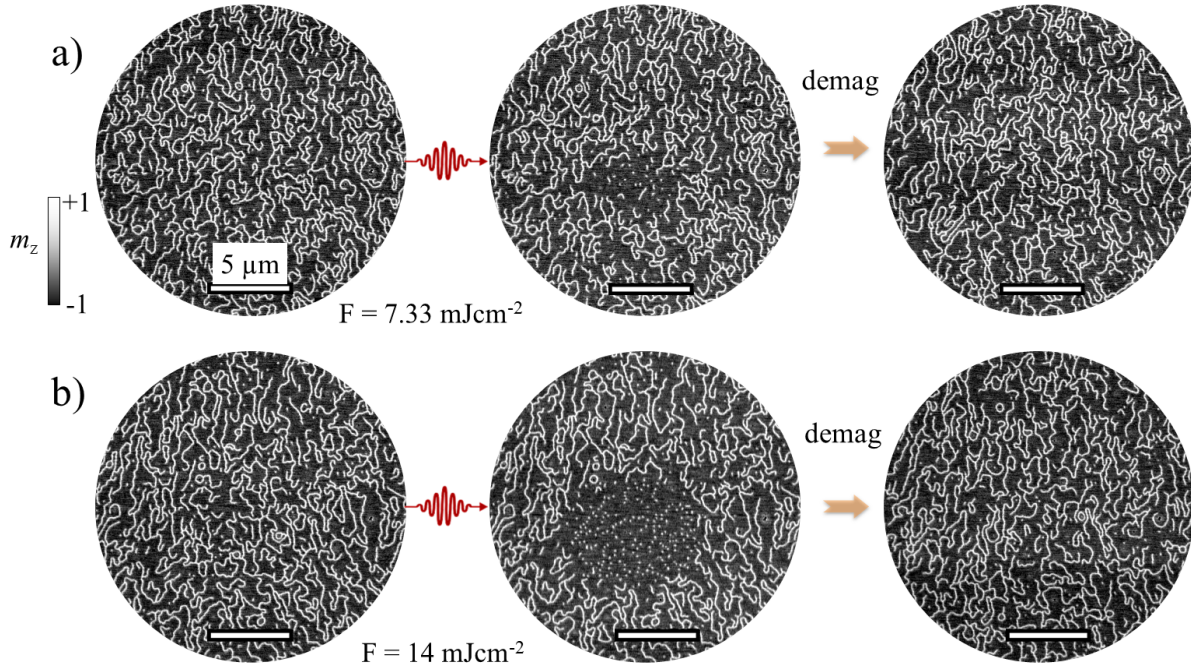


Figure 5.8: **Fluence-dependent laser-induced nucleation of AFM skyrmions.** STXM images acquired at the Co L_3 edge showing the evolution of magnetic domain textures in Stack #S3 at three representative laser fluences, under a fixed magnetic bias of $B_z = 140$ mT. Each panel displays the domain configuration before (left) and after (middle) a single 1 ps infra-red laser pulse, followed by an out-of-plane demagnetization step (right). **(a)** At the threshold fluence of $F = 7.33$ mJ/cm², isolated skyrmions nucleate within the laser-irradiated region. **(b)** At $F = 14$ mJ/cm², a dense skyrmion lattice is formed.

(Fig. 5.8(b)). The number and spatial extent of nucleated skyrmions increase systematically with fluence, consistent with the expanding region in which the transient temperature exceeds the nucleation threshold. At higher fluences between 28.3 and 60 mJ/cm² (Fig. 5.9(a-c)), the central region of the laser irradiated area transforms into a monodomain state, suggesting that the thermal energy surpasses the upper bound of the skyrmion-stabilizing regime and drives the system into a uniformly magnetized configuration. A qualitative change is observed here in Fig. 5.9(c), where the irradiated region does not recover the original multidomain state, even after repeated demagnetization. This irreversible behavior implies that the system undergoes structural modifications such as interfacial intermixing, local amorphization, or thermal degradation of the anisotropy and DMI.

To visualize the spatial extent of magnetic responses, Fig. 5.10(a) shows that the area modified by the laser increases with fluence, exhibiting a transition from no changes to a monodomain regime. Blue circles represent total spin texture changes, while red stars indicate skyrmion nucleation. As

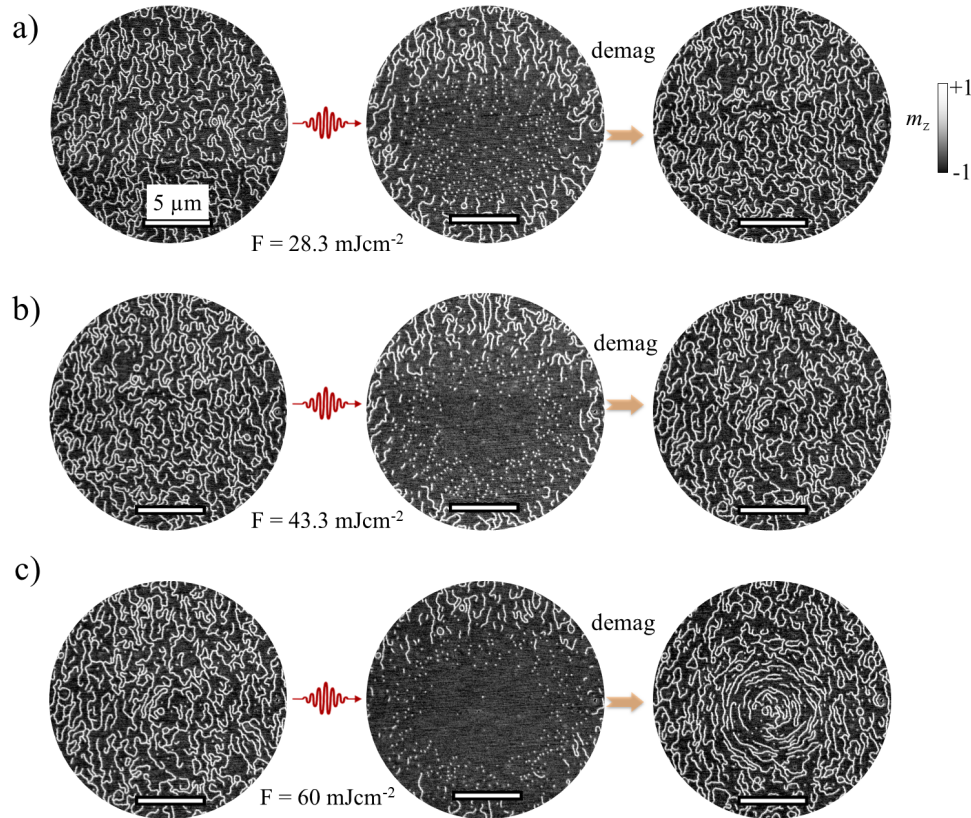


Figure 5.9: **Laser-induced skyrmion nucleation at high fluence.** STXM images at $B_z = 140$ mT recorded before (left), after laser excitation at fluence F (middle), and following demagnetization (right). **(a)** At $F = 28.3$ mJ/cm², the first signatures of a monodomain-like state emerge in the central region of the laser spot. **(b)** At $F = 43.3$ mJ/cm², the monodomain region further expands, reducing the available area for skyrmion nucleation. **(c)** At the highest fluence ($F = 60$ mJ/cm²), demagnetization is not sufficient to restore the original multidomain texture, indicating irreversible modification of the energy landscape due to overheating.

the fluence rises, the skyrmion nucleation area initially grows but then saturates and remains nearly constant despite further fluence increases. This divergence occurs because stronger laser-induced heating destabilizes skyrmion formation, favoring a transition toward a mono-domain state rather than additional skyrmion nucleation. Fig. 5.10(b) presents a quantitative analysis of laser-induced AFM skyrmion nucleation as a function of laser fluence, revealing a well-defined fluence-dependent phase window. Below a threshold of approximately 7 mJ/cm², no appreciable change in the skyrmion count is detected. Once the fluence surpasses this threshold, the number of nucleated skyrmions increases rapidly, reaching a saturation point around 30 mJ/cm². This plateau reflects the regime where the local temperature within the laser spot exceeds the nucleation threshold across its core,

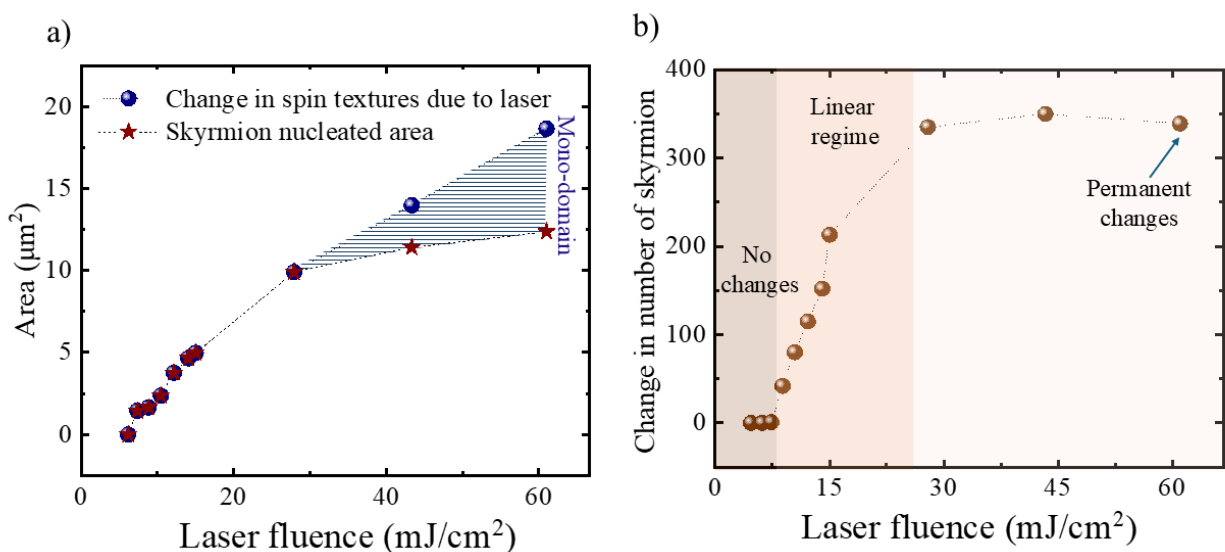


Figure 5.10: **Quantitative analysis of fluence-dependent AFM skyrmion nucleation.** (a) Area of laser-modified magnetic regions as a function of laser fluence. Blue circles indicate the total area of changed spin textures due to laser irradiation, while red stars represent the area where skyrmions are nucleated. The divergence between them at higher fluences reflects the transition to a monodomain state where skyrmion nucleation saturates despite growing overall magnetic changes. (b) Change in skyrmion number with increasing laser fluence, showing a clear nucleation threshold ($7.33 \text{ mJ}/\text{cm}^2$), saturation beyond $30 \text{ mJ}/\text{cm}^2$, and stays almost constant in the high-fluence regime.

maximizing the density of stable skyrmions. Beyond this range, at fluences exceeding $50 \text{ mJ}/\text{cm}^2$, the skyrmion count declines despite higher energy input.

In this section, we demonstrated the controlled nucleation of antiferromagnetic skyrmions in a SyAFM. Sublattice-resolved imaging confirms their antiferromagnetic nature, while systematic tuning of laser parameters reveals the narrow energetic window required for skyrmion nucleations. These results establish a robust framework for skyrmion generation via thermal pathways. In the following section, we shift our focus from skyrmion nucleation to the study of their current-induced dynamics, using nanosecond current pulses to probe their motion and stability.

5.4 Dynamics of Antiferromagnetic Skyrmions

When skyrmions are nucleated, their subsequent motion under current is primarily governed by intrinsic micromagnetic properties and remains largely independent of the specific nucleation mechanism. To probe skyrmion dynamics, two complementary experimental techniques are employed: time-resolved pump-probe X-ray microscopy and quasi-static imaging conducted before and after current injection. While both methods are utilized throughout this thesis, the emphasis in this chap-

ter is placed on time-resolved measurements, which enable real-time visualization of skyrmion motion with nanosecond temporal resolution.

In this chapter, two dynamic regimes of AFM skyrmions are investigated: (1) the current-driven skyrmion motion induced by spin–orbit torques, and (2) the out-of-equilibrium relaxation dynamics following current cessation. The relaxation behavior serves as a sensitive probe of various skyrmion interactions. For an isolated skyrmion navigating a non-flat energy landscape, these dynamics encode information about the underlying potential (subsection 5.4.1). In dense skyrmion lattices, where inter-skyrmion interactions are significant, the relaxation traces reveal details of the skyrmion–skyrmion repulsion. This is explored by driving the system into a novel incoherent flow regime, characterized by reproducible skyrmion interactions. Here, pinned skyrmions act as fixed scattering centers from which mobile skyrmions scatter, with their trajectories and characteristic timescales providing direct, real-space, and real-time visualization of skyrmion–skyrmion interactions (subsection 5.4.2). Finally, in the conventional viscous flow regime, we observe inertia-free skyrmion motion alongside real-time cancellation of the skyrmion Hall effect (subsection 5.4.3). The directional, coherent motion detected in this regime further confirms the topological character of the nucleated spin textures, reinforcing earlier conclusions drawn from domain morphologies and interfacial chiral interactions.

5.4.1 Dynamic Hopping of a Single AFM Skyrmion

In Chapter 2 Section 2.5.4, we discuss SOT-induced skyrmion dynamics under the idealized assumption of a pinning-free system at zero temperature.[§] However, in realistic room-temperature multilayer SyAFM stacks, skyrmions are inevitably subjected to thermal fluctuations, resulting in thermally activated diffusion. In the absence of pinning, such skyrmion motion resembles Brownian motion within the magnetic landscape. Skyrmion diffusion has been widely studied in ultra-thin single-layer ferromagnetic systems near room temperature [38, 260, 261]. Recent studies have shown that in bilayer synthetic antiferromagnets, thermally activated skyrmion diffusion is even more pronounced [233]. This enhancement arises from the suppressed gyrotropic response due to angular momentum compensation, which effectively reduces the Magnus force and leads to more than a tenfold increase in the diffusion coefficient compared to ferromagnetic skyrmions. Although the multilayer stacks employed in this thesis share structural similarities with previously studied bilayer SyAFM systems [134], the strong interlayer coupling effectively suppresses thermal fluctuations and enhances the effective pinning strength. As a result, the observation of skyrmions at fixed positions in static images suggests that the diffusion of AFM skyrmions is negligible on the timescale of imaging. When

[§]In the micromagnetic simulations, the material parameters correspond to the values at room temperature, while the LLG equation is solved without including any thermal noise term.

skyrmions are subjected to low-amplitude excitations, such as thermal fluctuations or weak current pulses, they may exhibit slight displacements but are rapidly restored to nearby energy minima. In this regime, the role of pinning potentials becomes evident, as the energy imparted to the system is insufficient to overcome the local potential barriers. Pump–probe measurements cannot capture thermal excitations, as they are stochastic in nature and would introduce noise into reproducible motions, effectively blurring out the magnetic contrast. However, the deterministic effect of the local energy landscape can still be resolved.

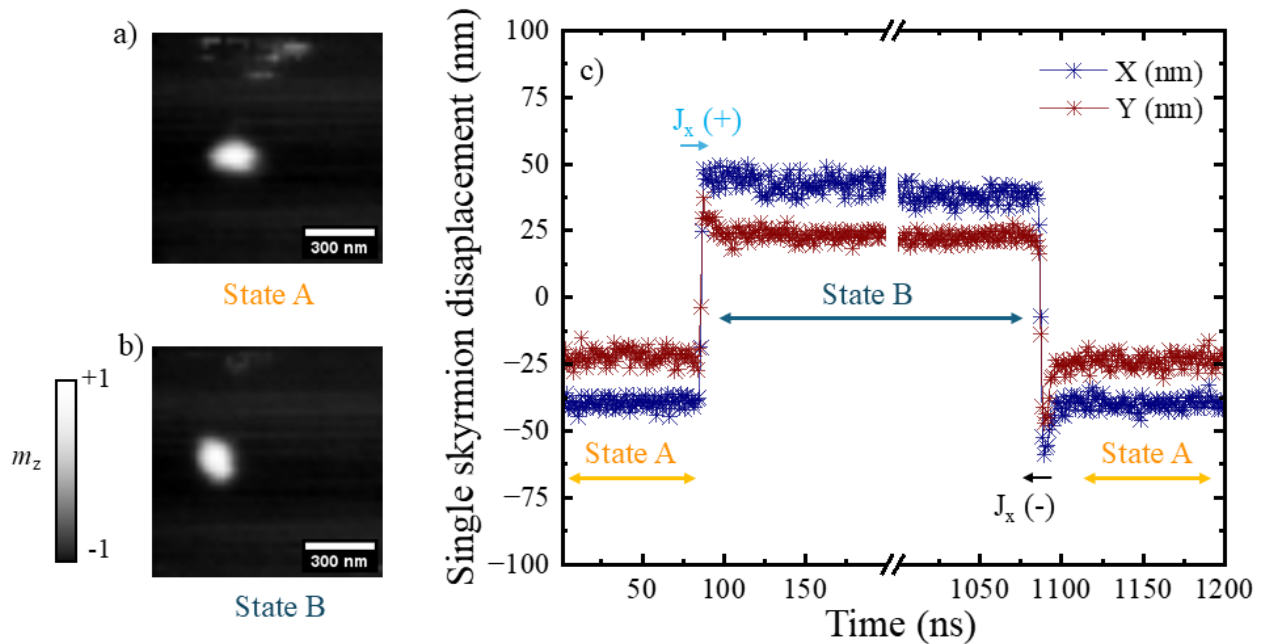


Figure 5.11: **Time-resolved single skyrmion displacement in a 90% compensated SyAFM.** (a,b) Static STXM images of a single skyrmion at two equilibrium positions, labeled as State A and State B, respectively. (c) Time evolution of the skyrmion displacement along the X (blue) and Y (red) directions under the application of a bipolar current pulse of 5 ns duration, with successive pulses separated by a 1 μ s interval.

This effect is studied in a SyAFM multilayer stack with 90% magnetic compensation. Devices were patterned with lateral dimensions of $2 \mu\text{m} \times 5 \mu\text{m}$, having a resistance of approximately 45Ω when fabricated on a 100 nm SiN membrane. The measurements focused on a single skyrmion localized at a pinning site. To induce motion, bipolar current pulses with a duration of 5 ns and a repetition frequency of 0.5 MHz were applied. To mitigate thermal accumulation during repeated excitations, particularly given the limited thermal conductivity of the 100 nm silicon nitride membrane, a 1 μ s interval was introduced between the positive and negative pulses. This excitation scheme facilitates skyrmion oscillation between two metastable equilibrium positions, ensuring its return to

the initial configuration at the end of each pump–probe cycle. Time-resolved STXM measurements were performed by scanning the pump–probe delay over a total range of 2 μs using 2001 equally spaced time channels, corresponding to a sampling step of 1 ns. It should be noted that the actual temporal resolution is determined by the pump–probe X-ray pulse width, which is below 100 ps. During the interval from 86 to 90 ns, a positive current pulse drives the skyrmion from its initial state (State A) to a displaced configuration (State B), as shown in Fig. 5.11(a,b). The subsequent negative pulse, applied between 1086 and 1090 ns, returns the skyrmion to its original position, completing a full cycle of confined, bidirectional motion. Since the skyrmion remains within the vicinity of its original pinning region, the observed dynamics result from a competition between the applied spin–orbit torque and the restoring force imposed by the local pinning potential. Fig. 5.11(c) shows the time-resolved displacement of a skyrmion during a 5 ns bipolar current pulse at a current density of 4.5×10^{11} A/m², capturing its real-time response to the applied stimulus. Following the termination of the current pulse sequence (at 1090 ns), the skyrmion relaxes toward a local equilibrium over a characteristic timescale of approximately 20 ns. The displacement traces reveal that the motion is not purely translational but is modulated by the spatial variation of the underlying energy landscape.

Fig. 5.12(a) shows the trajectory of the same single skyrmion discussed above. The skyrmion positions during the application of positive current pulses are represented by colored spheres, while those corresponding to negative pulses are denoted by stars. The positions after the current pulse has ceased are shown in gray: gray spheres for positive pulses and gray stars for negative pulses. When modeled as a point-like particle, the skyrmion motion outlines a closed loop in real space, indicating that it does not retrace an identical path upon reversal of current polarity. This non-reciprocal behavior appears as a hysteretic displacement loop. Importantly, the skyrmion motion is not a rigid particle motion. Instead, it proceeds through a well-defined sequence of shape transformations that resemble caterpillar-like locomotion, namely, a succession of asymmetric deformations that facilitate net displacement. As illustrated in the lower inset of Fig. 5.12(a), the contour evolution of the skyrmion during the positive current pulse (86–89 ns) is rendered using a temporal color scale, with each contour representing a distinct time frame. The skyrmion undergoes a three-step deformation-mediated motion during this interval.

In the first step, from 86 to 87 ns (p1 to p2), the skyrmion shrinks, reducing its overall area. This suggests the presence of a stronger local potential barrier near the domain wall along the direction of motion, as evidenced by the diminished spatial extent of the contour. In the second step, from 87 to 88 ns (p2 to p3), the skyrmion shifts laterally across the pinning site while maintaining approximately constant size. In the third step, from 88 to 89 ns (p3 to p4), the skyrmion re-expands as it approaches

a new metastable equilibrium configuration. This deformation-mediated propagation enables the skyrmion to transition between distinct local energy minima without undergoing complete unpinning. Once the positive pulse terminates, the skyrmion exhibits negligible residual motion, indicating that it has relaxed into a locally stable configuration. The application of a current pulse with reversed polarity (see top inset of Fig. 5.12(a)) initiates motion along a different return trajectory, thus completing the closed-loop path. Following this pulse, the skyrmion returns to its initial equilibrium position under the influence of the local potential landscape. The black-marked region in both insets corresponds to the skyrmion core area, where the contrast remains unchanged throughout the bipolar pulses, indicating the pinned region of the skyrmion. The green marked region (R1) in Fig. 5.12(a) identifies the area in which the skyrmion relaxes and falls into the nearest potential minimum after completion of the bipolar excitation cycle. The magnetic contrast within R1 is shown in Fig. 5.12(b), demonstrating that the skyrmion returns to its equilibrium state. The post pulse decay after 1091 ns is fitted with an exponential function, yielding a relaxation time constant $\tau_{\text{relax}} = 7.5$ ns. These dynamical processes underscore the critical role of skyrmion elasticity as well as the pinning landscape in enabling deterministic and reversible motion via a deformation-assisted mechanism. Note that the energy landscape varies from one skyrmion to another.

5.4.2 Dynamic Imaging of AFM Skyrmion Scattering

While the preceding sections have examined the dynamics of individual skyrmions within localized pinning potentials, the presence of multiple skyrmions introduces additional complexity arising from mutual interactions. These interactions become increasingly important in dense systems, where the spatial proximity of skyrmions leads to interparticle forces that influence both equilibrium configurations and dynamic behavior. A detailed understanding of the skyrmion–skyrmion interaction potential, defined as the effective potential energy as a function of skyrmion separation, is essential for describing the formation of ordered skyrmion arrays and assessing the maximum achievable density for information storage. It is equally important for elucidating the collective response of skyrmions to applied currents, encompassing processes such as mutual deflection, scattering, and correlated motion. In micromagnetic simulations, the interaction energy can be evaluated by stabilizing two skyrmions at a prescribed distance and comparing the total system energy to the case where they are well separated. Analytical approaches based on simplified models are also widely employed. For example, by assuming a rigid skyrmion spin structure, one can apply the Thiele formalism to describe skyrmion dynamics as those of effective particles subjected to interaction forces from neighboring skyrmions. The resulting equation of motion contains a force term expressed as $-\nabla U(r)$, where $U(r)$ represents the interaction potential between skyrmions. The explicit functional form of $U(r)$

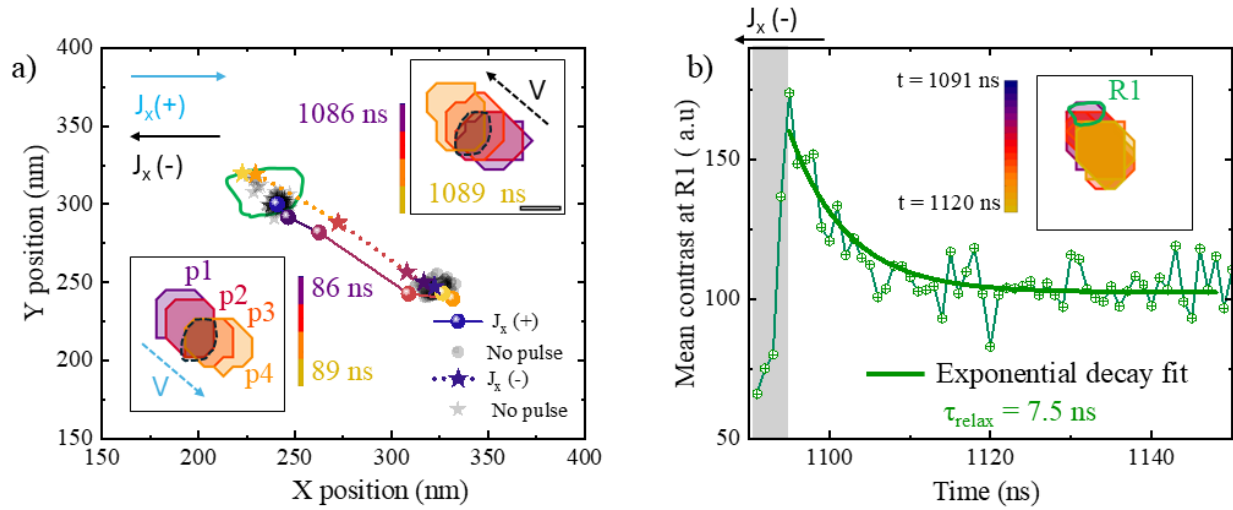


Figure 5.12: **Skyrmion dynamics in a non-flat energy landscape.** **(a)** Time-resolved trajectory of a single skyrmion under a bipolar pulse, showing partial displacement. Spheres and stars correspond to skyrmion positions during positive ($J_x > 0$) and negative ($J_x < 0$) pulses, respectively, while gray markers represent stationary positions after corresponding pulses. Insets show contour evolution at four representative positions (p1–p4) during the positive pulse: initial contraction at the trailing edge (p1 to p2), centroid shift with minimal size change (p3), and re-expansion at the leading edge (p4). For the negative pulse, the top inset highlights the contour evolution, with the black-marked region denoting the pinned core area that remains unchanged throughout the excitation cycle. **(b)** Time evolution of the mean magnetic contrast at region R1 (see inset), plotted after the negative current pulse is switched off. The skyrmion gradually relaxes back to equilibrium over a timescale of approximately 7.5 ns.

is not known in advance and must be derived from microscopic calculations or determined empirically. Recent work has demonstrated that coarse-graining methods such as iterative Boltzmann inversion [238] can be used to extract effective interaction potentials from experimental images of dense skyrmion ensembles.

This interaction potential has been theoretically predicted to be repulsive [262], attractive [241, 263], or oscillatory [264] depending on the underlying magnetic interactions. Experimental quantification of the skyrmion-skyrmion interaction has so far been limited to micrometer-scale skyrmion bubbles via indirect mapping [238], where the interactions are predominantly repulsive and governed by long-range magnetostatic forces. On device-relevant nanoscopic length scales, however, short-range contributions from the DMI [65, 66] dominate, giving rise to strongly interacting skyrmion lattices in which skyrmion–skyrmion scattering, lattice deformation, relaxation dynamics, and emergent transport signatures such as the topological Hall effect arise under external stimuli. These dynamic processes are inherently transient and remain inaccessible to conventional quasi-static

imaging techniques. Although time-resolved microscopy has revealed a range of nanosecond-scale dynamical phenomena in FM skyrmions [33, 239–241], analogous behavior remains elusive for AFM skyrmions. Moreover, a skyrmion lattice in fully compensated AFM systems has, to our knowledge, not yet been experimentally realized, despite its unique potential to simultaneously probe skyrmion–skyrmion interactions and suppression of the SkHE. Such a platform would allow for the study of emergent transport phenomena, including the topological spin Hall effect [242] and topological orbital Hall effect [243]. However, probing the collective dynamics of antiferromagnetic skyrmion lattices under external excitation remains challenging, as conventionally used quasi-static imaging cannot resolve transient deformation, relaxation, or interaction processes that occur on nanosecond timescales. So these challenges call for time-resolved microscopy measurements to reveal skyrmion scattering, skyrmion–skyrmion interactions, lattice stability, and dynamical response in antiferromagnetic systems.

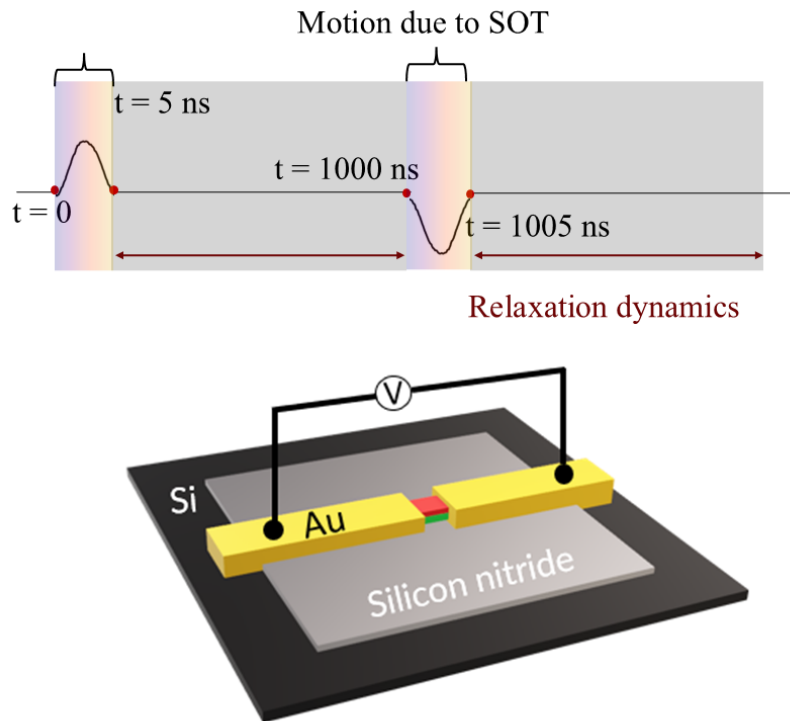


Figure 5.13: **Device layout and temporal pump-pulse pattern.** The SyAFM is deposited on a SiN membrane window with gold contact pads for bipolar current-pulse excitation. Adapted from [3].

In this section, we employ pump–probe X-ray microscopy with high spatiotemporal resolution (20 nm spatial and 1 ns temporal) to resolve the real-space trajectories and dynamic behavior of an

AFM skyrmion lattice in a SyAFM (stack #S5) confined within a magnetic nanotrack. Leveraging the element-specific contrast of X-ray imaging, we dynamically probe both magnetic sublattices of the AFM skyrmions, enabling direct observation of skyrmion–skyrmion interactions in real space and in real time. Devices were fabricated (see Fig. 5.13) with dimensions of 2 μm in length and 5 μm in width, and exhibit a resistance of $\approx 15.8 \Omega$. This geometry was selected to minimize lateral confinement and to facilitate efficient heat dissipation via the adjacent gold contacts. To further reduce heat accumulation during pump–probe imaging, a 200 nm thick aluminum layer was deposited beneath the SiN membrane to serve as a heat sink. Since only one X-ray energy can be used at a time, we repeat the measurement at two different X-ray energies to obtain sublattice-selective imaging. To investigate skyrmion–skyrmion interactions and the transient response of the antiferromagnetic skyrmion lattice to spin–orbit torque, stack #S5 was investigated. In this system, a skyrmion lattice was nucleated by applying bipolar current pulses, as shown in Fig. 5.5. Alternating bipolar current pulses were applied to drive the skyrmions back and forth over equal distances, thereby restoring the initial state after each pump cycle. Time-resolved imaging is achieved by synchronizing 70–100 ps X-ray probe pulses from the storage ring with the pump pulses at varying delays, such that each recorded frame corresponds to a distinct time point within the excitation sequence and captures the transient magnetic configuration during motion. Since the magnetic contrast is averaged over billions of bipolar excitation cycles, any non-reproducible skyrmion motion averages out and remains undetectable. Reproducibility of the skyrmion lattice dynamics is therefore essential for pump–probe measurements, as the method relies on consistent and well-defined signals to resolve the dynamic trajectories. Furthermore, because the imaging technique is based on photon transmission through the multilayer stack, the measured magnetic contrast represents an average over all repeated layers, thereby suppressing contributions from rare or stochastic events.

In an antiferromagnetic skyrmion lattice, long-range dipolar stray fields are suppressed, and short-range exchange and DMI, together with local anisotropy, dominate, setting the equilibrium lattice spacing. This is in stark contrast to ferromagnetic skyrmion lattices, where long-range dipolar interactions dominate over other contributions [262]. When subjected to weak excitations, the AFM lattice is driven out of equilibrium: pinned skyrmions serve as scattering centres for mobile ones, leading to either local lattice compression or trajectory deflection. Such scattering events encode the skyrmion–skyrmion interaction potential, which can be quantitatively extracted from measured real-space trajectories. Fully compensated SyAFMs offer an ideal platform for this, as the cancellation of gyrotropic terms suppresses the skyrmion Hall effect [37, 134, 246], isolating longitudinal motion and potentially enabling a direct mapping between scattering geometry and interaction forces. To resolve the spatiotemporal dynamics of an AFM skyrmion lattice, we employ pump–probe X-ray microscopy,

which enables real-time nanosecond tracking of individual skyrmion trajectories. This provides direct access to transient effects such as skyrmion–skyrmion repulsion and inertial responses, that are not resolved in quasi-static measurements. To observe the dynamics of each magnetic sublattice, we perform sequential measurements at the Fe and Co L_3 absorption edges, as only one X-ray energy can be used at a time.

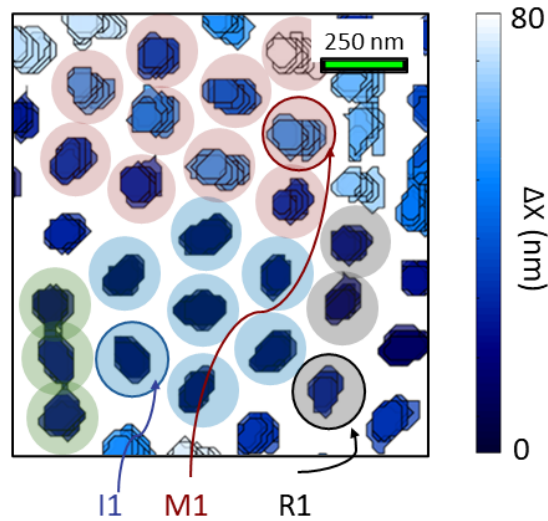


Figure 5.14: **Spatio-temporal evolution of an AFM skyrmion lattice during the cycle of bipolar current pulses.** x -displacement map following a negative pulse, used to classify the skyrmions into four categories: immobile (I, blue), mobile (M, red), laterally adjacent to the left (L, green), and to the right (R, black) of the mobile region. The colour scale encodes the net displacement along the x -direction. Circles indicate representative skyrmions from each class exhibiting distinct responses to current excitation. Adapted from [3].

The low-current regime ($J = 2.8 \times 10^{11}$ A/m²) corresponds to conditions where the spin–orbit torque generated by the applied current is comparable in magnitude to the local pinning potential. In this case, the motion is governed by a spatially inhomogeneous energy landscape, where variations in pinning strength give rise to an incoherent dynamical regime in which different parts of the lattice respond differently to the same uniform drive. Despite the application of a uniform current, the lattice response is spatially heterogeneous: some skyrmions remain pinned (e.g., I1 in Fig. 5.14), others translate smoothly (e.g., M1 in Fig. 5.14), and some undergo pronounced deformation (e.g., R1 in 5.14). The pinning sites correspond to energy minima associated with material inhomogeneities, defects, or grain boundaries that locally suppress skyrmion mobility. To address this strongly differing motion patterns within the imaged skyrmion ensemble, we first conduct a classification of skyrmions into four cluster, as colour coded in Fig. 5.14, according to their net displacement during current

excitation: immobile skyrmions (class I, blue), mobile skyrmions (class M, red), and those located immediately adjacent to the mobile cluster on the left (class L, green) and right (class R, black). Class M skyrmions exhibit a large displacement during the pulse, whereas class I skyrmions show only minimal motion. We define this behavior as an incoherent flow regime, where skyrmions in both sublattices move in synchrony, yet the overall lattice response remains spatially fragmented. The dynamics are highly reproducible across all cycles, confirming their non-stochastic origin. Thermal fluctuations, which generate statistically random variations that average out in pump–probe measurements, are therefore not detectable in the present study. The local behavior varies significantly, from pinned to deforming skyrmions and to those undergoing smooth displacements. Such spatial heterogeneity under uniform excitation reflects a breakdown of global lattice coherence and distinguishes this particular regime from both thermally activated creep and viscous-flow regimes.

Fig. 5.15(a–d) shows the evolution of skyrmion contours in sublattices A and B under a bipolar current pulse applied along the x -axis, illustrating their time-resolved response to spin–orbit torques during a pump cycle. Panels (a,b) correspond to sublattice A, while panels (c,d) correspond to sublattice B. The contours in the left panel are colour-coded over a 15 ns window, from purple at early times to yellow at late times, visualizing the progression of skyrmion boundary displacement. These contours are obtained by tracking individual skyrmion boundaries across consecutive frames. To analyse local lattice deformation, the skyrmion cores are modelled as point particles and Delaunay triangulations are constructed at each time step, as shown in the right panel of Fig. 5.15. This representation depicts the evolving geometry and local strain within the lattice during current excitation. Both sublattices A and B exhibit synchronized and coherent skyrmion motion, following identical trajectories. The synchronized motion of both sublattices, despite the spatially heterogeneous response, shows that even the relatively weak interlayer AFM exchange in thin-film SyAFMs, compared to the strong intrinsic exchange in bulk antiferromagnets, is sufficient to overcome local pinning effects in the individual layers, enabling robust sublattice locking and offering a key advantage for reliable AFM spintronic applications.

Pinned skyrmions act as rigid obstacles within the lattice, inducing constraints that can be described in a mechanics approach and lead to anisotropic strain in neighboring skyrmions. As adjacent skyrmions are pushed by the applied current, these constraints result in boundary elongation or compression. For instance, skyrmions located just outside the boundary of pinned regions (e.g., R1) cannot translate freely; instead, one domain wall is effectively anchored by the adjacent pinned skyrmion, while the opposite boundary remains free to move. Within the Thiele framework, this reflects a breakdown of the rigid-particle approximation, as asymmetric constraints induce spin structure deformation and redistribute internal stresses through the lattice. These deformations are visible

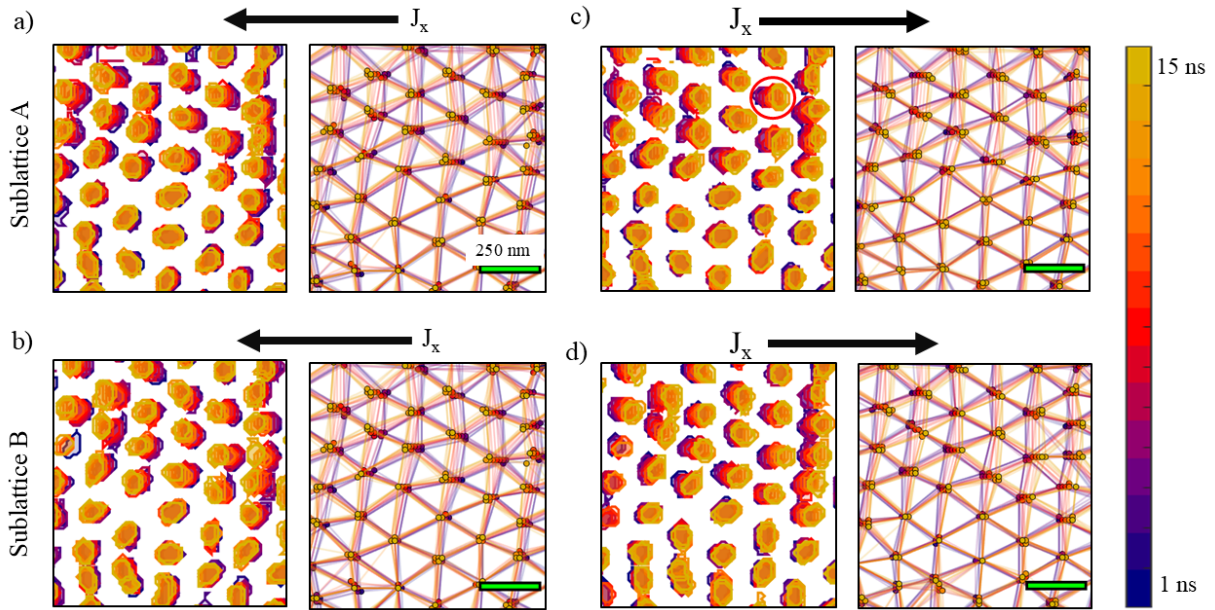


Figure 5.15: **Incoherent flow regime of AFM skyrmion dynamics.** (a) and (b) show the motion of skyrmions in sublattices A and B, respectively, under a positive current (J_x) with time evolution tracked over 15 ns. The skyrmion domain boundaries are color-coded to represent the time progression, from purple (earlier times) to yellow (later times). (c) and (d) illustrate the skyrmion behavior at sublattices A and B, respectively, under a reversed current direction ($-J_x$), demonstrating symmetric displacement and deformation. The time scale for the evolution is indicated by the color bar on the right. Adapted from [3].

in the right panel of 5.15(a-d) as irregularities in the triangulated lattice, where the otherwise regular hexagonal arrangement of skyrmions is locally distorted. Such distortions appear as variations in effective bond lengths and angles between neighboring skyrmions in the Delaunay triangulation, indicating areas of localized strain in the lattice. Fig. 5.16(a) and Fig. 5.16(b) display the average time-resolved displacement of each of the previously defined 4 classes of skyrmions, obtained by tracking the trajectories of colour-coded skyrmions throughout the duration of the bipolar pulse. Class M skyrmions exhibit substantial motion during the current pulse, while class I skyrmions show only minimal displacement. Strikingly, upon removal of the current drive, the absence of external forcing allows internal skyrmion–skyrmion interactions to restore equilibrium, yielding a recoil opposite to the prior current-driven motion, irrespective of the applied polarity. This recoil reflects a relaxation process in which mobile skyrmions scatter off their pinned neighbours, with the restoring forces arising from skyrmion–skyrmion repulsion and the surrounding pinning landscape. Rather than behaving as independent particles, the skyrmions respond collectively, revealing the elastically coupled and scattering-mediated nature of the lattice. This post-pulse relaxation is well described by

an exponential decay, from which a characteristic relaxation time constant (τ_{relax}) is extracted for each skyrmion class. These time constants vary significantly across the I, M, L, and R classes, both in magnitude and decay rate, suggesting differences in the local energy landscape experienced by each group and thereby providing a quantitative measure of skyrmion interaction potential. A table with the extracted values of magnitude and decay rate for each of the four classes and both current polarities is given as Table 5.1.

Table 5.1: **Relaxation time constants τ_{relax} and amplitudes for different skyrmion classes after positive and negative current polarities of the bipolar cycle.**

Skyrmion class	After $-J_x$		After $+J_x$	
	τ_{relax} (ns)	Amplitude (nm)	τ_{relax} (ns)	Amplitude (nm)
M	9.9	12.8	5.1	9.1
I	5.6	17.5	7.8	20.1
L	9.6	19.2	3.9	18.9
R	7.4	21.7	18.9	22.7

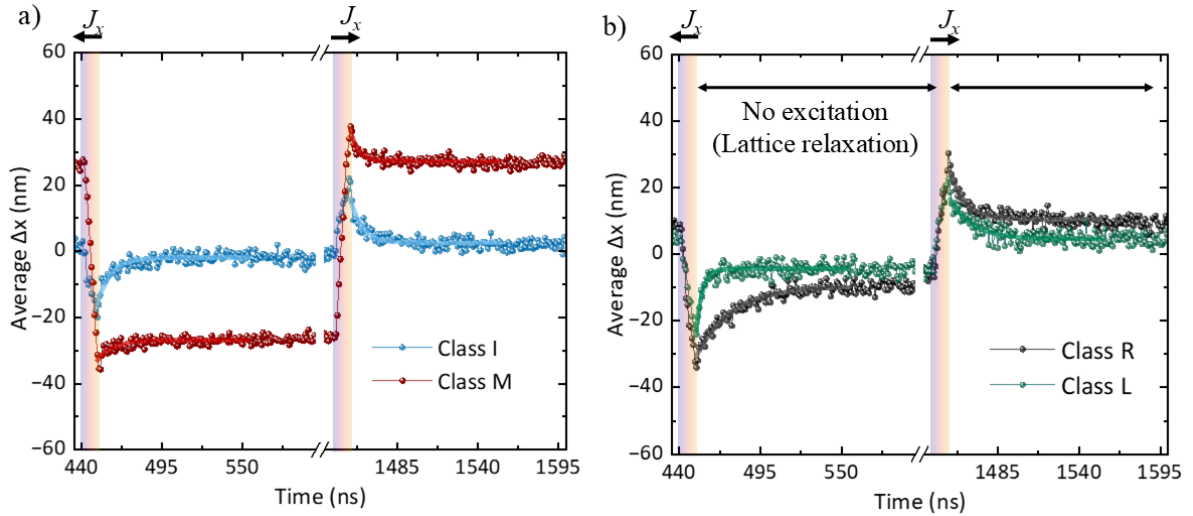


Figure 5.16: **Time-resolved skyrmion relaxation trajectories.** Average displacement traces for each class. Shaded regions indicate the duration of the negative and positive current pulses during the bipolar pulse. Upon pulse termination, all skyrmion classes exhibit recoil opposite to their preceding motion, regardless of previous current polarity. **(a)** I and M skyrmion classes, with the I-skyrmions showing the strongest recoil and M types the weakest. **(b)** The L and R skyrmion classes display asymmetric recoil dynamics, governed by their lateral position relative to the mobile class. All timescales for the recoil dynamics, as extracted via exponential fitting, fall within 3–20 ns. Adapted from [3].

This complex behavior now allows us to extract the skyrmion interaction potential directly from

the nanosecond relaxation dynamics of L and R skyrmions, which lie at the lateral boundary between mobile and pinned regions. In this geometry, the pinned I skyrmions act as fixed scattering centres, providing boundary conditions for quantifying the skyrmion–skyrmion interaction potential. We track the experimentally measured recoil trajectories of the L and R skyrmions following the termination of the nanosecond current pulse and employ an inverse estimation based on the Thiele equation [3]. In the fully compensated SyAFM configuration, the gyrotropic term contribution disappears, and long-range dipolar interactions are markedly suppressed, so that the dynamics reduce to a purely longitudinal balance between dissipative drag and the skyrmion–skyrmion force. By restricting the analysis to the immediate post-pulse relaxation window, we ensure that the motion is governed solely by skyrmion–skyrmion interactions and dissipation, free from external spin–orbit torques because the current is off and free from stochastic thermal activation. $F(r)$ is the interaction force one skyrmion exerts on another along the line connecting their centres, arising from the energy cost of adapting the spin texture between them as the separation between their centres changes. In our SyAFM system, this force is mediated predominantly by short-range exchange and interfacial DMI, with only local interlayer magnetostatic contributions. This stands in sharp contrast to the behavior of conventional FM skyrmions, whose interactions have been extensively characterized [238, 262]. We model the repulsive interaction as a radially symmetric exponentially decaying force [3],

$$\vec{F}_{(a,b)}(\vec{r}) = \frac{\vec{r}}{|\vec{r}|} F_{(a,b)}(|\vec{r}|), \quad \frac{F_{(a,b)}(r)}{D} = 1 \text{ m s}^{-1} \exp\left(-\frac{r-b}{a}\right), \quad (5.2)$$

where r is the skyrmion–skyrmion distance, a characterizes the steepness and effective range of the force, b determines the strength of the force, while D denotes the dissipation constant. This analysis has been done by *Kilian Leutner*. From the analysis of the scattering trajectories, we can determine only the ratio $F_{(a,b)}(r)/D$. Since the prefactor 1 m s^{-1} is of the same order of magnitude as the velocities in the system, b is also of the same order of magnitude as the approximate effective interaction distance. This physically grounded parametrization provides direct experimental access to the interaction law in the regime where exchange and DMI become significant, a regime that has so far remained experimentally elusive at the nanoscale.

Fig. 5.17(a) shows, as an example for skyrmion R1, the experimental trajectory and the predicted trajectory obtained using the estimated interaction potential parameters (a^* , b^*) [3]. Furthermore, micromagnetic simulations were carried out in a system closely matching the experimental dynamic simulation with skyrmion scattering, and the resulting interaction potential parameters in this case are $a^* = (28 \pm 4) \text{ nm}$ and $b^* = (238 \pm 9) \text{ nm}$. The interaction potential is then obtained via $V_{(a,b)}(r) = -\int dr F_{(a,b)}(r)$ resulting in an exponentially decaying repulsive functional dependence. Fig. 5.17(b) shows the experimentally estimated potential (orange) alongside the micromagnetic

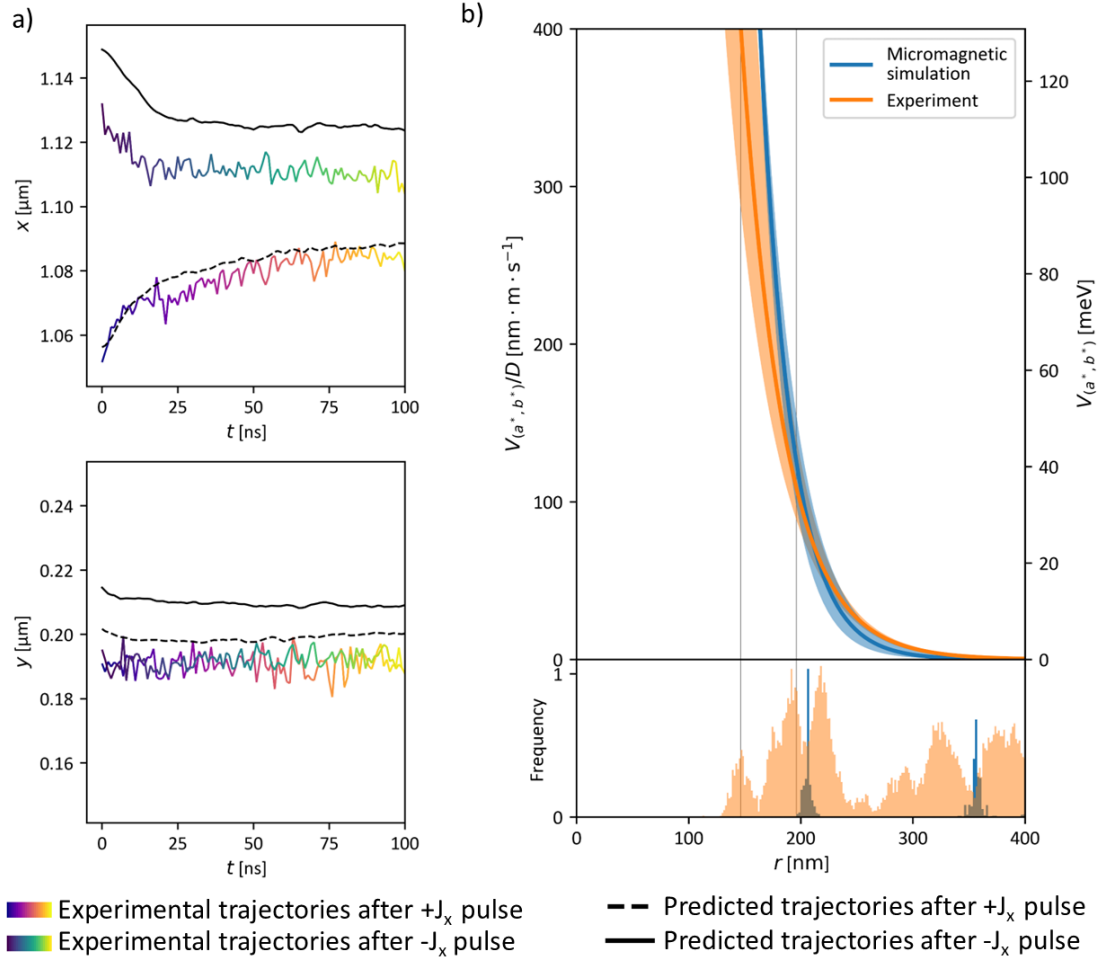


Figure 5.17: **Quantitative extraction of the skyrmion–skyrmion interaction potential from the scattering dynamics of skyrmions.** (a) Comparison between experimentally measured skyrmion trajectories and those predicted by the inverse method based on the Thiele equation for skyrmion R1, capturing their relaxation dynamics after the application of each polarity of the bipolar current pulse. Experimental trajectories are shown for both positive (purple to yellow) and negative (green to blue) current polarities, overlaid with model-predicted trajectories (black dashed and solid lines) obtained by numerical integration of the Thiele equation using the estimated interaction parameters a^* and b^* . (b) The extracted skyrmion–skyrmion interaction potential $V_{(a^*, b^*)} = -\partial_r F_{(a^*, b^*)}(r)$, where r is the skyrmion-skyrmion distance. This axis on the right, V , is not scaled to D and represents the interaction potential for a single bilayer, calculated from the left scale using the dissipation constant. Shaded regions represent uncertainty bands for the 68 % confidence intervals. The lower panel shows the skyrmion–skyrmion distances among skyrmions whose trajectories were predicted, as well as separations between those skyrmions and the boundary skyrmions, illustrating the range over which the potential is estimated by the data. Adapted from [3].

result (blue). The lower panel of Fig. 5.17(b) presents a histogram of skyrmion–skyrmion separations among skyrmions whose trajectories were predicted, as well as separations between those skyrmions and the boundary skyrmions, confirming that the potential is well constrained within the measurement window. The overlapping uncertainty bands between experiment and simulation validate the robustness of the inverse parameter estimation method and support the physical picture of a short-range, rapidly decaying repulsion governed by the finite spatial extent of the skyrmion spin texture. In Fig. 5.17(c), the overlap between experiment and simulation also shows that the significant contributions in both cases were identified, and that the potential from the Thiele equation can be fully explained in this study from the underlying micromagnetism. Such a determination of potential is enabled by the unique L and R skyrmions that reside at the lateral boundary between mobile and immobile regions, experiencing a well-defined repulsive interaction with pinned M skyrmions that act as fixed neighbours. This configuration produces reproducible skyrmion–skyrmion scattering trajectories that are absent in the conventional flow regime of skyrmion dynamics, where collective motion dominates and relative separations remain constant. This approach provides a direct and quantitative determination of the skyrmion–skyrmion interaction potential from the real-time relaxation of nanosecond scattering trajectories, without relying on equilibrium structure factors [262], thermal statistics [238], or other indirect inference methods[¶] By extracting the potential from well-defined scattering events, we probe the interaction on its intrinsic length and timescales, accessing a regime previously unreachable in experiment. In addition, by actively compressing the lattice, we continuously probe the potential over a length scale ranging from 25 % compression to 25 % expansion of the lattice, as seen in the histogram at the bottom of Fig. 5.17(b). While interaction potentials have been inferred in ferromagnetic systems, these measurements are largely qualitative [241, 263], and quantitative estimates have relied on indirect approaches such as iterative Boltzmann inversion [238], which require thermal equilibrium and stochastic motion. Such conditions are not applicable for dynamics that are reproducible over billions of cycles, which we, however, can analyze using our approach [3].

Having characterized the skyrmion-skyrmion interactions in the low-excitation regime, where dynamics are governed by a competition between local pinning potentials and mutual repulsion, we now investigate the response of the skyrmion lattice under increased current densities. In this regime, the applied spin–orbit torques exceed the characteristic pinning thresholds, enabling the skyrmions to overcome local energy barriers and the transition into a depinned state. Fig. 5.18 presents time-resolved skyrmion trajectories as a function of current density for a fixed pulse width of 7.5 ns, illustrating the dynamical crossover from localized motion to collective lattice translation. At lower

[¶]The analysis for extracting the potential has been done by Kilian Leutner (shown in Fig. 5.17).

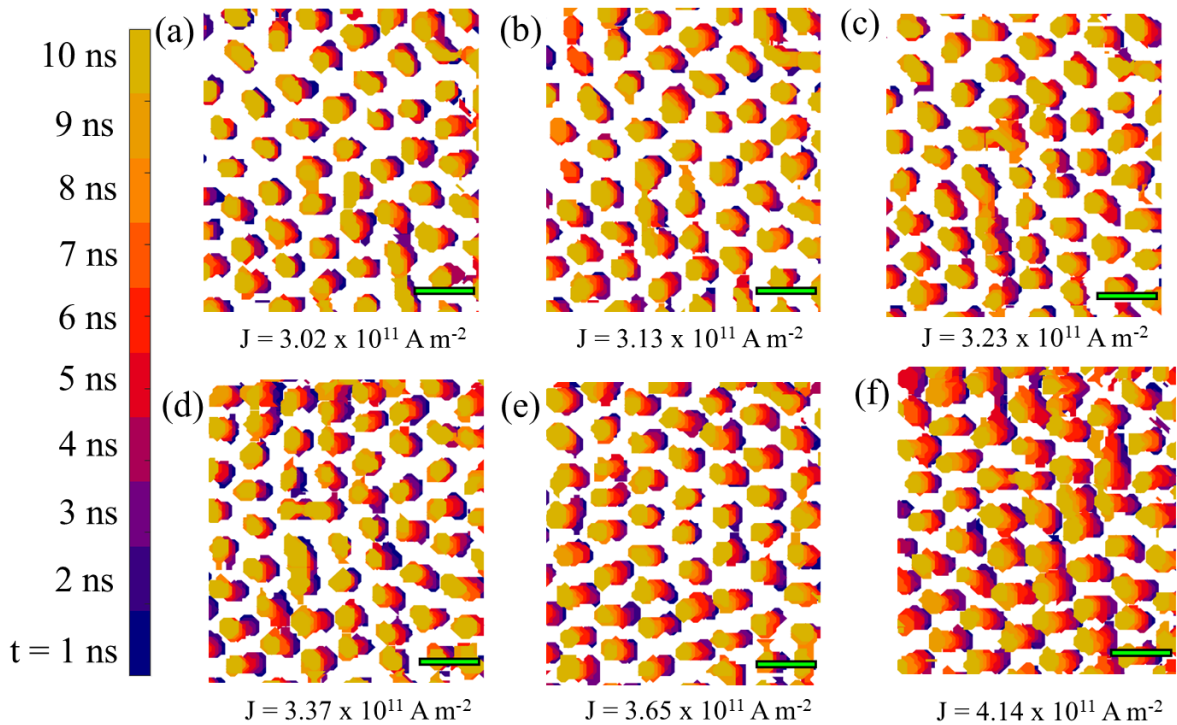


Figure 5.18: **AFM skyrmion dynamics from incoherent to viscous flow regime of motion.** **(a–c)** At lower current densities ($J_x = 3.02 - 3.23 \times 10^{11} \text{ A/m}^2$), skyrmion motion remains irregular due to pinning effects, leading to local lattice distortions and strain accumulation. **(d–f)** As the current density increases beyond $J_x = 3.37 \times 10^{11} \text{ A/m}^2$, the applied spin-orbit torque overcomes pinning barriers, enabling skyrmions to move coherently. This transition reduces lattice distortions and results in more uniform skyrmion trajectories. At the highest current density ($J_x = 4.14 \times 10^{11} \text{ A/m}^2$), the skyrmion lattice exhibits highly ordered motion with minimal deformation, marking the onset of a fully developed flow regime. The scale bar represents 250 nm. Adapted from [3].

current densities (Figs. 5.18a–c), the spin–orbit torque is insufficient to fully overcome pinning, resulting in intermittent motion and spatially heterogeneous trajectories. Individual skyrmions exhibit localized or incomplete displacements, reflecting the influence of the underlying energy landscape and spatial inhomogeneities. As the current density increases (Figs. 5.18d–f), the driving force becomes sufficient to overcome the pinning potential, initiating a depinning transition. In this high-drive regime, the skyrmions undergo coherent translation with synchronized trajectories, maintaining their relative spatial ordering and minimizing internal distortions. This behavior defines the onset of a viscous flow regime, where the energy landscape is effectively flattened by the dominant drive, and the dynamics become deterministic. The transition reflects a shift from thermally assisted, pinning-dominated creep motion to a regime governed by collective and coherent skyrmion translation. The

detailed characterization of this viscous flow regime is discussed in the following sections.

5.4.3 Real-Time Investigation of the cancellation of the Skyrmion Hall Effect

In this section, we explore the high current density regime where all skyrmions move, allowing us to probe the viscous-flow regime. Previous static imaging before and after a current pulse injection has reported efficient and fast AFM skyrmion motion [134, 246], based on position shifts measured before and after current pulses; however, without capturing the intermediate dynamics [134, 246]. However, ultrafast computation cannot be guaranteed by velocity alone, as inertial effects may set an upper bound on the response speed [247]. While such measurements provide valuable insights into the net displacement, they leave open questions regarding the precise temporal evolution of skyrmion motion. In particular, the transient response, including inertial effects, is crucial for device applications, as the inertial lag and damping-controlled settling place a stringent upper bound on the clock frequency of skyrmion-based logic operations. Notably, substantial shape deformations and morphological changes have also been observed during motion [246], complicating the interpretation of underlying SOT-driven behavior. In SyAFM systems, vertically coupled skyrmions in ferromagnetic layers exhibit opposite topological charges, leading to cancellation of the SkHE in the steady state. However, due to the finite interlayer exchange coupling strength, a transient separation between the skyrmions in the two-layer systems can arise during acceleration, giving rise to an effective inertial behavior [265]. The magnitude and duration of this inertial response are strongly dependent on the strength of the interlayer exchange interaction, with weaker coupling leading to larger separations and longer relaxation times. Micromagnetic simulations predict that, upon the application of a current pulse, skyrmions in SyAFMs initially experience a partial transient separation due to the gyroforce before subsequently realigning due to strong antiferromagnetic coupling [265].

To probe this dynamic response of the system, we perform time-resolved pump–probe X-ray microscopy under conditions where the applied current overcomes the local pinning potential for all skyrmions. The higher pulse voltage applied results in a four times higher current density of $1.2 \times 10^{12} \text{ A/m}^2$ and a shorter pulse duration of 2.5 ns was chosen to reduce the average heat load. We first analyse the skyrmion trajectories within each sublattice and compare their motion relative to the current direction. In both sublattices, all skyrmions translate homogeneously along the direction of the applied current. To graphically visualize this motion, in Figs. 5.19(a),(b), the contours of all skyrmions are overlaid with their relative displacements during negative and positive pulses. This produces a real-space map of the motion for approximately 25 skyrmions under alternating current pulses, with the temporal progression encoded in the given colour scales. The resulting paths reveal that the skyrmions retrace symmetric trajectories under current reversal. The coherent overlap

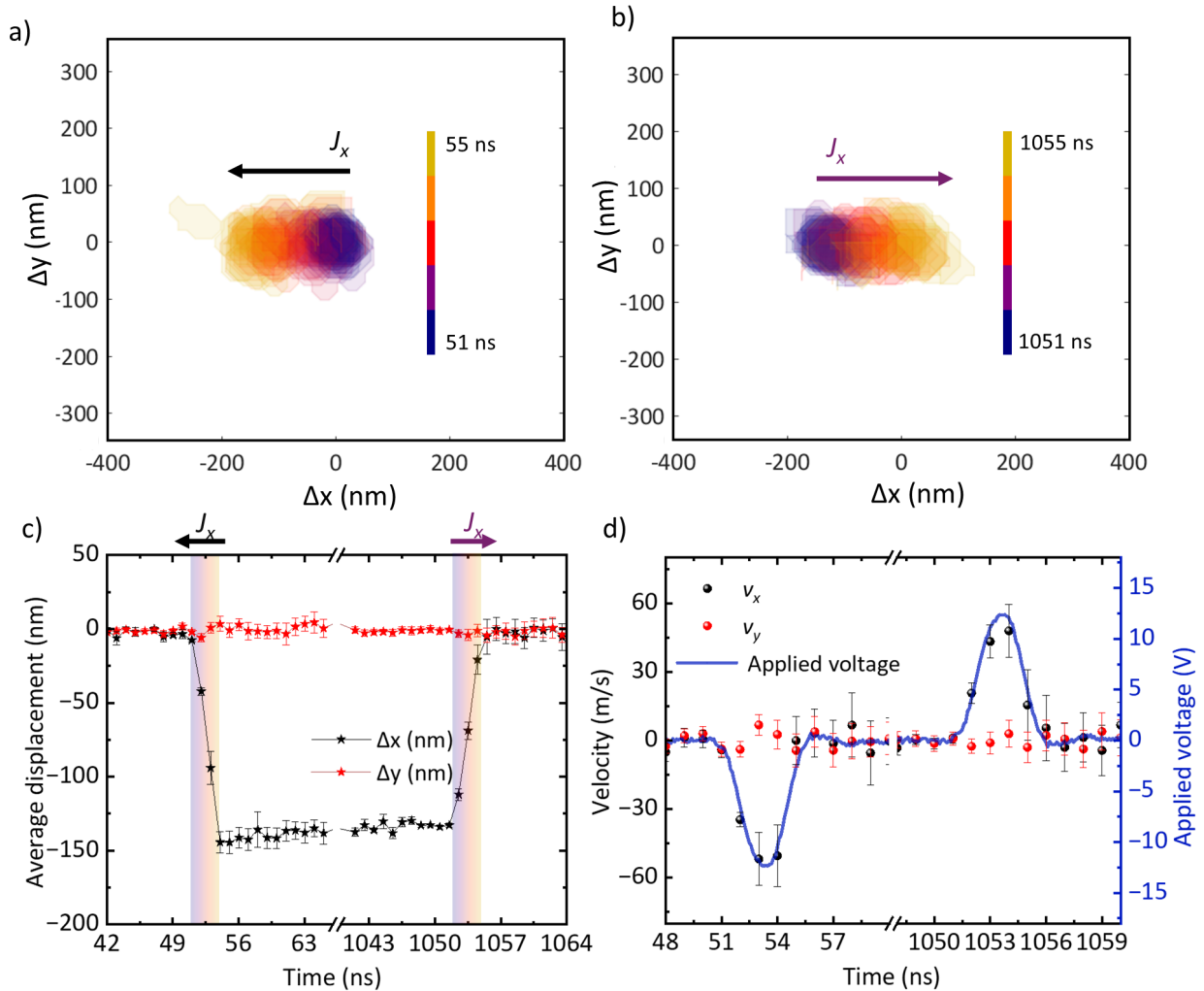


Figure 5.19: **Viscous flow regime of AFM skyrmion dynamics.** (a) Spatiotemporal evolution of skyrmion motion in sublattice A, visualized by overlaying skyrmion contours at different time steps. The color gradient represents the nanosecond-resolved motion of skyrmions under an applied bipolar current pulse. (b) Corresponding skyrmion dynamics under the reverse direction of current, showing synchronized transport under the same driving conditions. (c) Time-resolved average displacement of a magnetic skyrmion along the X (black) and Y (red) directions under application of current pulses. The grey-shaded regions indicate the duration of the current pulses (J_x). (d) Time-resolved velocity components V_x (black) and V_y (red) of skyrmions in response to the applied voltage (blue), illustrating a direct correlation between skyrmion motion and the external drive. Adapted from [3].

of contours defines the coherent viscous flow regime, in which all skyrmions maintain fixed relative positions and move in phase as a rigid lattice, in contrast to the spatially uncorrelated motion observed in the incoherent regime. This collective motion is further quantified in Fig. 5.19(c), where the average displacement over all skyrmions along the x-axis (black) reverses sign with current polarity,

while the y -axis displacement (red) remains near zero throughout the bipolar cycle. This absence of a transverse motion indicates the suppression of the skyrmion Hall effect, a direct consequence of the opposing Magnus forces in the two sublattices in our synthetic antiferromagnetic system. No delay or phase shift between the sublattices is detected within the 1 ns time resolution, in contrast to theoretical predictions that weaker AFM coupling in synthetic systems, relative to crystalline antiferromagnets, would endow AFM skyrmions with a larger effective mass [265]. This constrains the effective inertia from finite interlayer exchange, implying a coupling strength sufficient to suppress any measurable differential acceleration dynamics [265]. The time evolution of the average dynamic skyrmion velocity components v_x and v_y is shown in Fig. 5.19(d), together with the applied bipolar voltage pulse (blue). The velocity profile is symmetric and oscillatory, tracking the bipolar excitation without measurable delay, which indicates negligible inertia effects. The longitudinal component v_x (black points) dominates, remaining aligned with the current direction throughout the cycle, while the transverse component v_y (red points) only slightly fluctuates around zero. Since the core polarity of skyrmions in both the sublattices are opposite, the forces arising from the topological charge term $\mathbf{G} \times \mathbf{v}$ act in opposite directions. When the skyrmions move together, these forces cancel each other, eliminating any net transverse motion. This behavior is a defining signature of the absence of the skyrmion Hall effect, indicating that the opposing Magnus forces within the AFM skyrmion lattice compensate each other, leading to suppression of transverse motion [70]. The dissipative forces, governed by the term $-\alpha\mathbf{D} \times \mathbf{v}$, constructively add up, generating a net longitudinal velocity v_x , which can be expressed as $v_x = F_{\text{ext}}/2\alpha\mathbf{D}$, where F_{ext} represents the external driving force. Here, \mathbf{D} denotes the dissipative tensor of the AFM skyrmion. The external force driving the skyrmions is derived from the spin Hall effect and is expressed as $\mathbf{F}_{\text{ext}} = -\frac{\hbar}{4\pi}j\theta_{\text{SH}}B$, where J_x is the applied current density, θ_{SH} is the spin Hall angle, and B represents a factor that define the spin torque efficiency [4]. Note that no post-pulse relaxation or recoil is observed, indicating the absence of significant pinning or scattering for the observed skyrmions in this regime.

Fig. 5.20 presents the current-density dependence of the dynamic skyrmion velocity components v_x and v_y , extracted from time-resolved measurements across a range of applied current densities. The longitudinal velocity v_x (black stars) shows a clear linear dependence on J_x , confirming that the skyrmion velocity scales proportionally with the applied drive, as expected in the viscous flow regime where pinning is negligible [33]. The transverse velocity v_y (red stars) fluctuates around zero with no systematic trend, indicating that transverse deflection is entirely suppressed over the full range of current densities explored. The in-plane deflection of skyrmions is quantified by the skyrmion Hall angle, defined as $\theta_{\text{SKHA}} = \tan^{-1}(v_y/v_x)$. From the linear fits shown in Fig. 5.20, we extract a skyrmion Hall angle of $(1.4 \pm 1.5)^\circ$, consistent with zero within experimental uncertainty.

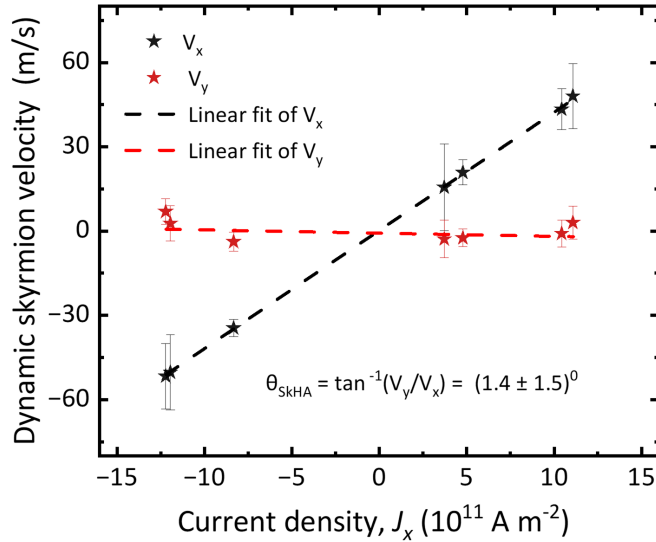


Figure 5.20: **Suppression of the skyrmion Hall effect in the viscous flow regime** Dynamic skyrmion velocity components v_x (black stars) and v_y (red stars) as a function of applied current density J_x . The skyrmion Hall angle θ_{skHA} is obtained from the slope of the linear fit to v_y versus v_x , yielding $(1.4 \pm 1.5)^\circ$. Adapted from [3].

This result directly confirms the suppression of a measurable skyrmion Hall effect, independent of the magnitude or polarity of the applied current. This behavior is in excellent agreement with theoretical predictions for compensated AFM skyrmion lattices, where the net topological charge vanishes and the skyrmion Hall effect is fully suppressed [266]. Notably, the extracted skyrmion Hall angle remains zero within experimental uncertainty. In fully compensated systems, the SkHE vanishes when the effective angular momentum, $\mathbf{L}_{S,\text{eff}}$, approaches zero. In ferrimagnets, the angular compensation point may differ from the magnetization compensation point due to unequal sublattice gyromagnetic ratios γ , especially in rare-earth/transition-metal alloys. By contrast, our SyAFM stack, composed of CoFeB and CoB with nearly identical γ , is designed to align both compensation points, theoretically eliminating the SkHE. Any small residual deflection observed may result from slight asymmetries in γ or interfacial properties.

5.5 Conclusion

This chapter investigates the stabilization, nucleation, and nanosecond-scale dynamics of antiferromagnetic skyrmions in SyAFM multilayers, with emphasis on the role of interlayer coupling, magnetic compensation, and external stimuli. By engineering multilayer stacks near the spin reorientation transition, where the effective anisotropy approaches zero, isolated AFM skyrmions and skyrmion lattices are stabilized via three independent mechanisms: magnetic field application, current injection, and

ultrafast laser excitation. These measurements reveal that skyrmion nucleation proceeds via the fragmentation of labyrinth domains and is facilitated by either Zeeman energy in uncompensated systems or thermally driven reconfiguration in compensated stacks. In particular, Joule heating and ultrafast laser excitation allow controlled skyrmion writing in highly compensated SyAFMs. STXM with XMCD contrast enables sublattice-resolved imaging of AFM skyrmions with 20 nm spatial and 1 ns temporal resolution. By exploiting skyrmion dynamics from the pinned to the viscous flow regime across the previously unexplored incoherent dynamics regime, we explore skyrmion motion and scattering. Our results reveal the full spatiotemporal dynamics within the resolution provided by the STXM of an antiferromagnetic skyrmion lattice in a synthetic antiferromagnet, exposing the key mechanisms that govern its collective behavior. By tuning the excitation amplitude, we access two distinct dynamical regimes: a fragmented, incoherent flow at low current densities and a coherent, rigid-lattice translation at higher drives. In the lower-drive range, the pinned skyrmions act as scattering centres for the mobile ones, and after the latter have been driven toward them by spin-orbit torques, once the current pulse terminates, the resulting repulsive interaction produces a recoil motion, with a characteristic timescale of 3–20 ns, that is opposite to the drive direction. This scattering-mediated recoil allows us to sample the underlying skyrmion-skyrmion interaction potential, enabling its quantitative extraction from the measured relaxation dynamics. We find excellent agreement with micromagnetic simulations, matching both the magnitude and range of the repulsive interaction. Upon increasing the excitation, the system undergoes a transition into a viscous-flow regime. The high temporal resolution of our measurements enables direct tracking of real-space AFM skyrmion trajectories, revealing purely longitudinal motion across a wide range of current densities. Importantly, the dynamics are highly reproducible, with virtually no significant inertia, no transverse drift, and no discernible deformation, underscoring the inherent robustness of AFM skyrmion dynamics. Ultrafast operation demands not only fast velocity but also negligible inertia. Our findings directly show that AFM skyrmion dynamics fulfill these criteria, enabling robust GHz-class operation in ultra-dense information and logic devices. The stability of the skyrmion lattice even at high current densities suggests that AFM skyrmions can overcome key limitations of their ferromagnetic counterparts, particularly in terms of robustness against pinning and stochastic motion. Optimizing interlayer coupling, DMI, and interfacial magnetic anisotropies could lead to further enhanced control over AFM skyrmion dynamics. Our work establishes a quantitative foundation for future exploration of antiferromagnetic topological textures and paves the way for low-power, robust, and scalable spintronic devices built on AFM skyrmions.

Non-reciprocal Current-Induced Dynamics of Hybrid Skyrmion Tubes *

Everything we call real is made of things that cannot be regarded as real.

Niels Bohr

6.1 Introduction

While the previous chapters focused on two-dimensional spin textures such as bimerons and skyrmions, this chapter shifts attention to topological spin textures in the third dimension, such as hybrid chiral skyrmion tubes. In multilayer thin film heterostructures, these textures are stabilized by the balance between *iDMI* and long-range dipolar interactions, giving rise to a helicity that varies continuously along the film thickness. The resulting modulation of chirality, ranging from left-handed Néel-type at one interface through a Bloch-type core to right-handed Néel-type at the opposite surface, constitutes a marked departure from conventional skyrmion tubes. Hybrid skyrmion tubes, therefore, host unconventional dynamic responses to external stimuli, whose nature remains largely unexplored [267].

In this chapter, the experimental observation of hybrid chiral skyrmion tubes is presented for

*The chapter is adapted from: Dohi, Takaaki, Bhukta, Mona, et al. Observation of a non-reciprocal skyrmion Hall effect of hybrid chiral skyrmion tubes in synthetic antiferromagnetic multilayers Nat. Commun. 16, 8525 (2025) <https://doi.org/10.1038/s41467-025-63759-7>.

SyAFM multilayers with 50% magnetic compensation. Their unconventional dynamics are further demonstrated, in particular, a current-induced non-reciprocal skyrmion Hall effect (NSkHE) in the flow regime at room temperature [4]. The SyAFM system consists of multiple ferromagnetic layers antiferromagnetically coupled via ultrathin nonmagnetic spacers. This configuration allows the degree of nonreciprocity to be tuned by controlling long-range dipolar interactions together with interfacial and interlayer exchange interactions. Notably, the dynamics that exhibit an NSkHE do not yield significant differences in the velocity, and are therefore qualitatively distinct from the previously reported non-reciprocal dynamics of conventional two-dimensional skyrmions induced by extrinsic in-plane symmetry breaking, such as asymmetric confinements or pinning [268], or exchange bias [33]. This identifies an intrinsic origin directly associated with the complex 3D spin structure. Micromagnetic modeling indicates that hybrid chiral skyrmion tubes experience an asymmetric SOT contribution for opposite current polarities, arising from helicity changes during their motion, which in turn induces the non-reciprocity observed in the skyrmion Hall effect. These results highlight the decisive role of the internal degrees of freedom of skyrmion tubes, which have often been neglected, but are shown here to govern the strong excitation regime relevant to the current densities studied [4]. Consequently, this work provides fundamental insights into the previously unexplored dynamics of 3D topological spin textures and establishes their unconventional dynamical responses as a promising basis for advanced skyrmion-based technologies. The experimental details, including sample structure and characterization for this chapter, can be found in (📖 labbook experiment ID 18907).

6.2 Strategy to Stabilize Hybrid Skyrmions

In ultrathin films with interfacial DMI, homochiral Néel walls are favored, whereas in systems with bulk DMI, chiral Bloch walls can be stabilized. In thicker films with negligible DMI, however, magnetostatic interactions favor achiral Bloch walls. In magnetic multilayers, long-range dipolar interactions can modify these ideal cases [269]. In FM stacks separated by nonmagnetic spacers, stray fields from one layer influence the magnetization in adjacent layers, producing a depth-dependent rotation of the domain wall that becomes energetically favorable once the magnetic thickness exceeds a critical scale $l_w = \epsilon_{\text{Néel}} / (\mu_0 M_s^2)$ (where $\epsilon_{\text{Néel}}$ denotes the domain wall energy density of a Néel wall), beyond which magnetostatic interactions favor flux-closure arrangements. In the absence of IDMI, dipolar interactions dominate the wall structure: the central layers adopt Bloch-type rotation to minimize magnetostatic charges, while the outer layers form Néel-like caps to close magnetic flux lines. This hybrid configuration reduces stray-field energy by allowing vertical circulation of magnetization, giving rise to a three-dimensional wall profile with opposite Néel chiralities at the two interfaces. Such

domain walls are referred to as hybrid domain walls [267, 269], as shown in Fig. 6.1(a). Hybrid domain walls were first experimentally observed by Legrand et al. [267] in $[\text{Pt}/\text{Co}/\text{AlO}_x]_N$ multilayers. In this system, the balance between *iDMI* and long-range dipolar interactions produces a thickness-dependent chirality: near the bottom Pt interface, the wall was Néel-type with one handedness, in the middle of the stack, it was Bloch-type, and near the top interface, it became Néel-type with the opposite handedness.

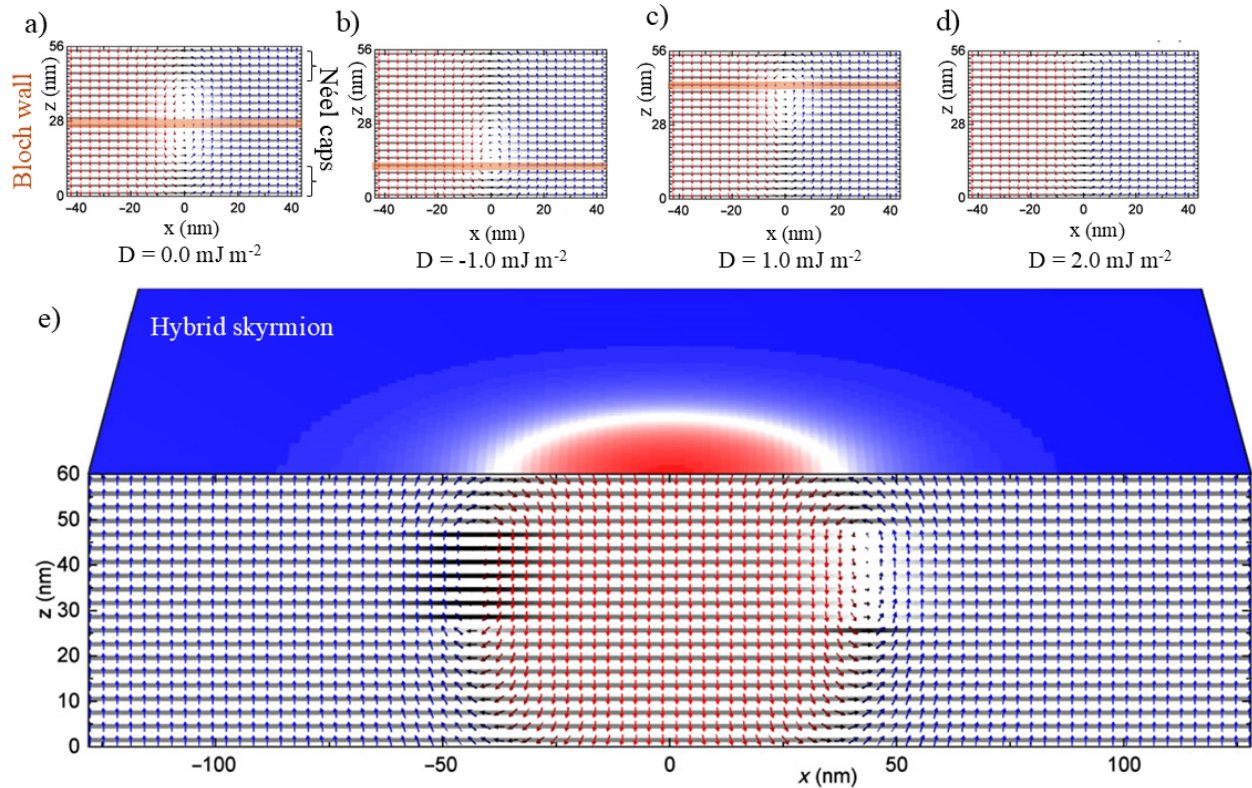


Figure 6.1: **Micromagnetic simulation of hybrid domain walls and hybrid skyrmions in magnetic multilayers.** (a–d) Cross-sectional magnetization profiles of domain walls for different values of interfacial DMI D . Arrows represent the in-plane magnetization, while the color scale denotes the out-of-plane magnetization component (m_z). For $D = 0.0 \text{ mJ m}^{-2}$ (a), dipolar interactions dominate, resulting in a Bloch core in the film mid-plane with Néel caps of opposite chirality at the top and bottom interfaces. For finite DMI ($D = \pm 1.0 \text{ mJ m}^{-2}$) in (b) and (c), the degeneracy between opposite Néel caps is lifted, and the Bloch core is displaced toward the interface with unfavored chirality. For sufficiently large DMI ($D = 2.0 \text{ mJ m}^{-2}$) in (d), the Bloch core is suppressed. (e) Three-dimensional magnetization structure of a hybrid skyrmion in the same multilayer geometry. Adapted from Ref. [267] with permission.

The introduction of interfacial *DMI* modifies the depth-dependent chirality imposed by dipolar interactions in multilayers. A finite *DMI* lowers the energy of Néel wall, making one sense of in-

plane rotation energetically favorable depending on the sign of $i\text{DMI}$. This lifts the degeneracy between Néel caps of opposite chirality and stabilizes the configuration whose handedness matches the DMI preference. This, in turn, results in a vertical displacement of the Bloch wall toward the interface where the Néel cap is energetically unfavorable. This behavior is evident in Figs. 6.1(b) and 6.1(c) for $D = -1.0$ and $D = 1.0 \text{ mJ m}^{-2}$, respectively, where the Bloch region shifts toward the bottom or top surface depending on the DMI sign. When the DMI contribution exceeds the dipolar term, the Bloch wall is completely suppressed, as shown for $D = 2.0 \text{ mJ m}^{-2}$ in Fig. 6.1(d). This competition provides a direct means of tuning and controlling the three-dimensional spin structure of domain walls in multilayers. In such systems, where hybrid domain walls are energetically favorable, skyrmions adopt a hybrid configuration in which the domain wall profile along the skyrmion perimeter exhibits Néel-type character near the interfaces and Bloch-type rotation in the central layers. Hybrid skyrmions have been directly imaged using a range of experimental techniques, including X-ray resonant magnetic scattering [267], small-angle neutron scattering [270], SEMPA [271, 272], LTEM [273–275], and NV magnetometry [276], all of which have revealed the three-dimensional spin structure and hybrid domain wall character along the film thickness. These hybrid skyrmion tubes can exhibit a multifaceted response to SOTs [277, 278], giving rise to a rich spectrum of dynamic behaviors.

Since the competition between dipolar interactions and interfacial DMI is the primary mechanism governing the formation of hybrid skyrmions and domain walls, this interplay in SyAFMs is further enriched by the ability to finely tune the magnetic compensation through controlled variation of the thickness and composition of the ferromagnetic sublattices, as discussed in Section 5.2 of the Chapter 5. We define the magnetic compensation as

$$m_c(\%) = 1 - \frac{|M_{s,A} \cdot t_A - M_{s,B} \cdot t_B|}{M_{s,A} \cdot t_A + M_{s,B} \cdot t_B} \quad (6.1)$$

where $M_{s,A}$ and $M_{s,B}$ denote the saturation magnetizations of the individual FM sublattices A and B, respectively, and t_A and t_B are their corresponding thicknesses. A value of $m_c = 100 \%$ corresponds to a fully compensated antiferromagnetic state, whereas $m_c = 0 \%$ indicates a ferromagnetic configuration. By adjusting the compensation between the magnetic layers, one can effectively tune the influence of long-range dipolar interactions and thereby stabilize skyrmions with distinct static and dynamic properties [4]. In particular, long-range dipolar interactions become increasingly prominent in SyAFM systems with substantial uncompensated moments, potentially serving as a stabilizing mechanism for antiferromagnetically coupled hybrid skyrmion tubes. The hybrid character of these tubes, determined by the relative amounts of their Néel and Bloch components, can be tuned by varying the magnetic compensation ratio and the number of repetitions within the SyAFM multilayers. This tun-

ability provides a pathway to tailor the internal structure and dynamic response of hybrid skyrmions. The uncompensated moment modulates the gyroforce (proportional to $4\pi(M_{s,A}t_A - M_{s,B}t_B)$) experienced by skyrmions, thereby influencing the skyrmion Hall angle under current-driven motion. To systematically investigate the influence of magnetic compensation, SyAFM stacks with varying degrees of net moment were engineered. Let us recall the Fig. 5.1(a), which represents the magnetic hysteresis loops that were measured using SQUID magnetometer for these stacks #S1- #S5. The projection of the normalized magnetic moment along the field axis reflects the stack's net uncompensated moment. In this chapter, stacks #S1 and #S2 are discussed to compare the current-induced dynamics of hybrid chiral skyrmion tubes with those of conventional Néel-type skyrmion tubes.

6.2.1 Observation of Hybrid Skyrmions and Néel Skyrmion Tubes

To provide direct evidence for the presence of Bloch-type contributions in the domain wall structure of the hybrid skyrmions, LTEM was performed on the stack #S1 exhibiting 50% magnetic compensation. The sample was deposited on a silicon nitride membrane to enable high-resolution imaging in transmission geometry. The LTEM measurements were conducted using a TFS Titan transmission electron microscope operated at an accelerating voltage of 300 kV in Lorentz mode by *Dr. Thibaud Denneulin* at Forschungszentrum Jülich. An out-of-plane magnetic field was applied via the objective lens, whose field strength was pre-calibrated using a Hall sensor. The resulting magnetic contrast was recorded with a Gatan UltraScan 1000 XP CCD camera. These measurements allow for the spatially resolved visualization of domain wall structures and enable the identification of finite Bloch components indicative of hybrid chiral character across the film thickness.

Fig. 6.2(a) and 6.2(b) present LTEM images acquired at tilt angles of 0° and 10° , respectively, from the stack #S1. These images reveal the presence of stripe-like magnetic domains. In out-of-plane magnetized systems, the Fresnel contrast observed in LTEM depends sensitively on the nature of the domain wall. Specifically, Bloch-type domain walls generate a detectable contrast at normal incidence ($\alpha = 0^\circ$), whereas Néel-type domain walls, due to their in-plane magnetization being aligned with the beam direction, remain largely invisible. Upon tilting the specimen, the projected out-of-plane magnetization component contributes to the observed contrast, allowing differentiation between domain wall types. In the present case, the LTEM contrast at 0° is significantly weaker than at 10° , indicating that the domain walls are predominantly of Néel character. To further analyze the domain wall structure, intensity profiles were extracted across individual domains, as shown in Fig. 6.2(c) and Fig. 6.2(d). The line profile in Fig. 6.2(c) exhibits a characteristic bright/dark/bright modulation, indicative of a finite, albeit small, Bloch component superimposed on the dominant Néel texture. In Fig. 6.2(d), the blue profile was extracted from a domain aligned perpendicular to the

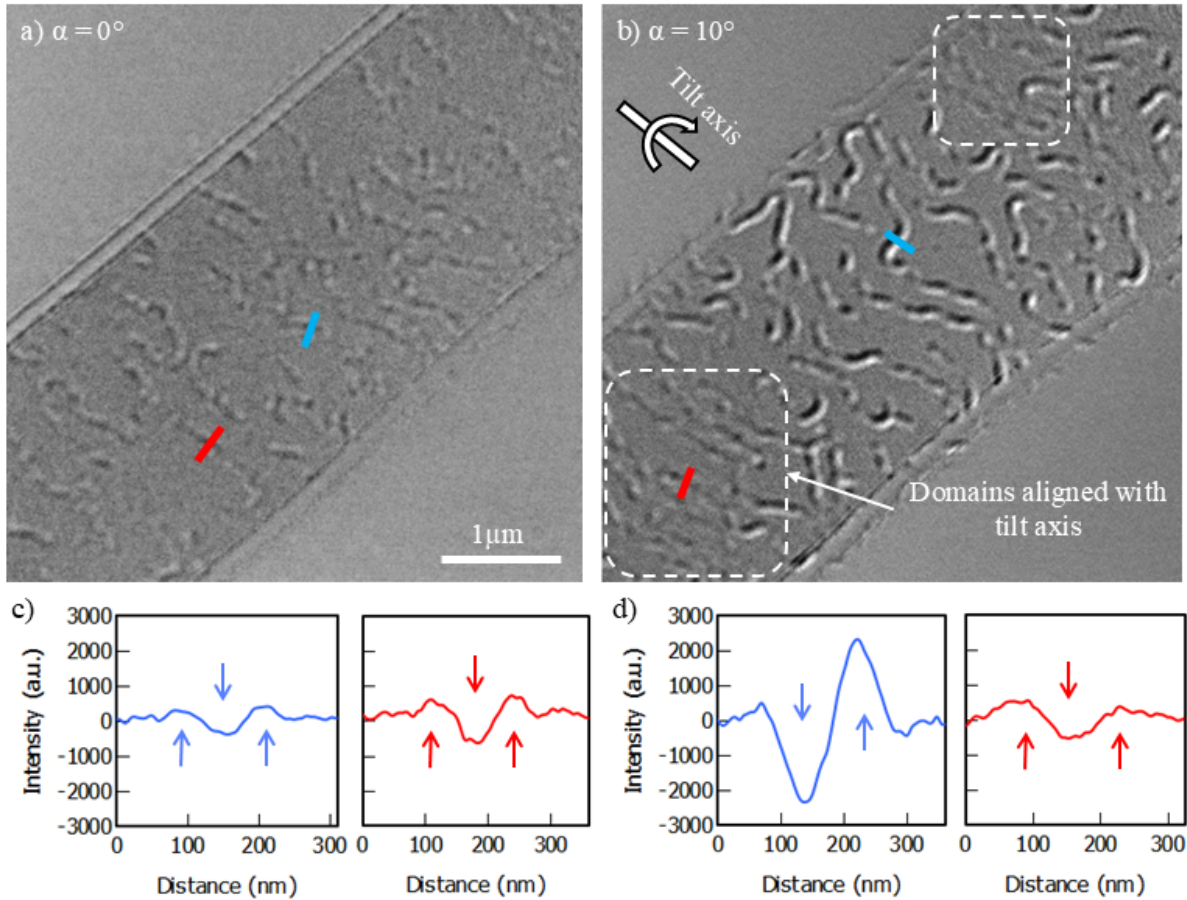


Figure 6.2: **Lorentz TEM imaging of hybrid chiral domain walls.** (a,b) LTEM images acquired with an underfocus of 4 mm and an applied out-of-plane magnetic field of 85 mT, recorded at tilt angles of (a) $\alpha = 0^\circ$ and (b) $\alpha = 10^\circ$. A non-magnetic background was subtracted by referencing images acquired after magnetic saturation. (c,d) Line profiles extracted from the regions marked by blue and red lines in (a) and (b), respectively. Adapted from [4].

tilt axis and reveals a strong dark/bright contrast, consistent with the projection of out-of-plane magnetization components. The red profile, taken from a domain aligned parallel to the tilt axis, shows a weaker bright/dark/bright distribution similar to the one observed at 0° , reinforcing the conclusion that a small Bloch component is present. For a tilt angle of 10° , the projected out-of-plane magnetization contributes approximately $\sin(10^\circ) \approx 17\%$ to the image contrast. Given that the Bloch-type contribution accounts for only one-sixth of the full LTEM contrast in this geometry, the Bloch component is estimated to contribute approximately 3% to the total magnetic contrast, thus confirming the hybrid Néel–Bloch character of the domain walls.

To demonstrate a direct comparison between hybrid chiral skyrmion tubes and conventional

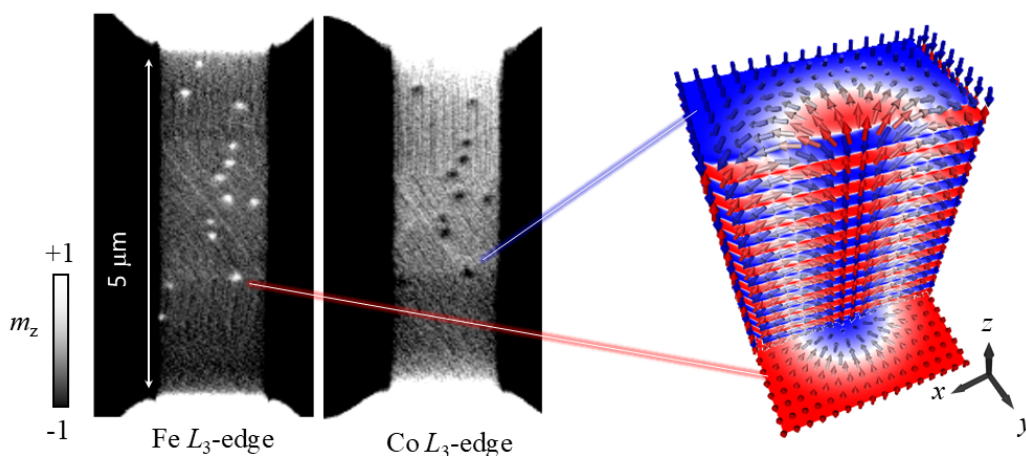


Figure 6.3: **Observation of Néel skyrmion tubes.** Direct observation of SyAFM coupling of skyrmion tubes under perpendicular magnetic field of 130 mT in stack #S2 at room temperature, and schematic of the spin structure of the SyAFM skyrmion tube. Adapted from [4].

Néel-type skyrmion tubes, element-specific [STXM](#) was employed to image stack #S2, which exhibits a magnetic compensation level of 80% and serves as a reference system hosting conventional Néel-type skyrmion tubes. These measurements were conducted at the MAXYMUS endstation at BESSY II (Helmholtz-Zentrum Berlin) and the PoLux beamline of the Swiss Light Source. [STXM](#), in combination with [XMCD](#) contrast, enables unambiguous detection of magnetic signals from individual elements due to the element- and energy-dependent nature of X-ray absorption. Prior to imaging, X-ray absorption spectra were acquired to determine the element-specific resonance energies, identifying the Fe L_3 edge at 708.1 eV and the Co L_3 edge at 778.6 eV. These energies allow selective probing of the magnetic response from each sublattice. The resulting [XMCD](#) images reveal a clear antiferromagnetic alignment of skyrmion contrast between the Fe and Co layers, as shown in Fig. 6.3, thereby confirming the presence of antiferromagnetically coupled skyrmion tubes in stack #S2. Since [STXM](#) is a transmission-based technique, the magnetic contrast is averaged over all layers containing the selected element, indicating that the observed textures extend coherently throughout the multilayer stack. The uniform and continuous contrast further confirms the formation of laterally aligned and vertically coherent skyrmion tubes. Additionally, no multilevel gray contrast is detected in the [XMCD](#) signal, ruling out the presence of vertical inhomogeneities such as skyrmion cocoons [279] or bobber-type terminations. These observations collectively confirm strong and uniform interlayer exchange coupling in stack #S2.

Note that the skyrmion tubes do not nucleate spontaneously near the spin reorientation transition at zero magnetic fields, where the effective perpendicular anisotropy approaches zero. In this

regime, the uniform out-of-plane magnetization is unstable, and modulated spin textures, including chiral skyrmions and stripe domains, are energetically favored. The *iDMI* and long-range dipolar interactions dominate over exchange and anisotropy energies, promoting a multidomain ground state. By adjusting the thickness of the ferromagnetic sublattices, the system is tuned into this regime, facilitating spontaneous multidomain formation. Isolated skyrmions are then stabilized by an external out-of-plane magnetic field, which suppresses antiparallel stripe domains and favors compact circular textures. Due to the near-degenerate energy landscape, additional external stimuli are required to overcome the nucleation barrier. To reliably initialize well-defined skyrmion tubes across different compensation levels, two approaches were employed: magnetic field cycling and current-induced nucleation [31, 248], as discussed in section 5.3 of Chapter 5. Following current assisted nucleation under perpendicular magnetic fields, the skyrmion tube diameter was adjusted to approximately 100 nm, with a size variation of less than 15 % achieved by fine-tuning the magnetic field amplitude. Specifically, out-of-plane fields of 70 mT and 130 mT were applied to stack #S1 and stack #S2, respectively, to stabilize skyrmions with uniform diameters across the entire field of view.

6.2.2 Role of Magnetic Compensation

Magnetic compensation in synthetic antiferromagnetic multilayers provides an effective means to tune the net magnetic moment and thereby control the strength of long-range dipolar interactions. These interactions, in turn, influence the emergence of Bloch-type in-plane spin components that contribute to the overall helicity of the skyrmion tube. Therefore, the compensation ratio plays a pivotal role in defining the internal spin structure and hybrid character of antiferromagnetic skyrmions. To systematically investigate this effect, micromagnetic simulations were conducted across a range of compensation levels. Fig. 6.4 shows two-dimensional magnetization maps for the topmost (panel a) and bottommost (panel b) layers of synthetic antiferromagnetic stacks with varying magnetic compensation. The arrow directions represent the in-plane magnetization orientation, while the color scale encodes the x -component of the magnetization. For high compensation levels of 80 % and 60 %, both layers exhibit nearly identical chirality, corresponding to a uniform Néel-type configuration stabilized by *iDMI*. At a compensation level of 50 %, a clear asymmetry between the top and bottom layers becomes apparent, reflecting the emergence of a helicity gradient along the multilayer thickness. This intermediate regime marks the onset of a hybrid configuration, wherein the interfacial Néel character is progressively modulated by Bloch-type contributions from dipolar interactions. As the compensation is further reduced to 40 % and 20 %, the contrast between top and bottom layers intensifies, indicating a dominant Bloch character in the spin structure. At 20 %, the skyrmion approaches a nearly pure Bloch-type configuration, signifying a transformation of the domain wall

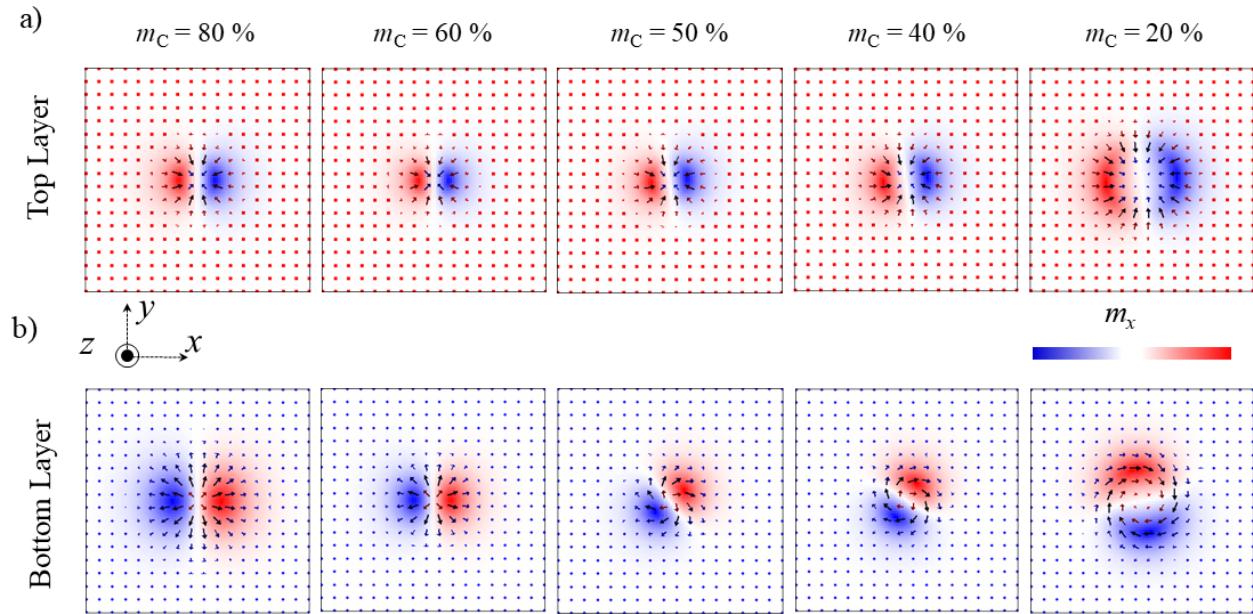


Figure 6.4: **Micromagnetic simulations of AFM hybrid chiral skyrmion tubes at varying compensation.** (a) Two-dimensional magnetization profiles of the topmost layer and (b) the bottom-most layer for skyrmions in SyAFM stacks with magnetic compensation levels of 80 %, 60 %, 50 %, 40 %, and 20 %, respectively. Arrows indicate the local in-plane magnetization direction, while the color scale represents the x-component of the magnetization. At 80 % and 60 % compensation, the helicity remains uniform across the multilayer, corresponding to a Néel-type skyrmion. At 50 %, a helicity gradient emerges through the stack, indicative of a hybrid Néel–Bloch character. At 40 % compensation, the Bloch component becomes more prominent, and at 20 %, the skyrmion exhibits a nearly pure Bloch-type configuration. Adapted from [4].

profile driven by reduced magnetic compensation.

6.3 Current-Induced Dynamics of SyAFM Skyrmion Tubes

Having discussed the stabilization and observation of hybrid skyrmions, this section now focuses on their current-induced dynamics. Unlike static configurations, dynamic behaviors such as skyrmion motion, deformation, or annihilation directly determine the functional performance for spintronics applications. In particular, skyrmion tubes in SyAFMs offer an attractive platform for current-driven applications due to their enhanced thermal stability, suppressed SkHE, and potential for high-speed motion [134, 246]. However, the internal structure of these three-dimensional textures, especially hybrid chiral configurations, adds complexity to their motion under SOTs. In this section, the current-induced dynamics of SyAFM skyrmion tubes are investigated using two representative stacks, stack #S1 (50% compensation) and stack #S2 (80% compensation). Skyrmion tubes were first

nucleated by applying a relatively high current density ($J \geq 15 \times 10^{11} \text{ A/m}^2$) under selected out-of-plane magnetic fields [31, 248], and the average skyrmion velocity as well as the average skyrmion Hall angle were subsequently measured for multilayer stacks with different magnetic compensation ratios. The nucleation of AFM skyrmions in stack #S1 and stack #S2 was achieved using bipolar current pulses, as described in Chapter 5, Section 5.3.2.

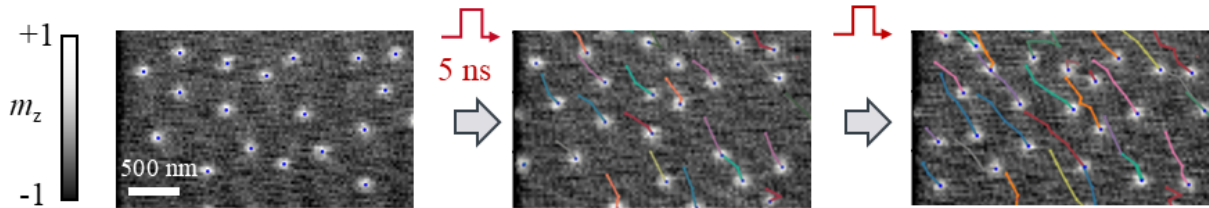


Figure 6.5: **Current-induced motion of SyAFM skyrmion tubes in stack #S1.** Static STXM images at the Fe L_3 and Co L_3 absorption edges of stack #S1 (50% compensation), acquired before and after the application of five unipolar current pulses (5 ns duration, $J = 1.3 \times 10^{12} \text{ A/m}^2$). Adapted from Ref. [4].

To investigate deterministic manipulation of SyAFM skyrmion tubes under current-driven conditions, element-specific STXM imaging was performed on stack #S1 and stack #S2. Fig. 6.5 presents one example from stack #S1 for $J = 1.3 \times 10^{12} \text{ A/m}^2$ imaged at Fe L_3 absorption edges. Figs 6.6(a) and (b) show static magnetic contrast images acquired at the Fe and Co L_3 absorption edges, corresponding to the A and B sublattices, respectively, for stack #S2. Prior to current injection (Fig. 6.6(a)), isolated skyrmion tubes are resolved, appearing with opposite contrast at the two edges due to the antiparallel alignment of the FM sublattices. After application of five unipolar current pulses (5 ns duration each, $J = 9.7 \times 10^{11} \text{ A/m}^2$), the skyrmions exhibit a net displacement along the current direction (Fig. 6.6(b)). The direction and magnitude of motion are identical for both sublattices, indicating strong interlayer coupling and coherent propagation of the antiferromagnetically bound spin textures. The observation that SyAFM skyrmion tubes move collinearly with the current confirms that SOTs are the dominant mechanism driving their motion, consistent with prior reports in both ferromagnetic [31, 33, 78, 181] and SyAFM multilayers [134].

To quantify the current-induced dynamics of SyAFM skyrmion tubes, trajectories were analyzed using the Python-based particle tracking package TrackPy. From these trajectories, the statistical distribution of skyrmion velocities v was obtained, as shown in Fig. 6.6(c). The average velocity v_{ave} , defined as the peak position of a Gaussian fit to each distribution, is plotted as a function of current density in Fig. 6.6(d). A comparison between stack #S1 and stack #S2 shows that skyrmions in stack #S2 reach higher velocities under identical drive conditions. This enhancement

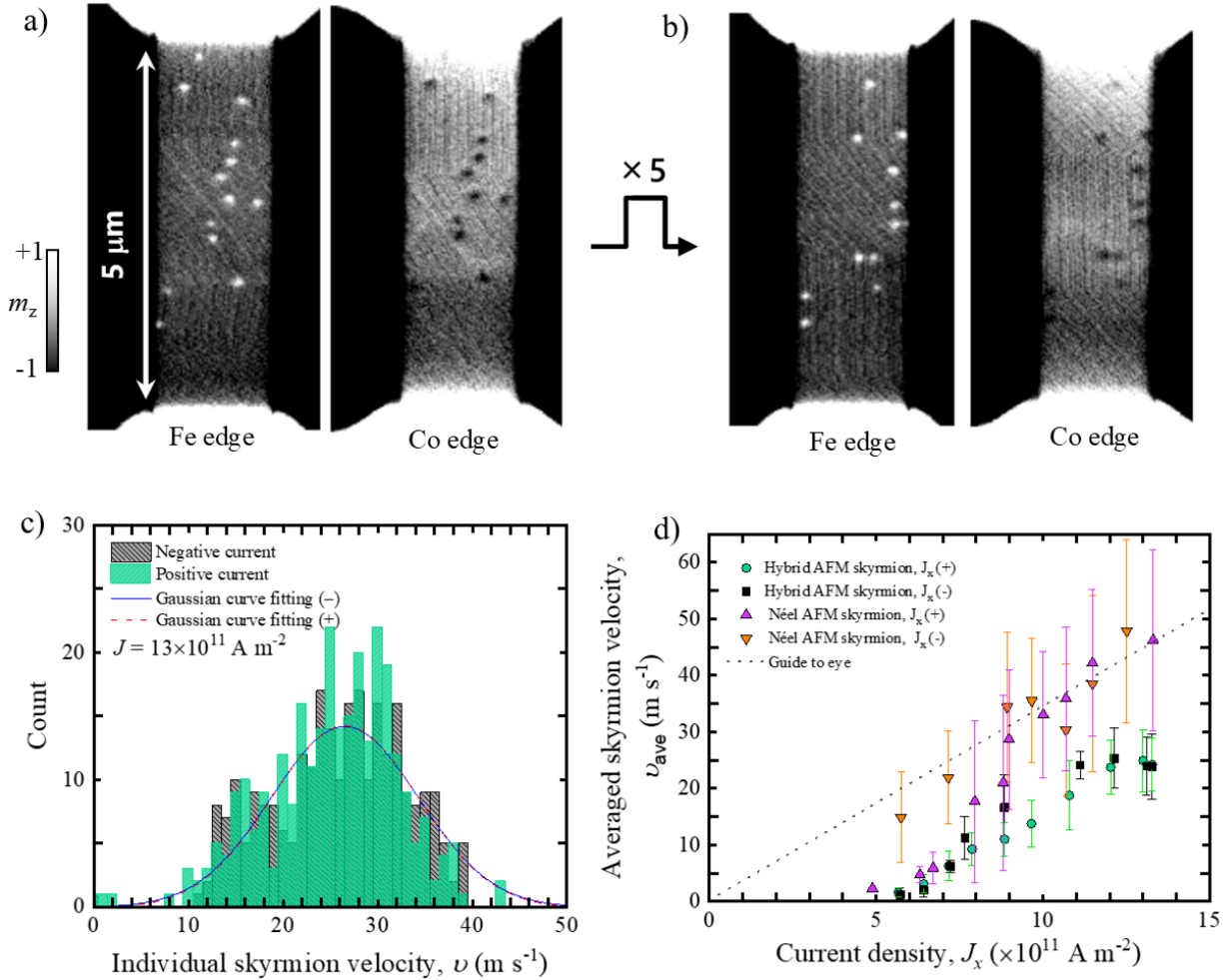


Figure 6.6: **Current-induced motion of SyAFM skyrmion tubes in stack #S2.** (a, b) Static STXM images at the Fe and Co L_3 absorption edges of stack #S2 (80% compensation), acquired before (a) and after (b) the application of five unipolar current pulses (5 ns duration, $J = 9.7 \times 10^{11} \text{ A/m}^2$). The skyrmion tubes exhibit coherent displacement along the current direction, with opposite contrast at Fe and Co edges confirming their antiferromagnetic nature. (c) Statistical distribution of individual SyAFM skyrmion tube velocities for stack #S1, measured under an out-of-plane magnetic field $\mu_0 H_z = 70 \text{ mT}$ and a current density $J = 1.3 \times 10^{12} \text{ A/m}^2$. Red and blue data points correspond to positive and negative current polarities, respectively. The solid curves represent Gaussian fits to the velocity distributions. (d) The current density dependence of the average velocity, v_{ave} , is defined by the Gaussian peak with $\pm 1\sigma$ bars of the curve fitting in (c). Green circles, black rectangles, magenta triangles, and orange inverse triangles represent positive current polarity (stack #S1), negative polarity (stack #S1), positive polarity (stack #S2), and negative polarity (stack #S2), respectively. Adapted from [4].

is attributed to the larger compensated magnetic moment m_c in stack #S2, consistent with earlier reports [134]. The velocity remains nearly symmetric for positive and negative current polarities. The

SyAFM skyrmion tubes exhibit clear diagonal trajectories, demonstrating a finite SkHE arising from the uncompensated magnetic moments. The absolute value of the skyrmion Hall angle depends on both the skyrmion size and the domain wall width [30], scaling inversely with the skyrmion radius for a fixed wall width. To elucidate the current-induced dynamics in greater detail, the SkHE is analyzed systematically in the following subsection.

6.3.1 Non-reciprocity in the SkHE

For a quantitative evaluation of the SkHE, the same analysis protocol as for the velocity was employed, where the average skyrmion Hall angle, θ_{ave} , was extracted from the peak position of a Gaussian fit to the statistical distribution. Fig. 6.7(a) shows the resulting histogram of θ_{ave} for skyrmion ensembles in stack #S1 ($m_c = 50\%$). At an average velocity of $v_{\text{ave}} = 10 \text{ m s}^{-1}$, corresponding to the creep/depinning regime, the values of θ_{ave} remain reciprocal with respect to current polarity. In contrast, at higher velocity in the flow regime ($v_{\text{ave}} = 25 \text{ m s}^{-1}$, see Fig. 6.7(b)), the Gaussian peaks for opposite current polarities separate, evidencing an NSkHE. To identify the physical origin of this non-reciprocity, the dependence of θ_{ave} on v_{ave} was systematically analyzed. The absence of SkHE in the creep/depinning regime indicates that the effect is not governed by extrinsic pinning but instead arises from an intrinsic mechanism linked to the internal degrees of freedom of the hybrid skyrmion tubes [30].

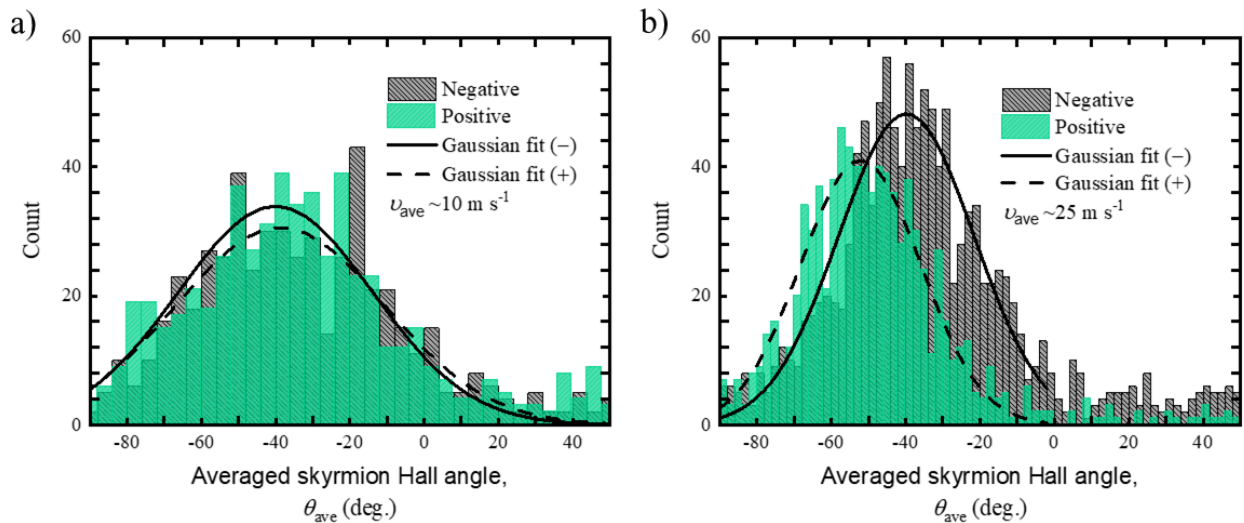


Figure 6.7: **Dependence of the non-reciprocal skyrmion Hall effect on the degree of magnetic compensation.** (a) The full statistics of the individual skyrmion Hall angle for stack #S1 ($m_c = 50\%$) under $\mu_0 H_z = 70 \text{ mT}$ at $v_{\text{ave}} = 10 \text{ m s}^{-1}$. (b) The corresponding distribution at $v_{\text{ave}} = 25 \text{ m s}^{-1}$. Adapted from [4].

Moreover, Fig. 6.8 displays the average velocity dependence of the skyrmion Hall angle, θ_{ave} , for Néel-type AFM skyrmions (left) and hybrid AFM skyrmion tubes (right). In both cases, θ_{ave} was obtained from Gaussian fits to the statistical distributions of individual trajectories, with the error bars representing the standard deviation of the fit. For Néel-type AFM skyrmions, θ_{ave} remains nearly constant over the entire velocity range and is reciprocal with respect to current polarity. In stark contrast, hybrid AFM skyrmion tubes display a pronounced increase of θ_{ave} with velocity, together with a clear asymmetry between positive and negative current polarities. This polarity-dependent response directly evidences the emergence of non-reciprocity of the motion in the flow regime. The comparison between the two cases demonstrates that the degree of magnetic compensation is a decisive control parameter, with the strong long-range dipolar interaction present in stack #S1 playing a central role in governing the NSkHE.

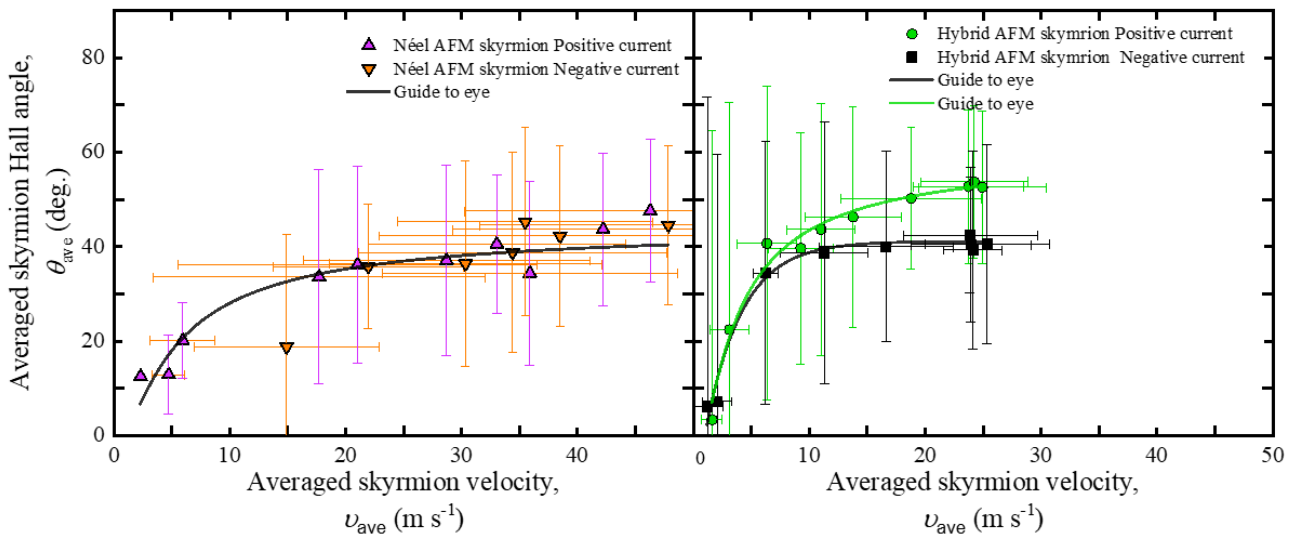


Figure 6.8: **Average velocity dependence of the skyrmion Hall angle.** The average velocity dependence of θ_{ave} with $\pm 1\sigma$ error bars obtained from the Gaussian fits to the peaks. Green circles, black rectangles, magenta triangles, and orange inverse triangles represent positive current polarity (stack #S1), negative current polarity (stack #S1), positive current polarity (stack #S2), and negative current polarity (stack #S2), respectively.

6.4 Micromagnetic Simulations of Hybrid Skyrmions

In hybrid skyrmions, the variation in spin texture along the vertical axis results from the competition between iDMI and long-range dipolar interactions. Theoretical studies have shown that hybrid skyrmions can respond to SOTs in a non-uniform way, due to the vertical variation in helic-

ity [277, 278]. As a result, their motion may not follow the behavior expected from simple rigid-body models. In SyAFMs with significant uncompensated magnetic moments, long-range dipolar interactions are expected to play a dominant role. These interactions may contribute to the stabilization of antiferromagnetically coupled hybrid skyrmion tubes. The hybrid character can be modulated by tuning the magnetic compensation ratio and the number of bilayer repetitions in the SyAFM stack. This provides a potential mechanism for controlling the dynamical behavior of SyAFM skyrmion tubes. To test this hypothesis, we performed micromagnetic simulations using the MuMax³ software package [280]. The simulation setup consists of a multilayer stack structure (12 ferromagnetic layers) where layers with opposite magnetization are coupled by interlayer exchange interaction. The multilayer stack geometry considered has each layer with a lateral size of $256 \times 256 \text{ nm}^2$ and a thickness of 1 nm. The system was discretized with a mesh size of $(1 \times 1 \times 1) \text{ nm}^3$ and periodic boundary conditions were imposed along the x and y directions with a period of 8 repetitions. The dipole-dipole interactions were included implicitly in the calculations to accurately account for interlayer dipolar effects. The material parameters used are (extracted experimentally from the stack #S1): exchange constant $A_{\text{ex}} = 10 \text{ pJ/m}$, interfacial DMI strengths $D_A = 0.45 \text{ mJ/m}^2$ and $D_B = 0.45 \text{ mJ/m}^2$, corresponding to the A and B magnetic sublattices, respectively, and Gilbert damping $\alpha = 0.1$. The interlayer exchange coupling strength is $J_{AFM} = 0.4 \text{ mJ/m}^2$, corresponding to the value obtained from the magnetometry. To match the compensation ratio of magnetic moments determined to be approximately 50%, the magnetic moments of CFB multilayers and CB multilayers are set to $M_{s,A} = 1.56 \text{ T}$ and $M_{s,B} = 0.5 \text{ T}$, respectively, which are the saturation magnetizations of the sublattice A and B, respectively. Similarly, the uniaxial anisotropies of the two layers were set to $K_{U,A} = 1 \text{ MJ/m}^3$ and $K_{U,B} = 1.1 \times 10^5 \text{ J/m}^3$, respectively.

6.4.1 Dynamics of Hybrid Skyrmion Tubes

Fig. 6.9(a) presents the simulated velocity of hybrid chiral skyrmion tubes as a function of applied current density, obtained from micromagnetic modeling. The velocity exhibits an almost linear increase with increasing current density, in agreement with the experimental trend in Fig. 6.6(b). More importantly, Fig. 6.9(b) reveals a qualitative transition in the dynamical response. In region 1, corresponding to the low-velocity regime, the skyrmion Hall angle is symmetric with respect to current polarity, indicative of reciprocal behavior without directional preference. This symmetry reflects the dominance of intrinsic gyrotropic forces, which are unaffected by current direction. Once a critical velocity threshold of approximately $\sim 30 \text{ m/s}$ is exceeded (region 2), the Hall angle not only increases in magnitude but also becomes asymmetric between positive and negative current directions. Such a polarity dependence constitutes a clear signature of the NSkHE. Comparable non-reciprocal

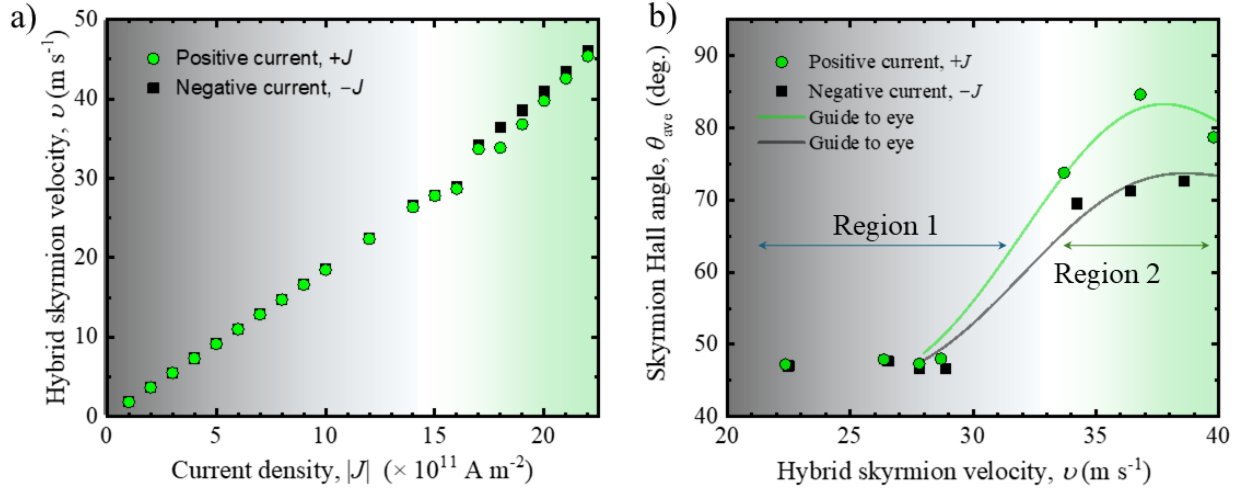


Figure 6.9: **Micromagnetic simulations of current-induced dynamics of hybrid chiral skyrmion tubes.** (a) The velocity of hybrid skyrmions in the $m_c = 50\%$ compensated SyAFM system, depicted as a function of the current density for two antiparallel in-plane (x -axis) current directions. (b) Variation of the skyrmion Hall angle for hybrid skyrmion tubes as a function of skyrmion velocity for two antiparallel in-plane (x -axis) current directions, showcasing the non-reciprocal response of skyrmions to applied electrical currents at higher current density. Adapted from [4].

effects have previously been reported in ferrimagnetic insulators under effective in-plane fields [268], where skyrmion core deformations induce asymmetries in the dissipation tensor through directional pinning [268, 281]. Moreover, field-like torques have been proposed to deform skyrmion structures during motion, thereby contributing to an asymmetric Hall response [33].

However, these mechanisms cannot account for the NSkHE observed in the SyAFM multi-layer stacks. If asymmetric pinning were the dominant factor, non-reciprocity would be expected to manifest already within the low-velocity creep or depinning regime, as reported in previous studies [28, 32, 33, 181, 281]. Furthermore, spin-torque ferromagnetic resonance measurements demonstrate that the field-like torque contribution is substantially weaker than the damping-like torque, as detailed in Appendix D section D.3, thereby excluding field-like torque as the primary origin of the observed asymmetry.

To substantiate the above discussion, the shape distortion effects were investigated by computing the dissipation tensor $D_{\mu\nu} = \int_S d^2r (\partial_\mu \mathbf{m}_i \cdot \partial_\nu \mathbf{m}_i)$ for the SyAFM hybrid chiral skyrmion in the two region of dynamics. Figs. 6.10 (a) and 6.10 (b) illustrate the differences $\tilde{D}_{\mu\nu} = D_{\mu\nu}[+J] - D_{\mu\nu}[-J]$ corresponding to the lateral average of the dissipation tensor for two antiparallel directions of the applied current for velocity 11 m/s (region 1) and 34 m/s (region 2) respectively. At the skyrmion velocity of $v = 11 \text{ m s}^{-1}$ (region 1), the tensor elements \tilde{D}_{xx} , \tilde{D}_{xy} , \tilde{D}_{yx} , and \tilde{D}_{yy} exhibit no de-

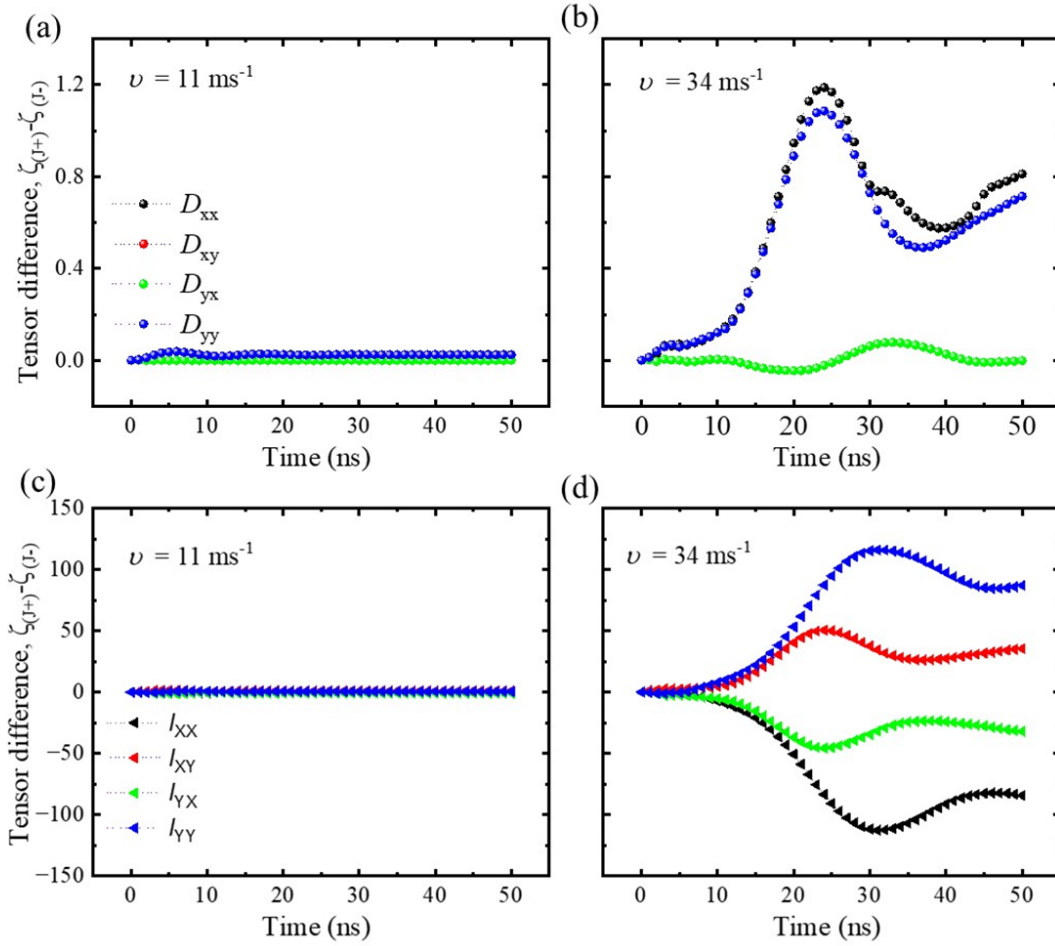


Figure 6.10: **Evolution of dissipation and SOT efficiency tensors in two different regions of skyrmion dynamics.** (a) Layer-averaged differences of the dissipation tensor components \tilde{D}_{ij} at skyrmion tube velocities of $v = 11 \text{ ms}^{-1}$ (left) and $v = 34 \text{ ms}^{-1}$ (right). (b) Corresponding layer-averaged differences of the SOT efficiency tensor components \tilde{I}_{ij} . The tensor components xx , xy , yx , and yy are shown in black, red, green, and blue, respectively.

viation, indicating that the skyrmion remains circular during its motion. At a higher velocity of $v = 34 \text{ ms}^{-1}$ (region 2), the tensor elements change when the direction of the applied current is reversed. However, these deviations remain small and are insufficient to account for the observed strong NSkHE.

To uncover the physical origin of the NSkHE in the SyAFM hybrid chiral skyrmion tube, we computed the SOT efficiency tensor $I_{\mu\nu} = \int_S d^2r [\partial_\mu \mathbf{m}_i m_i]_\nu$ in both dynamical regions of the skyrmion tube motion. Fig. 6.11 (c)-(d) displays the difference $\tilde{I}_{\mu\nu} = I_{\mu\nu}[+J] - I_{\mu\nu}[-J]$, corresponding to the lateral average of the SOT tensor for two opposite current directions. In region 1 (Fig. 6.11

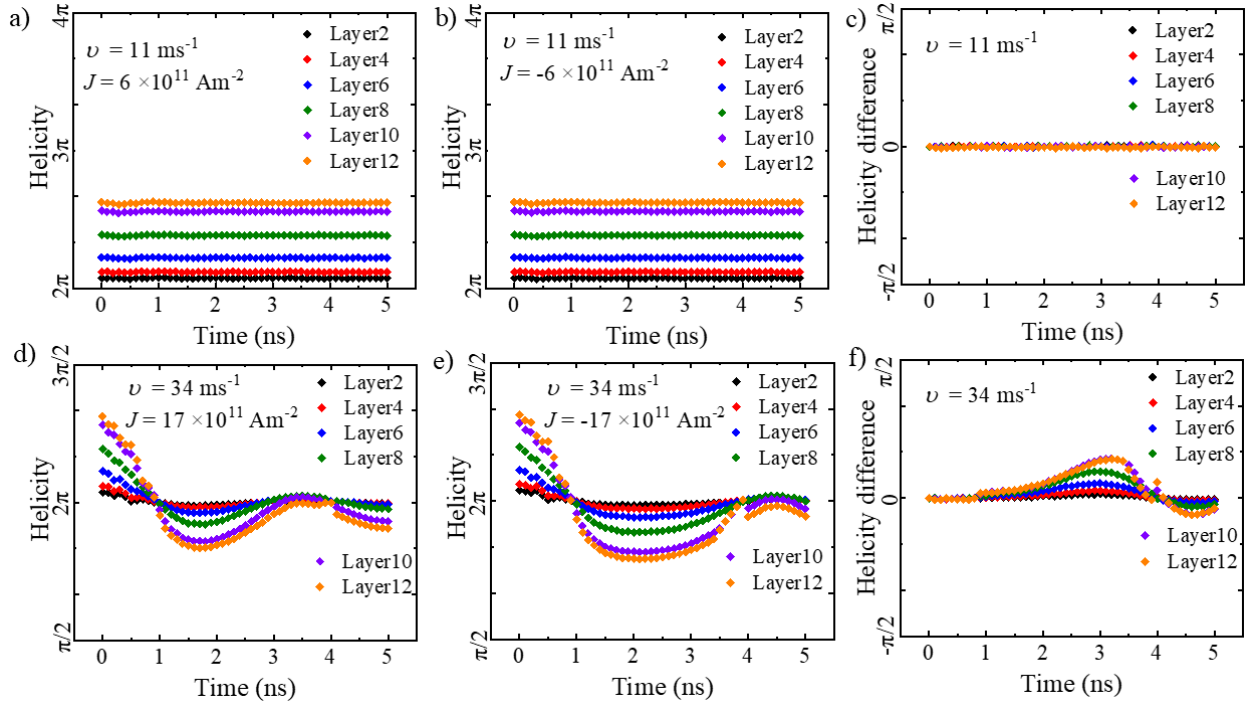


Figure 6.11: **Helicity evolution of hybrid skyrmions under different dynamic regimes.** (a) Helicity of alternating layers during a 5 ns pulse under a positive current direction ($J = 6 \times 10^{11} \text{ A/m}^2$) in region 1. (b) Helicity of alternating layers during a 5 ns pulse under a negative current direction ($J = -6 \times 10^{11} \text{ A/m}^2$) in region 1. (c) Helicity of alternating layers during a 5 ns pulse under a positive current direction ($J = 17 \times 10^{11} \text{ A/m}^2$) in region 2. (d) Helicity of alternating layers during a 5 ns pulse under a negative current direction ($J = -17 \times 10^{11} \text{ A/m}^2$) in region 2. In region 2, the helicity progressively transforms from a hybrid configuration toward a Néel-type profile during the pulse. (e) Layer-resolved helicity difference between positive and negative current directions at a skyrmion tube velocity of $v = 11 \text{ ms}^{-1}$. (f) Corresponding helicity difference at $v = 34 \text{ ms}^{-1}$, highlighting the layer-dependent asymmetry that gives rise to the non-reciprocity of the SkHE.

(c)), $\tilde{I}_{\mu\nu}$ is negligibly small and comparable to $\tilde{D}_{\mu\nu}$. In contrast, in region 2 (Fig. 6.11 (d)), $\tilde{I}_{\mu\nu}$ is at least two orders of magnitude larger than $\tilde{D}_{\mu\nu}$, indicating that this is the dominant contribution responsible for the non-reciprocity of the skyrmion Hall angle.

To understand the origin of the observed asymmetry in the SOT efficiency tensors, the layer-averaged evolution of skyrmion helicity during current-induced dynamics was computed. Figs. 6.11(a) and (b) show the evolution of helicity of alternating layers under low current densities ($\pm 6 \times 10^{11} \text{ A/m}^2$) in region 1, corresponding to panels (a) and (b), respectively. In this regime, the skyrmion retains its hybrid chiral character throughout the 5 ns pulse duration, with only minimal modification of the in-plane spin components. Consequently, the helicity of the hybrid skyrmion tubes remains nearly constant during motion, as illustrated in Fig. 6.11(c). In contrast, Figs. 6.11(d)

and (e) correspond to higher current densities ($\pm 17 \times 10^{11}$ A/m²) in region 2, where the helicity exhibits pronounced temporal evolution during the pulse. The spin structure undergoes a progressive transformation from a hybrid configuration toward a more symmetric Néel-type profile, indicative of a dynamic reconfiguration of the skyrmion tube under stronger driving conditions. This helicity evolution directly results in the emergence of non-reciprocity in the skyrmion Hall angle, as shown in Fig. 6.11(f). Notably, the helicity varies continuously across the vertical (z) direction, spanning from Néel to Bloch, with the largest changes occurring in layers that display Bloch-like character in equilibrium. The transition in helicity and its impact on skyrmion dynamics underscore the intricate interplay of magnetic interactions in SyAFM multilayers. This complexity is further compounded by dipolar interactions, which can be tuned by the degree of magnetic compensation. The results demonstrate that these interactions are essential not only for stabilizing hybrid chiral skyrmion tubes but also for modulating their response to applied currents. The combined effect of dipolar interactions and uncompensated magnetic moments creates a unique environment in which skyrmion dynamics can be finely controlled by adjusting the magnetic compensation ratio and the number of multilayer repetitions.

It is important to emphasize that, although the parameters used in the micromagnetic simulations were obtained experimentally (see Appendix D section D.3), certain limitations remain in the quantitative analysis. The phenomenological damping parameter, for example, contains contributions from inhomogeneous broadening and interfacial spin mixing. Furthermore, the experiments do not allow the Oersted-field contribution to be disentangled from the intrinsic symmetry of the field-like torque. These effects, together with the fact that the simulations were performed at zero temperature, preclude full quantitative agreement with experiment. Instead, the simulations provide key qualitative insights that explain the main features of the experimental observations. The central conclusion is that the observed NSkHE, which emerges without any extrinsic in-plane symmetry breaking, highlights the decisive role of the internal degree of freedom in governing the current-induced motion of hybrid chiral skyrmion tubes.

So far, the dynamics of topological spin structures in ferrimagnetic and antiferromagnetic systems have predominantly been analyzed in terms of angular momentum compensation, which can lead to a vanishing skyrmion Hall effect [77, 134, 246]. Another key aspect of antiferromagnetically coupled systems is the magnetic compensation, whose role in skyrmion dynamics has remained insufficiently understood. The present results demonstrate that the level of magnetic compensation plays a decisive role in the dynamics of skyrmion tubes in thin-film multilayers. Magnetic compensation directly modulates the helicity of skyrmions along its thickness, thereby enabling the NSkHE through changes in the SOT efficiency that originate from the helicity variation across the ferromagnetic

layers. This mechanism provides excellent tunability of the NSkHE. The observed non-reciprocal behavior arises from the complex interplay between magnetic dipolar interactions and the intrinsic properties of skyrmion strings. Since the intrinsic NSkHE reported here does not exhibit a significant velocity asymmetry, it is distinctly different from the non-reciprocal transport previously reported for two-dimensional skyrmions in systems with extrinsic in-plane symmetry breaking [181, 268], underscoring its unique nature as a three-dimensional topological quasi-particle. Such an intrinsic NSkHE, fully leveraging helicity modulation, offers a pathway toward simplified device configurations that are highly advantageous for applications.

Ferromagnetic hybrid skyrmion tubes stabilized by the competition between iDMI and long-range dipolar interaction may, in principle, display similar behavior, although this has not yet been demonstrated. In ferromagnetic skyrmion tubes, the degeneracy of Bloch chiralities is presumably not lifted when only interfacial DMI of C_{nv} symmetry and dipolar coupling are present. Recent work has shown, however, that interlayer DMI can lift this degeneracy and lead to a strong asymmetry in the population of Bloch chiralities [274]. The statistical asymmetry observed in Fig. 6.8 is consistent with this scenario. In this context, synthetic antiferromagnetic multilayers, combining AFM coupling with controlled interlayer DMI, represent a particularly promising platform for investigating current-induced dynamics that exploit internal degrees of freedom of three-dimensional topological spin textures.

6.5 Conclusion

In conclusion, this chapter has demonstrated the interlayer-exchange interaction-mediated coherent antiferromagnetic coupling of three-dimensional SyAFM skyrmion tubes revealed by element-specific STXM and LTEM. The comprehensive investigation of their dynamics uncovers a unique character inherent to three-dimensional topological spin profiles: an intrinsic NSkHE, originating from dynamic helicity variations rather than shape distortions. Owing to the tunability provided by magnetic compensation, this behavior offers a powerful handle for tailoring the dynamical response of hybrid chiral skyrmion tubes. The results open new avenues for the exploitation of three-dimensional topological textures in spintronic devices. In particular, logic and neuromorphic computing architectures, as well as energy-harvesting concepts leveraging the non-reciprocal emergent electric fields associated with the NSkHE, represent promising directions.

Skymeron: An Orthogonally Coupled Skyrmion–Bimeron Pair

*What we call the beginning is often the end.
And to make an end is to make a beginning.
The end is where we start from.*

T.S. Eliot

7.1 Introduction

The interplay between [iDMI](#) and [PMA](#) in thin-film multilayers stabilizes various chiral quasiparticles, such as skyrmions and bimerons, whose current-driven dynamics are confined to the two-dimensional plane. Extending these chiral quasiparticles into the third dimension broadens the accessible phase space and allows the realization of novel spin textures, as outlined in the introduction (Chapter 1). Although skyrmions and bimerons belong to the same homotopy class, their stabilization and symmetry differ: skyrmions form in out-of-plane magnetized backgrounds with radial rotational invariance, whereas bimerons form in in-plane backgrounds and are characterized by a meron–antimeron axis that breaks circular symmetry. This axis introduces an additional in-plane degree of freedom for current-induced motion [1, 51]. After establishing antiferromagnetic bimerons and skyrmions in Chapter 4 and Chapter 5, this chapter turns to a composite spin texture in which a skyrmion and a bimeron are intrinsically coupled. Such a composite state may exhibit a tunable dynamic response that cannot be realized in either constituent alone. One possible route to stabilize such a composite quasiparticle is

through the chiral interlayer exchange interaction (interlayer DMI [282–284]) between ferromagnetic layers with orthogonal magnetization. To date, however, three-dimensional spin textures stabilized or assisted by interlayer DMI have not been clearly experimentally demonstrated.

Intrinsic AFMs provide natural advantages for hosting skyrmions and bimerons, as they inherit the characteristic features of AFM order, such as cancellation of the SkHE and negligible stray fields [70, 72, 178]. SyAFMs, however, offer an additional degree of freedom by enabling independent engineering of the properties of two FM sublattices. Magnetic material parameters such as uniaxial magnetic anisotropy, saturation magnetization, and iDMI can be tailored individually in each sublattice, in contrast to intrinsic AFMs, where the sublattices are equivalent [82]. This sublattice-specific tunability has profound consequences. For example, by adjusting the magnetic compensation (renders the system analogous to ferrimagnets), SyAFMs can stabilize three-dimensional spin textures such as hybrid skyrmion tubes, as demonstrated in Chapter 6. Furthermore, SyAFMs uniquely allow the magnetic anisotropy of each sublattice to be engineered independently. This tunability produces striking effects during magnetic reversal under external fields: in the spin-flop transition, anisotropy difference induces asymmetric canting, with one sublattice tilting more strongly toward the in-plane direction. As a result, the two sublattices can lock into an orthogonal configuration, with one aligned out-of-plane and the other in-plane. In such an orthogonal state, the presence of topological spin textures can give rise to composite configurations. This chapter introduces one such spin texture: an orthogonally coupled state in which an out-of-plane skyrmion in one FM sublattice is intrinsically aligned with an in-plane bimeron in the other FM sublattice of a SyAFM. We term this tunable configuration a **"skymeron"***. In this system, the skymeron can be continuously tuned from an AFM state toward a near-orthogonal configuration, representing a distinct topological state that emerges from the transition between antiparallel and orthogonal spin alignment. This chapter first outlines the experimental strategy for stabilizing skymerons, a texture not previously reported in the literature to our knowledge, then presents micromagnetic simulations confirming their stability, and finally demonstrates their experimental realization via direct real-space X-ray microscopy. The realization of skymerons expands the accessible topological phase space of spin textures in SyAFMs. Experimental details, including sample structure and characterization, are provided in the eLabFTW logbook (labbook experiment ID 18985).

7.2 Energy Landscape to Stabilize Skyrmion–Bimeron Pair (Skymeron)

In this section, we discuss the conditions required for the stabilization of skymerons as composite quasiparticles. To understand the underlying mechanisms, it is essential to examine the influence of

*The term *skymeron* is coined by combining the names of its two constituent textures: a skyrmion in one sublattice and a bimeron in the other (**SKY**rmion + **biMERON** = **SKYMERON**).

external magnetic fields on SyAFMs. A SyAFM consists of two ferromagnetic layers antiferromagnetically coupled through interlayer exchange across a nonmagnetic spacer. Compared to the strong direct antiferromagnetic exchange interactions observed in crystalline AFMs, which typically require magnetic fields on the order of several tens of tesla to overcome, the interlayer exchange in SyAFMs is significantly weaker. This interlayer coupling is highly tunable, typically in the range of 5–500 mT, and enables magnetic switching at field strengths that are readily accessible under laboratory conditions.

The magnetic reversal behavior in SyAFMs can be broadly classified into two regimes, depending on the relative magnitudes of the interlayer exchange energy, magnetic anisotropy energy, and demagnetization energy. To illustrate this, consider a SyAFM comprising two ferromagnetic sublattices, labeled A and B, each of thickness t (assumed equal for simplicity), with saturation magnetizations $M_{s,A}$ and $M_{s,B}$, and corresponding unit magnetization vectors \mathbf{m}_A and \mathbf{m}_B . In the case of the strong interlayer coupling regime, the condition $|J_{AFM}| > K_{\text{eff}}t$ holds, where J_{AFM} represents the interlayer exchange strength and K_{eff} is the effective anisotropy of the ferromagnetic sublattices. For a magnetic field applied along the easy axis, magnetization reversal occurs through a collective spin flip once the Zeeman energy overcomes the interlayer exchange cost. The corresponding spin-flip field for a symmetric bilayer ($M_{s,A} = M_{s,B} = M_s$) is given by $H_f = \frac{2|J_{AFM}|}{\mu_0 M_s t}$ [285], where μ_0 is the vacuum permeability. In this limit, magnetization reversal is abrupt and closely resembles the spin-flip transition of intrinsic antiferromagnets with strong easy-axis anisotropy.

The second regime arises when interlayer exchange, anisotropy, and demagnetization energies are comparable ($|J_{AFM}| \sim K_{\text{eff}}t$). In this case, magnetization reversal proceeds through a spin-flop transition [285]. Unlike the abrupt spin-flip in the strong-coupling limit, the spin-flop transition produces a canted configuration in which the sublattice magnetizations possess both out-of-plane and in-plane components, thereby creating a canted background state. In multilayer SyAFMs, the magnetic reversal process becomes further complicated due to the surface spin-flop transitions [286, 287]. In such even-layer SyAFMs, the topmost or bottommost ferromagnetic layer, which is initially aligned opposite to the applied magnetic field, tends to switch its magnetization before the inner layers. This preferential switching arises because the outermost FM layers experience only half of the interlayer exchange coupling compared to the centrally located layers. As a result, non-collinear magnetic structures can emerge during the reversal process [286]. Specifically, a spin-spiral configuration develops along the thickness of the multilayer SyAFM stack, characterized by a gradual tilting of magnetic moments from layer to layer.

In the case of antiferromagnetic skyrmions and bimerons discussed in previous chapters of this thesis, both FM sublattices possess effective anisotropies of similar magnitude and identical sign. For

skyrmions, the effective anisotropies of the two sublattices are both positive [3] (favoring out-of-plane orientation), whereas for bimerons they are both negative [1] (favoring easy-plane orientation). We now consider a general scenario in which the two ferromagnetic sublattices have equal thickness t , identical iDMI D_{DMI} , exchange stiffness A_{ex} , and saturation magnetization M_s , but exhibit different effective anisotropies, with sublattice A characterized by a positive $K_{\text{eff},A}$ ($K_{\text{eff},A} > 0$) and sublattice B by a negative $K_{\text{eff},B}$ ($K_{\text{eff},B} < 0$)[†]. Then, the energy functional of the SyAFM can take the form

$$\begin{aligned} \mathcal{E}_{\text{skymeron}} = \int_S d^2r \{ & A_{\text{ex}}(\nabla \mathbf{m}_A)^2 + A_{\text{ex}}(\nabla \mathbf{m}_B)^2 \\ & + D_{\text{DMI}}[\mathbf{m}_A \cdot (\nabla \times \mathbf{m}_A)] + D_{\text{DMI}}[\mathbf{m}_B \cdot (\nabla \times \mathbf{m}_B)] \\ & - K_{\text{eff},A} m_{A,z}^2 - K_{\text{eff},B} m_{B,z}^2 \\ & - J_{\text{AFM}}(\mathbf{m}_A \cdot \mathbf{m}_B) \}. \end{aligned} \quad (7.1)$$

The effective anisotropy difference between the sublattices is defined as $\Delta K_{\text{eff}} = K_{\text{eff},A} - K_{\text{eff},B}$, and the net effective anisotropy as $K_{\text{eff,net}} = \frac{1}{2}(K_{\text{eff},A} + K_{\text{eff},B})$. In such a system with opposite signs of effective anisotropy, a characteristic feature emerges during magnetic reversal at the spin-flop transition: the canting of the two sublattices becomes asymmetric under the application of an external magnetic field. The degree of canting in each sublattice is governed by the relative magnitudes of their respective effective anisotropies. This anisotropy mismatch breaks the symmetry of the spin-flop process, resulting in unequal angular deviations from the easy axis in the two sublattices. Consequently, the presence of spin textures in each sublattice results in an asymmetric evolution across the spin-flop transition, introducing additional degrees of freedom and thereby enriching the accessible magnetic configurations.

Micromagnetic simulations based on a macrospin model were performed to illustrate this asymmetric canting behavior during magnetization reversal, and the results are presented in Fig. 7.1. To isolate the effect of anisotropy asymmetry at fixed net anisotropy, we compare two cases with $K_{\text{eff,net}} = 0.03 \text{ MJ m}^{-3}$: (i) equal effective anisotropy scenario (case I), ($K_{\text{eff},A} = K_{\text{eff},B} = 0.03 \text{ MJ m}^{-3}$); and (ii) scenario with different effective anisotropy sign (case II), ($K_{\text{eff},A} = 0.08 \text{ MJ m}^{-3}$ and $K_{\text{eff},B} = -0.02 \text{ MJ m}^{-3}$). The magnetization reversal in the case I ($K_{\text{eff},A} = K_{\text{eff},B}$) is shown in Fig. 7.1 (a). The magnetic parameters used in these simulations correspond to stack #S3d, ensuring relevance to the experimental system under investigation. The complete simulation code employed for this study is provided in Appendix E. Here, upon reducing the out-of-plane magnetic field from an initially saturated state, where the magnetizations of both FM sublattices are aligned along the field direction, the system undergoes a conventional and symmetric spin-flop transition.

[†]In experimental systems, the exchange stiffness A_{ex} and iDMI D_{DMI} are not identical for each layer. However, since the dominant difference arises from the opposite sign of the effective anisotropy K_{eff} , they are assumed to be equal in this model for simplicity.

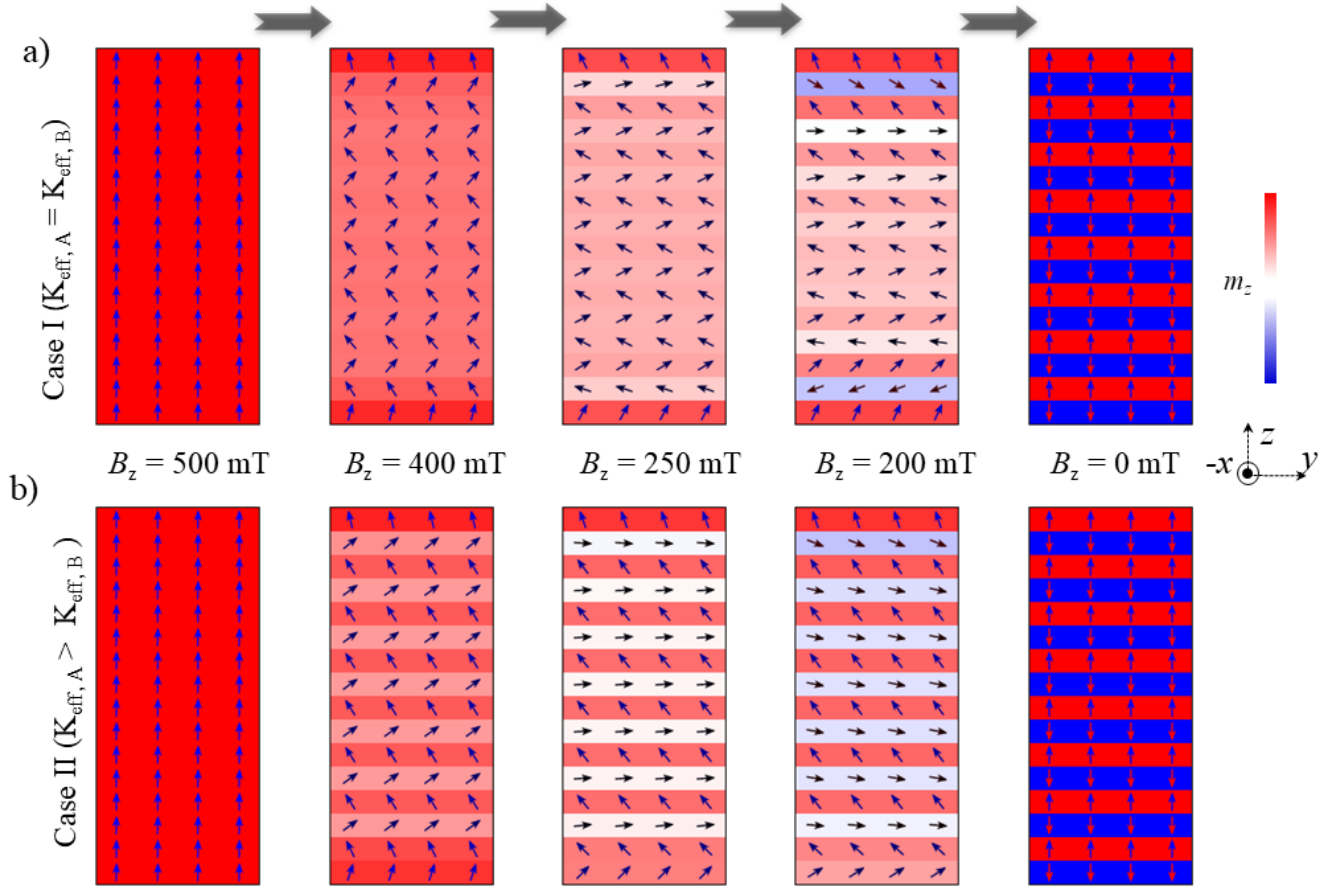


Figure 7.1: **Role of anisotropy in magnetic reversal via spin-flop transition in multilayer SyAFM.** Micromagnetic simulation snapshots showing the evolution of magnetization during the application and reduction of out-of-plane magnetic field, comparing two SyAFMs. **(a)** Case I: $K_{\text{eff},A} = K_{\text{eff},B} = 0.03 \text{ MJ m}^{-3}$ showing a symmetric spin flop. **(b)** Case II: $K_{\text{eff},A} = 0.08 \text{ MJ m}^{-3}$, $K_{\text{eff},B} = -0.02 \text{ MJ m}^{-3}$ where the sublattice with negative K_{eff} tilts more strongly toward the in plane direction. The color scale represents the out-of-plane magnetization component m_z .

This behavior is consistent with earlier studies on magnetic reversal in multilayer SyAFMs [286].

Fig. 7.1(b) illustrates a case with different anisotropies sign and strength. In this scenario, sublattice A, characterized by a positive effective anisotropy ($K_{\text{eff},A} > 0$), undergoes only a slight canting as the external magnetic field is reduced. In contrast, sublattice B, possessing a negative effective anisotropy, exhibits a significantly larger canting response, gradually aligning closer to the in-plane direction. This asymmetry arises due to the lower energetic cost for sublattice B to maintain an in-plane orientation, rather than canting further toward the magnetization direction of sublattice A. As a result, the two sublattices evolve toward a configuration in which their magnetizations become

nearly orthogonal. The evolution of the relative angle between the sublattice magnetizations is discussed in Section 7.4. Notably, this behavior is counterintuitive, as achieving an in-plane magnetic configuration through the application of an out-of-plane field defies conventional expectations. Most importantly, the transition is continuous, reflecting a smooth evolution of spin canting rather than an abrupt switching event. Now, this ability to induce asymmetric tilting through anisotropy difference serves as a starting point for stabilizing spin textures in three dimensions, where the magnetizations of the two sublattices are not merely antiparallel, but can adopt arbitrary relative angles, including near-orthogonal configurations[‡].

The role of external magnetic fields in skyrmion (or bimeron) stabilization for **FM** is well established in the literature; depending on the core orientation, an applied out-of-plane field can either expand or shrink a skyrmion, eventually annihilating it. However, the stabilization of topological spin textures under conditions of differing sublattice anisotropy occurs through a fundamentally distinct mechanism. In such cases, the **OOP** field no longer simply shrinks or expands the texture. Instead, it induces a coherent rotation of the background magnetization while preserving the topological structure. This provides an opportunity to directly observe real-space topological transformations, offering insights into this transition. Moreover, the dynamics of these textures can be finely tuned by varying the strength of the applied magnetic fields. This tunability opens the possibility of accessing regimes where the skyrmion Hall effect is suppressed (at antiparallel configuration), as well as regimes with nontrivial dynamics, in which the two sublattice components could exhibit distinct dynamics. Such control offers a promising pathway for engineering novel quasiparticle behaviors in **SyAFMs**.

Notably, the sublattice anisotropy tuning required to achieve an orthogonally coupled state is absent in intrinsic **AFM**, as both sublattices are identical, exhibiting the same material properties such as anisotropy, **iDMI**, and saturation magnetization. In contrast, transition metal—rare—earth ferrimagnets offer a high degree of tunability through temperature control, allowing variation in material properties. However, these sublattices are coupled via direct exchange interactions, which are significantly stronger, typically on the order of several tens of tesla. As a result, magnetic reversal in such systems generally proceeds through a spin-flip transition phase. **SyAFMs**, on the other hand, provide a unique platform for such tunability due to their independent control over interlayer exchange coupling and magnetic properties. The next section details the experimental conditions under which such states were stabilized and probed.

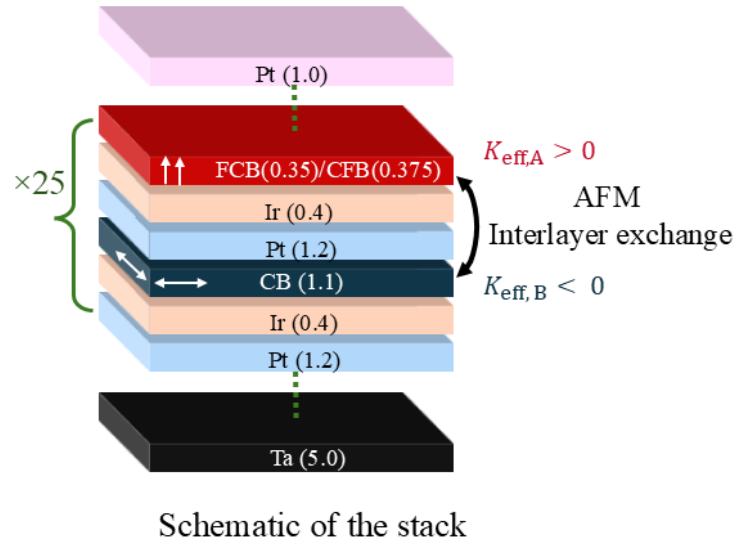


Figure 7.2: **Schematic of the SyAFM stack to host skymeron.** The structure consists of 25 repeats of FM bilayers separated by Ir spacers, enabling strong AFM interlayer exchange. Sublattice A has an effective perpendicular anisotropy $K_{\text{eff,A}} > 0$, favoring skyrmions, while sublattice B has an in-plane anisotropy $K_{\text{eff,B}} < 0$, favoring bimerons. The numbers in parentheses give the thickness in nm.

7.3 Experimental Conditions for the Stabilization of Skymerons

Having established the conditions under which two ferromagnetic sublattices can be antiferromagnetically coupled and further tuned to a near-orthogonal configuration, this section now turns to the stabilization of topological spin textures within each ferromagnetic layer and the study of their real-space evolution. The materials investigated in this thesis are thin films exhibiting **iDMI**, which stabilizes Néel-type spin textures. The most energetically favored topological textures in such systems are skyrmions (for out-of-plane anisotropy) and bimerons (for easy-plane anisotropy). As discussed in earlier chapters, both the material stack and the strategy have been optimized to stabilize skyrmions (see Chapter 5 section 5.2 for details) and bimerons (see Chapter 4 section 4.3 for details) in individual ferromagnetic layers solely through anisotropy engineering. Here, we combine two ferromagnetic layers, one favoring skyrmions and the other favoring bimerons, into a synthetic antiferromagnetic structure. In such a configuration, sublattice A is designed with an effective anisotropy $K_{\text{eff,A}} > 0$, promoting out-of-plane skyrmions, while sublattice B has $K_{\text{eff,B}} < 0$, favoring in-plane bimerons. The schematic of the proposed multilayer stack is shown in Fig. 7.2. To obtain finite **iDMI** and ensure

[‡]In the opposite case, where $K_{\text{eff,A}} > 0$, $K_{\text{eff,B}} < 0$, and $(K_{\text{eff,net}} < 0)$, the **SyAFM** corresponds to an AFM easy-plane system at zero magnetic field.

that the stabilized spin textures are homochiral within each ferromagnetic layer, the stack has been carefully engineered to break inversion symmetry. This asymmetry is also a prerequisite for observing SOT-induced dynamics of topological spin textures. Here, Ir is employed as the primary spacer layer, as it provides strong antiferromagnetic interlayer exchange coupling. While Ir is primarily responsible for enabling AFM coupling, its effective exchange character changes sign from AFM to FM within a narrow thickness range of 0.3–0.4 nm. To achieve more controlled tuning of the AFM interlayer strength, an alternative approach is adopted: rather than varying the Ir thickness, the thickness of the Pt layers adjacent to the Ir is modulated. As demonstrated in Fig. 5.1 of Chapter 5, increasing Pt thickness effectively reduces the interlayer exchange strength in a controllable manner. The motivation behind this strategy lies in achieving reduced AFM coupling, which allows topological spin textures to be stabilized and imaged under relatively low external magnetic fields (range of 100–200 mT). Such field ranges are compatible with in-situ imaging techniques available at most synchrotron facilities. Based on this, stack #S3d has been fabricated to stabilize and observe skymeron.

Conditions to Stabilize Skyrmion–Bimeron pair (Skymerons)

- Positive effective anisotropy ($K_{\text{eff,A}} > 0$) for sublattice A
- Negative effective anisotropy ($K_{\text{eff,B}} < 0$) for sublattice B
- Net positive effective anisotropy ($K_{\text{eff,net}} > 0$)
- Interlayer antiferromagnetic exchange between the sublattices
- Finite iDMI in both the sublattices
- Finite out-of-plane magnetic fields to induce canting

When complex spin textures such as skymerons are stabilized, their unambiguous detection requires imaging techniques capable of resolving the magnetization in each ferromagnetic sublattice independently. For this purpose, the stack is imaged using element-specific XMCD in combination with STXM. The two FM sublattices were deliberately designed with chemically distinct compositions, Fe-rich and Co-rich alloys, corresponding to sublattices A and B, respectively. By tuning the incident X-ray photon energy to the Fe L_3 edge or the Co L_3 edge, the magnetization of each sublattice can be selectively probed with nanometer spatial resolution and sub-nanosecond temporal resolution. This element-selective probing provides a direct and quantitative approach to image skyrmions, bimerons, and their hybrid combinations in real space.

7.3.1 Nucleation and Observation of the Skymerons

At remanence, our synthetic antiferromagnetic multilayers typically relax into stripe or labyrinth domain patterns (due to negative DW energy), determined by the magnetic preconditioning protocol. Depending on the demagnetization method, these domains may form either randomly or with directional order. In magnetically uncompensated SyAFMs, an OOP magnetic field couples to the system via the Zeeman interaction, favoring domains aligned with the field. As discussed before, in the SyAFM (stack #S3d, $K_{\text{eff,A}} = 8 \times 10^4 \text{ J/m}^3$ and $K_{\text{eff,B}} = -2 \times 10^4 \text{ J/m}^3$), the application of an OOP magnetic field induces asymmetric canting between the two magnetic sublattices. Specifically, the sublattice with lower effective anisotropy tilts toward the in-plane, owing to the reduced energetic cost of this reorientation as discussed in the above section. To directly visualize this behavior, stack #S3d was imaged using STXM at the MAXYMUS endstation at BESSY II synchrotron. Element-specific measurements were performed at both the Fe and Co L_3 -absorption edges, enabling independent imaging of the two magnetic sublattices, designated as sublattice A (Fe) and sublattice B (Co). Fig. 7.3(a–f) shows the evolution of the magnetic configuration under decreasing OOP magnetic field. At zero field ($\mu_0 H_z = 0$), the system resides in an antiferromagnetically coupled state, with sublattices A (Fig. 7.3(a)) and B (Fig. 7.3(d)) exhibiting antiparallel out-of-plane magnetization. Here, the black and white contrast represents the m_z component of the magnetization. Given that the SyAFM stack #S3d is 88% magnetically compensated, the application of an out-of-plane field ($\mu_0 H_z = -75 \text{ mT}$) modifies the relative population of white and black contrast, keeping the OOP coupling between the sublattices. In sublattice B (see Fig. 7.3(e)), domains parallel to the field (black contrast) expand at the expense of antiparallel domains, while in sublattice A (see Fig. 7.3(b)), the opposite behavior occurs due to the antiferromagnetic interlayer coupling.

The sublattice-resolved evolution of the spin textures at $\mu_0 H_z = -185 \text{ mT}$ is shown in Fig. 7.3(c,f). In sublattice A (Fe edge), isolated skyrmion-like textures appear, marked by red ellipses in Fig. 7.3(c). To quantify the out-of-plane magnetization m_z , a line scan across the stripes (red line L1, averaged over 25 pixels) was extracted and is plotted in Fig. 7.3(g). For an ideal Néel type DW, the magnetization profile is described by the polar angle $\theta(x)$, defined as the angle between the local magnetization vector $\mathbf{m}(x)$ and the out-of-plane axis (z), and is given by $\theta_{\text{DW}}(x) = 2 \arctan\left(e^{\frac{x-x_0}{\Delta_{\text{DW}}}}\right)$, where x_0 denotes the wall center and Δ_{DW} is the domain-wall width [132]. However, the line profile in sublattice A deviates significantly from the symmetric case, exhibiting an anisotropic shape that breaks rotational symmetry. Although these skyrmions are anisotropic and differ from the skyrmion description discussed in earlier chapters, in the following, these skyrmion-like structures in the sublattice A are referred to as skyrmions. The origin of the asymmetric magnetization profile is discussed in the later section 7.4 using micromagnetic simulations. In the corresponding region of sublattice B

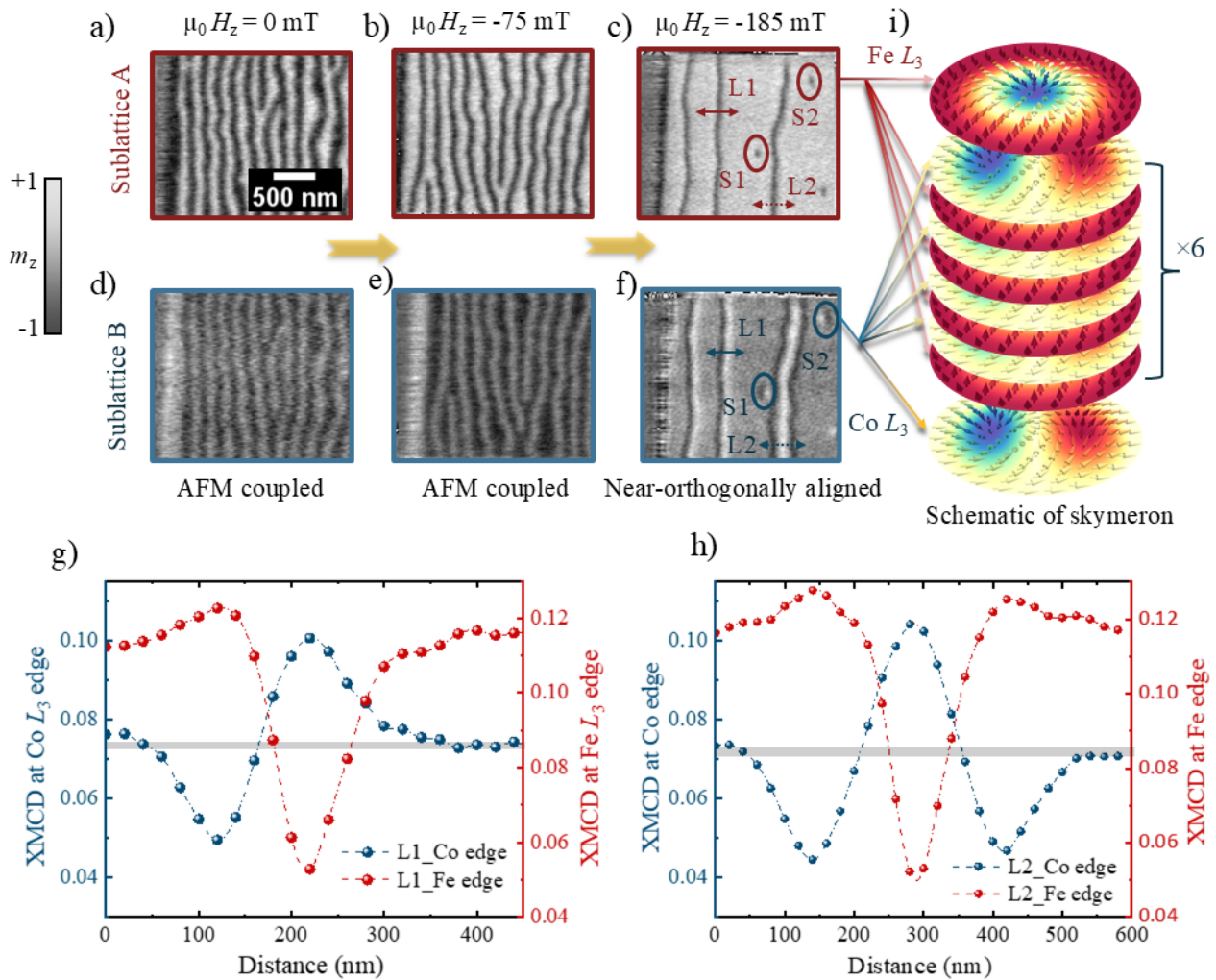


Figure 7.3: **Observation of skyrmion–bimeron pairs (skymerons).** XMCD-STXM images at the Fe L_3 edge (sublattice A) for (a) $\mu_0 H_z = 0$ mT, (b) -75 mT, and (c) -185 mT. Corresponding STXM images at the Co L_3 edge (sublattice B), evidencing AFM coupling at (d) $\mu_0 H_z = 0$ and (e) -75 mT, and orthogonally aligned bimerons at (f) -185 mT. The near-orthogonal skyrmion–bimeron configuration defines a skymeron, schematically illustrated in (i). The skyrmion and bimeron parts of the isolated skymerons are highlighted by red and blue ellipses in (c) and (f), respectively. (g) XMCD line profiles across L1 at the Fe (red) and Co (blue) edges show the out-of-plane skyrmion contrast in sublattice A and the two-lobed bimeron signature in sublattice B on a uniform in-plane background. (h) Sublattice-resolved Line profile across L2.

(Co edge), isolated textures with both black and white contrast embedded in a gray background are observed (Fig. 7.3(f)). Since STXM is sensitive only to the out-of-plane component m_z , bimerons, which are embedded in an in-plane background, appear as paired black and white lobes corresponding

to opposite m_z contributions from the meron–antimeron cores. These textures, marked by blue ellipses, are thus identified as bimerons, characterized by a three-level XMCD contrast. We term these orthogonally aligned skyrmion–bimeron pairs as **"skymerons"**, topological quasiparticles composed of a skyrmion-like spin texture in one sublattice and a bimeron in the other sublattice. The straight line connecting the meron and antimeron cores (black and white lobes) defines the orientation of the in-plane background, which in this case lies along the x-axis. From the spatial extent of the XMCD contrast within the in-plane background, the skymeron radius is estimated as (150 ± 20) nm. A schematic illustration of skymeron is given in Fig. 7.3(i). Fig. 7.3(f) shows that at the Co edge (sublattice B), corresponding to the out-of-plane stripes in sublattice A, a black–white stripe emerges in a gray background, identified as bimeron stripes. Moving along the horizontal direction across the bimeron stripe L1, the magnetization completes a full 360° rotation, resulting in an identical in-plane background on both sides of the stripe. The corresponding line profiles across L1 in sublattices A and B are shown by the red and blue curves in Fig. 7.3(g). The stripe L2, shown in Fig. 7.3(f), exhibits a black–white–black contrast from left to right, indicating that the magnetization undergoes a 540° rotation across the stripe. Consequently, the in-plane background to the left and right of L2 is antialigned along the x-axis. The corresponding line profiles of L2 in sublattices A and B are presented by the red and blue curves in Fig. 7.3(h). The skymerons S1 and S2, located on the left and right sides of L2, display black–white and white–black contrasts, respectively. The chirality of the two skymerons nevertheless remains identical, as the inversion of the meron–antimeron core contrast directly reflects the flipped background orientation.

A minor hysteresis loop protocol, in which the out-of-plane field was cycled from $-200 \rightarrow 180 \rightarrow -160 \rightarrow 140$ mT, leads to the formation of closed-loop spin textures at random positions. Under these conditions, a closed-loop object is stabilized, as shown in Figs. 7.4(a,b) for sublattices A and B, respectively. In sublattice A, the object exhibits the topology of a skyrmionium, whereas in sublattice B (Fe) it appears as a bimeronium. Together, these textures form a composite object, hereafter referred to as a *skymeronium*, schematically illustrated in Fig. 7.4(e). The background magnetization direction is determined from the line orthogonal to the meron–antimeron core (black–white contrast), and the corresponding line profiles across the red and blue cuts in Fig. 7.4(a,b) are presented in Fig. 7.4(d). Notably, in sublattice B, the background is not fully aligned in-plane, since the applied out-of-plane field is insufficient to completely tilt the spins in-plane. In Fig. 7.4(c), the contours of the cores with down and up magnetization from sublattice B are overlaid, with the points of overlap indicated by white circles.

The nucleation of skymerons discussed above is governed by the local energy landscape, where defect-induced energy barriers play a central role in stabilizing the textures at specific positions.

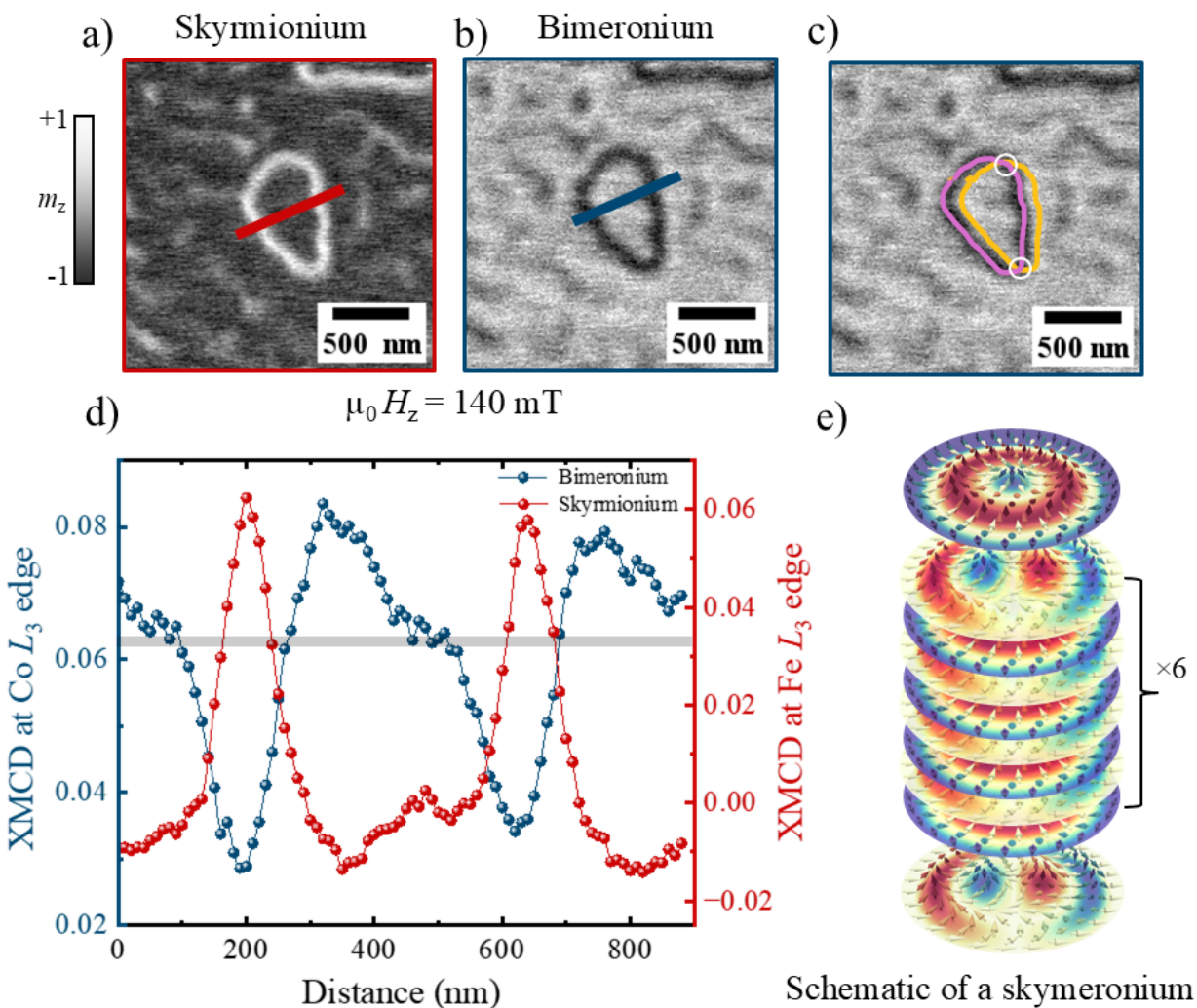


Figure 7.4: **Observation of a skyrmionium–bimeronium pair (skymeronium).** (a,b) STXM images of sublattices A and B after field cycling ($-200 \rightarrow 180 \rightarrow -160 \rightarrow 140$ mT), showing the nucleation of a closed-loop spin texture. In sublattice A, the object corresponds to a skyrmionium, whereas in sublattice B it appears as a bimeronium. Together, these textures form a composite object, referred to as a *skymeronium*. (c) Overlay of the down-core and up-core contours from sublattice B, with the points of overlap indicated by white circles. (d) Line profiles along the red and blue cuts in (a,b). (e) Schematic illustration of the skymeronium spin structure.

To overcome this limitation and to achieve isolated skymerons with improved spatial control, two additional nucleation methods were employed in this study: current-induced and laser-induced nucleation, both of which have been previously demonstrated for AFM skyrmions in Chapter 5, Section 5.3. Fig. 7.5 presents STXM images of stack #S3d acquired at the Fe and Co L_3 -absorption edges under an out-of-plane magnetic field of $\mu_0 H_z = 180$ mT, after the application of 100 bipolar current pulses

with a current density of 1.2×10^{12} A/m² and a pulse width of 7.5 ns. Here, discrete skymerons are observed with clear sublattice correspondence: Fig. 7.5(a) shows skyrmions at the Fe L_3 -edge (sublattice A, red circles), while Fig. 7.5(b) reveals matching bimerons at the Co L_3 -edge (sublattice B, blue circles).

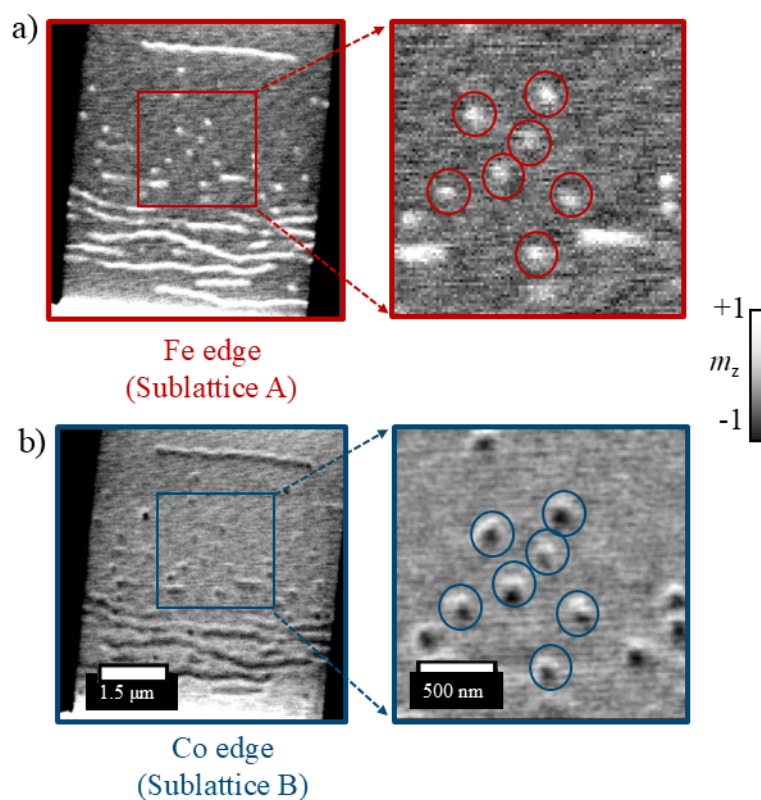


Figure 7.5: **Nucleation of skymerons using bipolar current pulses.** (a) STXM image at the Fe L_3 -edge showing isolated skymerons in sublattice A, marked by red circles. (b) Corresponding STXM image at the Co L_3 -edge showing isolated bimerons in sublattice B, marked by blue circles. Images were acquired under an out-of-plane magnetic field of $\mu_0 H_z = 180$ mT after the application of 100 bipolar current pulses with a current density of $J = 1.2 \times 10^{12}$ A/m² and a pulse width of 7.5 ns.

As discussed in Chapter 5, Section 5.3, skyrmions can be efficiently nucleated via ultrafast laser excitation. Here, we applied this concept for the nucleation of skymerons. Picosecond laser pulses provide a non-contact and spatially localized route to drive the system far from equilibrium, thereby enabling access to metastable topological states through thermally activated pathways. Fig. 7.6(a–d) presents STXM images acquired at the Co L_3 -absorption edge, illustrating the nucleation of skymerons following pulsed laser excitation at various magnetic fields. The experiments were performed at the MAXYMUS endstation using a 1 ps IR laser pulse (linear polarization, flu-

ence: 26 mJ/cm^2) under a constant out-of-plane magnetic field.[§] Before excitation, the SyAFM relaxes into skymeron stripe configurations. At 120 mT (see Fig. 7.6(a)), a single laser pulse does not nucleate isolated skymerons; however, the stripe pattern undergoes rearrangement, indicating that isolated skymerons are not energetically stable at this field. Keeping the laser fluence constant (and thus the transient heating unchanged), the bias out-of-plane magnetic field was subsequently increased, as shown in Fig. 7.6(b–d). Laser excitation induces rapid heating that transiently reduces the effective anisotropy [288]. During the ensuing nanosecond-scale cooling, the system passes through a reduced-anisotropy regime in which circular skymerons can nucleate (shown in blue circles). This pathway is thermally driven, relying on controlled access to transient states during the ultrafast heating–cooling cycle, without involvement of current-induced torques or structural pinning. Thus, skymerons can be stabilized and nucleated deterministically via different protocols. Having established their experimental stabilization and observation, the next section presents micromagnetic simulations that elucidate the stability of these spin textures.

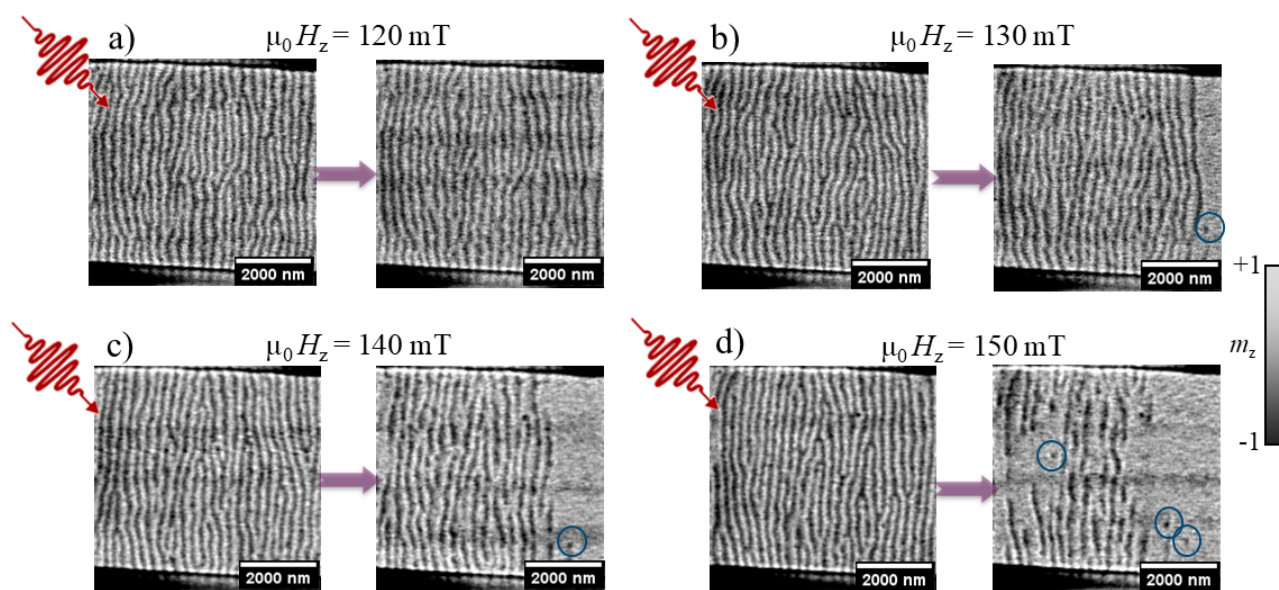


Figure 7.6: **Laser-induced nucleation of skymerons.** All STXM images were acquired at the Co L_3 -edge. Each panel shows the domain state before (left) and after (right) a single infrared laser pulse (fluence: 26 mJ/cm^2 , pulse duration: 1 ps). Applied out-of-plane fields: **(a)** 120 mT, **(b)** 130 mT, **(c)** 140 mT, and **(d)** 150 mT. Isolated skymerons are marked in blue circles.

[§]Due to the oblique incidence of the laser beam, the effective fluence at the sample surface is reduced by approximately a factor of three compared to the nominal fluence. Therefore, all fluence values reported correspond to the effective fluence at the sample. A calibration curve relating the applied laser current to the effective fluence is provided in Appendix C Section C.1.

7.4 Micromagnetic Study of Skymerons

The skyrmion component of the skymeron, as observed in the experiments and shown in Fig. 7.3(c), exhibits an anisotropic line profile (Fig. 7.3(g)), in contrast to the rotationally symmetric profile characteristic of conventional skyrmions. To understand the origin and energetics of this behavior, this section presents micromagnetic simulations addressing the stabilization of skymerons. The simulations were performed using the material parameters of a SyAFM with opposite effective anisotropy signs in the two sublattices, as detailed in Section 7.2

The simulations were initialized with an AFM skyrmion stabilized at zero magnetic field in a SyAFM. Fig. 7.7(a) displays the sublattice-resolved magnetization configurations of A and B, each hosting a skyrmion with opposite topological charge Q_{sk} . The color scale for the magnetization is shown in the inset of Fig. 7.7(g), while the sublattice-resolved m_z components in the bottom rows illustrate the contrast in STXM imaging. The subsequent evolution of the AFM skyrmions under out-of-plane magnetic fields from 50 to 250 mT in steps of 50 mT is presented in Figs. 7.7(b–f). With increasing field, the background magnetization progressively tilts toward the sample plane, most prominently in sublattice B due to $K_{\text{eff},B} < 0$, consistent with the macrospin model. This canting becomes more pronounced at higher fields (Figs. 7.7(c–f)), driving a continuous bifurcation: the skyrmion in sublattice B gradually transforms into a bimeron embedded in an in-plane background, while the skyrmion in sublattice A tilts slightly from the z-axis yet remains predominantly out-of-plane. At $B_z = 250$ mT, sublattice B is fully in-plane, as shown in Fig. 7.7(f), where the skyrmion in sublattice B has transformed into a bimeron. The resulting spin texture at this field corresponds to a skymeron (skyrmion–bimeron pair), characterized by a fully in-plane background in one of the sublattices.

To elucidate the microscopic mechanism underlying the AFM skyrmion to skymeron transition, the field-dependent evolution of the background m_z component in each magnetic sublattice is analyzed. As shown in Fig. 7.7(g), the magnetization response to the applied OOP field reveals a gradual, continuous transition from the antiferromagnetically coupled skyrmion state to the skymeron state. Although sublattice B is initially aligned with the applied field direction, increasing the out-of-plane field causes the background m_z in sublattice B to decrease continuously toward zero, indicating progressive canting of its magnetization away from the field axis. This reduction in m_z results from the competition between interlayer AFM exchange, the Zeeman interaction, and the anisotropy of sublattice B. In contrast, sublattice A, being antialigned to the applied field, tilts toward the plane to reduce the interlayer exchange energy cost. The relative angle between the background magnetization directions of the two sublattices, shown in Fig. 7.7(h), decreases from -180° at zero field to about -45° at high fields. Above 250 mT, a spin-flop transition occurs,

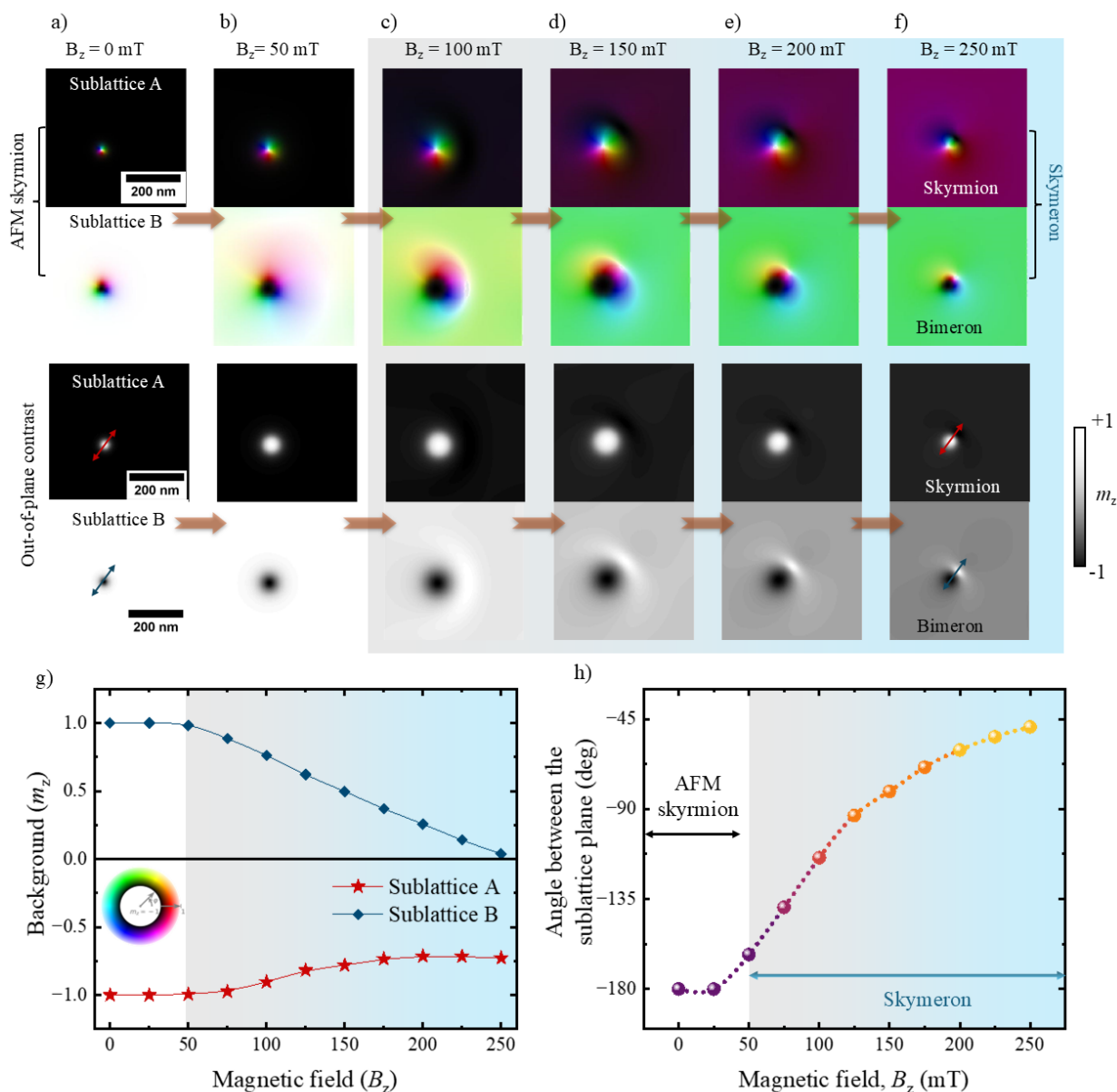


Figure 7.7: **Micromagnetic simulation of the topological transformation from an AFM skyrmion to skymeron.** (a) Sublattice-resolved AFM skyrmions at zero field with opposite topological charges. (b–f) Evolution under increasing out-of-plane magnetic field (50–250 mT), where the skyrmion in sublattice B progressively transforms into a bimeron embedded in an in-plane background, while sublattice A retains a predominantly out-of-plane skyrmion, yielding the skymeron configuration. (g) Field-dependent evolution of the normalized background out-of-plane magnetization component m_z in sublattices A and B. (h) Evolution of the relative angle between the background magnetization directions of sublattices A and B as a function of OOP fields. The shaded region denotes the skymeron regime.

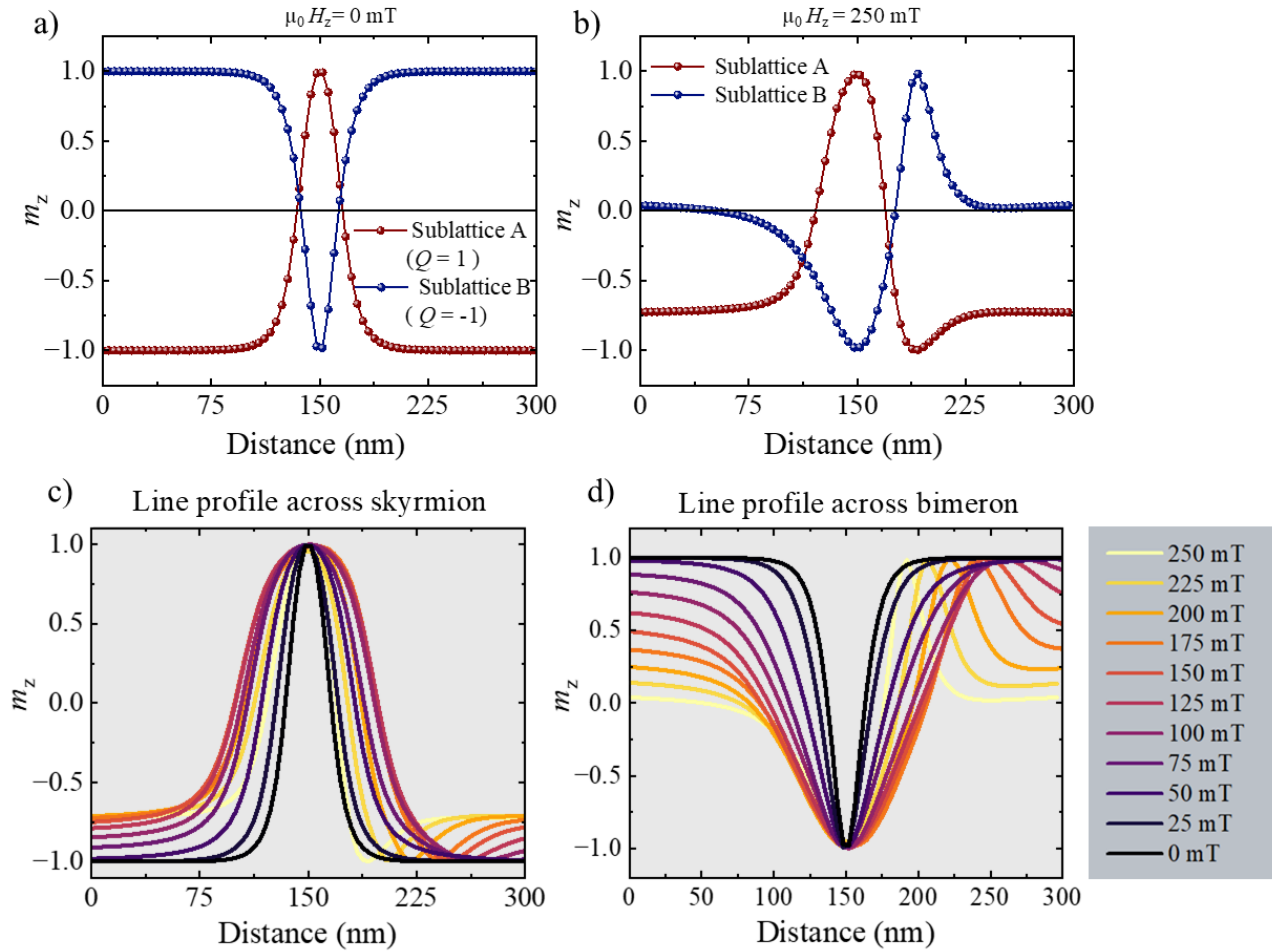


Figure 7.8: **Evolution of a skymeron from an AFM skyrmion as a function of applied OOP field.** **(a,b)** Simulated line profiles of m_z across the texture centers for sublattices A and B at $\mu_0 B_z = 0$ and 250 mT, corresponding to the AFM skyrmion and skymeron states, respectively. At zero field, both sublattices show symmetric skyrmion profiles with opposite polarity. At 250 mT, sublattice A develops an asymmetric skyrmion profile, while sublattice B transforms into a bimeron with a two-lobed signature. **(c,d)** Evolution of m_z line profiles with field: (c) skyrmion in sublattice A showing progressive asymmetry, and (d) bimeron in sublattice B displaying the characteristic splitting as the background rotates towards the plane.

with the m_z component of sublattice B aligning to the direction of the applied field. Notably, at 125 mT, the skymeron attains a fully orthogonal configuration ($\approx -90^\circ$), with the skyrmion plane in sublattice A perpendicular to the bimeron plane in sublattice B. The applied field thereby tunes the inter-sublattice alignment continuously from antiparallel to -45° . The central field window in Figs. 7.7(g,h), highlighted in gray–skyblue, marks the skymeron regime, where the sublattice magnetizations are neither fully antiparallel nor parallel but adopt a near-orthogonal orientation. This

smooth evolution of the background m_z confirms that skymeron formation is a field-tunable process.

The simulated line profiles across the AFM skyrmion ($B_z = 0$ mT) and the skymeron ($B_z = 250$ mT) are shown in Figs. 7.8(a) and 7.8(b), respectively. At zero field, the skyrmions in the two sublattices are symmetric and antiparallel. In the skymeron state, the skyrmion component in sublattice A exhibits an asymmetry due to canting toward the in-plane direction, as evident in panel (b). This deformation results in an anisotropic line profile in sublattice A, consistent with the experimentally observed profile in Fig. 7.3(g). The close correspondence between experiment and simulation provides strong evidence for the skymeron state and identifies the asymmetric skyrmion profile as a characteristic fingerprint of skymerons. The asymmetry originates from the competition between Zeeman energy, interlayer exchange, and anisotropy energy, which together favor a slight canting of sublattice A, while the negative effective anisotropy $K_{\text{eff},B}$ drives sublattice B into a fully in-plane configuration. The antiferromagnetic interlayer coupling J_{AFM} maintains lateral correlation between the two textures in the different sublattices. Importantly, in this transformation between AFM skyrmion and skymeron, the topological charge is preserved in both sublattices. The skyrmion in sublattice A and the emerging bimeron in sublattice B each retain a winding number $|w| = 1$, and no singularities are required during the evolution since both structures share the same topology. Figs. 7.8(c,d) quantify the transformation through line profiles of m_z across the texture centers, with panel (c) showing the skyrmion and panel (d) the bimeron. Notably, the skymeron phase appears only above a critical out-of-plane field $B_z^* \approx 50$ mT, at which canting of sublattice B becomes energetically favorable.

Thus, micromagnetic simulations reveal that the AFM skyrmion undergoes a continuous, field-driven transformation into a skymeron, where one sublattice retains a skyrmion and the other hosts a bimeron. The evolution is governed by the competition between interlayer exchange, Zeeman interaction, and anisotropy, leading to a near-orthogonal sublattice alignment. The resulting asymmetric skyrmion profile provides a clear fingerprint of the skymeron state, consistent with experimental observations.

7.5 Conclusion

This chapter introduces and experimentally realizes a new topological spin texture, the skymeron, which arises from the near-orthogonal alignment of skyrmions and bimerons in synthetic antiferromagnets. Building on the stabilization mechanisms of Néel-type skyrmions and bimerons discussed in earlier chapters, this chapter demonstrates that SyAFM multilayers with opposite effective anisotropy signs in the ferromagnetic sublattices can host a hybrid configuration combining these topological spin textures. The asymmetric spin-flop transition in such systems drives a continuous transforma-

tion from antiferromagnetically coupled skyrmions to skymerons under moderate out-of-plane fields. Sublattice-resolved micromagnetic simulations and element-specific X-ray microscopy confirm this pathway, revealing that one sublattice evolves into a bimeron while the other retains a deformed skyrmion, whose asymmetric profile serves as a fingerprint of the skymeron state. The controlled stabilization of skymerons establishes them as tunable topological quasiparticles, bridging the physics of conventional skyrmions and bimerons, and opening new directions for the study of emergent spin textures in *SyAFMs*. From the perspective of emergent electrodynamics, such hybridization offers unique opportunities. Skyrmions generate emergent magnetic fields aligned with their out-of-plane core magnetization, whereas bimerons produce fields perpendicular to the net moment [43]. A skyrmion–bimeron hybrid is therefore expected to give rise to both out-of-plane and in-plane components of emergent magnetic fields, which could enable unconventional and anisotropic transport responses [243].

Summary And Outlook

*If we assume we have arrived: we stop searching,
we stop developing.*

Jocelyn Bell Burnell

Stabilizing and observing topological spin textures in antiferromagnets has been a challenge over the past years, precisely because of their possibility to exhibit ultrafast spin dynamics in a minimal stray field configuration and therefore hold strong promise for spintronics applications. In this context, [SyAFMs](#) have emerged as an experimentally accessible and technologically versatile alternative to intrinsic [AFMs](#). By coupling ferromagnetic layers antiferromagnetically across metallic spacers, [SyAFMs](#) combine the absence of overall stray fields and elimination of the skyrmion Hall effect with tunability of interfacial properties such as anisotropy and [iDMI](#). This has enabled the stabilization of homochiral solitons while retaining the favorable dynamical properties of compensated systems. Based on this, this thesis has systematically demonstrated the stabilization of a rich spectrum of quasiparticles such as merons, antimerons, bimerons, skyrmions, hybrid skyrmion tubes, and orthogonally coupled skyrmion–bimeron pair (skymeron) within the [SyAFMs](#).

In **Chapter 4**, the experimental realization of in-plane topological spin textures, namely Néel merons, Bloch merons, antimerons, and bimerons, is demonstrated at ambient conditions in multilayer [SyAFMs](#) [1, 2]. Using multimodal vector imaging, achieved by combining in-house imaging techniques, namely [SEMPA](#) and [MFM](#), the full three-dimensional Néel order is reconstructed. This has enabled an unambiguous determination of helicity, polarity, and topological charge, confirm-

ing the presence of homochiral Néel configurations that overcome the random chirality inherent to single-crystalline AFMs. Statistical analysis shows that meron cores have diameters of 230 ± 50 nm, and that the separation between opposite polarity cores is shorter than between like polarity cores, implying an attractive interaction that favours bimeron formation. Furthermore, by varying magnetic compensation, the helicity of merons is tailored from Néel-type to Bloch-type. Synchrotron-based XMCD-PEEM imaging provides direct visualization of the real-space antiferromagnetic nature of these (bi)merons. Micromagnetic simulations reproduce the meron spin textures and yield phase diagrams demonstrating the role of iDMI, PMA, and interlayer demag in (bi)meron stabilization.

Beyond the in-plane spin textures, **Chapter 5** presents an engineered route to stabilize antiferromagnetic OOP topological spin textures (skyrmions) having radii of 50 to 100 nm across a broad range of magnetic compensation from 50 to 100 percent, thereby yielding skyrmions with distinct static and dynamic properties [3]. Furthermore, we investigate the nucleation of antiferromagnetic skyrmions using complementary methods. In uncompensated SyAFM stacks, the application of a magnetic field yields discrete skyrmions within a finite field window. Current pulses generate Joule heating that fragments stripe domains into skyrmions even in fully compensated stacks. IR picosecond pulses nucleate skyrmions within narrow windows of field and fluence. Synchrotron-based XMCD-STXM imaging reveals opposite contrast in the two sublattices, confirming antiferromagnetic coupling between skyrmions in the ferromagnetic sublattices. Subsequently, we employ time-resolved pump-probe soft X-ray microscopy to resolve three distinct nanosecond dynamical regimes of AFM skyrmions driven by current-induced SOTs. (a) *Hopping*: In a non-flat energy landscape, where an individual AFM skyrmion remains pinned at a domain wall, it exhibits dynamic hopping between adjacent pinning sites through a caterpillar-like motion. The skyrmion sequentially undergoes shrinking, lateral displacement, and re-expansion under the applied SOT. After the pulse is switched off, the skyrmion relaxes back to a nearby equilibrium position with a characteristic timescale of approximately 7.5 ns. (b) *Scattering*: In a skyrmion lattice at low current density, some skyrmions become mobile while others remain pinned. The mobile skyrmions scatter from pinned neighbours and recoil nearly to their original positions, relaxing with a timescale τ_{relax} in the range of 3 – 20 ns after the current is terminated. Analyzing the recoil trajectories enables the extraction of the skyrmion-skyrmion interaction potential $U(r)$, found to decay exponentially. (c) *Viscous flow*: At high current densities, the skyrmion lattice enters a viscous-flow regime in which all skyrmions translate coherently, exhibiting purely longitudinal motion with a vanishing skyrmion Hall angle. The dynamic Hall angle remains zero within experimental uncertainty across all applied current densities, confirming the cancellation of Magnus forces in fully compensated SyAFMs.

Beyond the two-dimensional spin textures, **Chapter 6** addresses the three-dimensional exten-

sion of skyrmions and discusses the strategy to stabilize *hybrid skyrmions* in SyAFMs by tuning the magnetic compensation [4]. By combining LTEM with element-specific STXM, the real-space observation of a AFM hybrid skyrmion is achieved. The dynamics of these hybrid tubes reveal a pronounced non-reciprocal skyrmion Hall effect, in sharp contrast to the reciprocal motion of Néel-type AFM skyrmions. Statistical analysis demonstrates that at low velocities, the Hall angle is reciprocal, whereas at higher velocities, the distribution splits for opposite current directions. The NSkHE originates from helicity changes during motion rather than from pinning or shape distortions. Micromagnetic simulations reveal that above a critical velocity, the helicity evolves toward a more symmetric Néel profile during the current pulse, which induces an asymmetric SOT efficiency and thereby a polarity-dependent Hall angle.

Finally, in **Chapter 7**, a new quasiparticle, termed *skymeron*, is introduced. It is defined as an orthogonally coupled skyrmion–bimeron pair. Unlike conventional AFMs, where both sublattices share identical anisotropies, SyAFMs allow the anisotropies of each layer to be tuned individually. During the spin flop transition, this difference results in asymmetric canting, with one sublattice tilting more strongly toward the in-plane direction. Consequently, the two sublattices can approach a nearly perpendicular configuration, in which an out-of-plane skyrmion in one layer is intrinsically aligned with an in-plane bimeron in the adjacent layer. This orthogonal alignment represents a distinct and tunable topological state, which we term the *skymeron*, emerging from the transition between antiferromagnetic and near-perpendicular alignment of the sublattice. A multilayer SyAFM is designed to host skymerons, and their real-space observation is achieved by element-specific X-ray microscopy. Furthermore, skymerons are observed to nucleate spontaneously under finite out-of-plane magnetic fields or upon excitation of IR laser pulses. Micromagnetic simulations demonstrate their stabilization in SyAFMs. The stabilization and observation of skymerons highlights that SyAFMs serve as hosts for established topological textures.

Overall, the findings of this thesis demonstrate that synthetic antiferromagnets can host a broad spectrum of compensated topological spin textures, ranging from merons and bimerons to skyrmions, hybrid tubes, and skymerons. These results should be regarded as part of a broader effort to establish the physics of antiferromagnetic spin structures across diverse material platforms, including intrinsic antiferromagnets, ferrimagnets, and the emerging class of altermagnets [289]. The central challenge for the coming years is to chart the full parameter space in which such solitons can exist and to identify the emergent phenomena they may give rise to. Of particular interest are emergent responses such as the topological spin Hall effect [43, 242] and the topological orbital Hall effect [243], which are predicted to arise in antiferromagnetic skyrmion and bimeron lattices. Orbital angular momentum, the counterpart of electron spin angular momentum, provides an efficient

means to manipulate magnetization [290–292] and can be used to drive topological spin textures more efficiently. Moreover, the pronounced thermal diffusion of antiferromagnetic quasiparticles provides a natural benchmark for evaluating their potential as nonlinear magnon reservoirs, while simultaneously enabling the exploitation of stochastic dynamics for reservoir computing architectures.

Part III

Appendices

Author Contributions for each Experimental Chapter

Merons, Antimerons and Bimerons in Synthetic Antiferromagnet

- Samples are grown by Dr. Takaaki Dohi and Maria-Andromachi Syskaki (JGU Mainz)
- Low temperature MFM images by Dr. Ankit Sharma (Attocube)
- XMCD-PEEM measurements with Edgar Felipe Galíndez Ruales, Arnab Bose, and Adithya Rajan (JGU Mainz).
- Theoretical modeling by V. K. Bharadwaj, Ricardo Zarzuela, and Jairo Sinova (JGU Mainz).
- Takaaki Dohi, Ricardo Zarzuela, Robert Frömter, and Mathias Kläui helped during the drafting of the paper manuscript.
- Own contribution: Design of the sample stack, SEMPA and MFM imaging (Room temperature) of the samples, Analysis of the SEMPA imaging using MATLAB scripts, patterning of the structures using EBL, SQUID measurements and analysis, micromagnetic simulations of the (bi)merons and phase diagram, conducting XMCD-PEEM beamtimes.

Stabilization, Nucleation, and Dynamics of Antiferromagnetic Skyrmions

- Samples are grown by Maria-Andromachi Syskaki (JGU Mainz).
- STXM measurements with Dr. Takaaki Dohi, Robert Frömter, Duc Tran, and Robin Tietgen (JGU Mainz).

- Extracting the form of interaction potential of AFM skyrmions by Kilian Leutner.
- Robert Frömter and Mathias Kläui helped with drafting the paper manuscript.
- Own contribution: Design of the sample stack, MFM imaging (Room temperature) of the samples, patterning of the structures using EBL on the membranes, STXM beamtime proposals and report, SQUID measurements and analysis, conducting and managing STXM beamtimes, analysis of the STXM data by MATLAB and Python codes.

Non-reciprocal Current-Induced Dynamics of Hybrid Skyrmion Tubes

- Samples are grown by Dr. Takaaki Dohi and Maria-Andromachi Syskaki (JGU Mainz).
- Lorentz TEM images by Dr. Thibaud Denneulin (Julich).
- STXM measurements with Dr. Takaaki Dohi, and Fabian Kammerbauer (JGU Mainz).
- Theoretical modeling by V. K. Bharadwaj, Ricardo Zarzuela, and Jairo Sinova (JGU Mainz).
- Takaaki Dohi, Robert Frömter, and Mathias Kläui helped with the drafting of the paper manuscript.
- Own contribution: MFM imaging (Room temperature) of the samples, patterning of the structures using EBL on the membranes, SQUID measurements and analysis, conducting STXM beamtimes, Micromagnetic simulation and analysis.

Skymeron: An Orthogonally Coupled Skyrmion–Bimeron Pair

- Samples are grown by Maria-Andromachi Syskaki (JGU Mainz).
- STXM measurements with Robert Frömter, Fabian Kammerbauer, and Robin Tietgen, (JGU Mainz).
- Own contribution: Design of the sample stack, MFM imaging (Room temperature) of the samples, patterning of the structures using EBL on the membranes, STXM beamtime proposals and report, SQUID measurements and analysis, conducting and managing STXM beamtimes, analysis of the STXM data by MATLAB and Python codes, Micromagnetic simulation and analysis.

Additional Information for Chapter 04

B.1 XAS Spectra

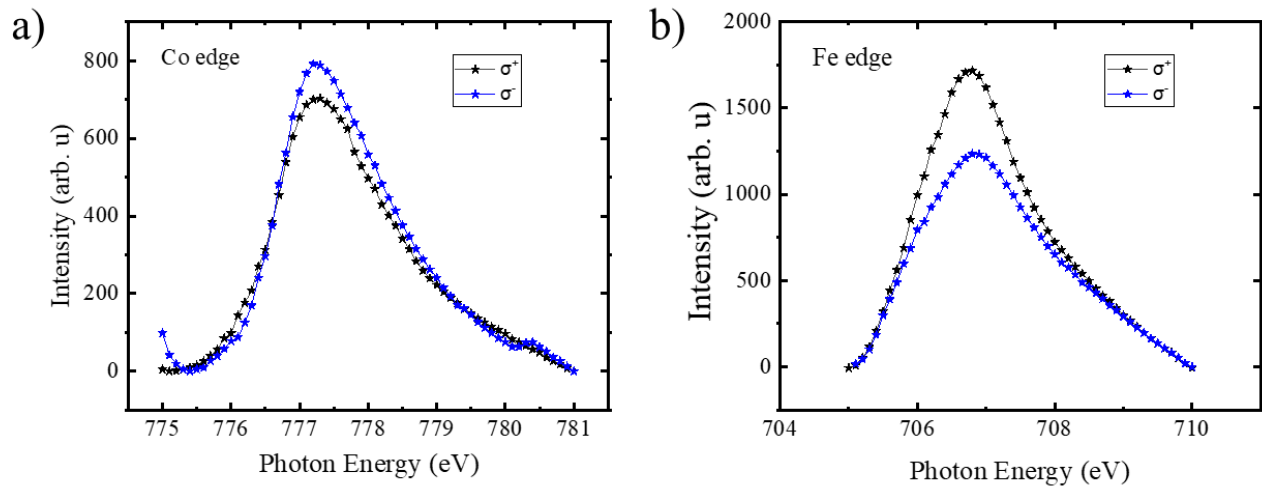


Figure B.1: **X-ray absorption spectra (XAS) at the Co and Fe L_3 edges using XMCD-PEEM** (a) XAS recorded at the Co L_3 edge, showing absorption intensity as a function of photon energy for left (σ^- , blue) and right (σ^+ , black) circularly polarized light. (b) Corresponding XAS at the Fe L_3 edge, revealing a stronger XMCD contrast compared to Co, indicative of higher net moment contribution from the Fe sublattice under these conditions.

The XAS presented in Fig. B.1 are acquired using XMCD-PEEM at the CIRCE beamline of the ALBA synchrotron and correspond to the meron-supporting SyAFM multilayer stacks. Panels (a) and (b) show the element-specific absorption profiles at the Co and Fe L_3 edges, respectively, under circularly polarized X-rays of opposite helicities (σ^+ and σ^-). A pronounced dichroism is observed in both cases, confirming the presence of robust magnetic contrast and enabling sublattice-resolved

magnetic imaging. Importantly, the absence of a secondary peak or spectral shoulder in either spectrum indicates that the metal layers remain chemically intact, with no measurable oxidation. This spectral integrity supports the reliability of subsequent magnetic imaging and confirms the high structural and chemical quality of the multilayer stack.

B.2 XMCD-PEEM Images of Stack #M12

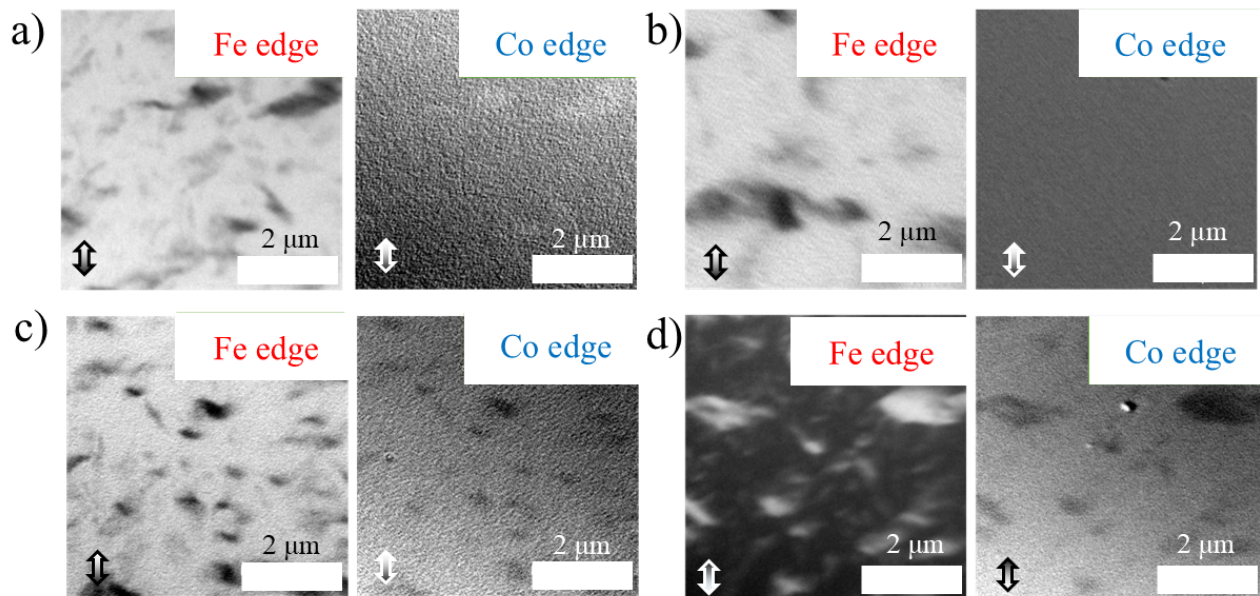


Figure B.2: **XMCD-PEEM images of domains in the SyAFM at Fe edge and Co edge** (a) strong contrast in Fe and weak opposite contrast at Co edge (b) strong contrast in Fe and no contrast at Co edge (c) strong contrast in Fe and weak similar contrast at Co edge (d) 180-degree rotated image showing strong contrast in Fe and weak opposite contrast at Co edge.

Fig. B.2 presents XMCD-PEEM images of stack #M12 acquired at room temperature under zero external magnetic field. In this stack, Fe is confined to the topmost FM layer, while Co is more concentrated in the second FM layer. As a result, the Fe L_3 -edge contrast selectively reveals the magnetization of the top layer, whereas the Co L_3 edge is used to probe the underlying 2nd FM layer. Initial imaging at both edges reveals strong magnetic contrast at the Fe edge and a weaker, oppositely oriented contrast at the Co edge (see Fig.B.2(a)), confirming antiferromagnetic alignment between the two ferromagnetic layers. However, during subsequent high-resolution imaging at the same location, the contrast at the Co edge diminished significantly, Fig.B.2(b). This reduction is attributed to surface carbon contamination that accumulates over time, attenuating the photoemis-

sion signal from deeper layers. At this point, the XMCD signal from the upper Co layer cancels that from the lower Co layer (located 3–4 nm beneath the surface), effectively suppressing the net Co contrast—consistent with uniform AFM coupling. In later measurements, contrast at the Co edge reappeared but matched the Fe edge in polarity (see Fig.B.2(c)), indicating that the signal originates exclusively from the topmost FM layer, as the contribution from the second layer was no longer detectable. When the imaging position was shifted to a fresh area, magnetic contrast from both Fe and Co edges, again with opposite polarity, was recovered (see Fig.B.2(d)). This further supports the existence of robust and spatially uniform AFM coupling across the SyAFM structure.

B.3 Deleting and Recreating the (Anti)merons

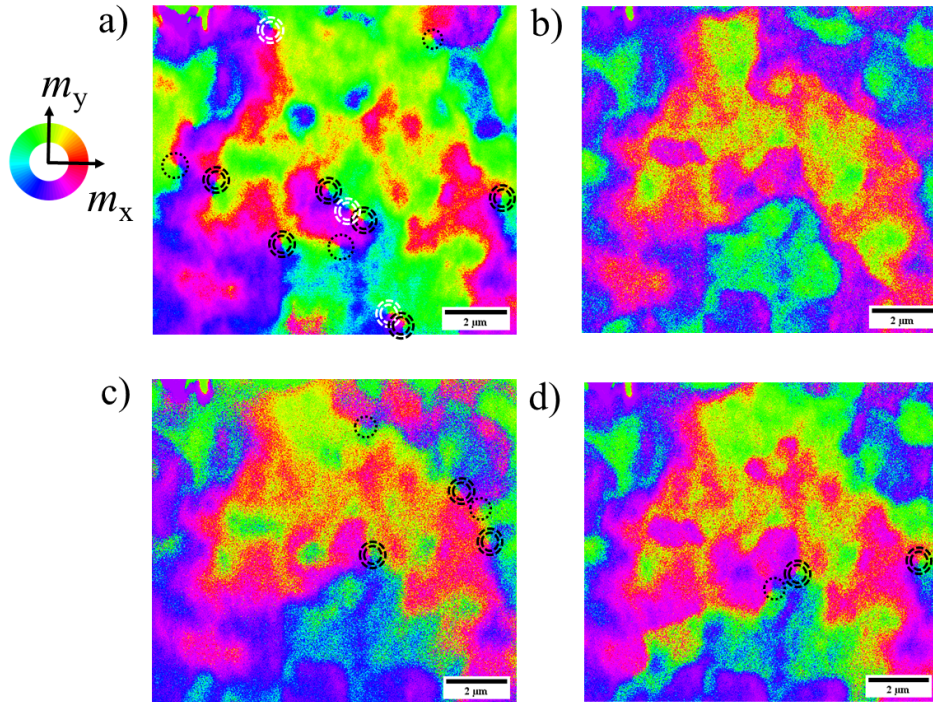


Figure B.3: **Deleting and re-creating (anti)merons.** (a) Out-of-plane demagnetized state, (b) state after the application of +50 mT magnetic field along the x -direction, (c) state after the application of -50 mT magnetic field along the x -direction, (d) in-plane demagnetized state. The demagnetized state is achieved following the application of an oscillating magnetic field. Black single circles and white double circles indicate merons with helicity $\gamma = 0$ and $\gamma = \pi$, respectively. Antimerons are marked using a double black circle.

Here, we investigate the effect of magnetic fields on the stability of (anti)merons. Using SEMPA measurements, the sample of stack #M11 was analyzed at room temperature and under various

magnetic field conditions. Fig. B.3(a) depicts the state of the sample after being subjected to out-of-plane demagnetization, revealing the presence of (anti)merons. In contrast, Fig. B.3(b) illustrates the deletion of these meron spin textures upon the application of an in-situ magnetic field of 50 mT along the x -direction. The application of an in-situ magnetic field of -50 mT along the x -direction, as depicted in figure B.3(c), results in the re-emergence of the (anti)merons in a different region of the sample. Lastly, Fig. B.3(d) shows the spin state after the application of an in-plane oscillating magnetic field. These results demonstrate the ability to manipulate topological spin structures by applying magnetic fields.

B.4 SEMPA-Based Identification of Merons and Antimerons

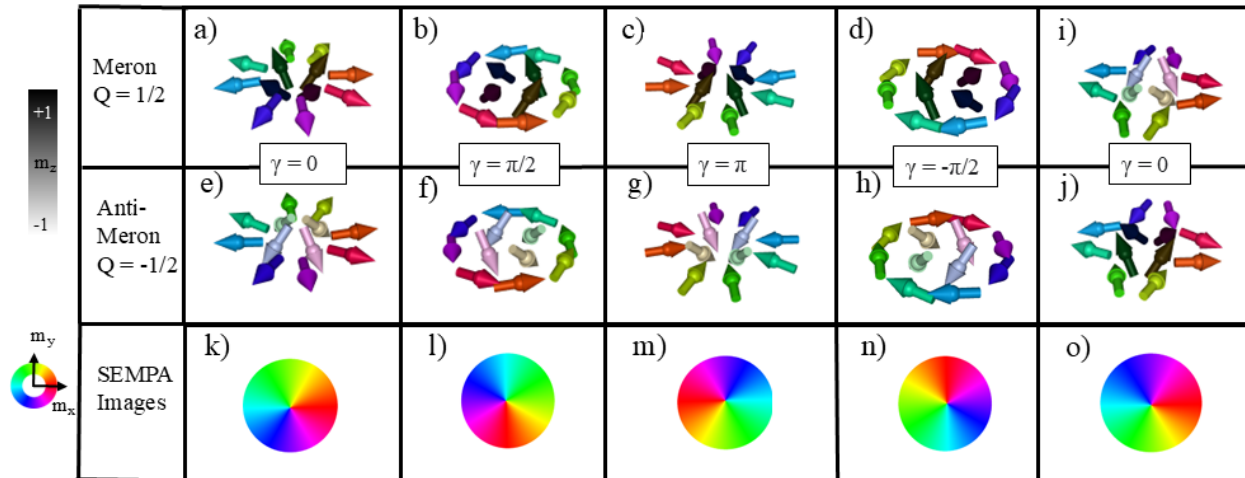


Figure B.4: Schematic classification of meron and antimeron spin textures with varying helicity. Panels (a–d) illustrate merons with topological charge $Q = +1/2$ and helicity values $\gamma = 0, \pi/2, \pi, -\pi/2$, respectively. Panels (e–h) show corresponding antimerons with $Q = -1/2$ for the same helicities. The third row (k–o) shows the corresponding SEMPA in-plane spin textures mapped using a color wheel representation of the m_x and m_y components. The out-of-plane component m_z is encoded by grayscale in the top two rows, as indicated by the vertical color bar on the left.

B.5 Parameters for Micromagnetic Simulation

Micromagnetic simulations were performed using the Mumax³ software [280, 293]. The following setup was implemented in the simulations leading to Fig. 4.16. A bilayer square geometry of lateral size 512 nm and thickness 1 nm for each of the ferromagnetic layers was considered, and dipolar

interaction was included. The system was discretized with a mesh size of $1 \times 1 \times 1 \text{ nm}^3$ and periodic boundary conditions along the x and y directions were imposed, with a period equal to 16 repetitions. The material parameters are $A_{\text{ex}} = 1 \times 10^{-11} \text{ Jm}^{-1}$ for the exchange constant, $M_s = 0.145 \text{ MAm}^{-1}$ for the saturation magnetization and $\alpha = 0.01$ for the Gilbert damping. The strength of the interlayer exchange coupling was chosen to be $2J_{\text{AFM}} = 0.44 \times 10^{-3} \text{ Jm}^{-2}$, which corresponds to the value obtained from SQUID measurements. We note that in Mumax³, interlayer exchange interactions are properly accounted for by rescaling the material parameters by the thickness of the spacer (see `ext_scaleExchange` function) [293]. To explore the $D - K_{\text{eff}}$ phase diagram, the effective out-of-plane uniaxial anisotropy K_{eff} and the iDMI D were varied in the range $[-3 \times 10^5, 3 \times 10^5] \text{ Jm}^{-3}$ and $[0, 2 \times 10^{-3}] \text{ Jm}^{-2}$, respectively. An initial meron configuration is chosen in the simulations, which is minimized to find the equilibrium configuration. The parameter space of (D, K_{eff}) was swept to obtain the light green shaded region in Fig. 4.16.

B.6 Open Questions

This section addresses the open questions for Chapter 04.

Possibility of Meron–Antimeron Lattice

An important difference between isolated skyrmions and isolated merons lies in the absolute value of the total spin rotation across these spin textures. Skyrmions exhibit a 2π rotation of the magnetization from left to right, whereas merons display only a π rotation, as illustrated in Fig. B.5 (a, b). When creating a lattice of skyrmions, it is straightforward to align them side by side to form a periodic array. However, for merons, the situation is different. In the example of Fig. B.5 (b), the meron begins with a green arrow on the left side and ends with a violet arrow on the right. Therefore, alternating merons and (anti)merons are required to achieve a periodic spin rotation; an example of a meron–antimeron lattice is shown in Fig. B.5 (c). If the merons and antimerons have opposite core polarities, a bimeron lattice can be formed; otherwise, this results in a trivial meron–antimeron lattice. Theoretical predictions of meron–antimeron lattices have been reported in the literature [138, 294], along with experimental observations [139]. Additionally, Yu *et al.* [139] demonstrated the transition from a square meron–antimeron lattice to a hexagonal skyrmion lattice upon applying magnetic fields. While our specific study did not observe meron/antimeron lattices, it is worth mentioning that there are promising theoretical predictions regarding the potential generation of such structures using ultrafast laser pulses [143].

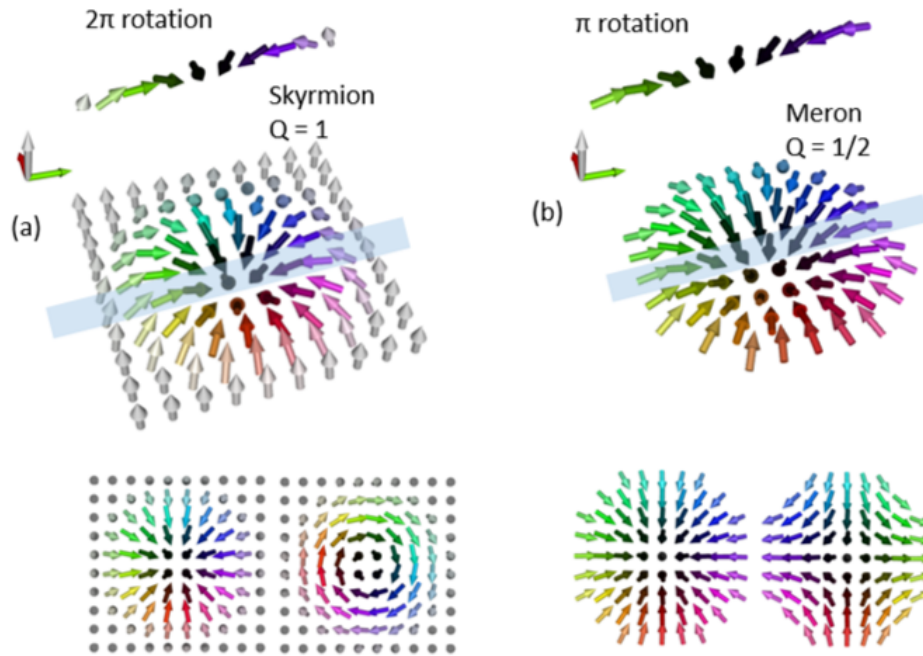


Figure B.5: **Comparison of an isolated skyrmion and meron spin textures.** (a) Isolated skyrmion with topological charge $Q = 1$. (b) Isolated meron with $Q = 1/2$. The spin structure along the indicated grey line is replicated above each 2D image for clarity. Color code reference is shown on the left side of each panel. (c) An example of a meron–antimeron lattice.

Potential Influence from the Other Layers

In Chapter 4, we performed multimodal vector imaging of the three-dimensional Néel order parameters. This analysis primarily involves vector operations of the IP and OOP spin components. While the system under study comprises a multi-layer SyAFM stack, the experimental observations are restricted to the first two magnetic layers of the film. In this section, we also address the potential influence of the deeper magnetic layers, which may impact the overall magnetic response and the interpretation of the observed spin textures.

We conducted micromagnetic simulations to scrutinize the potential impact of insufficient interlayer coupling strength. Using the experimentally determined parameters for stack #M4, we systematically simulated the magnetic response of a SyAFM consisting of 28 magnetic layers, all of which were antiferromagnetically coupled. The resulting OOP and IP hysteresis loops are shown as the red curves in Fig. B.6(a) and Fig. B.6(a), respectively. For comparison, the blue curve represents

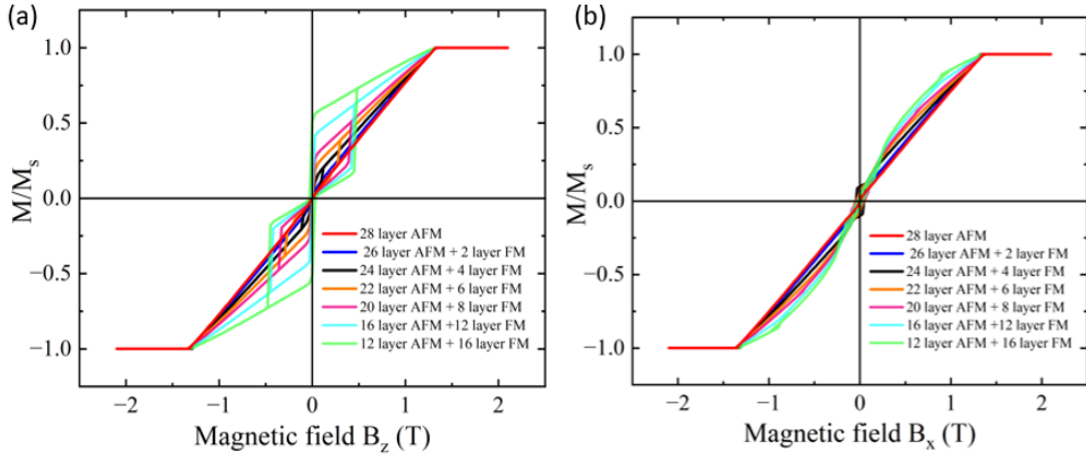


Figure B.6: **Micromagnetic simulation of magnetic hysteresis loops as influenced by the presence of ferromagnetically coupled layers within the stack.**

a configuration in which 26 layers are AFM coupled and 2 layers are ferromagnetically coupled with equal coupling strength, effectively creating an uncompensated SyAFM. This uncompensated character is distinctly visible in the hysteresis loop. Moreover, by progressively increasing the number of FM-coupled layers, we observed a corresponding increase in the degree of effective uncompensation. This trend serves as strong evidence that the AFM coupling in our experimental stack is robust and uniform across all layers, thereby precluding the possibility of significant effective uncompensation, as would otherwise be reflected in the measured hysteresis loops.

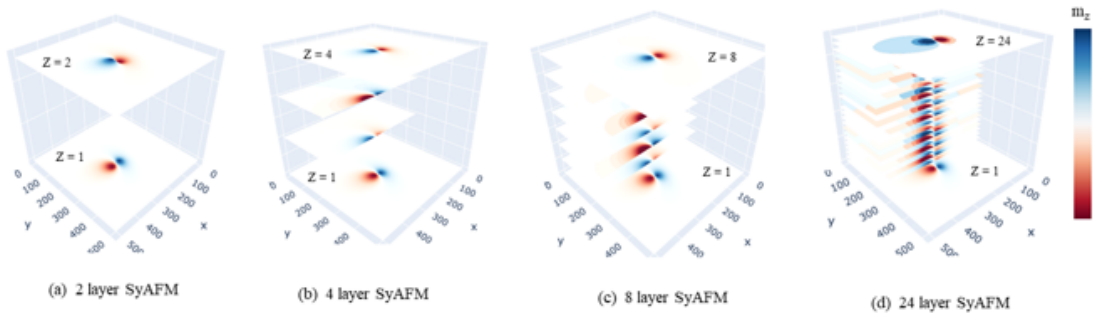


Figure B.7: **Bimeron evolution in SyAFM with varying repetitions.** (a) 2-layer SyAFM, (b) 4-layer SyAFM, (c) 8-layer SyAFM, and (d) 24-layer SyAFM. Here, Z denotes the number of FM layers that are antiferromagnetically coupled.

In our SyAFM stack, we have carefully optimized the thickness of the Ir layer to 0.4 nm, a choice that maximizes the strength of the AFM exchange coupling. Furthermore, our stack incorporates a repeated structure, specifically 14 repetitions of the SyAFM layer, which significantly enhances the

stack's effective saturation field. We have established a robust AFM exchange coupling in this stack, as evidenced by our analysis of the SQUID hysteresis loop data. It is noteworthy that the current stack configuration may support a three-dimensional spin texture. To investigate this, we conducted micromagnetic simulations by varying the number of repetitions of the SyAFM, extending up to $Z = 24$, where Z represents the number of ferromagnetic (FM) layers that are antiferromagnetically coupled. Our results revealed that the size of the bimeron remains consistent even as the number of repetitions increases, leading to a structure resembling a bimeron tube. This stability in bimeron size suggests that the spin texture, being AFM-coupled across the FM layers, does not vary significantly throughout the thickness. Consequently, these spin textures can be effectively represented using a two-dimensional model, as discussed in Chapter 4.

Spin Textures Observed in the Stacks #M2–#M10

This section contains a selection of various (bi)meron samples that were investigated during this thesis. Imaging of the samples was performed in SEMPA.

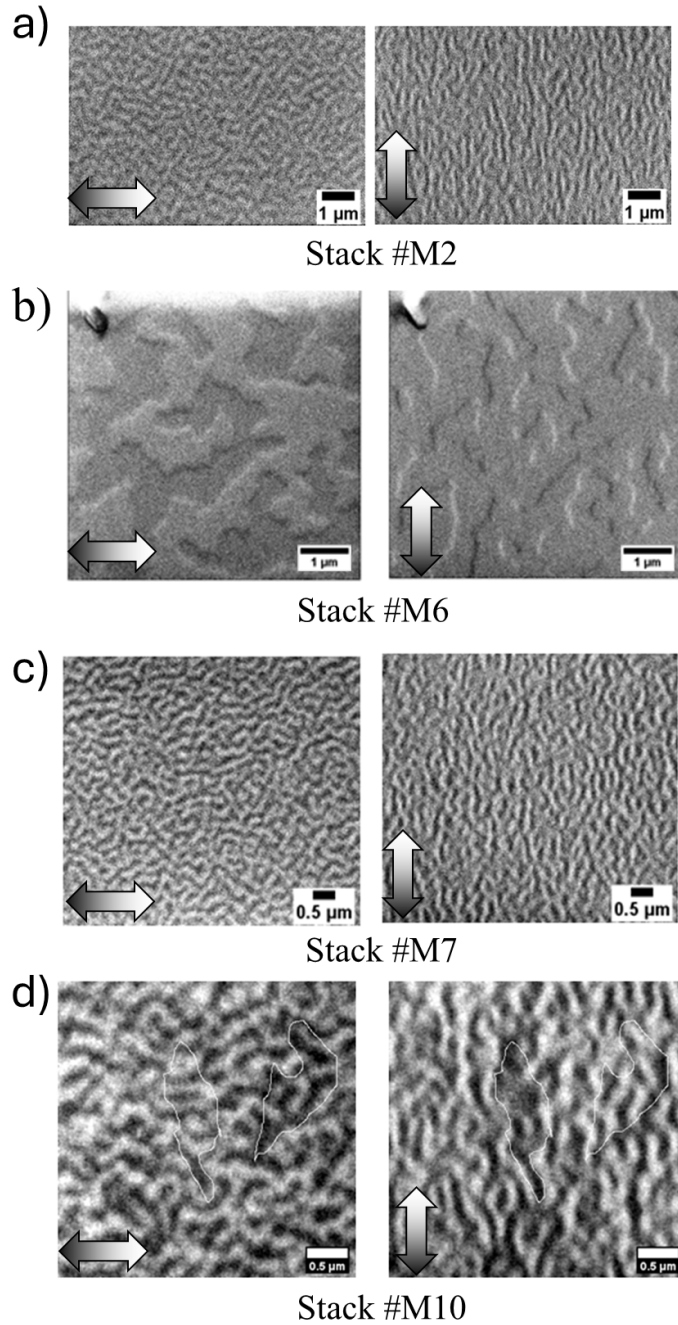
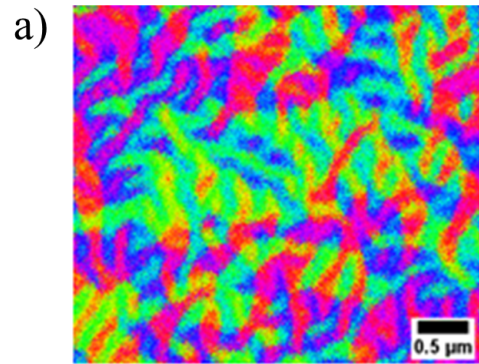
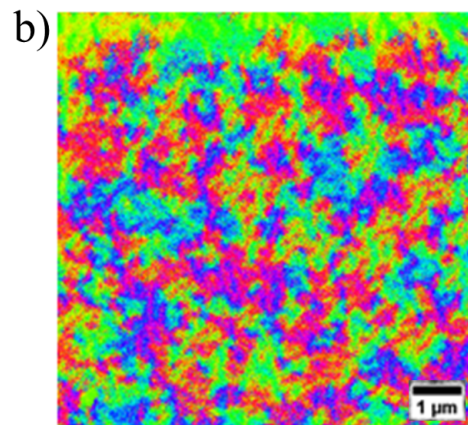


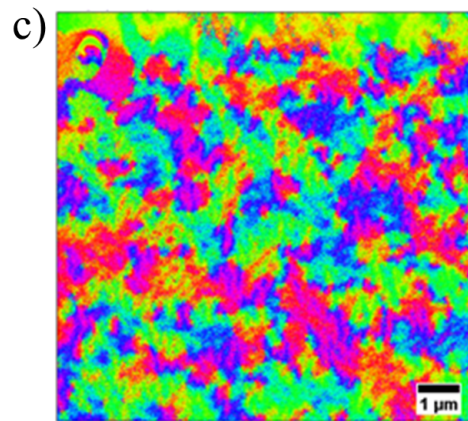
Figure B.8: **SEMPA images of the stack #M12, #M6, #M7 and #M10.** Horizontal and vertical in-plane components of the surface magnetization. The direction of magnetization is indicated by the grayscale contrast, as displayed on the double arrows.



Stack #M3



Stack #M8



Stack #M9

Figure B.9: **SEMPA images of stacks #M3, #M8, and #M9.** The images display the IP spin components of the topmost FM_A layer. The color code for the spin direction is consistent with that used in Fig. B.3.

Additional Information for Chapter 05

C.1 Structural and Compositional Details of the SyAFM Stacks

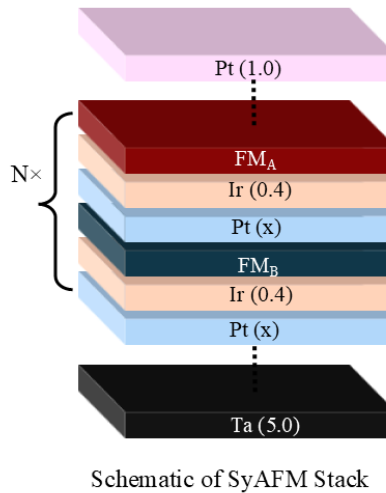


Figure C.1: **Schematic illustration of the SyAFM multilayer stack studied in this thesis.** Each repetition unit consists of $[Pt(x)/Ir(0.4)/FM_B/Pt(x)/Ir(0.4)/FM_A]$, repeated N times on a Ta(5.0) seed layer and capped with Pt(1.0). Here, FM_A and FM_B represent the two ferromagnetic sublattices (see Table C.1 for detailed sublattice thickness), while x denotes the Pt spacer thickness that tunes the interlayer exchange coupling.

The schematic in Fig. C.1 illustrates the synthetic antiferromagnetic (SyAFM) multilayer architecture composed of repeated $[Pt(x)/Ir(0.4)/FM_B/Pt(x)/Ir(0.4)/FM_A]$ units on a Ta(5.0) seed and capped with Pt(1.0). All thicknesses are given in nm. The layer compositions, repetition number N , and Pt spacer thickness x are summarized in Table C.1. Variations in FM_A , FM_B , and x govern the interlayer coupling strength and overall magnetic compensation of each sample.

Table C.1: List of SyAFM stacks investigated in Chapter 05.

Sample names	N	FM _A	FM _B	x = Pt (nm)
#S1 (TDMM005)	15	FCB(0.5) / CFB(0.4)	CB(0.225)/Ta(0.06)/CB(0.225)/Ta(0.06)/CB(0.225)	1
#S2 (TDMM010)	25	FCB(0.5) / CFB(0.4)	CB(0.4)/Ta(0.06)/CB(0.35)/Ta(0.06)/CB(0.35)	1
#S3 (MASA673)	25	FCB(0.4) / CFB(0.375)	CB(0.4)/Ta(0.06)/CB(0.35)/Ta(0.06)/CB(0.35)	1
#S3a (MASA675)	25	FCB(0.35) / CFB(0.375)	CB(0.4)/Ta(0.06)/CB(0.35)/Ta(0.06)/CB(0.35)	1.25
#S3b (MASA677)	25	FCB(0.35) / CFB(0.375)	CB(0.4)/Ta(0.06)/CB(0.35)/Ta(0.06)/CB(0.35)	1.3
#S3c (MASA681)	25	FCB(0.35) / CFB(0.375)	CB(0.4)/Ta(0.06)/CB(0.35)/Ta(0.06)/CB(0.35)	1.35
#S3d (MASA674)	25	FCB(0.35) / CFB(0.375)	CB(0.4)/Ta(0.06)/CB(0.35)/Ta(0.06)/CB(0.35)	1.2
#S4 (TMD550)	25	FCB(0.3) / CFB(0.3)	CB(0.4)/Ta(0.06)/CB(0.35)/Ta(0.06)/CB(0.35)	1
#S5 (MASA683)	25	FCB(0.4) / CFB(0.4)	CB(0.4)/Ta(0.06)/CB(0.35)/Ta(0.06)/CB(0.35)	1
#S5a (MASA684)	25	FCB(0.4) / CFB(0.2)	CB(0.4)/Ta(0.06)/CB(0.35)/Ta(0.06)/CB(0.35)	1.3

Calibration Curve for Laser Fluence

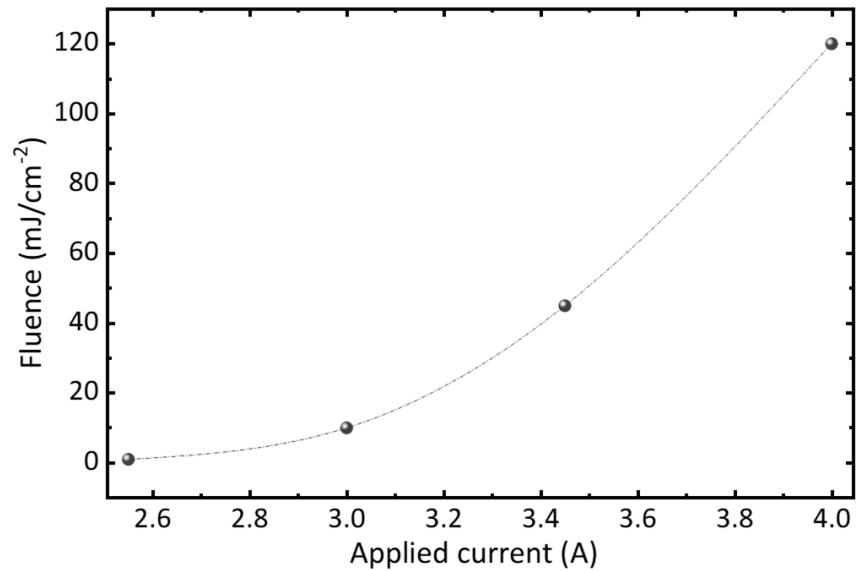


Figure C.2: Calibration curve showing the laser fluence as a function of applied current.

Nanofabrication Procedure on Silicon Nitride Membranes

1. A bilayer of electro-sensitive resist, consisting of MMA (methyl methacrylate) having a thickness of 550 nm and PMMA (polymethyl methacrylate) having a thickness of 200 nm^a, was spin-coated onto the substrate and baked at 100°C for 2 min to remove solvent residues, harden the resist, and improve surface adhesion.
2. The resist layer was patterned using an EBL system (Raith PIONEER). The focused electron beam (dose of 208 $\mu\text{C}/\text{cm}^2$, determined from a dose test on a reference sample and operated at 10 kV with a 30 μm aperture), guided by a computer-controlled pattern layout, locally modifies the resist by breaking polymer chains and reducing their molecular weight. Consequently, the exposed regions become soluble in a developer solution (MIBK:IPA, 1:3) for 30 s, which selectively removes them and thereby defines the desired pattern.
3. Afterwards, sputter deposition at Singulus was used to grow the magnetic film. The material was deposited directly onto the substrate in the developed regions, while elsewhere it adhered only to the resist. Subsequent lift-off (using acetone) removed the resist and overlying film, leaving the patterned wires on the membrane^b.
4. Contact pads were then fabricated on top of the magnetic tracks through a second EBL, deposition at contact sputtering, and lift-off process. The pads consisted of Cr(5 nm)/Au(150 nm), providing good adhesion and high electrical conductivity.
5. For the samples used for pump-probe measurements, a 100 nm Al layer was deposited on the backside of the membranes to improve heat dissipation during the time-resolved imaging.

^aAlthough the entire process can be performed using PMMA as a single-layer resist, the inclusion of an MMA underlayer offers improved control over the fabricated structures, particularly important for fabrication on membranes. For the same exposure dose that defines patterns in PMMA, the MMA layer produces slightly overdeveloped features, creating an undercut profile. This undercut enhances the subsequent deposition quality by preventing the deposited material from contacting the resist sidewalls, thereby ensuring a smoother lift-off process.

^bNote that during the lift-off process, the membranes must be gently placed in acetone, and the solvent should be slowly circulated using a dropper. Ultrasonic agitation should be avoided, as it can easily damage or break the fragile membranes.

Additional Information for Chapter 06

D.1 Types of Hybrid AFM Skyrmion in SyAFM

Figs. D.1(a) and D.1(b) show the two degenerate configurations, labeled Type A and Type B, obtained under identical simulation conditions. In both cases, the skyrmion cores remain strictly antiferromagnetically aligned across adjacent layers, confirming that the interlayer exchange coupling is strong enough to preserve antiparallel core orientation. The only difference between the two states lies in the sign of the Bloch component: in Type A, the in-plane rotation is clockwise, while in Type B it is counterclockwise. The simulated helicity profile reveals a Néel-type wall ($\gamma = 0$) at one interface, a progressive buildup of Bloch character toward the film mid-plane, and a reversal to the opposite Néel chirality at the other interface. The in-plane magnetization direction is represented using a color scale, with red and blue corresponding to $+x$ and $-x$ alignment, respectively. These results demonstrate that hybrid skyrmion tubes in partially compensated SyAFMs possess an intrinsically three-dimensional helicity structure that emerges from the superposition of interfacially imposed Néel components and dipolar-induced Bloch components, and that both helicity senses are equally accessible under symmetric conditions.

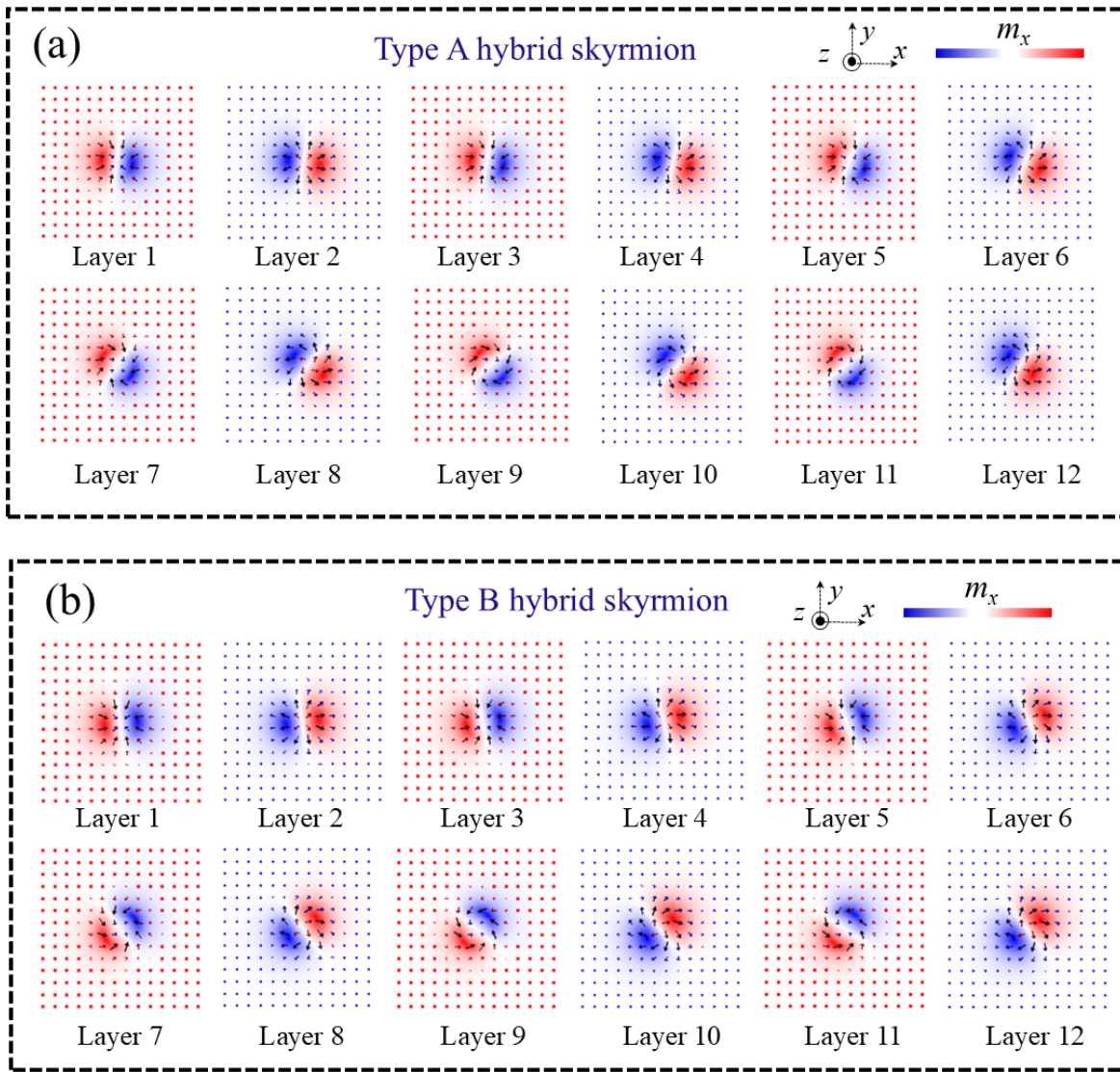


Figure D.1: **Micromagnetic simulations of hybrid antiferromagnetic skyrmions.** Layer-resolved simulation of skyrmion tubes in a twelve-layer synthetic antiferromagnet. **(a)** Type A hybrid antiferromagnetic skyrmion, characterized by an in-plane Bloch component with a fixed helicity throughout the stack. **(b)** Type B hybrid antiferromagnetic skyrmion, stabilized under identical conditions, exhibiting the opposite Bloch helicity. Both configurations result from the superposition of interfacial Néel chirality, stabilized by iDMI, and Bloch contributions induced by long-range dipolar interactions. The two helicity states, clockwise and counterclockwise, are energetically degenerate. In-plane magnetization orientation is color coded, with red indicating alignment along the $+x$ direction and blue along the $-x$ direction.

D.2 Derivation of SkHE for Hybrid Skyrmion

The analytical description of the skyrmion dynamics in the synthetic antiferromagnetic (SyAFM) system is based on modeling the SyAFM as a multilayer stack of ferromagnetic layers separated by a metallic spacer, coupled antiferromagnetically through interlayer exchange interactions. The energy functional incorporates the principal interactions required to stabilize magnetic skyrmions: ferromagnetic exchange interactions within each layer, Dzyaloshinskii-Moriya interactions (DMI), and on-site uniaxial anisotropy. The energy functional for each layer i , describing the multilayer SyAFM, can be written as

$$\begin{aligned} \mathcal{E}_{\text{eff}} = \int_s d^2r \left\{ A_{\text{ex}}(\nabla \mathbf{m}_A)^2 + A_{\text{ex}}(\nabla \mathbf{m}_B)^2 \right. \\ \left. + D_{\text{DMI}}[\mathbf{m}_A \cdot (\nabla \times \mathbf{m}_A)] + D_{\text{DMI}}[\mathbf{m}_B \cdot (\nabla \times \mathbf{m}_B)] \right. \\ \left. - K_{\text{eff},A} m_{A,z}^2 - K_{\text{eff},B} m_{B,z}^2 \right. \\ \left. - J_{\text{AFM}}(\mathbf{m}_A \cdot \mathbf{m}_B) \right\}. \end{aligned} \quad (\text{D.1})$$

where

$$D_{\text{DMI}}[\mathbf{m}_i \cdot (\nabla \times \mathbf{m}_i)] = D_{\text{DMI}}[(\mathbf{m}_i \cdot \nabla) m_{z,i} - m_{z,i}(\nabla \cdot \mathbf{m}_i)],$$

and $\mathbf{m}_i(\mathbf{r})$ denotes the order parameter of the i -th layer normalized by the saturation magnetization $M_{s,i}$. Here, A_{ex} and D_{DMI} represent the spin stiffness constant and the DMI strength of the ferromagnetic layers, respectively, while J_{AFM} denotes the interlayer exchange constant, which strongly depends on the thickness of the spacer layer.

To derive the equation of motion for the skyrmion, the LLG equation is employed, incorporating both field-like and damping-like spin-orbit torques. The LLG equation for each layer i is expressed as

$$\frac{\partial \mathbf{m}_i}{\partial t} = -\gamma \mathbf{m}_i \times \mathbf{H}_{\text{eff},i} + \alpha \mathbf{m}_i \times \frac{\partial \mathbf{m}_i}{\partial t} + \mathbf{T}_{\text{SOT},i}, \quad (\text{D.2})$$

where γ is the gyromagnetic ratio, α is the phenomenological Gilbert damping parameter, $\mathbf{H}_{\text{eff},i}$ is the effective magnetic field, and $\mathbf{T}_{\text{SOT},i}$ represents the spin-orbit torque (SOT) acting on layer i .

The field-like and damping-like spin-orbit torque contributions are given as follows:

$$\mathbf{T}_{\text{SOT},i} = \tau_{\text{DL}} \mathbf{m}_i \times [\mathbf{m}_i \times (\hat{\mathbf{z}} \times \mathbf{j})] + \tau_{\text{FL}} \mathbf{m}_i \times (\hat{\mathbf{z}} \times \mathbf{j}), \quad (\text{D.3})$$

where τ_{DL} and τ_{FL} denote the damping-like and field-like torque coefficients, respectively. Assuming that the skyrmion tube spin texture in the multilayer remains rigid during its steady-state motion, the skyrmion dynamics in each layer can be described by the Thiele equation:

$$\mathbf{G}_i \times \dot{\mathbf{R}}_i - \alpha \mathcal{D}_i \dot{\mathbf{R}}_i - \tau_{\text{FL}} \mathbf{F}_{\text{FL},i} - \tau_{\text{DL}} \mathbf{F}_{\text{DL},i} = 0, \quad (\text{D.4})$$

where \mathbf{G}_i is the gyrotropic tensor generating the gyrotropic force perpendicular to the current, \mathcal{D}_i is the dissipative tensor describing the generalized drag force along the current, and $\mathbf{F}_{\text{FL},i}$ and $\mathbf{F}_{\text{DL},i}$ represent the effective forces arising from the field-like and damping-like components of the SOT, respectively. These quantities are defined as follows:

$$\mathcal{G}_{i|p,q} = \int_S d^2r [\mathbf{m}_i \cdot (\partial_p \mathbf{m}_i \times \partial_q \mathbf{m}_i)], \quad (\text{D.5})$$

$$\mathcal{D}_{i|p,q} = \int_S d^2r (\partial_p \mathbf{m}_i \cdot \partial_q \mathbf{m}_i), \quad (\text{D.6})$$

$$\mathbf{F}_{\text{FL},i|p} = \int_S d^2r [(\hat{\mathbf{z}} \times \mathbf{j}) \cdot \partial_p \mathbf{m}_i], \quad (\text{D.7})$$

$$\mathbf{F}_{\text{DL},i|p} = \int_S d^2r [((\hat{\mathbf{z}} \times \mathbf{j}) \times \partial_p \mathbf{m}_i) \cdot \mathbf{m}_i]. \quad (\text{D.8})$$

Upon solving the Thiele equations for the skyrmion velocity $(\dot{R}_{x,i}, \dot{R}_{y,i})$, the skyrmion Hall angle, $\vartheta_{\text{SkHE},i}$, is obtained as

$$\tan \vartheta_{\text{SkHE},i} = -\frac{\mathcal{G}(\tau_{\text{FL}} F_{\text{FL},x} + \tau_{\text{DL}} F_{\text{DL},x}) + \alpha \mathcal{D}_{xy} (\tau_{\text{FL}} F_{\text{FL},x} + \tau_{\text{DL}} F_{\text{DL},x}) - \alpha \mathcal{D}_{xx} (\tau_{\text{FL}} F_{\text{FL},y} + \tau_{\text{DL}} F_{\text{DL},y})}{\mathcal{G}(\tau_{\text{FL}} F_{\text{FL},y} + \tau_{\text{DL}} F_{\text{DL},y}) + \alpha \mathcal{D}_{yy} (\tau_{\text{FL}} F_{\text{FL},x} + \tau_{\text{DL}} F_{\text{DL},x}) - \alpha \mathcal{D}_{xy} (\tau_{\text{FL}} F_{\text{FL},y} + \tau_{\text{DL}} F_{\text{DL},y})}. \quad (\text{D.9})$$

The index “ i ” for the tensor elements is omitted here for the sake of brevity. The expression for ϑ_{SkHE} in Eq. D.9 can be simplified by assuming that the skyrmion structure in the multilayer stack corresponds to a centrosymmetric cylindrical tube. In this case, the magnetization in each layer can be expressed in cylindrical coordinates as

$$\mathbf{m}_i(r, \phi) = [\sin \Theta(r) \cos \Phi(\phi), \sin \Theta(r) \sin \Phi(\phi), \cos \Theta(r)],$$

where r is the radial coordinate and ϕ the azimuthal angle. This yields the following simplified expression for the skyrmion Hall angle:

$$\tan \vartheta_{\text{SkHE},i} = \frac{\alpha \mathcal{D}_{xx} \sin(\eta - \nu) - (\alpha \mathcal{D}_{xy} + 4\pi) \cos(\eta - \nu)}{(4\pi - \alpha \mathcal{D}_{xy}) \sin(\eta - \nu) + \alpha \mathcal{D}_{yy} \cos(\eta - \nu)}, \quad (\text{D.10})$$

where the current is injected into each layer at an angle η with respect to the x -axis. It is important

to note that the profile function $\Theta(r)$ of the skyrmion is assumed to vary from 0 (or π) at $r = 0$ to π (or 0) as $r \rightarrow \infty$. Eq. D.10 reproduces the SkHE measurements at low current densities, corresponding to the low-velocity regime. At higher current densities, in the extreme case [295], the skyrmion helicity evolves over time, requiring an additional degree of freedom (helicity) to be included in the equations of motion in order to account for these changes during current-driven motion. This would result in an additional force term in the Thiele equation, providing a more accurate representation of skyrmion dynamics. Such an extension, however, is beyond the scope of the present work. Instead, the accurate Hall angles are evaluated by micromagnetic simulations, which corroborate the experimental observations.

D.3 Sample Optimization and Extraction of the Material Parameters

The sample properties, including the effective damping parameter and the interlayer exchange coupling field $\mu_0 H_{\text{ex}}$ for the SyAFM systems, were determined using ferromagnetic resonance (FMR) spectroscopy [296, 297]. The sample stack #s1 (main text) was placed upside down on a co-planar waveguide, and broadband spin dynamics characterization was performed following the method in Refs. [296, 297]. By sweeping the external magnetic field, which was modulated with a small AC component of a few Oersteds, resonance spectra were obtained for different microwave frequencies. The measurements were done by Dr. Aakanksha Sud from the Laboratory for Nanoelectronics and Spintronics, Research Institute of Electrical Communication, Tohoku University. Fig. D.2(a) presents the color plot of the resonance spectra together with the resonance frequencies extracted by fitting a sum of symmetric and antisymmetric Lorentzians [298]. This protocol was performed with the magnetic field applied perpendicular to the microwave RF field. The measurements were repeated with the field applied parallel to the RF field, as shown by the blue data points in Fig. D.2(b). The resonance frequencies were fitted using Eqs. (1) and (2) of Ref. [296], yielding the quadratic interlayer exchange field $\mu_0 H_{\text{ex}} = 0.15 \pm 0.01$ T and the biquadratic interlayer exchange field $\mu_0 H_{\text{bi-ex}} = 0.018 \pm 0.002$ T. The linewidth, extracted by fitting the resonance spectra with the theoretical model of Ref. [296], is shown in Fig. D.2(c). The solid lines correspond to the fits, from which an effective damping parameter $\alpha = 0.10 \pm 0.01$ is obtained. This comparatively large phenomenological damping is attributed to the presence of multiple ultrathin Ta layers inserted between the CoB layers, which reduce pinning effects. These measurements are performed by Dr. Aakanksha Sud at Tohoku University.

In addition, spin-orbit torque parameters were quantified through spin torque-ferromagnetic resonance (ST-FMR) measurements [297]. A representative resonance curve for the acoustic mode is shown in Fig. D.3(a), where the data were fitted to extract the symmetric and antisymmetric voltage components, denoted as V_{sym} and V_{asym} , respectively. From the angular dependence of

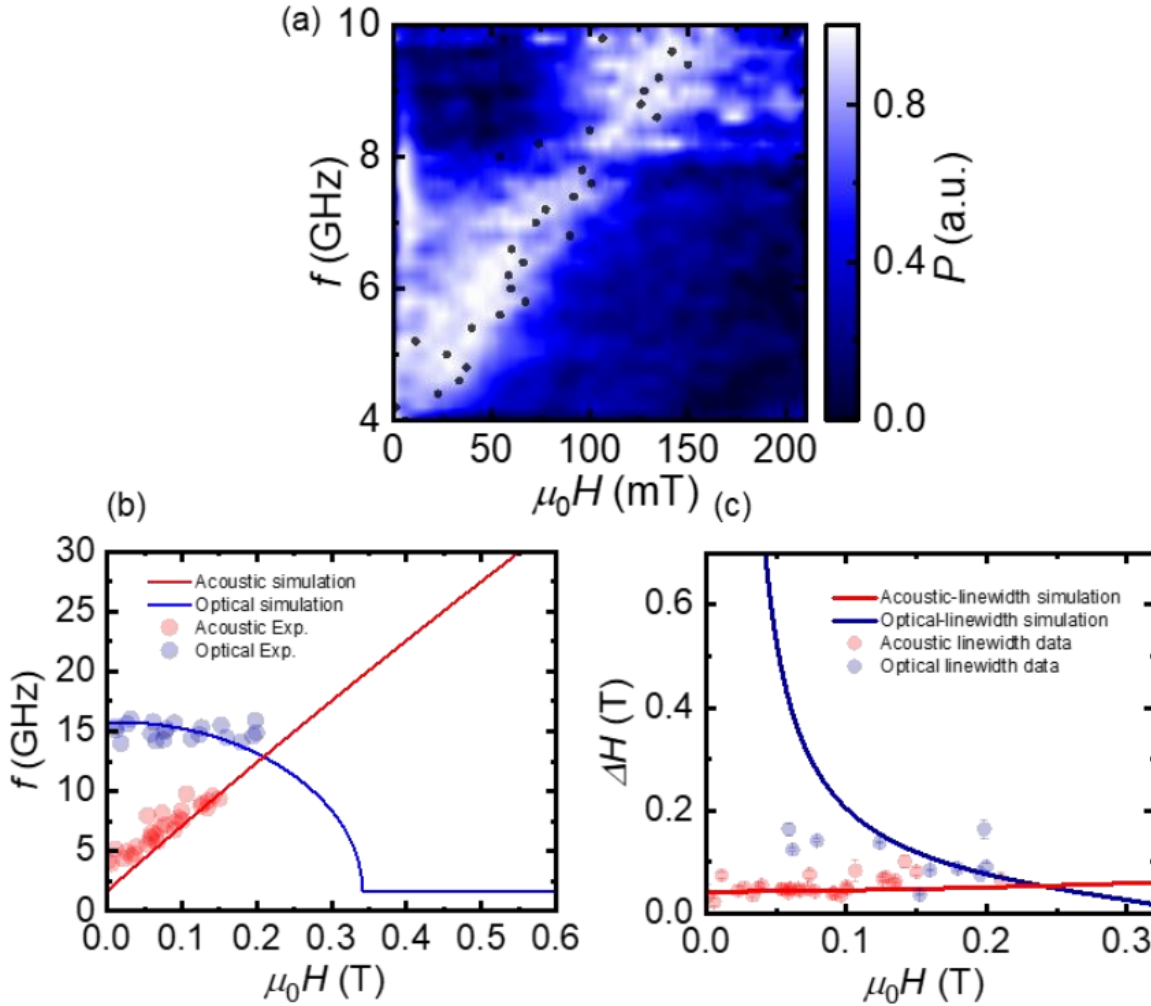


Figure D.2: **Ferromagnetic resonance characterizing the magnetic properties.** (a) Resonance spectra for the field applied parallel to the injected microwave current. (b) Resonance frequency as a function of the field for two modes, obtained by fitting the spectra. The solid lines are the fittings. (c) Resonance linewidth extracted from the spectra in panel (a). Adapted from [4].

V_{sym} and V_{asym} , the spin-orbit torque parameters were determined. Only the acoustic mode was experimentally detected; nevertheless, parameters obtained from the optical mode are expected to be similar, as shown previously [297].

For the ST-FMR measurements, a bar with dimensions of $5 \mu\text{m}$ width and $40 \mu\text{m}$ length was fabricated by standard lithography, and a Cr/Au waveguide was deposited on top. Microwave current at a fixed frequency of 5 GHz was injected while sweeping the magnetic field in different in-plane directions. The definition of the azimuthal angle θ is shown in Supplementary Fig. D.3(b). The

ST-FMR spectra were recorded for each angle and fitted using Eq. (3) in Ref. [297]. The extracted V_{sym} and V_{asym} components are shown in Supplementary Figs. D.3(c) and (d), both exhibiting the expected $\sin^2 \theta \sin \theta$ dependence, consistent with Eqs. (S1) and (S2). The torque parameters were quantified by fitting these dependencies, and the results are summarized in Supplementary Table D.1. These measurements are performed by *Dr. Aakanksha Sud* at Tohoku University.

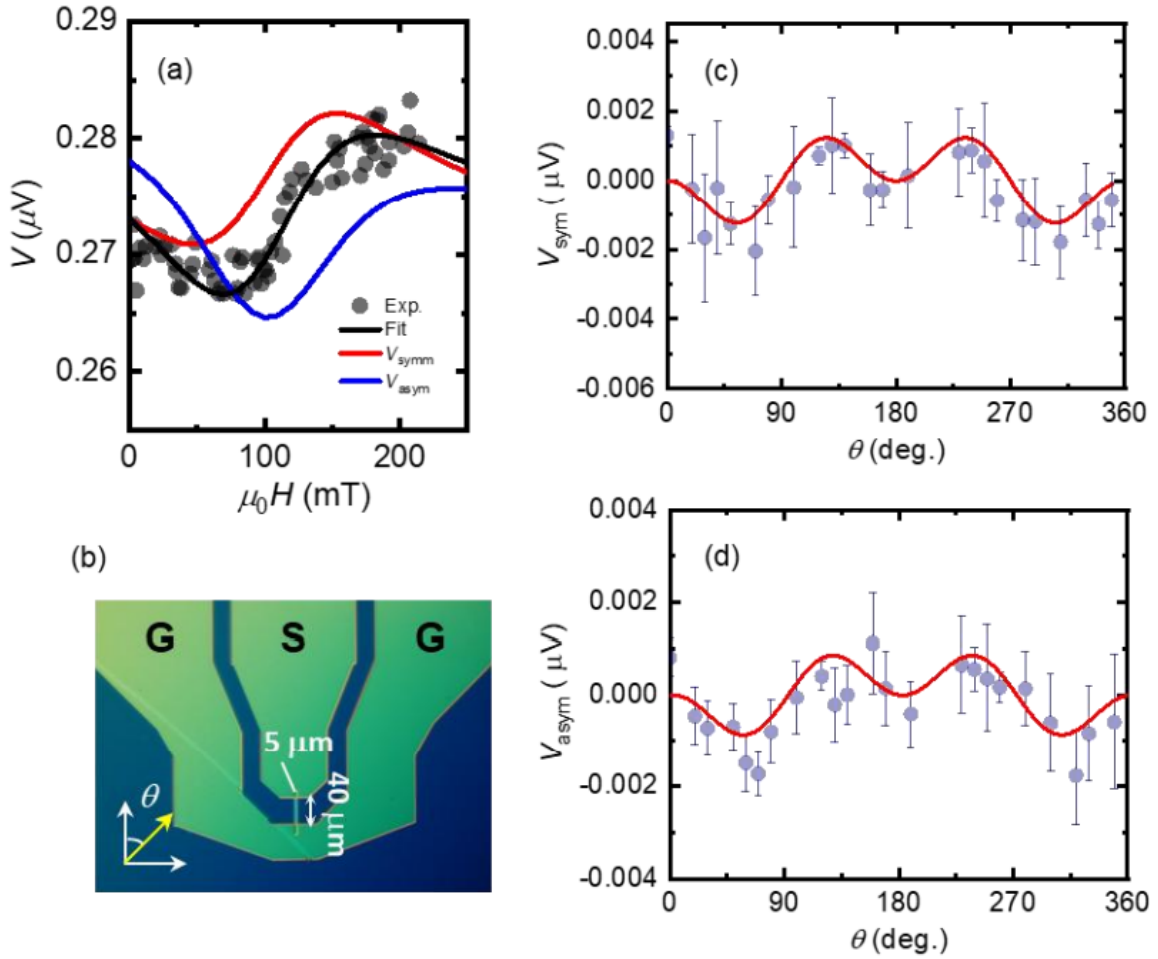


Figure D.3: **Spin torque–ferromagnetic resonance (ST-FMR) characterization.** (a) Microwave absorption spectra for the acoustic mode at 5 GHz resonance frequency and $\theta = 40^\circ$. (b) Microscope image of the device used. (c) V_{sym} and (d) V_{asym} components as a function of θ . Solid lines are fits using Eqs. (S1) and (S2). Adapted from [4].

Table D.1: **ST-FMR-related parameters obtained experimentally and used in the micromagnetic simulations of SyAFM skyrmion tube dynamics. Adapted from [4].**

Parameter	Value
Spin Hall field, B_{SHE}	$-43 \pm 1.5 \mu\text{T}$
Oersted field, B_{Oe}	$6.3 \pm 0.2 \mu\text{T}$
Linewidth, ΔB_{ac}	$0.15 \pm 0.03 \text{ T}$
Current amplitude, I_0	$10 \pm 0.5 \text{ mA}$
Width of microbar, w	$5 \mu\text{m}$
Saturation magnetization, M_s	0.9 T
AMR change, ΔR_{AMR}	$7 \pm 1 \text{ m}\Omega$
Asymmetry factor, η_{asym}	$(5 \pm 0.2) \times 10^{-3}$
Exchange field, B_{ex}	$0.20 \pm 0.04 \text{ T}$
Shunt ratio, η_{HM}	0.65 ± 0.1
Spin Hall angle, θ_{SH}	-0.10 ± 0.05

Additional Information for Chapter 07

E.1 MuMax³ Code for Skymeron Stabilization

MuMax³ Code for Fully Balanced anisotropy case (Hysteresis loop)

```
// Grid and geometry definition
Ngrid := 4 // lateral grid size
N := 16 // number of layers
setgridsize(Ngrid, Ngrid, N)

c := 2.3e-9 // vertical cell size
cxy := 4e-9 // lateral cell size
setcellsize(cxy, cxy, c)

// Define region for each layer
for i := 0; i < N; i++ {
    defRegion(i, layer(i))
}

// Magnetic parameters
l := 0.9 / 2.3
Msat = 1 * 850e3 // A/m
Aex = 1 * 10e-12 // J/m
Dind = 1 * 0.6e-3 // J/m^2
```

```

RKKY := -0.12e-3    // Interlayer exchange coupling (J/m^2)
scale := (RKKY * c) / (2 * Aex.Average())
for j := 0; j < N - 1; j++ {
    ext_scaleExchange(j, j + 1, scale)
}

// Anisotropy values (alternating layers)
Ke1 := 81000
Ke2 := 81000

Ku1.setRegion(0, Ke1)
Ku1.setRegion(1, Ke2)
Ku1.setRegion(2, Ke1)
Ku1.setRegion(3, Ke2)

AnisU = vector(0, 0, 1)
setPBC(16, 16, 0)
m = randomMag()

// External field sweep setup
Bmax := 1100.0e-3
Bstep := 10.0e-3
MinimizerStop = 1e-6

TableAdd(B_ext)
TableAdd(E_total)
TableAdd(E_anis)
TableAdd(E_demag)
TableAdd(E_exch)
TableAdd(E_Zeeman)
for k := 0; k < N; k++ {
    TableAdd(m.Region(k))
}

```

```
EnableDemag = true
B_ext = vector(0, 0.02 * Bmax, Bmax)
relax()
save(m)
counter := 0

// Field sweep: decreasing
for B := Bmax; B >= -Bmax; B -= Bstep {
  B_ext = vector(0, 0.02 * B, B)
  minimize()
  tablesave()
  save(m)
}

// Field sweep: increasing
for B := -Bmax; B <= Bmax; B += Bstep {
  B_ext = vector(0, 0.02 * B, B)
  minimize()
  tablesave()
  save(m)
}
```

MuMax³ Code for Imbalanced Anisotropy Case (single skymeron stabilization)

```
Ngrid := 128 // lateral grid size
N := 4      // number of layers
setgridsize(Ngrid, Ngrid, N)

c := 2.3e-9 // vertical cell size
cxy := 4e-9 // lateral cell size
setcellsize(cxy, cxy, c)

// Define a region for every layer for interlayer exchange coupling
for i := 0; i < N; i++ {
```

```
    defRegion(i, layer(i))
}

// Magnetic parameters
l := 0.9 / 2.3
M1 := 850e3
M2 := 850e3

Msat.setRegion(0, l * M1)
Msat.setRegion(1, l * M2)
Msat.setRegion(2, l * M1)
Msat.setRegion(3, l * M2)

Aex = 1 * 10e-12 // J/m
Dind = 1 * 0.6e-3 // J/m^2

RKKY := -0.12e-3 // J/m^2
scale := (RKKY * c) / (2 * Aex.Average())
for j := 0; j < N - 1; j++ {
    ext_scaleExchange(j, j + 1, scale)
}

// Anisotropy setup
Ke1 := 61000
Ke2 := 101000

Ku1.setRegion(0, Ke1) // J/m^3
Ku1.setRegion(1, Ke2)
Ku1.setRegion(2, Ke1)
Ku1.setRegion(3, Ke2)

alpha = 0.1
AnisU = vector(0, 0, 1)
```

```
EnableDemag = true
B_ext = vector(0, 0, 300e-3)
setPBC(3, 3, 0)

// Load pre-relaxed state at 175 mT and evolve at 300 mT
m.loadfile("/data/mona/MASA684_sample/Masa684/Function_of_Bz/128cell_2chimera/1_chimera_175mt.ovf")
minimize()
relax()
save(m)
SaveAs(m, sprintf("1_chimera_300mt.ovf"))

// Uncomment below for SOT dynamics setup
// alpha = 0.1
// SOTxi := -0.1455
// AlphaH := 0.1
// Pol = alphaH
// Lambda = 1
// Epsilonprime = alphaH / 2 * SOTxi
// Fixedlayer = vector(0, -1, 0)
// J = vector(0, 0, 0.8e11)
// autosave(m, 1e-10)
// tableAutosave(1e-10)
// tableAdd(ext_bubblepos)
// tableAdd(E_total)
// tableAdd(Edens_total)
// tableAdd(Edens_exch)
// tableAdd(Edens_demag)
// tableAdd(Edens_anis)
// tableAdd(Edens_Zeeman)
// tableAdd(E_exch)
// tableAdd(E_demag)
// tableAdd(E_anis)
// tableAdd(E_total)
```

```
// tablesave()  
// run(10e-9)
```

Use of AI Tools

The following table documents the use of AI-based tools during the preparation of this thesis. All scientific content, data analysis, and interpretations were independently developed by the author. AI tools were employed solely for linguistic refinement, formatting, and code assistance.

AI Tool	Used for	Purpose	When / Where
ChatGPT	Language refinement, LaTeX formatting suggestions, and MATLAB debugging assistance	To improve the clarity and scientific readability of text sections, and resolve syntax-related issues in MATLAB scripts	Throughout the thesis
DeepL Translator	Translation of English text into German for the abstract	To ensure linguistic precision and maintain stylistic consistency between English and German versions	German translation of the abstract
Grammarly	Grammar, punctuation, and stylistic correction	To enhance grammatical accuracy and maintain a consistent academic tone	During the final proofreading phase
Gemini	Generation of illustrative schematics and conceptual visualizations	To create schematic representations that aid in the visual explanation of physical concepts and sample architectures	Figures in Chapter 2 and Chapter 3

Table F.1: **Overview of AI-based tools used during the preparation of this thesis. All AI-generated outputs were critically reviewed, corrected, and integrated only after scientific verification by the author.**

Bibliography

- [1] Bhukta, M. *et al.* Homochiral antiferromagnetic merons, antimerons and bimerons realized in synthetic antiferromagnets. *Nature Communications* **15**, 1641 (2024).
- [2] Bhukta, M. *et al.* Temperature-driven transition from meron-type spin textures to stripe domains and revealing the nanosecond dynamics of antiferromagnetic quasiparticles through sublattice-resolved x-ray microscopy. In *Spintronics XVIII*, vol. 13586, 117–121 (SPIE, 2025).
- [3] Bhukta, M. *et al.* Antiferromagnetic skyrmion scattering revealed by direct time-resolved imaging of collective dynamics. *arXiv preprint arXiv:2508.17967* (2025).
- [4] Dohi, T. *et al.* Observation of a non-reciprocal skyrmion hall effect of hybrid chiral skyrmion tubes in synthetic antiferromagnetic multilayers. *Nature Communications* **16**, 8285 (2025).
- [5] Moore, G. E. Cramming more components onto integrated circuits. *Electronics Magazine* 114–117 (1965).
- [6] Waldrop, M. M. The chips are down for moore’s law. *Nature News* **530**, 144 (2016).
- [7] Wolf, S. A. *et al.* Spintronics: A spin-based electronics vision for the future. *Science* **294**, 1488–1495 (2001).
- [8] Parkin, S. S., Hayashi, M. & Thomas, L. Magnetic domain-wall racetrack memory. *Science* **320**, 190–194 (2008).
- [9] Grünberg, P., Schreiber, R., Pang, Y., Brodsky, M. á. & Sowers, H. Layered magnetic structures: Evidence for antiferromagnetic coupling of fe layers across cr interlayers. *Physical Review Letters* **57**, 2442 (1986).
- [10] Baibich, M. N. *et al.* Giant magnetoresistance of (001) Fe/ (001) Cr magnetic superlattices. *Physical Review Letters* **61**, 2472 (1988).

-
- [11] Dieny, B. *et al.* Giant magnetoresistive in soft ferromagnetic multilayers. *Physical Review B (R)* **43**, 1297 (1991).
- [12] Parkin, S. *et al.* Magnetically engineered spintronic sensors and memory. *Proceedings of the IEEE* **91**, 661–680 (2003).
- [13] Julliere, M. Tunneling between ferromagnetic films. *Physics Letters A* **54**, 225–226 (1975).
- [14] Moodera, J. S., Kinder, L. R., Wong, T. M. & Meservey, R. Large magnetoresistance at room temperature in ferromagnetic thin film tunnel junctions. *Physical Review Letters* **74**, 3273 (1995).
- [15] Miyazaki, T. & Tezuka, N. Giant magnetic tunneling effect in Fe/Al₂O₃/Fe junction. *Journal of Magnetism and Magnetic Materials* **139**, L231–L234 (1995).
- [16] Huai, Y. *et al.* Spin-transfer torque mram (stt-mram): Challenges and prospects. *AAPPS bulletin* **18**, 33–40 (2008).
- [17] McCray, W. P. How spintronics went from the lab to the ipod. *Nature Nanotechnology* **4**, 2–4 (2009).
- [18] Memory with a spin. *Nature Nanotechnology* **10**, 185 (2015).
- [19] Koh, I. & Josephson, L. Magnetic nanoparticle sensors. *Sensors* **9**, 8130–8145 (2009).
- [20] Tran, N. & Webster, T. J. Magnetic nanoparticles: biomedical applications and challenges. *Journal of Materials Chemistry* **20**, 8760–8767 (2010).
- [21] Chen, R., Romero, G., Christiansen, M. G., Mohr, A. & Anikeeva, P. Wireless magnetothermal deep brain stimulation. *Science* **347**, 1477–1480 (2015).
- [22] Parkin, S. & Yang, S.-H. Memory on the racetrack. *Nature Nanotechnology* **10**, 195–198 (2015).
- [23] Miron, I. M. *et al.* Perpendicular switching of a single ferromagnetic layer induced by in-plane current injection. *Nature* **476**, 189–193 (2011).
- [24] Liu, L. *et al.* Spin-torque switching with the giant spin hall effect of tantalum. *Science* **336**, 555–558 (2012).
- [25] Muhlbauer, S. *et al.* Skyrmion lattice in a chiral magnet. *Science* **323**, 915–919 (2009).
- [26] Yu, X. *et al.* Real-space observation of a two-dimensional skyrmion crystal. *Nature* **465**, 901–904 (2010).
- [27] Everschor-Sitte, K., Masell, J., Reeve, R. M. & Kläui, M. Perspective: Magnetic skyrmions—overview of recent progress in an active research field. *Journal of Applied Physics* **124**, 240901 (2018).

-
- [28] Dohi, T., Reeve, R. M. & Kläui, M. Thin film skyrmionics. *Annual Review of Condensed Matter Physics* **13**, 73–95 (2022).
- [29] Nagaosa, N. & Tokura, Y. Topological properties and dynamics of magnetic skyrmions. *Nature Nanotechnology* **8**, 899–911 (2013).
- [30] Büttner, F., Lemesh, I. & Beach, G. S. Theory of isolated magnetic skyrmions: From fundamentals to room temperature applications. *Scientific Reports* **8** (2018).
- [31] Woo, S. *et al.* Observation of room-temperature magnetic skyrmions and their current-driven dynamics in ultrathin metallic ferromagnets. *Nature Materials* **15**, 501–506 (2016).
- [32] Jiang, W. *et al.* Direct observation of the skyrmion hall effect. *Nature Physics* **13**, 162–169 (2017).
- [33] Litzius, K. *et al.* Skyrmion hall effect revealed by direct time-resolved x-ray microscopy. *Nature Physics* **13**, 170–175 (2017).
- [34] Fert, A., Cros, V. & Sampaio, J. Skyrmions on the track. *Nature Nanotechnology* **8**, 152 (2013).
- [35] Luo, S. *et al.* Reconfigurable skyrmion logic gates. *Nano Letters* **18**, 1180–1184 (2018).
- [36] Tomasello, R. *et al.* A strategy for the design of skyrmion racetrack memories. *Scientific Reports* **4**, 1–7 (2014).
- [37] Zhang, X., Ezawa, M. & Zhou, Y. Magnetic skyrmion logic gates: conversion, duplication and merging of skyrmions. *Scientific Reports* **5**, 1–8 (2015).
- [38] Zázvorka, J. *et al.* Thermal skyrmion diffusion used in a reshuffler device. *Nature Nanotechnology* **14**, 658–661 (2019).
- [39] Song, K. M. *et al.* Skyrmion-based artificial synapses for neuromorphic computing. *Nature Electronics* **3**, 148–155 (2020).
- [40] da Câmara Santa Clara Gomes, T. *et al.* Neuromorphic weighted sums with magnetic skyrmions. *Nature Electronics* **8**, 204–214 (2025).
- [41] Raab, K. *et al.* Brownian reservoir computing realized using geometrically confined skyrmion dynamics. *Nature Communications* **13**, 1–6 (2022).
- [42] Beneke, G. *et al.* Gesture recognition with brownian reservoir computing using geometrically confined skyrmion dynamics. *Nature Communications* **15**, 8103 (2024).

-
- [43] Göbel, B., Mertig, I. & Tretiakov, O. A. Beyond skyrmions: Review and perspectives of alternative magnetic quasiparticles. *Physics Reports* **895**, 1–28 (2021).
- [44] Yu, X. *et al.* Biskyrmion states and their current-driven motion in a layered manganite. *Nature Communications* **5**, 1–7 (2014).
- [45] Wang, W. *et al.* A centrosymmetric hexagonal magnet with superstable biskyrmion magnetic nanodomains in a wide temperature range of 100–340 K. *Advanced Materials* **28**, 6887–6893 (2016).
- [46] Peng, L. *et al.* Real-space observation of nonvolatile zero-field biskyrmion lattice generation in manganite magnet. *Nano Letters* **17**, 7075–7079 (2017).
- [47] Zhang, X. *et al.* Control and manipulation of a magnetic skyrmionium in nanostructures. *Physical Review B* **94**, 094420 (2016).
- [48] Seng, B. *et al.* Direct imaging of chiral domain walls and Néel-type skyrmionium in ferrimagnetic alloys. *Advanced Functional Materials* **31**, 2102307 (2021).
- [49] Foster, D. *et al.* Two-dimensional skyrmion bags in liquid crystals and ferromagnets. *Nature Physics* **15**, 655–659 (2019).
- [50] Jani, H. *et al.* Antiferromagnetic half-skyrmions and bimerons at room temperature. *Nature* **590**, 74–79 (2021).
- [51] Moon, K.-W., Yoon, J., Kim, C. & Hwang, C. Existence of in-plane magnetic skyrmion and its motion under current flow. *Physical Review Applied* **12**, 064054 (2019).
- [52] Zarzuela, R., Bharadwaj, V. K., Kim, K.-W., Sinova, J. & Everschor-Sitte, K. Stability and dynamics of in-plane skyrmions in collinear ferromagnets. *Physical Review B* **101**, 054405 (2020).
- [53] Amin, O. *et al.* Antiferromagnetic half-skyrmions electrically generated and controlled at room temperature. *Nature Nanotechnology* 1–5 (2023).
- [54] Fernández-Pacheco, A. *et al.* Three-dimensional nanomagnetism. *Nature Communications* **8**, 15756 (2017).
- [55] Gubbiotti, G. *et al.* 2025 roadmap on 3d nano-magnetism. *Journal of Physics: Condensed Matter* (2025).
- [56] Birch, M. *et al.* Real-space imaging of confined magnetic skyrmion tubes. *Nature Communications* **11**, 1726 (2020).

- [57] Wolf, D. *et al.* Unveiling the three-dimensional magnetic texture of skyrmion tubes. *Nature Nanotechnology* **17**, 250–255 (2022).
- [58] Birch, M. *et al.* Toggle-like current-induced bloch point dynamics of 3d skyrmion strings in a room temperature nanowire. *Nature Communications* **13**, 3630 (2022).
- [59] Kent, N. *et al.* Creation and observation of hopfions in magnetic multilayer systems. *Nature Communications* **12**, 1562 (2021).
- [60] Zheng, F. *et al.* Hopfion rings in a cubic chiral magnet. *Nature* **623**, 718–723 (2023).
- [61] Azhar, M., Shaju, S. C., Knapman, R., Pignedoli, A. & Everschor-Sitte, K. 3d magnetic textures with mixed topology: Unlocking the tunable hopf index. *arXiv preprint arXiv:2411.06929* (2024).
- [62] Ran, K. *et al.* Creation of a chiral bobber lattice in helimagnet-multilayer heterostructures. *Physical Review Letters* **126**, 017204 (2021).
- [63] Zheng, F. *et al.* Experimental observation of chiral magnetic bobbers in b20-type fege. *Nature Nanotechnology* **13**, 451–455 (2018).
- [64] Zhang, Z. *et al.* Magnon scattering modulated by omnidirectional hopfion motion in antiferromagnets for meta-learning. *Science Advances* **9**, eade7439 (2023).
- [65] Dzyaloshinsky, I. A thermodynamic theory of “weak” ferromagnetism of antiferromagnetics. *Journal of Physics and Chemistry of Solids* **4**, 241–255 (1958).
- [66] Moriya, T. Anisotropic superexchange interaction and weak ferromagnetism. *Physical Review* **120**, 91 (1960).
- [67] Thiaville, A., Rohart, S., Jué, É., Cros, V. & Fert, A. Dynamics of dzyaloshinskii domain walls in ultrathin magnetic films. *Europhysics Letters* **100**, 57002 (2012).
- [68] Lemesh, I. & Beach, G. S. Walker breakdown with a twist: Dynamics of multilayer domain walls and skyrmions driven by spin-orbit torque. *Physical Review Applied* **12**, 044031 (2019).
- [69] Chen, G. Skyrmion hall effect. *Nature Physics* **13**, 112–113 (2017).
- [70] Barker, J. & Tretiakov, O. A. Static and dynamical properties of antiferromagnetic skyrmions in the presence of applied current and temperature. *Physical Review Letters* **116**, 147203 (2016).
- [71] Jungwirth, T., Marti, X., Wadley, P. & Wunderlich, J. Antiferromagnetic spintronics. *Nature Nanotechnology* **11**, 231–241 (2016).

-
- [72] Zhang, X., Zhou, Y. & Ezawa, M. Antiferromagnetic skyrmion: stability, creation and manipulation. *Sci. Rep.* **6**, 24795 (2016).
- [73] Baltz, V. *et al.* Antiferromagnetic spintronics. *Reviews of Modern Physics* **90**, 015005 (2018).
- [74] Ross, A. *et al.* Structural sensitivity of the spin hall magnetoresistance in antiferromagnetic thin films. *Physical Review B* **102**, 094415 (2020).
- [75] Chmiel, F. P. *et al.* Observation of magnetic vortex pairs at room temperature in a planar α - $\text{Fe}_2\text{O}_3/\text{Co}$ heterostructure. *Nature Materials* **17**, 581–585 (2018).
- [76] Schmitt, C. *et al.* Identification of neél vector orientation in antiferromagnetic domains switched by currents in NiO/Pt thin films. *Physical Review Applied* **15**, 034047 (2021).
- [77] Caretta, L. *et al.* Fast current-driven domain walls and small skyrmions in a compensated ferrimagnet. *Nature Nanotechnology* **13**, 1154–1160 (2018).
- [78] Woo, S. *et al.* Current-driven dynamics and inhibition of the skyrmion hall effect of ferrimagnetic skyrmions in GdFeCo films. *Nature Communications* **9**, 959 (2018).
- [79] Hirata, Y. *et al.* Vanishing skyrmion hall effect at the angular momentum compensation temperature of a ferrimagnet. *Nature Nanotechnology* **14**, 232–236 (2019).
- [80] Hirata, Y. *et al.* Correlation between compensation temperatures of magnetization and angular momentum in GdFeCo ferrimagnets. *Physical Review B* **97**, 220403 (2018).
- [81] Parkin, S., More, N. & Roche, K. Oscillations in exchange coupling and magnetoresistance in metallic superlattice structures: Co/Ru , Co/Cr , and Fe/Cr . *Physical Review Letters* **64**, 2304 (1990).
- [82] Duine, R., Lee, K.-J., Parkin, S. S. & Stiles, M. D. Synthetic antiferromagnetic spintronics. *Nature Physics* **14**, 217–219 (2018).
- [83] Houssameddine, D. *et al.* Spin torque driven excitations in a synthetic antiferromagnet. *Applied Physics Letters* **96** (2010).
- [84] Bi, C. *et al.* Anomalous spin-orbit torque switching in synthetic antiferromagnets. *Physical Review B* **95**, 104434 (2017).
- [85] Lau, Y.-C., Betto, D., Rode, K., Coey, J. & Stamenov, P. Spin-orbit torque switching without an external field using interlayer exchange coupling. *Nature Nanotechnology* **11**, 758–762 (2016).

-
- [86] Schäfer, R. Magnetic domains. In Coey, J. M. D. & Parkin, S. S. P. (eds.) *Handbook of Magnetism and Magnetic Materials*, 391–434 (Springer, Cham, 2021). URL https://doi.org/10.1007/978-3-030-63210-6_8.
- [87] Coey, J. M. D. *Magnetism and Magnetic Materials* (Cambridge University Press, Cambridge, UK, 2010).
- [88] Hubert, A. & Schäfer, R. *Magnetic Domains: The Analysis of Magnetic Microstructures* (Springer Science & Business Media, Berlin, Germany, 2008).
- [89] Blundell, S. *Magnetism in Condensed Matter* (Oxford University Press, Oxford, UK, 2001).
- [90] Griffiths, D. J. & Schroeter, D. F. *Introduction to quantum mechanics* (Cambridge university press, 2019).
- [91] Massimi, M. *Pauli's exclusion principle: The origin and validation of a scientific principle* (Cambridge University Press, 2005).
- [92] Sethu, K. K. V. *Spin orbit torques in magnetic materials*. Master's thesis, Katholieke Universiteit Leuven, Belgium (2017).
- [93] Stoner, E. C. Collective electron ferromagnetism. *Proceedings of the Royal Society of London. Series A. Mathematical and Physical Sciences* **165**, 372–414 (1938).
- [94] Böttcher, T. *et al.* Quantifying symmetric exchange in ultrathin ferromagnetic films with chirality. *Physical Review B* **107**, 094405 (2023).
- [95] Vaz, C., Bland, J. & Lauhoff, G. Magnetism in ultrathin film structures. *Reports on Progress in Physics* **71**, 056501 (2008).
- [96] Exl, L., Suess, D. & Schrefl, T. Micromagnetism. In *Handbook of Magnetism and Magnetic Materials*, 347–390 (Springer, Cham, Switzerland, 2021).
- [97] Johnson, M., Bloemen, P., Den Broeder, F. & De Vries, J. Magnetic anisotropy in metallic multilayers. *Reports on Progress in Physics* **59**, 1409 (1996).
- [98] Dieny, B. & Chshiev, M. Perpendicular magnetic anisotropy at transition metal/oxide interfaces and applications. *Reviews of Modern Physics* **89**, 025008 (2017).
- [99] Krishnia, S. *et al.* Interfacial spin-orbitronic effects controlled by different oxidation levels at the co/al interface. *Physical Review Applied* **24**, 024055 (2025).
- [100] Zeper, W., Greidanus, F., Carcia, P. & Fincher, C. Perpendicular magnetic anisotropy and magneto-optical kerr effect of vapor-deposited co/pt-layered structures. *Journal of Applied Physics* **65**, 4971–4975 (1989).

- [101] Nakajima, N. *et al.* Perpendicular magnetic anisotropy caused by interfacial hybridization via enhanced orbital moment in co/pt multilayers: Magnetic circular x-ray dichroism study. *Physical Review Letters* **81**, 5229 (1998).
- [102] Bogdanov, A. N. & Yablonskii, D. Thermodynamically stable “vortices” in magnetically ordered crystals. the mixed state of magnets. *Zh. Eksp. Teor. Fiz* **95**, 178 (1989).
- [103] Fert, A. & Levy, P. M. Role of anisotropic exchange interactions in determining the properties of spin-glasses. *Physical Review Letters* **44**, 1538 (1980).
- [104] Ryu, K.-S., Yang, S.-H., Thomas, L. & Parkin, S. S. Chiral spin torque arising from proximity-induced magnetization. *Nature Communications* **5**, 3910 (2014).
- [105] Yang, H., Thiaville, A., Rohart, S., Fert, A. & Chshiev, M. Anatomy of dzyaloshinskii-moriya interaction at co/pt interfaces. *Physical Review Letters* **115**, 267210 (2015).
- [106] Belabbes, A., Bihlmayer, G., Bechstedt, F., Blügel, S. & Manchon, A. Hund’s rule-driven dzyaloshinskii-moriya interaction at 3 d-5 d interfaces. *Physical Review Letters* **117**, 247202 (2016).
- [107] Kim, S. *et al.* Correlation of the dzyaloshinskii–moriya interaction with heisenberg exchange and orbital asphericity. *Nature Communications* **9**, 1–9 (2018).
- [108] Jadaun, P., Register, L. F. & Banerjee, S. K. The microscopic origin of dmi in magnetic bilayers and prediction of giant dmi in new bilayers. *npj Computational Materials* **6**, 88 (2020).
- [109] Finocchio, G., Büttner, F., Tomasello, R., Carpentieri, M. & Kläui, M. Magnetic skyrmions: from fundamental to applications. *Journal of Physics D: Applied Physics* **49**, 423001 (2016).
- [110] Hartmann, D. M., Duine, R. A., Meijer, M. J., Swagten, H. J. & Lavrijsen, R. Creep of chiral domain walls. *Physical Review B* **100**, 094417 (2019).
- [111] Lau, D., Pellegren, J. P., Nembach, H., Shaw, J. & Sokalski, V. Disentangling factors governing dzyaloshinskii domain-wall creep in co/ni thin films using pt x ir 1- x seed layers. *Physical Review B* **98**, 184410 (2018).
- [112] Shepley, P. M., Tunncliffe, H., Shahbazi, K., Burnell, G. & Moore, T. A. Magnetic properties, domain-wall creep motion, and the dzyaloshinskii-moriya interaction in pt/co/ir thin films. *Physical Review B* **97**, 134417 (2018).
- [113] Kim, D.-H., Yoo, S.-C., Kim, D.-Y., Min, B.-C. & Choe, S.-B. Wide-range probing of dzyaloshinskii–moriya interaction. *Scientific Reports* **7**, 45498 (2017).

-
- [114] Quinsat, M. *et al.* Dzyaloshinskii-moriya interaction in pt/co/pt films prepared by chemical vapor deposition with various substrate temperatures. *AIP Advances* **7** (2017).
- [115] Franken, J. H., Herps, M., Swagten, H. J. & Koopmans, B. Tunable chiral spin texture in magnetic domain-walls. *Scientific Reports* **4**, 5248 (2014).
- [116] Brown Jr, W. F. & LaBonte, A. E. Structure and energy of one-dimensional domain walls in ferromagnetic thin films. *Journal of Applied Physics* **36**, 1380–1386 (1965).
- [117] Bruno, P. Theory of interlayer magnetic coupling. *Physical Review B* **52**, 411 (1995).
- [118] Salamon, M. *et al.* Long-range incommensurate magnetic order in a dy-y multilayer. *Physical Review Letters* **56**, 259 (1986).
- [119] Slonczewski, J. C. Conductance and exchange coupling of two ferromagnets separated by a tunneling barrier. *Physical Review B* **39**, 6995 (1989).
- [120] Binasch, G., Grünberg, P., Saurenbach, F. & Zinn, W. Enhanced magnetoresistance in layered magnetic structures with antiferromagnetic interlayer exchange. *Physical Review B* **39**, 4828 (1989).
- [121] Rohart, S. & Thiaville, A. Skyrmion confinement in ultrathin film nanostructures in the presence of dzyaloshinskii-moriya interaction. *Physical Review B—Condensed Matter and Materials Physics* **88**, 184422 (2013).
- [122] Emori, S., Bauer, U., Ahn, S.-M., Martinez, E. & Beach, G. S. Current-driven dynamics of chiral ferromagnetic domain walls. *Nature Materials* **12**, 611–616 (2013).
- [123] Heide, M., Bihlmayer, G. & Blügel, S. Dzyaloshinskii-moriya interaction accounting for the orientation of magnetic domains in ultrathin films: Fe/w (110). *Physical Review B—Condensed Matter and Materials Physics* **78**, 140403 (2008).
- [124] Giess, E. A. Magnetic bubble materials. *Science* **208**, 938–943 (1980).
- [125] Skyrme, T. A unified field theory of mesons and baryons. *Nuclear Physics* **31**, 556–569 (1962).
- [126] Binz, B., Vishwanath, A. & Aji, V. Theory of the helical spin crystal: A candidate for the partially ordered state of mnsi. *Physical Review Letters* **96** (2006).
- [127] Yu, X. Z. *et al.* Real-space observation of a two-dimensional skyrmion crystal. *Nature* **465**, 901–904 (2010).

-
- [128] Yu, X. Z. *et al.* Near room-temperature formation of a skyrmion crystal in thin-films of the helimagnet *FeGe*. *Nature Materials* **10**, 106–109 (2010).
- [129] Yu, X. *et al.* Skyrmion flow near room temperature in an ultralow current density. *Nature Communications* **3**, 1–6 (2012).
- [130] Du, H. *et al.* Edge-mediated skyrmion chain and its collective dynamics in a confined geometry. *Nature Communications* **6** (2015).
- [131] Jiang, W. *et al.* Blowing magnetic skyrmion bubbles. *Science* **349**, 283–286 (2015).
- [132] Boulle, O. *et al.* Room-temperature chiral magnetic skyrmions in ultrathin magnetic nanostructures. *Nature Nanotechnology* **11**, 449–454 (2016).
- [133] Moreau-Luchaire, C. *et al.* Additive interfacial chiral interaction in multilayers for stabilization of small individual skyrmions at room temperature. *Nature Nanotechnology* **11**, 444–448 (2016).
- [134] Dohi, T., DuttaGupta, S., Fukami, S. & Ohno, H. Formation and current-induced motion of synthetic antiferromagnetic skyrmion bubbles. *Nature Communications* **10**, 1–6 (2019).
- [135] Wang, X., Yuan, H. & Wang, X. A theory on skyrmion size. *Communications Physics* **1**, 31 (2018).
- [136] Belavin, A. & Polyakov, A. Metastable states of two-dimensional isotropic ferromagnets. *JETP Lett* **22**, 245–248 (1975).
- [137] Rohart, S., Miltat, J. & Thiaville, A. Path to collapse for an isolated Néel skyrmion. *Physical Review B* **93**, 214412 (2016).
- [138] Kharkov, Y., Sushkov, O. & Mostovoy, M. Bound states of skyrmions and merons near the Lifshitz point. *Physical Review Letters* **119**, 207201 (2017).
- [139] Yu, X. *et al.* Transformation between meron and skyrmion topological spin textures in a chiral magnet. *Nature* **564**, 95–98 (2018).
- [140] Göbel, B., Mook, A., Henk, J., Mertig, I. & Tretiakov, O. A. Magnetic bimerons as skyrmion analogues in in-plane magnets. *Physical Review B* **99**, 060407 (2019).
- [141] Janson, O. *et al.* The quantum nature of skyrmions and half-skyrmions in Cu_2OSeO_3 . *Nature Communications* **5**, 5376 (2014).
- [142] Bachmann, D., Lianeris, M. & Komineas, S. Meron configurations in easy-plane chiral magnets. *Physical Review B* **108**, 014402 (2023).

-
- [143] Ghosh, S., Blügel, S. & Mokrousov, Y. Ultrafast optical generation of antiferromagnetic meron-antimeron pairs with conservation of topological charge. *Physical Review Research* **5**, L022007 (2023).
- [144] Gao, N. *et al.* Creation and annihilation of topological meron pairs in in-plane magnetized films. *Nature Communications* **10**, 5603 (2019).
- [145] Landau, L. & Lifshitz, E. On the theory of the dispersion of magnetic permeability in ferromagnetic bodies. *Phys. Z. Sowjetunion* **8**, 101–114 (1935).
- [146] Gilbert, T. L. A phenomenological theory of damping in ferromagnetic materials. *IEEE transactions on magnetics* **40**, 3443–3449 (2004).
- [147] Brataas, A., Kent, A. D. & Ohno, H. Current-induced torques in magnetic materials. *Nature Materials* **11**, 372–381 (2012).
- [148] Berger, L. Low-field magnetoresistance and domain drag in ferromagnets. *Journal of Applied Physics* **49**, 2156–2161 (1978).
- [149] Berger, L. Domain drag effect in the presence of variable magnetic field or variable transport current. *Journal of Applied Physics* **50**, 2137–2139 (1979).
- [150] Berger, L. Emission of spin waves by a magnetic multilayer traversed by a current. *Physical Review B* **54**, 9353 (1996).
- [151] Slonczewski, J. C. Current-driven excitation of magnetic multilayers. *Journal of Magnetism and Magnetic Materials* **159**, L1–L7 (1996).
- [152] Xiao, J., Zangwill, A. & Stiles, M. D. Spin-transfer torque for continuously variable magnetization. *Physical Review B* **73**, 054428 (2006).
- [153] Zhang, J., Levy, P. M., Zhang, S. & Antropov, V. Identification of transverse spin currents in noncollinear magnetic structures. *Physical Review Letters* **93**, 256602 (2004).
- [154] Thiaville, A., Nakatani, Y., Miltat, J. & Suzuki, Y. Micromagnetic understanding of current-driven domain wall motion in patterned nanowires. *Europhysics Letters* **69**, 990 (2005).
- [155] Kato, Y. K., Myers, R. C., Gossard, A. C. & Awschalom, D. D. Observation of the spin hall effect in semiconductors. *Science* **306**, 1910–1913 (2004).
- [156] Sinova, J., Valenzuela, S. O., Wunderlich, J., Back, C. H. & Jungwirth, T. Spin hall effects. *Reviews of Modern Physics* **87**, 1213–1260 (2015).

-
- [157] Hirsch, J. Spin hall effect. *Physical Review Letters* **83**, 1834 (1999).
- [158] Niimi, Y. & Otani, Y. Reciprocal spin hall effects in conductors with strong spin–orbit coupling: a review. *Reports on Progress in Physics* **78**, 124501 (2015).
- [159] Kontani, H., Tanaka, T., Hirashima, D., Yamada, K. & Inoue, J. Giant intrinsic spin and orbital hall effects in sr_2mo_4 ($m = ru, rh, mo$). *Physical Review Letters* **100**, 096601 (2008).
- [160] Kurebayashi, H. *et al.* An antidamping spin–orbit torque originating from the berry curvature. *Nature Nanotechnology* **9**, 211–217 (2014).
- [161] Ishizuka, H. & Nagaosa, N. Spin chirality induced skew scattering and anomalous hall effect in chiral magnets. *Science Advances* **4**, eaap9962 (2018).
- [162] Berger, L. Side-jump mechanism for the hall effect of ferromagnets. *Physical Review B* **2**, 4559 (1970).
- [163] Gupta, K., Wesselink, R. J., Liu, R., Yuan, Z. & Kelly, P. J. Disorder dependence of interface spin memory loss. *Physical Review Letters* **124**, 087702 (2020).
- [164] Lim, M. & Lee, H.-W. Spin-memory loss induced by bulk spin–orbit coupling at ferromagnet/heavy-metal interfaces. *Applied Physics Letters* **118** (2021).
- [165] Zhu, L., Ralph, D. C. & Buhrman, R. A. Effective spin-mixing conductance of heavy-metal–ferromagnet interfaces. *Physical Review Letters* **123**, 057203 (2019).
- [166] Panda, S., Mondal, S., Sinha, J., Choudhury, S. & Barman, A. All-optical detection of interfacial spin transparency from spin pumping in β -ta/cofeb thin films. *Science Advances* **5**, eaav7200 (2019).
- [167] Edelstein, V. M. Spin polarization of conduction electrons induced by electric current in two-dimensional asymmetric electron systems. *Solid State Communications* **73**, 233–235 (1990).
- [168] Gambardella, P. & Miron, I. M. Current-induced spin–orbit torques. *Philosophical Transactions of the Royal Society A: Mathematical, Physical and Engineering Sciences* **369**, 3175–3197 (2011).
- [169] Mihai Miron, I. *et al.* Current-driven spin torque induced by the rashba effect in a ferromagnetic metal layer. *Nature Materials* **9**, 230–234 (2010).
- [170] Miron, I. M. *et al.* Fast current-induced domain-wall motion controlled by the rashba effect. *Nature Materials* **10**, 419–423 (2011).
- [171] Wang, C., Xiao, D., Chen, X., Zhou, Y. & Liu, Y. Manipulating and trapping skyrmions by magnetic field gradients. *New Journal of Physics* **19**, 083008 (2017).

-
- [172] Casiraghi, A. *et al.* Individual skyrmion manipulation by local magnetic field gradients. *Communications Physics* **2**, 145 (2019).
- [173] Brataas, A. & Hals, K. M. Spin-orbit torques in action. *Nature Nanotechnology* **9**, 86–88 (2014).
- [174] Thiele, A. Steady-state motion of magnetic domains. *Physical Review Letters* **30**, 230 (1973).
- [175] Honda, S. & Tanaka, M. Micromagnetic investigations of néel-and bloch-type skyrmion dynamics induced by spin hall effect of cap layers. *Japanese Journal of Applied Physics* **56**, 098001 (2017).
- [176] Sampaio, J., Cros, V., Rohart, S., Thiaville, A. & Fert, A. Nucleation, stability and current-induced motion of isolated magnetic skyrmions in nanostructures. *Nature Nanotechnology* **8**, 839–844 (2013).
- [177] Thiele, A. Application of the gyrocoupling vector and dissipation dyadic in the dynamics of magnetic domains. *Journal of Applied Physics* **45**, 377–393 (1974).
- [178] Zhang, X. *et al.* Skyrmion-skyrmion and skyrmion-edge repulsions in skyrmion-based racetrack memory. *Scientific Reports* **5**, 7643 (2015).
- [179] Toscano, D. *et al.* Suppression of the skyrmion hall effect in planar nanomagnets by the magnetic properties engineering: Skyrmion transport on nanotracks with magnetic strips. *Journal of Magnetism and Magnetic Materials* **504**, 166655 (2020).
- [180] Hrabec, A. *et al.* Current-induced skyrmion generation and dynamics in symmetric bilayers. *Nature Communications* **8**, 15765 (2017).
- [181] Litzius, K. *et al.* The role of temperature and drive current in skyrmion dynamics. *Nature Electronics* **3**, 30–36 (2020).
- [182] Göbel, B., Mook, A., Henk, J. & Mertig, I. Antiferromagnetic skyrmion crystals: Generation, topological hall, and topological spin hall effect. *Physical Review B* **96**, 060406 (2017).
- [183] Zhang, X. *et al.* Control and manipulation of a magnetic skyrmionium in nanostructures. *Physical Review B* **94** (2016).
- [184] Panigrahy, S. K., Singh, C. & Nayak, A. K. Current-induced nucleation, manipulation, and reversible switching of antiskyrmioniums. *Applied Physics Letters* **115**, 182403 (2019).
- [185] Rozsa, L., Palots, K. & *et al.* Formation and stability of metastable skyrmionic spin structures with various topologies in an ultrathin film. *Physical Review B* **95**, 094423 (2017).

-
- [186] Hoffmann, M. *et al.* Antiskyrmions stabilized at interfaces by anisotropic dzyaloshinskii-moriya interactions. *Nature Communications* **8**, 308 (2017).
- [187] Hagedorn, F. Domain wall motion in bubble domain materials. In *AIP Conference Proceedings*, vol. 5, 72–90 (American Institute of Physics, 1972).
- [188] Haltz, E., Krishnia, S., Berges, L., Mougín, A. & Sampaio, J. Domain wall dynamics in antiferromagnetically coupled double-lattice systems. *Physical Review B* **103**, 014444 (2021).
- [189] Scholl, A. Applications of photoemission electron microscopy (peem) in magnetism research. *Current Opinion in Solid State and Materials Science* **7**, 59–66 (2003).
- [190] Funk, T., Deb, A., George, S. J., Wang, H. & Cramer, S. P. X-ray magnetic circular dichroism—a high energy probe of magnetic properties. *Coordination Chemistry Reviews* **249**, 3–30 (2005).
- [191] Weigand, M. *Realization of a new magnetic scanning X-ray microscope and investigation of Landau structures under pulsed field excitation* (Cuvillier Verlag, 2015).
- [192] Farotex Limited. Farotex limited. <http://farotex.com/> (2018).
- [193] Buchner, M., Höfler, K., Henne, B., Ney, V. & Ney, A. Tutorial: Basic principles, limits of detection, and pitfalls of highly sensitive squid magnetometry for nanomagnetism and spintronics. *Journal of Applied Physics* **124** (2018).
- [194] Bloch, F. Josephson effect in a superconducting ring. *Physical Review B* **2**, 109 (1970).
- [195] MicroChem Corp. *PMMA Electron Beam Resist Series: Product Datasheet* (2016). Available at https://kayakuam.com/wp-content/uploads/2020/07/PMMA_Data_Sheet.pdf.
- [196] Vieu, C. *et al.* Electron beam lithography: resolution limits and applications. *Applied Surface Science* **164**, 111–117 (2000).
- [197] Chen, Y. Nanofabrication by electron beam lithography and its applications: A review. *Microelectronic Engineering* **135**, 57–72 (2015).
- [198] Kläui, M. *et al.* Domain wall behaviour at constrictions in ferromagnetic ring structures. *Physica B: Condensed Matter* **343**, 343–349 (2004).
- [199] Schreiber, F. *et al.* Concurrent magneto-optical imaging and magneto-transport readout of electrical switching of insulating antiferromagnetic thin films. *Applied Physics Letters* **117** (2020).
- [200] Argyres, P. N. Theory of the faraday and kerr effects in ferromagnetics. *Physical Review* **97**, 334 (1955).

-
- [201] Josephson, B. D. Possible new effects in superconductive tunnelling. *Physics Letters* **1**, 251–253 (1962).
- [202] Foner, S. Versatile and sensitive vibrating-sample magnetometer. *Review of Scientific Instruments* **30**, 548–557 (1959).
- [203] Bitter, F. Experiments on the nature of ferromagnetism. *Physical Review* **41**, 507 (1932).
- [204] Reeve, R. M., Elmers, H.-J., Büttner, F. & Kläui, M. Magnetic imaging and microscopy. In *Handbook of Magnetism and Magnetic Materials*, 1–52 (Springer, 2021).
- [205] Fowler Jr, C. A. & Fryer, E. M. Magnetic domains by the longitudinal kerr effect. *Physical Review* **94**, 52 (1954).
- [206] McCord, J. Progress in magnetic domain observation by advanced magneto-optical microscopy. *Journal of Physics D: Applied Physics* **48**, 333001 (2015).
- [207] DiStefano, T. Technology for detecting small magnetic domains and beam-addressed memory therewith. *IBM Tech. Disc. Bull* **20**, 4212–4215 (1978).
- [208] Unguris, J., Pierce, D. T., Galejs, A. & Celotta, R. Spin and energy analyzed secondary electron emission from a ferromagnet. *Physical Review Letters* **49**, 72 (1982).
- [209] Koike, K. & Hayakawa, K. Scanning electron microscope observation of magnetic domains using spin-polarized secondary electrons. *Japanese Journal of Applied Physics* **23**, L187 (1984).
- [210] Koike, K. Spin-polarized scanning electron microscopy. *Microscopy* **62**, 177–191 (2013).
- [211] Scheinfein, M., Unguris, J., Kelley, M. H., Pierce, D. T. & Celotta, R. Scanning electron microscopy with polarization analysis (sempa). *Review of Scientific Instruments* **61**, 2501–2527 (1990).
- [212] Allenspach, R. Spin-polarized scanning electron microscopy. *IBM Journal of Research and Development* **44**, 553–570 (2000).
- [213] Chrobok, G. & Hofmann, M. Electron spin polarization of secondary electrons ejected from magnetized europium oxide. *Physics Letters A* **57**, 257–258 (1976).
- [214] Oepen, H. P. & Frömter, R. Scanning electron microscopy with polarisation analysis. *Handbook of Magnetism and Advanced Magnetic Materials* (2007).
- [215] Kirschner, J. & Koike, K. Spin polarization of secondary electrons from fe (110) excited by unpolarized primary electrons. *Surface Science* **273**, 147–159 (1992).

- [216] Kisker, E., Gudat, W. & Schröder, K. Observation of a high spin polarization of secondary electrons from single crystal Fe and Co. *Solid State Communications* **44**, 591–595 (1982).
- [217] Hopster, H., Raue, R., Kisker, E., Güntherodt, G. & Campagna, M. Evidence for spin-dependent electron-hole-pair excitations in spin-polarized secondary-electron emission from Ni (110). *Physical Review Letters* **50**, 70 (1983).
- [218] Schönhense, G. & Siegmann, H. Transmission of electrons through ferromagnetic material and applications to detection of electron spin polarization. *Annalen der Physik* **505**, 465–474 (1993).
- [219] Kirschner, J. & Feder, R. Spin polarization in double diffraction of low-energy electrons from W (001): experiment and theory. *Physical Review Letters* **42**, 1008 (1979).
- [220] Wang, G.-C., Celotta, R. & Pierce, D. T. Polarized low-energy-electron diffraction from W (100). *Physical Review B* **23**, 1761 (1981).
- [221] Porthun, S., Abelmann, L. & Lodder, C. Magnetic force microscopy of thin film media for high density magnetic recording. *Journal of Magnetism and Magnetic Materials* **182**, 238–273 (1998).
- [222] Hartmann, U. Magnetic force microscopy. *Annual Review of Materials Science* **29**, 53–87 (1999).
- [223] Brown, G., Halbach, K., Harris, J. & Winick, H. Wiggler and undulator magnets—a review. *Nuclear Instruments and Methods in Physics Research* **208**, 65–77 (1983).
- [224] Erskine, J. L. & Stern, E. Calculation of the m_{23} magneto-optical absorption spectrum of ferromagnetic nickel. *Physical Review B* **12**, 5016 (1975).
- [225] Schütz, G. *et al.* Absorption of circularly polarized X-rays in iron. *Physical Review Letters* **58**, 737 (1987).
- [226] Stöhr, J. Exploring the microscopic origin of magnetic anisotropies with X-ray magnetic circular dichroism (XMCD) spectroscopy. *Journal of Magnetism and Magnetic Materials* **200**, 470–497 (1999).
- [227] Thole, B., Carra, P., Sette, F. & van der Laan, G. X-ray circular dichroism as a probe of orbital magnetization. *Physical Review Letters* **68**, 1943 (1992).
- [228] Cascales-Sandoval, M. A. *et al.* Determination of optimal experimental conditions for accurate 3D reconstruction of the magnetization vector via XMCD-PEEM. *Synchrotron Radiation* **31**, 336–342 (2024).
- [229] Schaffers, T. *et al.* Extracting the dynamic magnetic contrast in time-resolved X-ray transmission microscopy. *Nanomaterials* **9**, 940 (2019).

-
- [230] Weigand, M. *et al.* Timemaxyne: A shot-noise limited, time-resolved pump-and-probe acquisition system capable of 50 ghz frequencies for synchrotron-based x-ray microscopy. *Crystals* **12**, 1029 (2022).
- [231] Stoll, H. *et al.* Imaging spin dynamics on the nanoscale using x-ray microscopy. *Frontiers in Physics* **3**, 26 (2015).
- [232] Cui, Q., Zhu, Y., Liang, J., Cui, P. & Yang, H. Antiferromagnetic topological magnetism in synthetic van der waals antiferromagnets. *Physical Review B* **107**, 064422 (2023).
- [233] Dohi, T. *et al.* Enhanced thermally-activated skyrmion diffusion with tunable effective gyrotropic force. *Nature Communications* **14**, 5424 (2023).
- [234] Hellwig, O., Berger, A., Kortright, J. B. & Fullerton, E. E. Domain structure and magnetization reversal of antiferromagnetically coupled perpendicular anisotropy films. *Journal of Magnetism and Magnetic Materials* **319**, 13–55 (2007).
- [235] Schönke, D., Oelsner, A., Krautscheid, P., Reeve, R. M. & Kläui, M. Development of a scanning electron microscopy with polarization analysis system for magnetic imaging with ns time resolution and phase-sensitive detection. *Review of Scientific Instruments* **89**, 083703 (2018).
- [236] Legrand, W. *et al.* Room-temperature stabilization of antiferromagnetic skyrmions in synthetic antiferromagnets. *Nature Materials* **19**, 34–42 (2020).
- [237] Shen, L. *et al.* Current-induced dynamics and chaos of antiferromagnetic bimerons. *Physical Review Letters* **124**, 037202 (2020).
- [238] Ge, Y. *et al.* Constructing coarse-grained skyrmion potentials from experimental data with iterative boltzmann inversion. *Communications Physics* **6**, 30 (2023).
- [239] Woo, S. *et al.* Deterministic creation and deletion of a single magnetic skyrmion observed by direct time-resolved x-ray microscopy. *Nature Electronics* **1**, 288–296 (2018).
- [240] Kern, L.-M. *et al.* Time-resolved imaging reveals transiently chaotic spin-orbit-torque-driven dynamics under controlled conditions. *arXiv preprint arXiv:2401.12130* (2024).
- [241] Shimojima, T. *et al.* Nano-to-micro spatiotemporal imaging of magnetic skyrmion's life cycle. *Science Advances* **7**, eabg1322 (2021).
- [242] Akosa, C. A., Tretiakov, O., Tatara, G. & Manchon, A. Theory of the topological spin hall effect in antiferromagnetic skyrmions: Impact on current-induced motion. *Physical Review Letters* **121**, 097204 (2018).

-
- [243] Göbel, B., Schimpf, L. & Mertig, I. Topological orbital hall effect caused by skyrmions and antiferromagnetic skyrmions. *Communications Physics* **8**, 17 (2025).
- [244] Büttner, F. *et al.* Observation of fluctuation-mediated picosecond nucleation of a topological phase. *Nature Materials* **20**, 30–37 (2021).
- [245] Thiele, A. Steady-state motion of magnetic domains. *Physical Review Letters* **30**, 230–233 (1973).
- [246] Pham, V. T. *et al.* Fast current-induced skyrmion motion in synthetic antiferromagnets. *Science* **384**, 307–312 (2024).
- [247] Büttner, F. *et al.* Dynamics and inertia of skyrmionic spin structures. *Nature Physics* **11**, 225–228 (2015).
- [248] Lemesh, I. *et al.* Current-induced skyrmion generation through morphological thermal transitions in chiral ferromagnetic heterostructures. *Advanced Materials* **30**, 1805461 (2018).
- [249] Je, S.-G. *et al.* Creation of magnetic skyrmion bubble lattices by ultrafast laser in ultrathin films. *nano Letters* **18**, 7362–7371 (2018).
- [250] Juge, R. *et al.* Skyrmions in synthetic antiferromagnets and their nucleation via electrical current and ultra-fast laser illumination. *Nature Communications* **13**, 4807 (2022).
- [251] Mallick, S., Panigrahy, S., Pradhan, G. & Rohart, S. Current-induced nucleation and motion of skyrmions in zero magnetic field. *Physical Review Applied* **18**, 064072 (2022).
- [252] Tomasello, R. *et al.* Performance of synthetic antiferromagnetic racetrack memory: domain wall versus skyrmion. *Journal of Physics D: Applied Physics* **50**, 325302 (2017).
- [253] Büttner, F. *et al.* Field-free deterministic ultrafast creation of magnetic skyrmions by spin–orbit torques. *Nature Nanotechnology* **12**, 1040–1044 (2017).
- [254] Kern, L.-M. *et al.* Tailoring optical excitation to control magnetic skyrmion nucleation. *Physical Review B* **106**, 054435 (2022).
- [255] Gerlinger, K. *et al.* Application concepts for ultrafast laser-induced skyrmion creation and annihilation. *Applied Physics Letters* **118** (2021).
- [256] Khusyainov, D. *et al.* Laser-induced helicity and texture-dependent switching of nanoscale stochastic domains in a ferromagnetic film. *arXiv preprint arXiv:2412.11700* (2024).
- [257] Olleros-Rodríguez, P. *et al.* Non-equilibrium heating path for the laser-induced nucleation of metastable skyrmion lattices. *Nanoscale* **14**, 15701–15712 (2022).

-
- [258] Viñas Boström, E., Rubio, A. & Verdozzi, C. Microscopic theory of light-induced ultrafast skyrmion excitation in transition metal films. *npj Computational Materials* **8**, 62 (2022).
- [259] Gerlinger, K. *et al.* Pump–probe x-ray microscopy of photo-induced magnetization dynamics at mhz repetition rates. *Structural Dynamics* **10** (2023).
- [260] Miltat, J., Rohart, S. & Thiaville, A. Brownian motion of magnetic domain walls and skyrmions, and their diffusion constants. *Physical Review B* **97**, 214426 (2018).
- [261] Kerber, N. *et al.* Anisotropic skyrmion diffusion controlled by magnetic-field-induced symmetry breaking. *Physical Review Applied* **15**, 044029 (2021).
- [262] Huang, P. *et al.* Melting of a skyrmion lattice to a skyrmion liquid via a hexatic phase. *Nature Nanotechnology* **15**, 761–767 (2020).
- [263] Du, H. *et al.* Interaction of individual skyrmions in a nanostructured cubic chiral magnet. *Physical Review Letters* **120**, 197203 (2018).
- [264] Rózsa, L. *et al.* Skyrmions with attractive interactions in an ultrathin magnetic film. *Physical Review Letters* **117**, 157205 (2016).
- [265] Panigrahy, S., Mallick, S., Sampaio, J. & Rohart, S. Skyrmion inertia in synthetic antiferromagnets. *Physical Review B* **106**, 144405 (2022).
- [266] Zhang, X., Zhou, Y. & Ezawa, M. Magnetic bilayer-skyrmions without skyrmion hall effect. *Nature Communications* **7**, 10293 (2016).
- [267] Legrand, W. *et al.* Hybrid chiral domain walls and skyrmions in magnetic multilayers. *Science advances* **4**, eaat0415 (2018).
- [268] Vélez, S. *et al.* Current-driven dynamics and ratchet effect of skyrmion bubbles in a ferrimagnetic insulator. *Nature Nanotechnology* **17**, 834–841 (2022).
- [269] Lemesh, I. & Beach, G. S. Twisted domain walls and skyrmions in perpendicularly magnetized multilayers. *Physical Review B* **98**, 104402 (2018).
- [270] Singh, D. *et al.* Transition between distinct hybrid skyrmion textures through their hexagonal-to-square crystal transformation in a polar magnet. *Nature Communications* **14**, 8050 (2023).
- [271] Lucassen, J. *et al.* Tuning magnetic chirality by dipolar interactions. *Physical Review Letters* **123**, 157201 (2019).

- [272] Meijer, M. J. *et al.* Magnetic chirality controlled by the interlayer exchange interaction. *Physical Review Letters* **124**, 207203 (2020).
- [273] Fallon, K. *et al.* Quantitative imaging of hybrid chiral spin textures in magnetic multilayer systems by lorentz microscopy. *Physical Review B* **100**, 214431 (2019).
- [274] Pollard, S. D. *et al.* Bloch chirality induced by an interlayer dzyaloshinskii-moriya interaction in ferromagnetic multilayers. *Physical Review Letters* **125**, 227203 (2020).
- [275] Garlow, J. A. *et al.* Quantification of mixed bloch-néel topological spin textures stabilized by the dzyaloshinskii-moriya interaction in co/pd multilayers. *Physical Review Letters* **122**, 237201 (2019).
- [276] Dovzhenko, Y. *et al.* Magnetostatic twists in room-temperature skyrmions explored by nitrogen-vacancy center spin texture reconstruction. *Nature Communications* **9**, 2712 (2018).
- [277] Kim, K.-W., Moon, K.-W., Kerber, N., Nothhelfer, J. & Everschor-Sitte, K. Asymmetric skyrmion hall effect in systems with a hybrid dzyaloshinskii-moriya interaction. *Physical Review B* **97**, 224427 (2018).
- [278] Liu, Y. *et al.* Dynamics of hybrid magnetic skyrmion driven by spin-orbit torque in ferrimagnets. *Applied Physics Letters* **122** (2023).
- [279] Grelier, M. *et al.* Three-dimensional skyrmionic cocoons in magnetic multilayers. *Nature Communications* **13**, 6843 (2022).
- [280] Vansteenkiste, A. *et al.* The design and verification of mumax3. *AIP advances* **4** (2014).
- [281] Yu, X. *et al.* Realization and current-driven dynamics of fractional hopfions and their ensembles in a helimagnet fege. *Advanced Materials* **35**, 2210646 (2023).
- [282] Han, D.-S. *et al.* Long-range chiral exchange interaction in synthetic antiferromagnets. *Nature Materials* **18**, 703–708 (2019).
- [283] Avci, C. O., Lambert, C.-H., Sala, G. & Gambardella, P. Chiral coupling between magnetic layers with orthogonal magnetization. *Physical Review Letters* **127**, 167202 (2021).
- [284] Fernández-Pacheco, A. *et al.* Symmetry-breaking interlayer dzyaloshinskii-moriya interactions in synthetic antiferromagnets. *Nature Materials* **18**, 679–684 (2019).
- [285] Bloemen, P., Van Kesteren, H., Swagten, H. & De Jonge, W. Oscillatory interlayer exchange coupling in co/ru multilayers and bilayers. *Physical Review B* **50**, 13505 (1994).

-
- [286] Böhm, B. *et al.* Antiferromagnetic domain wall control via surface spin flop in fully tunable synthetic antiferromagnets with perpendicular magnetic anisotropy. *Physical Review B* **100**, 140411 (2019).
- [287] Böhm, B., Fallarino, L., Pohl, D., Rellinghaus, B. & Hellwig, O. Noncollinear remanent textures induced by surface spin flop in synthetic antiferromagnets with perpendicular anisotropy. *Physical Review Applied* **16**, 014028 (2021).
- [288] Richter, N. *et al.* Temperature-dependent magnetic anisotropy in the layered magnetic semiconductors CrI₃ and CrBr₃. *Physical Review Materials* **2**, 024004 (2018).
- [289] Šmejkal, L., Sinova, J. & Jungwirth, T. Emerging research landscape of altermagnetism. *Physical Review X* **12**, 040501 (2022).
- [290] Go, D., Jo, D., Kim, C. & Lee, H.-W. Intrinsic spin and orbital hall effects from orbital texture. *Physical Review Letters* **121**, 086602 (2018).
- [291] Go, D., Jo, D., Lee, H.-W., Kläui, M. & Mokrousov, Y. Orbitronics: Orbital currents in solids. *Europhysics Letters* **135**, 37001 (2021).
- [292] Ding, S. *et al.* Harnessing orbital-to-spin conversion of interfacial orbital currents for efficient spin-orbit torques. *Physical Review Letters* **125**, 177201 (2020).
- [293] De Clercq, J., Leliaert, J. & Van Waeyenberge, B. Modelling compensated antiferromagnetic interfaces with mumax3. *Journal of Physics D: Applied Physics* **50**, 425002 (2017).
- [294] Hayami, S. & Yambe, R. Meron-antimeron crystals in noncentrosymmetric itinerant magnets on a triangular lattice. *Physical Review B* **104**, 094425 (2021).
- [295] Back, C. *et al.* The 2020 skyrmionics roadmap. *Journal of Physics D: Applied Physics* **53**, 363001 (2020).
- [296] Sud, A. *et al.* Tunable magnon-magnon coupling in synthetic antiferromagnets. *Physical Review B* **102**, 100403 (2020).
- [297] Sud, A. *et al.* Parity-controlled spin-wave excitations in synthetic antiferromagnets. *Applied Physics Letters* **118** (2021).
- [298] Rogdakis, K. *et al.* Spin transport parameters of nbn thin films characterized by spin pumping experiments. *Physical Review Materials* **3**, 014406 (2019).

List of Abbreviations

CMOS Complementary metal-oxide-semiconductor

GMR Giant magneto resistance

TMR Tunnel agnetoresistance

MTJ Magnetic tunnel junction

MRAM magnetoresistive random access memory

STT spin-transfer torque

SOT Spin-orbit torque

3D three-dimension

DMI Dzyaloshinskii-Moriya interaction

FM Ferromagnet

SkHE Skyrmion Hall effect

AFM Antiferromagnet

MCP Magnetic moment compensation point

ACP Angular moment compensation point

SyAFM Synthetic antiferromagnet

NSkHE Non-reciprocal skyrmion Hall effect

LLG	Landau–Lifshitz–Gilbert
DOS	Density of states
SOC	spin-orbit coupling
PMA	Perpendicular magnetic anisotropy
SRT	Spin reorientation transition
OOP	Out-of-plane
IP	In-plane
iDMI	interfacial DMI
HM	Heavy-metal
PIM	proximity-induced magnetic moment
RKKY	Ruderman–Kittel–Kasuya–Yosida
IEC	Interlayer exchange coupling
DW	Domain wall
LL	Landau–Lifshitz
CPP	Current-perpendicular-to-plane
DL	Damping-like
FL	Field-like
CIP	Current-in-plane
SHE	Spin Hall effect
iSGE	Inverse Spin–Galvanic effect
SKHA	Skyrmion Hall angle
UHV	Ultra-high vacuum
TEM	Transmission electron microscopy

- HAADF** High-angle annular dark-field
- EDX** Energy-dispersive X-ray spectroscopy
- EBL** Electron-beam lithography
- MFM** Magnetic force microscopy
- SEM** Scanning electron microscopy
- SEMPA** Scanning electron microscopy with polarization analysis
- SPLEED** Spin-polarized low-energy electron diffraction
- LTEM** Lorentz transmission electron microscopy
- XMCD** X-ray magnetic circular dichroism
- CL** Circular left polarization
- CR** Circular right polarization
- CCD** Charge-coupled device
- FZP** Fresnel zone plate
- OSA** Order-separating aperture
- PEEM** Photoemission electron microscopy
- STXM** Scanning transmission X-ray microscopy
- SQUID** Superconducting quantum interference device magnetometer
- FWHM** Full width at half maximum
- XAS** X-ray absorption spectra

List of Figures

1.1	Overview of topological quasiparticles in synthetic antiferromagnets discussed and experimentally observed in this thesis.	6
2.1	Five levels of magnetic modeling across spatial scales: (1) atomistic theory (< 1 nm); (2) micromagnetic analysis (1–1000 nm), modeling magnetization as a continuous vector field; (3) domain analysis (1–1000 μm), capturing domain structures and boundaries; (4) phase analysis (> 100 μm), describing domain orientation distributions; and (5) macroscopic-scale magnetization curves, representing the average magnetic response to external fields. Adapted from Ref. [86].	10
2.2	Band diagrams representing the density of states (DOS), $g(E)$. (a) Band structure of a non-magnetic metal with partially filled 4s and 3d bands. The spin-up and spin-down sub-bands are equally populated. (b) Band structure of a ferromagnetic metal. Exchange splitting shifts the spin sub-bands, resulting in a net magnetic moment. The figure is schematic and not to scale; the 3d bands host a larger electron population than the 4s bands. Taken from Ref [92].	13
2.3	Origin of DMI due to SOC. (a) Schematic representation of the DMI vector \mathbf{D}_{12} (blue arrow) in a bulk material. Adapted from [34]. (b) Illustration of the DMI vector \mathbf{D}_{12} at the interface between a ferromagnetic layer and a HM layer with strong SOC. In this case, \mathbf{D}_{12} lies perpendicular to the plane formed by the two ferromagnetic atoms (blue) and the atom with strong SOC (red), pointing along the interface. Adapted from [34]. (c) DMI and the filling of the 5d-band, which illustrates the relationship for various transition metals including V, Cr, Mn, Fe, Co, and Ni. Adapted from [106].	18
2.4	RKKY interaction and SyAFMs. (a) Oscillatory dependence of the interlayer exchange interaction on the spacer layer thickness. Taken from [117]. (b) Schematic representation of SyAFMs: (i) bilayers with in-plane magnetization, (ii) bilayers with out-of-plane magnetization, and (iii) multilayer structures. The arrows indicate the magnetization direction in each ferromagnetic layer. Taken from [82].	21
2.5	Different wall types and their profile. (a) Left-handed Bloch wall and (b) right-handed Bloch DW. (c) Left-handed chiral Néel DW and (d) right-handed chiral Néel DW. (e) Bloch and (f) Néel domain walls with their corresponding magnetization profiles.	23

2.6	Field-driven evolution of magnetic bubble domains in a uniaxial thin film under an increasing out-of-plane bias field. Beginning from the zero field state, the external field is increased from (a) to (c) , resulting in the nucleation of bubble domains. Adapted from [124].	25
2.7	Spin texture and topology of a Néel skyrmion and an antiskyrmion. (a) Schematic of a Néel skyrmion and (b) an antiskyrmion, each shown both as a two-dimensional spin texture and as the corresponding mapping onto the unit sphere. The color scale indicates the out-of-plane magnetization component: red corresponds to spins aligned along $+\hat{z}$, blue to spins aligned along $-\hat{z}$, and green to in-plane magnetization.	28
2.8	Magnetization textures of skyrmions and antiskyrmions for different helicities. The top row (a)–(d) corresponds to skyrmions with $w = +1$, while the bottom row (e)–(h) represents antiskyrmions with $w = -1$. Columns (a)–(d) correspond to helicities $\gamma = 0, \pi/2, \pi,$ and $3\pi/2$, respectively. These configurations represent: (a) clockwise (CW) Néel, (b) counterclockwise (CCW) Néel, (c) CCW Bloch, and (d) CW Bloch textures.	29
2.9	Spin texture and topology of a Néel meron and an antimeron. (a) Schematic of a Néel-type meron and (b) an antimeron, each represented both in the two-dimensional spin texture and in a corresponding mapping onto the unit sphere. The color scale indicates the out-of-plane magnetization component: red denotes spins aligned along $+\hat{z}$, blue along $-\hat{z}$, and green corresponds to in-plane magnetization.	32
2.10	Topological charge composition of a meron–antimeron pair and a bimeron. (a) A trivial meron–antimeron pair formed by combining a Néel meron and an antimeron with the same core polarity. Each substructure carries the opposite topological charge, resulting in a total topological charge $Q_{sk} = 0$. (b) A bimeron formed by pairing a meron and an antimeron with opposite core polarities. In this case, both constituents carry the same topological charge $Q_{sk} = 1/2$, yielding a net topological charge $Q_{sk} = \pm 1$	33
2.11	Magnetization dynamics: showing the effect of precession and damping term. Whereas precession induces an angular motion around the effective field, damping progressively orients the spin toward the field axis, producing a spiral path.	35
2.12	Spin-transfer torques in CPP and CIP geometry. (a) A spin-polarized current generated in a fixed magnetic layer is transmitted into the free layer, where itinerant spins reorient with the local magnetization, exerting a torque through angular momentum conservation. (b) In a magnetic stripe, itinerant spins progressively reorient in response to a magnetization gradient, which is displaced along the electron flow direction.	36
2.13	Mechanisms of spin Hall effect. Schematic illustration of (a) skew scattering and (b) side-jump contributions to the SHE. Adapted from [158].	39

- 2.14 **Current-induced motion of chiral Néel domain walls driven by damping-like spin-orbit torque.** (a) For a right-handed Néel wall ($D_{\text{iDMI}} > 0$), the wall core magnetization points along $+x$, yielding an effective damping-like field H_{DL} oriented upward $+z$ at the wall center. (b) For a left-handed Néel wall ($D_{\text{iDMI}} < 0$), the wall core magnetization points along $-x$, resulting in a reversed H_{DL} along $-z$ and domain wall motion in the direction $-x$ under the same current polarity. 40
- 2.15 **Skyrmion Hall effect.** Schematic illustration of skyrmion motion under a spin-orbit torque SOT driving force F_{SOT} . The skyrmion with topological charge $Q_{\text{sk}} = 1$ experiences a transverse gyrotropic force and a dissipative drag in addition to the driving force. The resulting velocity \mathbf{v} acquires both longitudinal and transverse components, giving rise to the SkHE. 43
- 3.1 **Schematic illustration of the magnetron sputtering process.** Argon gas is ionized near the target, and the resulting Ar^+ ions are accelerated toward the negatively biased target, ejecting metal atoms that deposit on the substrate to form a thin film. Redrawn based on [192]. 50
- 3.2 **Structural and compositional analysis of stack #S3d.** (a) Cross-sectional TEM image of the multilayer showing 25 repetitions of the SyAFM unit. The magnified view highlights the well-defined multilayer periodicity and uniform layer thickness. (b) High-angle annular dark-field (HAADF) image revealing sharp interfaces and clear contrast between the heavy-metal and ferromagnetic layers. (c) EDX elemental maps for Fe (red), Co (blue), Pt (yellow), and Ir (green). The maps confirm distinct chemical layering of Fe- and Co-rich sublattices and precise control of spacer layers. 51
- 3.3 **Illustration of the working principle of SQUID magnetometry.** (a) Schematic of a DC SQUID consisting of a superconducting loop with two Josephson junctions. The magnetic flux threading the loop is quantized in integer multiples of the flux quantum Φ_0 . (b) Variation of I_S with the applied magnetic flux Φ , showing its periodic behavior arising from flux quantization. (c) Schematic of the SQUID magnetometer setup. The sample is moved through superconducting pick-up coils, inducing a current that is transferred to the SQUID input coil via a flux transformer. A perpendicular magnetic field can be applied to the sample using a superconducting magnet. The resulting flux in the input coil is detected by the SQUID, which converts it into a voltage signal proportional to the sample's magnetic moment. (d) Example of the measured SQUID voltage signal as a function of the sample position within the pick-up coils. 53

-
- 3.4 **Nanofabrication procedure on silicon nitride membranes.** (a) Schematic illustration of the fabrication process. The SiN membrane (300 μm window) is first coated with an MMA/PMMA bilayer resist, patterned using EBL, and developed. The magnetic multilayer is then deposited by sputtering (using a Singulus system), followed by lift-off to define the magnetic wires. A second EBL step is used to pattern the contact pads, which are deposited by sputtering and finalized after lift-off. (b) Optical micrograph of a completed device showing the patterned magnetic tracks and contact pads. (c) Example of membrane wrinkling observed when the film is deposited directly on a bare SiN membrane. 55
- 3.5 **Working principle and vector magnetization mapping in SEMPA.** (a) Schematic illustration of the SEMPA setup showing the detection of spin-polarized secondary electrons scattered from a W(100) SPLEED crystal and counted by four Channeltron detectors positioned at the LEED diffraction spots. (b, c) Spatially resolved spin contrast along two orthogonal in-plane magnetization components obtained from an $\text{MgAl}_2\text{O}_4/\text{Fe}(001)/\text{Pt}(1\text{ nm})$ sample. (d) Reconstructed color-coded vector magnetization map, where the hue represents the in-plane magnetization direction. 58
- 3.6 **Basic principle of MFM.** MFM in double pass mode showing the first pass topo-scan for surface topography and the second pass lift for the magnetic image. 60
- 3.7 **Illustration of the XMCD two-step model.** (a) Schematic illustration of the XMCD process. Circularly polarized X-rays (σ^+ and σ^-) excite electrons from the spin-orbit split $2p_{3/2}$ and $2p_{1/2}$ core levels into unoccupied $3d$ states, giving rise to the L_3 and L_2 absorption edges, respectively. (b) and (c) XAS recorded at the Co and Fe L_3 edges for stack #M12 at a mono-domain state (discussed in Chapter 4). 64
- 3.8 **Schematic of the operating principle of PEEM.** Photoelectrons excited by incident X-rays are spin polarized and emitted from the sample surface. A high accelerating voltage accelerates the electrons through an electromagnetic lens system that focuses and magnifies the image onto a detector screen. Magnetic contrast can be achieved either by using circularly polarized photons or by incorporating a spin detector into the electron path (not shown here). In the schematic, gray on the sample indicates regions with magnetization perpendicular to the X-ray beam, while white and black regions correspond to magnetization parallel and antiparallel to the X-ray beam, respectively. To obtain a full in-plane 360° magnetization map, the sample is rotated by 90° , and the two orthogonal images are combined to reconstruct the complete in-plane color-coded magnetization vector field. 66

- 3.9 **Schematic illustration of the STXM.** Circularly polarized X-rays are focused onto the sample by an FZP and pass through an OSA to isolate the first diffraction order. The transmitted photons are collected by a photodiode. The sample consists of two ferromagnetic sublattices (Fe-rich and Co-rich) separated by nonmagnetic spacers, allowing element-specific imaging at the respective Fe and Co L_3 absorption edges. A picosecond IR laser provides localized heating that transiently modifies the magnetic energy landscape, leading to skyrmion nucleation. Contact pads enable in-situ electrical excitation during measurements. 68
- 4.1 **Spin configuration of AFM merons and antimerons in a SyAFM platform having $Q = \frac{1}{2}$.** (a)–(d) $Q = \frac{1}{2}$ AFM meron with helicities $\gamma = 0, \frac{\pi}{2}, \pi,$ and $\frac{3\pi}{2}$, respectively. (e)–(h) $Q = \frac{1}{2}$ AFM antimeron with helicities $\gamma = 0, \frac{\pi}{2}, \pi,$ and $\frac{3\pi}{2}$, respectively. Adapted from [1] 74
- 4.2 **Spin configuration of AFM merons and antimerons in a SyAFM platform having $Q = -\frac{1}{2}$.** (a)–(d) $Q = -\frac{1}{2}$ AFM meron with helicities $\gamma = 0, \frac{\pi}{2}, \pi,$ and $\frac{3\pi}{2}$, respectively. (e)–(h) $Q = -\frac{1}{2}$ AFM antimeron with helicities $\gamma = 0, \frac{\pi}{2}, \pi,$ and $\frac{3\pi}{2}$, respectively. 75
- 4.3 **Sketch of the bilayer SyAFM.** The metallic spacer (grey) is sandwiched between two ferromagnetic layers (red), which present different saturation magnetizations, $M_{s,A}$ (sub-lattice A) and $M_{s,B}$ (sub-lattice B). The itinerant charges flowing through the spacer mediate the interlayer (antiferromagnetic) exchange interaction. Furthermore, the two ferromagnetic layers also interact via a demagnetizing field H_d along the normal to the heterostructure. An effective low-energy long-wavelength description of the SyAFM can be obtained in terms of the Néel order $L = M_A - M_B$ and macroscopic spin density $M = M_A + M_B$, which corresponds to that of a ferrimagnet (far from the compensation point $\Theta = M_{s,A}^2 - M_{s,B}^2 = 0$). Adapted from [1] 76
- 4.4 **Material stack and composition of the SyAFM.** (a) Schematic representation of the multilayer SyAFM stack, consisting of alternating ferromagnetic sublattices A (FM_A) and B (FM_B) that are antiferromagnetically coupled via interlayer exchange. The layers are separated by Pt and Ir, with thicknesses (in nm) indicated in parentheses. (b) Composition map of the SyAFM sublattices for the sample stacks #M1–#M11. Each grid cell represents a sample with sublattice compositions defined by the x and y axes, indicating the respective richnesses of $Co_{0.6}Fe_{0.2}B_{0.2}$ (CFB) and $Fe_{0.6}Co_{0.2}B_{0.2}$ (FCB) in sublattices A and B. 78
- 4.5 **Magnetic properties and OOP domains in stack # M1.** (a) Magnetic hysteresis loop as a function of the number of repetitions (2, 12, and 20 layers) of the stack # M1 measured using SQUID magnetometry. (b,c) SEMPA images of the same stack. (b) Horizontal and (c) vertical in-plane components of the surface magnetization. The direction of magnetization is indicated by the grayscale contrast, as displayed on the double arrows. 80

- 4.6 **Magnetic properties of SyAFM stacks #M2 to #M11.** (a)–(i) OOP (blue) curves and IP (red) hysteresis loops measured using SQUID magnetometry. Insets show the corresponding MFM images taken at room temperature and zero magnetic field. Stacks #M2, #M3, #M6, and #M7 ((a), (b), (d), and (e)) exhibit a separation between the IP and OOP loops, indicating a positive K_{eff} . In contrast, stacks #M4, #M8–#M11 ((c), (f)–(i)) show nearly identical IP and OOP loops, indicating vanishing effective anisotropy ($K_{\text{eff}} \approx 0$), a key requirement for stabilizing (anti)merons and bimerons. MFM images of stack #M11 show the presence of merons and antimerons as marked in black and green circles, respectively. Hysteresis loops having positive K_{eff} are shown on a white background, while those with near-zero anisotropy are highlighted with a light red background. 82
- 4.7 **Imaging the Néel order parameter of (anti)merons and bimerons in synthetic antiferromagnets.** (a) SEMPA image showing the IP spin components of the topmost FM_A layer, or, equivalently, the IP component of the Néel order of the meron texture in the stack #M11. (b) MFM image showing the OOP spin component of the FM_A layers, that is, the OOP component of the Néel order of the meron structure from the same area. Dark brown and white MFM contrasts indicate the upward and downward direction, respectively. The color map for the SEMPA image is shown on the right side. Black dotted circles represent merons of helicity $\gamma = \pi$, whereas double black dotted circles indicate antimerons, both with $Q = -\frac{1}{2}$. White circles represent merons having an arbitrary helicity with $Q = \frac{1}{2}$ and white double circles denote merons of helicity $\gamma = 0$ and $Q = \frac{1}{2}$. Two adjacent black circles (single and double) are identified as bimerons with net topological charge $Q = -1$ and are additionally highlighted by ellipses. (c) an AFM Néel meron having $\gamma = 0$ and $Q = \frac{1}{2}$, (d) an AFM Néel meron having $\gamma = \pi$ and $Q = -\frac{1}{2}$ and (e) an AFM antimeron having $Q = \frac{1}{2}$. Adapted from [1] 84
- 4.8 **Structure of a single bimeron.** Zoomed-in view of IP (a) and OOP (b) component of single bimeron. (c) Micromagnetic simulation results giving the spin structures of a bimeron. (d) Simulated MFM phase contrast of the bimeron. 85
- 4.9 **Quantitative analysis of the MFM contrast.** (a) Line profiles b1, b2, and b3 show the MFM signal of the up core polarity. (b) The line profiles w1, w2, and w3 represent the MFM signal of the down core polarity. The solid curves correspond to fits of the measured points using Gaussian peak functions. The horizontal axis gives the distance along each corresponding line profile from the meron cores, as depicted in the insets. 86

-
- 4.10 **Quantitative analysis of (anti)merons cores.** (a) Distribution of different core diameters obtained from various MFM images. (b) Histogram of the next-neighbour separation between the centers of structures with up-up, down-down, and up-down core polarities from the MFM phase contrast. Adapted from [1] 87
- 4.11 **Uncompensated SyAFM stack and its magnetic properties.** (a) Schematic illustration of the uncompensated SyAFM stack, composed of 14 repetitions of asymmetric ferromagnetic sublayers separated by spacer layers, designed to yield an uncompensated magnetic moment. (b) Normalized IP (red) and OOP (blue) $M(H)$ hysteresis loops for stack #M12, measured via SQUID magnetometry. 89
- 4.12 **Controlling the helicity of (anti)merons in SyAFM.** (a) SEMPA image showing the IP spin components of the meron spin texture in the stack #M4, indicating the IP orientation of the staggered magnetization. Black and white circles denote antimerons and merons, respectively. (b) Distribution of helicities of the merons present in SyAFM. The abundance of helicity values around 0 and π indicates homochiral Néel merons in the stack. (c) SEMPA image showing the IP spin components of the meron spin texture in the (uncompensated) case of stack #M12. (d) shows the prevalence of Bloch merons having helicities of $\pi/2$ and $3\pi/2$ in this stack. Adapted from [1] 90
- 4.13 **Temperature-dependent evolution of (bi)merons in stack #M6.** (a–e) MFM phase images acquired from the same scan area at temperatures of 300 K, 250 K, 200 K, 150 K, and 100 K, respectively. A progressive enhancement in phase contrast and an apparent increase in the core size of (anti)merons are observed upon cooling. (f) Line profiles across individual (bi)merons (shown as T1) at each temperature, showing a systematic broadening of the phase signal with decreasing temperature. (g) Extracted core diameters, defined as the FWHM from Gaussian fits to the line profiles, as a function of temperature. Adapted from [2] 92
- 4.14 **Temperature-driven transition of (bi)merons to OOP stripe domains.** (a) OOP magnetic hysteresis loops measured at various temperatures reveal a spin reorientation transition near 50 K. The inset shows the coercive field region in greater detail, confirming the emergence of remanent magnetization with decreasing temperature. (b) Corresponding MFM images acquired at 300 K, 50 K, and 3 K, demonstrating the transition of spin textures across the SRT. At 300 K, the sample exhibits dense (anti)meron-like textures, characteristic of in-plane magnetized systems. At 3 K, the system transitions into a fully OOP multidomain state, with labyrinthine stripe domains replacing isolated meronic textures. Adapted from [2] 93

- 4.15 **XMCD-PEEM Imaging of stack #M13.** (a) Sample structure for stack #M13. XMCD-PEEM images of domains in the SyAFM at (b) Co edge and (c) Fe. The white circle shows meronic spin texture in the two top layers of the SyAFM. Presence of the same sign but with opposite contrast confirms the antiferromagnetic coupling between the layers. 94
- 4.16 **Phase Diagram and micromagnetic simulation of bimerons in synthetic antiferromagnets.** (a-c) D vs K_{eff} phase diagrams corresponding to different values of J_{AFM} : (a) $J_{\text{AFM}} = 4.4 \times 10^{-4} \text{ Jm}^{-2}$, (b) $J_{\text{AFM}} = 1 \times 10^{-5} \text{ Jm}^{-2}$, and (c) $J_{\text{AFM}} = 1 \times 10^{-6} \text{ Jm}^{-2}$. The ground-state phases converge at the triple point D_c in the $D - K_{\text{eff}}$ phase diagram, indicated by a black star. Dark green, yellow, and bronze colors represent the uniform IP, uniform OOP, and helical ground-state phases in the rz plane, respectively, with r being any radial direction. The light green color depicts the region where AFM merons are stabilized in micromagnetic simulations. The phase diagrams in (b-c) illustrate a displacement of the triple point to the right. (d) Evolution of the separation between the two cores of different polarities of a bimeron and its energy terms; anisotropy energy (E_{ani}), and demagnetizing energy (E_{demag}) as a function of the interlayer exchange strength. The material parameters used in the simulations, including the volume contribution, are provided in Appendix B, Section B.5. Adapted from [1] 96
- 4.17 **Evolution of the separation between meron-antimeron and the energy terms, including total energy (E_{total}), demag energy (E_{demag}), and anisotropy (E_{ani}) energy as a function of (a) iDMI, and (b) effective anisotropy ($|K_{\text{eff}}|$).** 97
- 5.1 **Tuning magnetic compensation and interlayer exchange strength in SyAFM stacks.** (a) OOP hysteresis loops measured via SQUID magnetometry for Stacks #S1-#S5, demonstrating systematic control of magnetic compensation (m_c) through layer thickness engineering. (b) Hysteresis loops for Stacks #S3-#S3c, where the Pt spacer thickness is varied to modulate the interlayer exchange coupling and consequently the saturation field (H_{sat}). 104
- 5.2 **AFM skyrmions observed using MFM.** AFM skyrmions are nucleated via annealing at 170°C for 15 minutes in zero magnetic field in a fully compensated SyAFM stack. (a) AFM topography image confirming uniform surface morphology. (b) MFM phase image showing a dense lattice of skyrmions. (c) Binarized MFM image used to analyze individual skyrmions. (d) Skyrmion circularity map based on $C = 4\pi A/P^2$, where A and P are the area and perimeter of each skyrmion. (e) Histogram of skyrmion radii extracted from the MFM image shown in (b), yielding an average skyrmion radius of $(50 \pm 20) \text{ nm}$ 106

- 5.3 **Magnetic-field-induced AFM skyrmion nucleation.** **(a)** Zoomed-in view of hysteresis loops measured via SQUID magnetometry for stack #S3. Insets in (a) display STXM images acquired at the Fe and Co L_3 edges, revealing domain textures with opposite contrast and confirming the antiparallel alignment of sublattices A and B. **(b)** Field-driven nucleation of AFM skyrmions in stack #S3, imaged using STXM at the Fe L_3 edge. Starting from a worm-like multidomain state at $B_z = 0$ mT, skyrmions are nucleated upon application of a 200 mT out-of-plane magnetic field. As the field is decreased from 200 mT to 100 mT, skyrmions increase in size and eventually extend into stripe domains. The multidomain state is recovered at 0 mT, and skyrmions are re-nucleated upon reapplication of 150 mT. 108
- 5.4 **Current-induced AFM skyrmion nucleation driven by transient Joule heating.** All STXM images were acquired at the Fe L_3 absorption edge. **(a)** At zero magnetic field, the system exhibits a disordered labyrinth domain configuration. **(b)** Application of a static out-of-plane magnetic field ($B = 50$ mT) reduces the density of domains in sublattice A. **(c)** Injection of 20 bipolar current pulses (7.5 ns duration) at $B = 50$ mT initiates AFM skyrmion nucleation. **(d)** Application of 100 bipolar pulses results in the formation of a dense and uniform skyrmion lattice across the racetrack. 110
- 5.5 **AFM skyrmion lattice in a fully compensated SyAFM.** **(a, b)** Sublattice-resolved STXM images acquired at the Fe L_3 (a) and Co L_3 (b) absorption edges reveal the antiferromagnetically coupled skyrmion lattice in stack #S5. The inversion of magnetic contrast between the two sublattices confirms strong AFM interlayer coupling across the multilayer structure. **(c)** Schematic three-dimensional illustration of the AFM skyrmion lattice, showing alternating out-of-plane magnetization in sublattices A (red) and B (blue). **(d)** Magnetic field dependence of the AFM skyrmion lattice, demonstrating its stability over a wide range of out-of-plane fields from -250 mT to $+250$ mT. Adapted from [3]. 112

- 5.6 **Laser-induced nucleation of AFM skyrmions.** (a) Schematic of the SyAFM stack. (b) Magnetic domain configuration of the sample ($B_z = 110$ mT) prior to laser exposure. The red-circled region denotes the area subsequently irradiated by the laser pulse. (c) Image acquired at the Fe L_3 edge (sublattice A) after laser exposure. Isolated circular skyrmions appear within the laser-irradiated region, emerging from the initial labyrinth domain state. (e) Image at the Co L_3 edge (sublattice B), showing opposite magnetic contrast within the same region, confirming the antiparallel alignment of the skyrmions in the two sublattices. (d) Circularity map derived from (c), quantifying the geometric symmetry of the binarized contours using $C = 4\pi A/P^2$, where A and P denote the area and perimeter, respectively. High circularity values ($C \approx 1$, yellow) correspond to localized skyrmion textures within the irradiated region, while lower values (red) indicate elongated stripe domains outside. 114
- 5.7 **Magnetic field dependence of laser-induced AFM skyrmion nucleation.** (a–g) STXM images acquired at the Fe L_3 edge, illustrating the effect of a single 1 ps, 1040 nm laser pulse (fluence = 16 mJ/cm²) on the domain configuration of Stack #S3 under varying out-of-plane magnetic fields, ranging from $B_z = -130$ mT to 200 mT. For each field value, the sample was first initialized into a labyrinth multidomain state via out-of-plane demagnetization, followed by (left image) laser excitation and post-irradiation imaging. (h) The change in skyrmion number as a function of magnetic fields, extracted from the right STXM images. 116
- 5.8 **Fluence-dependent laser-induced nucleation of AFM skyrmions.** STXM images acquired at the Co L_3 edge showing the evolution of magnetic domain textures in Stack #S3 at three representative laser fluences, under a fixed magnetic bias of $B_z = 140$ mT. Each panel displays the domain configuration before (left) and after (middle) a single 1 ps infra-red laser pulse, followed by an out-of-plane demagnetization step (right). (a) At the threshold fluence of $F = 7.33$ mJ/cm², isolated skyrmions nucleate within the laser-irradiated region. (b) At $F = 14$ mJ/cm², a dense skyrmion lattice is formed. 117
- 5.9 **Laser-induced skyrmion nucleation at high fluence.** STXM images at $B_z = 140$ mT recorded before (left), after laser excitation at fluence F (middle), and following demagnetization (right). (a) At $F = 28.3$ mJ/cm², the first signatures of a monodomain-like state emerge in the central region of the laser spot. (b) At $F = 43.3$ mJ/cm², the monodomain region further expands, reducing the available area for skyrmion nucleation. (c) At the highest fluence ($F = 60$ mJ/cm²), demagnetization is not sufficient to restore the original multidomain texture, indicating irreversible modification of the energy landscape due to overheating. 118

-
- 5.10 **Quantitative analysis of fluence-dependent AFM skyrmion nucleation.** (a) Area of laser-modified magnetic regions as a function of laser fluence. Blue circles indicate the total area of changed spin textures due to laser irradiation, while red stars represent the area where skyrmions are nucleated. The divergence between them at higher fluences reflects the transition to a monodomain state where skyrmion nucleation saturates despite growing overall magnetic changes. (b) Change in skyrmion number with increasing laser fluence, showing a clear nucleation threshold (7.33 mJ/cm^2), saturation beyond 30 mJ/cm^2 , and stays almost constant in the high-fluence regime. 119
- 5.11 **Time-resolved single skyrmion displacement in a 90% compensated SyAFM.** (a,b) Static STXM images of a single skyrmion at two equilibrium positions, labeled as State A and State B, respectively. (c) Time evolution of the skyrmion displacement along the X (blue) and Y (red) directions under the application of a bipolar current pulse of 5 ns duration, with successive pulses separated by a $1 \mu\text{s}$ interval. 121
- 5.12 **Skyrmion dynamics in a non-flat energy landscape.** (a) Time-resolved trajectory of a single skyrmion under a bipolar pulse, showing partial displacement. Spheres and stars correspond to skyrmion positions during positive ($J_x > 0$) and negative ($J_x < 0$) pulses, respectively, while gray markers represent stationary positions after corresponding pulses. Insets show contour evolution at four representative positions (p1–p4) during the positive pulse: initial contraction at the trailing edge (p1 to p2), centroid shift with minimal size change (p3), and re-expansion at the leading edge (p4). For the negative pulse, the top inset highlights the contour evolution, with the black-marked region denoting the pinned core area that remains unchanged throughout the excitation cycle. (b) Time evolution of the mean magnetic contrast at region R1 (see inset), plotted after the negative current pulse is switched off. The skyrmion gradually relaxes back to equilibrium over a timescale of approximately 7.5 ns. 124
- 5.13 **Device layout and temporal pump-pulse pattern.** The SyAFM is deposited on a SiN membrane window with gold contact pads for bipolar current-pulse excitation. Adapted from [3]. 125
- 5.14 **Spatio-temporal evolution of an AFM skyrmion lattice during the cycle of bipolar current pulses.** x-displacement map following a negative pulse, used to classify the skyrmions into four categories: immobile (I, blue), mobile (M, red), laterally adjacent to the left (L, green), and to the right (R, black) of the mobile region. The colour scale encodes the net displacement along the x-direction. Circles indicate representative skyrmions from each class exhibiting distinct responses to current excitation. Adapted from [3]. 127

- 5.15 **Incoherent flow regime of AFM skyrmion dynamics.** **(a)** and **(b)** show the motion of skyrmions in sublattices A and B, respectively, under a positive current (J_x) with time evolution tracked over 15 ns. The skyrmion domain boundaries are color-coded to represent the time progression, from purple (earlier times) to yellow (later times). **(c)** and **(d)** illustrate the skyrmion behavior at sublattices A and B, respectively, under a reversed current direction ($-J_x$), demonstrating symmetric displacement and deformation. The time scale for the evolution is indicated by the color bar on the right. Adapted from [3]. 129
- 5.16 **Time-resolved skyrmion relaxation trajectories.** Average displacement traces for each class. Shaded regions indicate the duration of the negative and positive current pulses during the bipolar pulse. Upon pulse termination, all skyrmion classes exhibit recoil opposite to their preceding motion, regardless of previous current polarity. **(a)** I and M skyrmion classes, with the I-skyrmions showing the strongest recoil and M types the weakest. **(b)** The L and R skyrmion classes display asymmetric recoil dynamics, governed by their lateral position relative to the mobile class. All timescales for the recoil dynamics, as extracted via exponential fitting, fall within 3–20 ns. Adapted from [3]. 130
- 5.17 **Quantitative extraction of the skyrmion–skyrmion interaction potential from the scattering dynamics of skyrmions.** **(a)** Comparison between experimentally measured skyrmion trajectories and those predicted by the inverse method based on the Thiele equation for skyrmion R1, capturing their relaxation dynamics after the application of each polarity of the bipolar current pulse. Experimental trajectories are shown for both positive (purple to yellow) and negative (green to blue) current polarities, overlaid with model-predicted trajectories (black dashed and solid lines) obtained by numerical integration of the Thiele equation using the estimated interaction parameters a^* and b^* . **(b)** The extracted skyrmion–skyrmion interaction potential $V_{(a^*,b^*)} = -\partial_r F_{(a^*,b^*)}(r)$, where r is the skyrmion-skyrmion distance. This axis on the right, V , is not scaled to D and represents the interaction potential for a single bilayer, calculated from the left scale using the dissipation constant. Shaded regions represent uncertainty bands for the 68 % confidence intervals. The lower panel shows the skyrmion–skyrmion distances among skyrmions whose trajectories were predicted, as well as separations between those skyrmions and the boundary skyrmions, illustrating the range over which the potential is estimated by the data. Adapted from [3]. 132

- 5.18 **AFM skyrmion dynamics from incoherent to viscous flow regime of motion.** (a–c) At lower current densities ($J_x = 3.02\text{--}3.23 \times 10^{11} \text{ A/m}^2$), skyrmion motion remains irregular due to pinning effects, leading to local lattice distortions and strain accumulation. (d–f) As the current density increases beyond $J_x = 3.37 \times 10^{11} \text{ A/m}^2$, the applied spin-orbit torque overcomes pinning barriers, enabling skyrmions to move coherently. This transition reduces lattice distortions and results in more uniform skyrmion trajectories. At the highest current density ($J_x = 4.14 \times 10^{11} \text{ A/m}^2$), the skyrmion lattice exhibits highly ordered motion with minimal deformation, marking the onset of a fully developed flow regime. The scale bar represents 250 nm. Adapted from [3]. 134
- 5.19 **Viscous flow regime of AFM skyrmion dynamics.** (a) Spatiotemporal evolution of skyrmion motion in sublattice A, visualized by overlaying skyrmion contours at different time steps. The color gradient represents the nanosecond-resolved motion of skyrmions under an applied bipolar current pulse. (b) Corresponding skyrmion dynamics under the reverse direction of current, showing synchronized transport under the same driving conditions. (c) Time-resolved average displacement of a magnetic skyrmion along the X (black) and Y (red) directions under application of current pulses. The grey-shaded regions indicate the duration of the current pulses (J_x). (d) Time-resolved velocity components V_x (black) and V_y (red) of skyrmions in response to the applied voltage (blue), illustrating a direct correlation between skyrmion motion and the external drive. Adapted from [3]. 136
- 5.20 **Suppression of the skyrmion Hall effect in the viscous flow regime** Dynamic skyrmion velocity components v_x (black stars) and v_y (red stars) as a function of applied current density J_x . The skyrmion Hall angle θ_{SkHA} is obtained from the slope of the linear fit to v_y versus v_x , yielding $(1.4 \pm 1.5)^\circ$. Adapted from [3]. 138
- 6.1 **Micromagnetic simulation of hybrid domain walls and hybrid skyrmions in magnetic multilayers.** (a–d) Cross-sectional magnetization profiles of domain walls for different values of interfacial DMI D . Arrows represent the in-plane magnetization, while the color scale denotes the out-of-plane magnetization component (m_z). For $D = 0.0 \text{ mJ m}^{-2}$ (a), dipolar interactions dominate, resulting in a Bloch core in the film mid-plane with Néel caps of opposite chirality at the top and bottom interfaces. For finite DMI ($D = \pm 1.0 \text{ mJ m}^{-2}$) in (b) and (c), the degeneracy between opposite Néel caps is lifted, and the Bloch core is displaced toward the interface with unfavored chirality. For sufficiently large DMI ($D = 2.0 \text{ mJ m}^{-2}$) in (d), the Bloch core is suppressed. (e) Three-dimensional magnetization structure of a hybrid skyrmion in the same multilayer geometry. Adapted from Ref. [267] with permission. 142

- 6.2 **Lorentz TEM imaging of hybrid chiral domain walls. (a,b)** LTEM images acquired with an underfocus of 4 mm and an applied out-of-plane magnetic field of 85 mT, recorded at tilt angles of (a) $\alpha = 0^\circ$ and (b) $\alpha = 10^\circ$. A non-magnetic background was subtracted by referencing images acquired after magnetic saturation. **(c,d)** Line profiles extracted from the regions marked by blue and red lines in (a) and (b), respectively. Adapted from [4]. 145
- 6.3 **Observation of Néel skyrmion tubes.** Direct observation of SyAFM coupling of skyrmion tubes under perpendicular magnetic field of 130 mT in stack #S2 at room temperature, and schematic of the spin structure of the SyAFM skyrmion tube. Adapted from [4]. 146
- 6.4 **Micromagnetic simulations of AFM hybrid chiral skyrmion tubes at varying compensation. (a)** Two-dimensional magnetization profiles of the topmost layer and **(b)** the bottommost layer for skyrmions in SyAFM stacks with magnetic compensation levels of 80 %, 60 %, 50 %, 40 %, and 20 %, respectively. Arrows indicate the local in-plane magnetization direction, while the color scale represents the x -component of the magnetization. At 80 % and 60 % compensation, the helicity remains uniform across the multilayer, corresponding to a Néel-type skyrmion. At 50 %, a helicity gradient emerges through the stack, indicative of a hybrid Néel–Bloch character. At 40 % compensation, the Bloch component becomes more prominent, and at 20 %, the skyrmion exhibits a nearly pure Bloch-type configuration. Adapted from [4]. 148
- 6.5 **Current-induced motion of SyAFM skyrmion tubes in stack #S1.** Static STXM images at the Fe L_3 and Co L_3 absorption edges of stack #S1 (50% compensation), acquired before and after the application of five unipolar current pulses (5 ns duration, $J = 1.3 \times 10^{12}$ A/m²). Adapted from Ref. [4]. 149
- 6.6 **Current-induced motion of SyAFM skyrmion tubes in stack #S2. (a, b)** Static STXM images at the Fe and Co L_3 absorption edges of stack #S2 (80% compensation), acquired before (a) and after (b) the application of five unipolar current pulses (5 ns duration, $J = 9.7 \times 10^{11}$ A/m²). The skyrmion tubes exhibit coherent displacement along the current direction, with opposite contrast at Fe and Co edges confirming their antiferromagnetic nature. **(c)** Statistical distribution of individual SyAFM skyrmion tube velocities for stack #S1, measured under an out-of-plane magnetic field $\mu_0 H_z = 70$ mT and a current density $J = 1.3 \times 10^{12}$ A/m². Red and blue data points correspond to positive and negative current polarities, respectively. The solid curves represent Gaussian fits to the velocity distributions. **(d)** The current density dependence of the average velocity, v_{ave} , is defined by the Gaussian peak with $\pm 1\sigma$ bars of the curve fitting in (c). Green circles, black rectangles, magenta triangles, and orange inverse triangles represent positive current polarity (stack #S1), negative polarity (stack #S1), positive polarity (stack #S2), and negative polarity (stack #S2), respectively. Adapted from [4]. 150

-
- 6.7 **Dependence of the non-reciprocal skyrmion Hall effect on the degree of magnetic compensation.** **(a)** The full statistics of the individual skyrmion Hall angle for stack #S1 ($m_c = 50\%$) under $\mu_0 H_z = 70$ mT at $v_{\text{ave}} = 10$ m s⁻¹. **(b)** The corresponding distribution at $v_{\text{ave}} = 25$ m s⁻¹. Adapted from [4]. 151
- 6.8 **Average velocity dependence of the skyrmion Hall angle.** The average velocity dependence of θ_{ave} with $\pm 1\sigma$ error bars obtained from the Gaussian fits to the peaks. Green circles, black rectangles, magenta triangles, and orange inverse triangles represent positive current polarity (stack #S1), negative current polarity (stack #S1), positive current polarity (stack #S2), and negative current polarity (stack #S2), respectively. 152
- 6.9 **Micromagnetic simulations of current-induced dynamics of hybrid chiral skyrmion tubes.** **(a)** The velocity of hybrid skyrmions in the $m_c = 50\%$ compensated SyAFM system, depicted as a function of the current density for two antiparallel in-plane (x -axis) current directions. **(b)** Variation of the skyrmion Hall angle for hybrid skyrmion tubes as a function of skyrmion velocity for two antiparallel in-plane (x -axis) current directions, showcasing the non-reciprocal response of skyrmions to applied electrical currents at higher current density. Adapted from [4]. 154
- 6.10 **Evolution of dissipation and SOT efficiency tensors in two different regions of skyrmion dynamics.** **(a)** Layer-averaged differences of the dissipation tensor components \tilde{D}_{ij} at skyrmion tube velocities of $v = 11$ m s⁻¹ (left) and $v = 34$ m s⁻¹ (right). **(b)** Corresponding layer-averaged differences of the SOT efficiency tensor components \tilde{I}_{ij} . The tensor components xx , xy , yx , and yy are shown in black, red, green, and blue, respectively. 155
- 6.11 **Helicity evolution of hybrid skyrmions under different dynamic regimes.** **(a)** Helicity of alternating layers during a 5 ns pulse under a positive current direction ($J = 6 \times 10^{11}$ A/m²) in region 1. **(b)** Helicity of alternating layers during a 5 ns pulse under a negative current direction ($J = -6 \times 10^{11}$ A/m²) in region 1. **(c)** Helicity of alternating layers during a 5 ns pulse under a positive current direction ($J = 17 \times 10^{11}$ A/m²) in region 2. **(d)** Helicity of alternating layers during a 5 ns pulse under a negative current direction ($J = -17 \times 10^{11}$ A/m²) in region 2. In region 2, the helicity progressively transforms from a hybrid configuration toward a Néel-type profile during the pulse. **(e)** Layer-resolved helicity difference between positive and negative current directions at a skyrmion tube velocity of $v = 11$ m s⁻¹. **(f)** Corresponding helicity difference at $v = 34$ m s⁻¹, highlighting the layer-dependent asymmetry that gives rise to the non-reciprocity of the SkHE. 156

- 7.1 **Role of anisotropy in magnetic reversal via spin-flop transition in multilayer SyAFM.** Micro-magnetic simulation snapshots showing the evolution of magnetization during the application and reduction of out-of-plane magnetic field, comparing two SyAFMs. **(a)** Case I: $K_{\text{eff,A}} = K_{\text{eff,B}} = 0.03 \text{ MJ m}^{-3}$ showing a symmetric spin flop. **(b)** Case II: $K_{\text{eff,A}} = 0.08 \text{ MJ m}^{-3}$, $K_{\text{eff,B}} = -0.02 \text{ MJ m}^{-3}$ where the sublattice with negative K_{eff} tilts more strongly toward the in plane direction. The color scale represents the out-of-plane magnetization component m_z 163
- 7.2 **Schematic of the SyAFM stack to host skymeron.** The structure consists of 25 repeats of FM bilayers separated by Ir spacers, enabling strong AFM interlayer exchange. Sublattice A has an effective perpendicular anisotropy $K_{\text{eff,A}} > 0$, favoring skyrmions, while sublattice B has an in-plane anisotropy $K_{\text{eff,B}} < 0$, favoring bimerons. The numbers in parentheses give the thickness in nm. 165
- 7.3 **Observation of skyrmion–bimeron pairs (skymerons).** XMCD-STXM images at the Fe L_3 edge (sublattice A) for **(a)** $\mu_0 H_z = 0$ mT, **(b)** -75 mT, and **(c)** -185 mT. Corresponding STXM images at the Co L_3 edge (sublattice B), evidencing AFM coupling at **(d)** $\mu_0 H_z = 0$ and **(e)** -75 mT, and orthogonally aligned bimerons at **(f)** -185 mT. The near-orthogonal skyrmion–bimeron configuration defines a skymeron, schematically illustrated in **(i)**. The skyrmion and bimeron parts of the isolated skymerons are highlighted by red and blue ellipses in **(c)** and **(f)**, respectively. **(g)** XMCD line profiles across L1 at the Fe (red) and Co (blue) edges show the out-of-plane skyrmion contrast in sublattice A and the two-lobed bimeron signature in sublattice B on a uniform in-plane background. **(h)** Sublattice-resolved Line profile across L2. 168
- 7.4 **Observation of a skyrmionium–bimeronium pair (skymeronium).** **(a,b)** STXM images of sublattices A and B after field cycling ($-200 \rightarrow 180 \rightarrow -160 \rightarrow 140$ mT), showing the nucleation of a closed-loop spin texture. In sublattice A, the object corresponds to a skyrmionium, whereas in sublattice B it appears as a bimeronium. Together, these textures form a composite object, referred to as a *skymeronium*. **(c)** Overlay of the down-core and up-core contours from sublattice B, with the points of overlap indicated by white circles. **(d)** Line profiles along the red and blue cuts in (a,b). **(e)** Schematic illustration of the skymeronium spin structure. 170
- 7.5 **Nucleation of skymerons using bipolar current pulses.** **(a)** STXM image at the Fe L_3 -edge showing isolated skymerons in sublattice A, marked by red circles. **(b)** Corresponding STXM image at the Co L_3 -edge showing isolated bimerons in sublattice B, marked by blue circles. Images were acquired under an out-of-plane magnetic field of $\mu_0 H_z = 180$ mT after the application of 100 bipolar current pulses with a current density of $J = 1.2 \times 10^{12} \text{ A/m}^2$ and a pulse width of 7.5 ns. 171

- 7.6 **Laser-induced nucleation of skymerons.** All STXM images were acquired at the Co L_3 -edge. Each panel shows the domain state before (left) and after (right) a single infrared laser pulse (fluence: 26 mJ/cm², pulse duration: 1 ps). Applied out-of-plane fields: **(a)** 120 mT, **(b)** 130 mT, **(c)** 140 mT, and **(d)** 150 mT. Isolated skymerons are marked in blue circles. 172
- 7.7 **Micromagnetic simulation of the topological transformation from an AFM skyrmion to skymeron.** **(a)** Sublattice-resolved AFM skyrmions at zero field with opposite topological charges. **(b–f)** Evolution under increasing out-of-plane magnetic field (50—250 mT), where the skyrmion in sublattice B progressively transforms into a bimeron embedded in an in-plane background, while sublattice A retains a predominantly out-of-plane skyrmion, yielding the skymeron configuration. **(g)** Field-dependent evolution of the normalized background out-of-plane magnetization component m_z in sublattices A and B. **(h)** Evolution of the relative angle between the background magnetization directions of sublattices A and B as a function of OOP fields. The shaded region denotes the skymeron regime. 174
- 7.8 **Evolution of a skymeron from an AFM skyrmion as a function of applied OOP field.** **(a,b)** Simulated line profiles of m_z across the texture centers for sublattices A and B at $\mu_0 B_z = 0$ and 250 mT, corresponding to the AFM skyrmion and skymeron states, respectively. At zero field, both sublattices show symmetric skyrmion profiles with opposite polarity. At 250 mT, sublattice A develops an asymmetric skyrmion profile, while sublattice B transforms into a bimeron with a two-lobed signature. **(c,d)** Evolution of m_z line profiles with field: (c) skyrmion in sublattice A showing progressive asymmetry, and (d) bimeron in sublattice B displaying the characteristic splitting as the background rotates towards the plane. 175
- B.1 **X-ray absorption spectra (XAS) at the Co and Fe L_3 edges using XMCD-PEEM** **(a)** XAS recorded at the Co L_3 edge, showing absorption intensity as a function of photon energy for left (σ^- , blue) and right (σ^+ , black) circularly polarized light. **(b)** Corresponding XAS at the Fe L_3 edge, revealing a stronger XMCD contrast compared to Co, indicative of higher net moment contribution from the Fe sublattice under these conditions. 185
- B.2 **XMCD-PEEM images of domains in the SyAFM at Fe edge and Co edge** **(a)** strong contrast in Fe and weak opposite contrast at Co edge **(b)** strong contrast in Fe and no contrast at Co edge **(c)** strong contrast in Fe and weak similar contrast at Co edge **(d)** 180-degree rotated image showing strong contrast in Fe and weak opposite contrast at Co edge. 186

B.3	Deleting and re-creating (anti)merons. (a) Out-of-plane demagnetized state, (b) state after the application of +50 mT magnetic field along the x -direction, (c) state after the application of -50 mT magnetic field along the x -direction, (d) in-plane demagnetized state. The demagnetized state is achieved following the application of an oscillating magnetic field. Black single circles and white double circles indicate merons with helicity $\gamma = 0$ and $\gamma = \pi$, respectively. Antimerons are marked using a double black circle.	187
B.4	Schematic classification of meron and antimeron spin textures with varying helicity. Panels (a–d) illustrate merons with topological charge $Q = +1/2$ and helicity values $\gamma = 0, \pi/2, \pi, -\pi/2$, respectively. Panels (e–h) show corresponding antimerons with $Q = -1/2$ for the same helicities. The third row (k–o) shows the corresponding SEMPA in-plane spin textures mapped using a color wheel representation of the m_x and m_y components. The out-of-plane component m_z is encoded by grayscale in the top two rows, as indicated by the vertical color bar on the left.	188
B.5	Comparison of an isolated skyrmion and meron spin textures. (a) Isolated skyrmion with topological charge $Q = 1$. (b) Isolated meron with $Q = 1/2$. The spin structure along the indicated grey line is replicated above each 2D image for clarity. Color code reference is shown on the left side of each panel. (c) An example of a meron–antimeron lattice.	190
B.6	Micromagnetic simulation of magnetic hysteresis loops as influenced by the presence of ferromagnetically coupled layers within the stack.	191
B.7	Bimeron evolution in SyAFM with varying repetitions. (a) 2-layer SyAFM, (b) 4-layer SyAFM, (c) 8-layer SyAFM, and (d) 24-layer SyAFM. Here, Z denotes the number of FM layers that are antiferromagnetically coupled.	191
B.8	SEMPA images of the stack #M12, #M6, #M7 and #M10. Horizontal and vertical in-plane components of the surface magnetization. The direction of magnetization is indicated by the grayscale contrast, as displayed on the double arrows.	193
B.9	SEMPA images of stacks #M3, #M8, and #M9. The images display the IP spin components of the topmost FM_A layer. The color code for the spin direction is consistent with that used in Fig. B.3.	194
C.1	Schematic illustration of the SyAFM multilayer stack studied in this thesis. Each repetition unit consists of $[Pt(x)/Ir(0.4)/FM_B/Pt(x)/Ir(0.4)/FM_A]$, repeated N times on a Ta(5.0) seed layer and capped with Pt(1.0). Here, FM_A and FM_B represent the two ferromagnetic sublattices (see Table C.1 for detailed sublattice thickness), while x denotes the Pt spacer thickness that tunes the interlayer exchange coupling.	195
C.2	Calibration curve showing the laser fluence as a function of applied current.	196

- D.1 **Micromagnetic simulations of hybrid antiferromagnetic skyrmions.** Layer-resolved simulation of skyrmion tubes in a twelve-layer synthetic antiferromagnet. **(a)** Type A hybrid antiferromagnetic skyrmion, characterized by an in-plane Bloch component with a fixed helicity throughout the stack. **(b)** Type B hybrid antiferromagnetic skyrmion, stabilized under identical conditions, exhibiting the opposite Bloch helicity. Both configurations result from the superposition of interfacial Néel chirality, stabilized by iDMI, and Bloch contributions induced by long-range dipolar interactions. The two helicity states, clockwise and counterclockwise, are energetically degenerate. In-plane magnetization orientation is color coded, with red indicating alignment along the $+x$ direction and blue along the $-x$ direction. 199
- D.2 **Ferromagnetic resonance characterizing the magnetic properties.** **(a)** Resonance spectra for the field applied parallel to the injected microwave current. **(b)** Resonance frequency as a function of the field for two modes, obtained by fitting the spectra. The solid lines are the fittings. **(c)** Resonance linewidth extracted from the spectra in panel (a). Adapted from [4]. 203
- D.3 **Spin torque–ferromagnetic resonance (ST-FMR) characterization.** **(a)** Microwave absorption spectra for the acoustic mode at 5 GHz resonance frequency and $\theta = 40^\circ$. **(b)** Microscope image of the device used. **(c)** V_{sym} and **(d)** V_{asym} components as a function of θ . Solid lines are fits using Eqs. (S1) and (S2). Adapted from [4]. 204

List of Tables

- 5.1 **Relaxation time constants τ_{relax} and amplitudes for different skyrmion classes after positive and negative current polarities of the bipolar cycle. 130**
- C.1 **List of SyAFM stacks investigated in Chapter 05. 196**
- D.1 **ST-FMR-related parameters obtained experimentally and used in the micromagnetic simulations of SyAFM skyrmion tube dynamics. Adapted from [4]. 205**
- F.1 **Overview of AI-based tools used during the preparation of this thesis. All AI-generated outputs were critically reviewed, corrected, and integrated only after scientific verification by the author. 212**

Publications Related to this Thesis

1. [Mona Bhukta](#), Takaaki Dohi, Venkata Krishna Bharadwaj, Ricardo Zarzuela, Maria-Andromachi Syskaki, Michael Foerster, Miguel Angel Niño, Jairo Sinova, Robert Frömter, and Mathias Kläui, *Homochiral antiferromagnetic merons, antimerons and bimerons realized in synthetic antiferromagnets*, *Nature Communications* **15**, 1641 (2024).
<https://www.nature.com/articles/s41467-024-45375-z>
2. *Takaaki Dohi, *[Mona Bhukta](#), *Fabian Kammerbauer, Venkata Krishna Bharadwaj, Ricardo Zarzuela, Aakanksha Sud, Maria-Andromachi Syskaki, Duc Minh Tran, Thibaud Denneulin, Sebastian Wintz, Markus Weigand, Simone Finizio, Jörg Raabe, Robert Frömter, Rafal E. Dunin-Borkowski, Jairo Sinova, and Mathias Kläui, *Observation of a non-reciprocal skyrmion Hall effect of hybrid chiral skyrmion tubes in synthetic antiferromagnetic multilayers*, *Nature Communications* **16**, 8285 (2025).
<https://www.nature.com/articles/s41467-025-63759-7>
3. [Mona Bhukta](#), Takaaki Dohi, Kilian Leutner, Maria-Andromachi Syskaki, Fabian Kammerbauer, Duc Minh Tran, Sebastian Wintz, Markus Weigand, Robert Frömter, and Mathias Kläui, *Antiferromagnetic Skyrmion Scattering Revealed by Direct Time-Resolved Imaging of Collective Dynamics*, *arXiv:2508.17967* (2025) (Rebuttal stage Nature Physics).
<https://doi.org/10.48550/arXiv.2508.17967>
4. [Mona Bhukta](#), Ankit Sharma, Takaaki Dohi, Maria-Andromachi Syskaki, Robert Frömter, and Mathias Kläui, *Temperature-driven transition from Meron-type spin textures to stripe domains and revealing the nanosecond dynamics of antiferromagnetic quasiparticles through sublattice-resolved X-ray microscopy*, *Proceedings of SPIE, Spintronics XVIII*, **135860K**, (2025).
<https://doi.org/10.1117/12.3063453>

5. Mona Bhukta, Fabian Kammerbauer, Robin Tietgen, Takaaki Dohi, Maria-Andromachi Syskaki, Sebastian Wintz, Markus Weigand, Oleg A. Tretiakov, Bastian Pfau, Robert Frömter, and Mathias Kläui, *Laser-induced Skyrmion Nucleation Through Thermal Transitions in Antiferromagnetically Coupled Multilayers*, (In Preparation),

6. Mona Bhukta, Robert Frömter, and Mathias Kläui et al., *Skyrmeron; An orthogonal Skyrmion-Bimeron Pair and its Current Induced Dynamics*, (In Preparation),

Mona Minakshee Manjaree Bhukta

CV Removed for data protection.

Acknowledgements

Acknowledgements are deleted for data protection.

